Effects of Extreme Impulsive Loads on RC Structures with a view to Strengthening

Isaac, Philip

Award date:
2014

Awarding institution:
University of Bath

Effects of Extreme Impulsive Loads on RC Structures with a view to Strengthening

Philip Michael Isaac

A thesis submitted for the degree of Doctor of Philosophy

University of Bath
Department of Architecture and Civil Engineering

March 2014

Acknowledgments

In finally completing this thesis I owe a huge debt to a number of people.

I'd like to start by thanking my supervisors, Dr Antony Darby, Professor Tim Ibell and Dr Mark Evernden who have been incredibly helpful throughout the journey. In particular I'd like to say a special thanks to Antony for always providing great discussion as well as constant support and encouragement throughout. I'd like to thank Dr Pedro Silva and Dr Tona Rodriguez-Nikl for help with experimental data and providing useful discussions throughout the process.

The technicians in the Structures Laboratory at the University of Bath also deserve special thanks, particularly Will Bazely and Brian Purnell.

A special thanks is owed to all my friends and colleagues in Bath who helped me along the way, particularly those I worked with everyday in the MORG, including Peter Gates, Christopher Gross and Daniel Maskell.

I'd also like to thank friends from AKTII, starting work whilst still writing up wasn't easy but their constant reminders that I hadn't finished and inspiration to finally get me over the line really has meant a lot to me.

Undoubtedly the biggest thanks though are saved to last and that's owed to my family. There have been bumps along the road but their unrelenting and unconditional support is the main reason I've got to this point, so thank you.

Declaration

The author wishes to declare that, except for commonly understood or accepted ideas, or where specific reference is made to the works of others, the content of this dissertation is his own work. The dissertation has not been submitted previously to any University or institution for any degree, diploma, or other qualification. The full length of this dissertation is 214 pages.

Abstract

Accurately predicting the response of reinforced concrete columns to blast and impact loads is essential if structures are to be designed with sufficient robustness. The failure of load bearing columns can have devastating and costly consequences for the inhabitants of the building as history has shown.

Current methods of analysis in this field tend to be either over simplified or too reliant on numerical modelling. It is shown from the literature review that significant gaps exist in our understanding of the complicated response of a member to these types of loads. Presented in this thesis is a range of theoretical modelling and experimental work aimed at addressing some of the limitations identified from the literature review.

Impact tests have shown that as the rate of loading increases the failure mode can become increasingly brittle. It has also been shown that in some cases members that are designed to respond flexurally can actually fail in a catastrophic shear mode. Failure in this way can have potentially devastating consequences for a structure, leaving load bearing columns with little or no residual capacity.

To address this issue this thesis presents the results of a theoretical model developed to predict the forces acting on an impacted member at the initial stage of the response. This model treats the response as a wave like phenomenon, making use of experimental data which showed that a finite time existed between an impact occurring and the supports experiencing the force. Using this theory it was shown that the initial forces generated from a higher velocity, lighter mass impact were greater than those generated from a lower velocity, heavier mass impact. This model is thought to be the first of its kind which is able to demonstrate this increasing brittleness of failure as the rate of loading increases.

The second part of this thesis presents the results of a separate theoretical model, developed to predict the peak displacement of flexurally deforming members subjected to blast and impact loads. The model implicitly assumes that shear failure has been avoided, which, it was shown from the literature and through experimental testing, can be achieved through the application of externally applied fibre reinforced

polymers. The model uses a plasticity based energy method to predict peak displacements and is developed predominantly for blast situations, although the extension to impact situations is also discussed. A major benefit of this approach is that the strain-rates in a section can be calculated during the analysis and employed directly to determine a sections capacity through material dynamic increase factors. When compared with the limited test data available, it is shown that this new model is more accurate than other alternative simplified analysis methods.

In addition to the theoretical models developed, the results from a comprehensive range of testing, carried out using a purpose built impact test rig, are presented. In particular data for the time delay between an impact occurring, and the supports experiencing the force, were instrumental in the development of the model to predict the initial forces on a member.

Contents

Figures

Tables

List of symbols

A_s	Area of steel
b	Width of specimen
c	Longitudinal wave speed in an elastic medium
d	Depth of specimen from compression face to tension steel
E	Young's modulus
F_b	Member bending/shear global stiffness force
F_c	Compression force
f_{ck}	Characteristic concrete compressive strength
F_{imp}	Impact force
F_{ine}	Inertia force
f_t	Tensile strength
f_y	Yield strength
G	Shear modulus
h	Full depth of specimen
i	Impulse
I	Second moment of area
i_e	Impulse per unit length
i_s	Positive phase impulse
k_c	Contact zone stiffness
L	Length
L_{eff}	Effective length
L_p	Plastic hinge length
m	Weight per unit length of member
M	Moment
M_{cr}	Moment in a section at which concrete cracks
M_m	Weight of impacting mass
M_p	Plastic moment capacity of a section
$\dot{P}$	Rate of impact load
P_s	Peak blast pressure
Q	End moment
R	Stand-off distance

T	Natural period
t	Time
t_c	Critical time when first crack forms
t_d	Load duration
t_L	Layer thickness
u	displacement
$\bar{u}$	Wave front velocity
u_w	Distance travelled by shear wave
v	Member velocity
V_{imp}	Impact velocity
W	Force per unit length
Z	Scaled distance
δ	displacement
ε	Strain
$\dot{\varepsilon}$	Strain rate
θ	Hinge rotation
$\dot{\theta}$	Rotational velocity
$\dot{\xi}$	Plastic hinge propagation velocity
μ	Force propagation velocity
ρ	Material density
σ	Stress
χ	Curvature

1. Introduction

1.1. Background

Incidents involving blast and impacts on civil structures fortunately occur relatively rarely. However, despite the rarity of these events many examples exist of situations where disproportionately high levels of damage and loss of life have occurred from these loads. Examples such as the Oklahoma City bomb, 1995 and the attacks of September 11th on the World trade centre indicate how devastating these types of loads can be.

Whilst these events are often considered in the design of new structures, particularly the issue of progressive and disproportionate collapse following Ronan point (1968), the lack of fundamental understanding engineers have of these complex situations limits their ability to effectively design and mitigate the potential effects. In many situations it is also considered financially prohibitive to prevent failure from the full range of loads that could be encountered, particularly considering the low frequency of these events. This situation has led to a rise in more performance based design which, to be useful, requires accurate methods for predicting the effects of a wide range of loads. These methods must contain sufficient detail to represent accurately the intricacies and important aspects of the behaviour of structures and structural members. However, at the same time they must be sufficiently simple and readily applied that engineers with limited expertise in the field can make use of them when designing structures to resist these loads.

Being able to accurately analyse and predict the behaviour of reinforced concrete (RC) members subject to blast and impact loads is complicated due to the wide range of dynamic phenomena that are encountered which are not seen in quasi-static loading situations. This includes phenomena such as stress wave propagation, dynamically enhanced material properties, localised high intensity crushing and micro-crack growth and propagation. One of the most important observations from impact and blast tests on RC members is that, as the rate of loading increases or the pressure intensity increases, so the failure mode of RC members becomes more brittle. It has been shown that where a member would have been designed with sufficient ductility to respond flexurally under quasi-static loads it is often found that it fails in shear under high intensity dynamic loads, leaving the member with little or no residual strength.

Due to the complexity of the situation there tends to be a dependence on either numerical modelling or simplified single degree of freedom systems. However, both have their associated drawbacks. In the case of numerical modelling the lack of a fundamental understanding of some of the features of a member's response hinders the development of accurate models. These models also have a lack of transparency and tend to rely too greatly on user controlled parameters which are often poorly understood. In contrast, single degree of freedom (SDOF) models tend to over simplify the analysis procedure, sacrificing accuracy for ease and conservatism in the solutions. These models are fine in principle and useful for providing initial estimates for behaviour. However, in situations where a more accurate and detailed knowledge of a members behaviour is required then a more comprehensive understanding of the complex response is needed.

1.2. Scope

Given the current limitations with work in this field, the research project described in this thesis is focused on two main objectives:

1. To develop a theoretical model which demonstrates why the rate of loading affects the failure mode of an RC member.
2. To improve the accuracy of current simplified analysis techniques for predicting the peak displacement of blast and impact loaded RC members.

The first part of this work is primarily concerned with assessing the vulnerability of structural RC members. The proposed model is shown to be effective in demonstrating theoretically that the shear demand increases as the rate of loading increases. To date theoretically demonstrating why this change in failure mode occurs has proved difficult with a number of different theories suggested which are outlined in the literature review. It is hoped that eventually this model can be used to predict accurately the susceptibility of structural members to premature shear failures given a range of possible design loads. Where members are deemed susceptible to premature shear failure then it is necessary to provide additional shear reinforcement. In the case of existing structures this can be achieved primarily through external reinforcement with FRP. For strengthened structures where shear failure has been prevented the primary requirement from the analysis is to predict the peak deflection of the member.

To this end the proposed plasticity model in Chapter 6 is shown to be more accurate than alternative simplified methods.

1.3. Outline

This thesis contains eight Chapters, covering both theoretical modelling and experimental testing.

Chapter 2 contains a general overview of the literature in this field, covering the limitations of the current work, which this thesis seeks to address.

Preliminary experimental testing is presented in Chapter 3. This chapter discusses in detail the design and construction of a new impact test rig, built in the structures laboratory at the University of Bath specifically for this project. Also discussed in detail are issues of data acquisition. Only by being able to record the relevant data can useful conclusions be drawn from the work.

Chapter 4 presents the development of a new theoretical model aimed at demonstrating the transition in failure mode seen with increasing rates of loading, for impact loads. This chapter presents important experimental data, which clearly shows the finite time it takes the force from an impact to propagate to the reactions. This observation forms the basis of the proposed model which considers the behaviour of the member during this time period up until the force reaches the reactions. The proposed method treats the member as having a reduced effective length with fixed end conditions during this time. Considering the member in this way and solving the equation of motion over a number of time-steps shows that initially the shear demand on a member is significantly greater than the flexural demand. It is also shown that the forces predicted from higher velocity impacts are greater. Due to the availability of test data this chapter focuses on the behaviour of members subject to impact loads rather than blast loads. Tests to validate this theory are outlined in Chapter 5.

The theoretical and experimental work presented in Chapters 4 and 5 is intended to predict the initial demand on RC members and show why shear failures can occur even when the shear capacity is greater than the flexural capacity. Where shear failure

is avoided and a flexural response is ensured, the primary aim is then to predict the peak displacement of the member. This forms the basis of Chapter 6. The theory in this chapter develops a plasticity model to predict the peak displacement of flexurally deforming members, which includes a novel method for determining accurately the strain-rates within a section and applying them directly in the analysis. Including strain-rate effects is shown to improve the accuracy of predictions made with this model when compared with alternative methods of analysis. The theory in this chapter is developed first for uniformly distributed loads as would be expected in blast situations before being extended to concentrated loads, which are more representative of impact loads.

Chapter 7 presents the results of tests to validate the work presented in Chapter 6 and also demonstrates the improvement in the performance of members which are externally strengthened with FRP.

2. Literature review

The effects of severe impulsive loads have long been of interest to engineers and represent some of the most complex and arduous loading conditions a structure can face. Blast and impact situations are the most commonly encountered severe impulsive loads and it is the response of structures to these types of loads that will be the primary focus of this thesis.

The origins of the field of blast engineering and the design of structures to resist the effects of explosions can be traced back to the First World War (1914-1918). During this time it became necessary for engineers to more accurately predict the effects of explosions both from an offensive perspective but also in terms of designing defence structures and munitions storage facilities. Out of this period came a great deal of empirical work to qualitatively assess the effect of particular explosives. Over the years the focus of those researching in this field has shifted. With the outbreak of the Cold War researchers became primarily concerned about the effects of nuclear explosions (Bulson, 1997). In recent years the focus has shifted again to the effects of terrorist activities, devastating examples of which are shown in Figure 2.1(a) and Figure 2.1(b).

Figure 2.1: (a) Alfred P Murrah building, Oklahoma, 1995; (b) US embassy, Beirut, 1983

2.1. Characteristics of severe impulsive loads

Severe impulsive loads can originate from many sources. Blast loads for example are most often associated with intentional threats, such as ballistics in wartime, or through terrorism, but these loads can also occur through accidental situations such as gas or dust explosions. Impact loads are most readily associated with the collision of vehicles with bridge piers or with buildings. However, other situations, such as falling masses during construction and rock falls in mountainous regions, have the potential to cause significant damage. Also considered within this field are the effects of aircraft or missile impacts (Bangash, 1993). Impact and blast types of situations occur rarely, but events littered through history show that they have the potential to cause significant numbers of casualties and fatalities. For example, 168 people were killed in the Oklahoma city bomb, 1995 (Malvar *et al.*, 2007).

Blast loads are typically characterised by having very high pressure, very short duration and are typically considered as a uniformly distributed load (although this to an extent does depend on the stand-off, which will be discussed in more detail below). A great deal of information on the various types of explosions exists in the many informative books written on this subject e.g. Mays and Smith (1995).

The most common form of explosives are termed 'high explosives' which are typically liquids or solids. When a high explosive is detonated a violent reaction occurs with very high pressures and temperatures forming at the charge. These pressures expand rapidly forcing the air to expand outward with it, causing a layer of compressed air to form (the blast wave) which contains most of the energy of the blast. The pressure in the blast wave decays exponentially with distance from the source. The air around the explosive eventually over expands causing the pressure to drop below atmospheric pressure and the flow reverses in the direction of the explosive, this is commonly referred to as the negative phase. The key properties discussed here are shown in Figure 2.2, where the area under the pressure-time graph is the specific impulse of the blast, *i*, which can be divided into the positive phase impulse and the negative phase impulse. The positive phase impulse, i_s, is given by the integral of force over time, equation 2.1:

$$i_s = \int_0^{t_d^+} p_s(t)\ dt \tag{2.1}$$

The pressure is usually considered to decay exponentially (Cormie *et al.*, 2009), however, this is commonly simplified to a triangular load with a duration t_d (Figure 2.2). With this assumption, equation 2.1 can be simplified to:

$$i_s = \frac{p_s t_d}{2} \tag{2.2}$$

The positive impulse will later be shown to be one of the most convenient ways of comparing blast loads. p_s is the peak pressure, t_d^+ is the positive phase load duration and t_o^- is the negative phase duration.

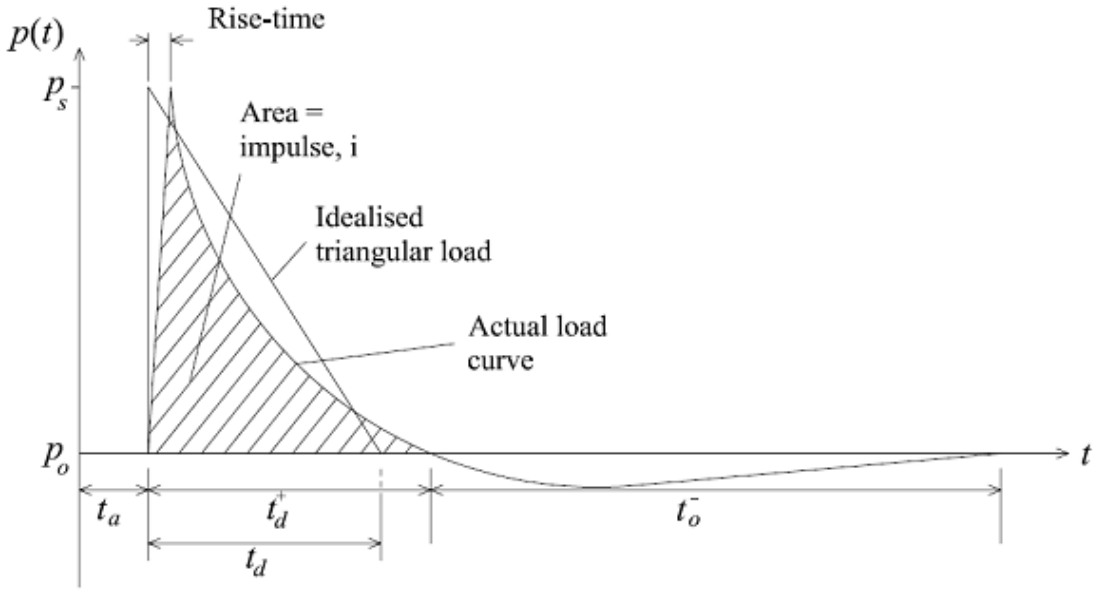

Figure 2.2: Characteristics of blast wave (Adapted from (Smith and Hetherington, 1994) and (Wu and Hao, 2007))

A convenient method for comparing the effects of different size explosions at different stand-off distances is the scaled distance, *Z*, which was first described by Bertram Hopkinson in 1919 (Bulson, 1997). The scaled distance is given by:

$$Z = \frac{R}{W^{\frac{1}{3}}} \quad Z = {}^{R}/_{W^{1/3}} \tag{2.3}$$

where *R* is the stand-off distance (the distance of the explosive from the location under consideration) and *W* is the mass of the explosive (given as a TNT equivalent). Explosive events with constant *Z* values are considered to have identical characteristics as can be seen from the equations for the peak overpressure, p_s, and the positive duration of the load, t_d, which are shown for completeness below:

$$p_s = \frac{6.7}{Z^3} + 1\ bar \qquad (p_s > 10\ bar) \tag{2.4a}$$

$$p_s = \frac{0.975}{Z} + \frac{1.455}{Z^2} + \frac{5.85}{Z^3} - 0.019\ bar \qquad (0.1 < p_s < 10\ bar) \tag{2.4b}$$

$$\log_{10}\left(\frac{t_d}{W^{1/3}}\right) \approx -2.75 + 0.27\log_{10}(Z) \qquad (Z \geq 1.0) \tag{2.5a}$$

$$\log_{10}\left(\frac{t_d}{W^{1/3}}\right) \approx -2.75 + 1.95\log_{10}(Z) \qquad (Z \leq 1.0) \tag{2.5b}$$

Equations 2.4 to 2.5 show that as the scaled distance increases, the static peak overpressure on the structure reduces and the duration of the positive phase becomes longer.

As an example of the predicted characteristics of a blast from equations 2.2-2.5, the Oklahoma bomb, which killed 168 people and destroyed a significant portion of the Alfred P Murrah building (Malvar *et al.*, 2007), was estimated to have a mass of 1814 kg TNT equivalent and was around 4.9 m from the closest column (Campbell, 2001). In this case the peak overpressure would have been 11.2 MPa, the specific impulse 19.8 MPa.ms and the duration of the positive phase 3.5 ms.

When considering columns, there are a number of factors that can affect the precise magnitude and duration of the blast pressure, including the height above ground of the explosive, whether the column is free-standing or part of an infill system and whether the explosion is internal or external (Smith and Hetherington, 1994; Cormie *et al.*, 2009).

The distributed loading from an explosion is generally considered to be uniform when considering an individual member. However, the validity of this assumption is questionable when the stand-off distance is small. Figure 2.3 shows the general spatial variation of the pressure wave. It can be seen that the uniformity increases at larger distances, although it is not clear from the literature at what distance the blast wave can be considered uniform. This is undoubtedly an important issue but for the purposes of the current work, the load is assumed to be uniform.

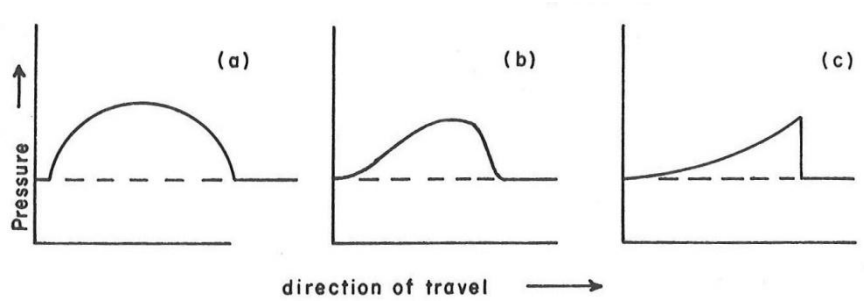

Figure 2.3: Spatial variation of blast pressure wave with inreasing time (Kinney, 1962)

In contrast to blast loads, impact loads tend to have longer durations but the load tends to be applied over a more concentrated area. It would be normal in analysis situations to consider an impact load as a point load (Highways Agency, 2004). Given the large disparity in types of impact loads it is difficult to comment on general design loads that engineers would have to deal with as these would vary significantly between a lorry colliding with a bridge column and a dropped mass on a construction site for example.

The UK's Highways Agency (HA) design standard BD 60/04 requires engineers to design bridge piers to withstand a point load of 1000 kN at the most severe point between 0.75 m and 1.5 m above the carriageway level. This simplified approach avoids the need for a full dynamic assessment. However, it also neglects some of the potentially important dynamic effects, which will be discussed in the following sections.

Given the wide range of possible impact situations it appears that no widely applicable simplified theory has been established that can be used for design across the full range of situations encountered. It is therefore apparent that significant work is required towards this goal of providing a better understanding of structural response to a general impact load. Indeed work is still continuing in quantifying the actual impact force caused by a simple falling mass onto a reinforced concrete member (Cotsovos, 2010) despite some solutions first being presented many years ago (Comite euro-international du beton, 1988) and the apparent simplicity of this situation.

2.2. Effect on structural members

Impact and blast loads both have the potential to cause massive and devastating damage to civil infrastructure. The specific response is often very complicated due to the rapid time varying nature of the load and the incredibly high forces generated.

As a starting point it is useful to consider the range of modes by which energy delivered from a blast or impact can be dissipated by a structure. These modes are indicated in Figure 2.4, which is taken from Gilardi and Sharf (2002). It is generally desirable that structures exhibit ductility which ensures that, under quasi-static loading, warning is given prior to failure. Therefore, dissipating energy through plastic straining is the most desirable mode. With respect to this, the effects of high rates of straining and stress wave propagation become increasingly important. These issues are usually not considered in structural analysis under quasi-static loading. However, under high rate dynamic loading these factors become important in determining the response of a member. The following sections outline the most important of these dynamic effects and the way in which they contribute to the response of a member.

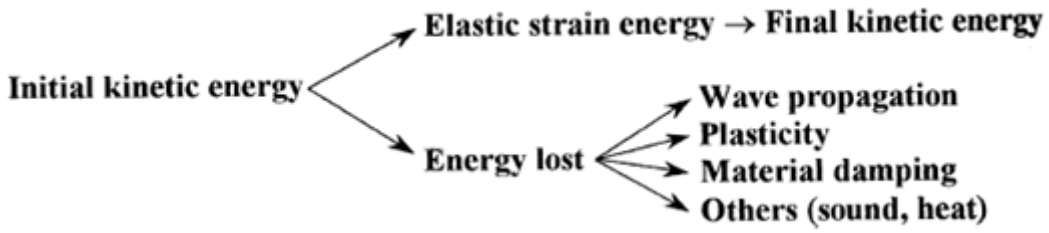

Figure 2.4: Energy dissipation in an impact or blast event (Gilardi and Sharf, 2002)

2.2.1. Strain-rate effects

It has been observed in many experimental studies that the strength of both concrete and steel can increase substantially at high strain-rates, with the biggest gains in strength witnessed at the highest rates (Bischoff and Perry, 1991; Malvar, 1998). A complete theoretical explanation of this phenomenon has yet to receive wide acceptance although a number of theories have been suggested. These include the Stefan effect, which relates to the viscosity of free water in the concrete (Zheng and Li, 2004), inertia effects (Rossi and Toutlemonde, 1996) or that cracks have insufficient time to find the weakest path and instead propagate through the most

direct route (Bischoff and Perry, 1991). It has also been suggested that stress waves are responsible for the observed behaviour. As the magnitude of the stress wave is many times greater than the strength of the material, many micro-cracks are able to grow simultaneously. It was shown by Avnon and Yankelevsky (1992) that when two advancing cracks meet, one or both will stop causing the development of the macro-crack and subsequent failure of the material to be hindered. Contrary to this, under quasi-static rates of loading, as the stress is increased slowly, only the largest flaw will grow and this is responsible for failure of the material (Grady and Kipp, 1985).

Testing at high strain-rates can be complex. A study on the compressive behaviour of concrete at high strain-rates by Bischoff and Perry (1991) provides a detailed description of the test methods employed and the challenges that result from these. It is stated by Bischoff and Perry that impact loads can cause strain-rates in the region of 1-35 s^{-1} and blast loads can cause strain-rates in the region of 100-1000 s^{-1} which compares to a quasi-static loading rate in the region of 10^{-5} s^{-1} (Figure 2.5). However, it is likely that these high strain-rates are due to stress waves rather than longitudinal straining caused by global deformation, which are of more interest when predicting the dynamic capacity of a structural member. Testing at high strain-rates is most often carried out with a Hopkinson bar or split Hopkinson bar (or through actual blast testing, although this has its own associated problems and can be difficult to instrument). High strain-rate testing is made complicated due to the effects of inertia within the specimen, the specimen geometry, difficulties in creating uniform stress and strain profiles, stress wave propagation effects and limitations in the 1-dimensional wave theory used in the analysis (Bischoff and Perry, 1991).

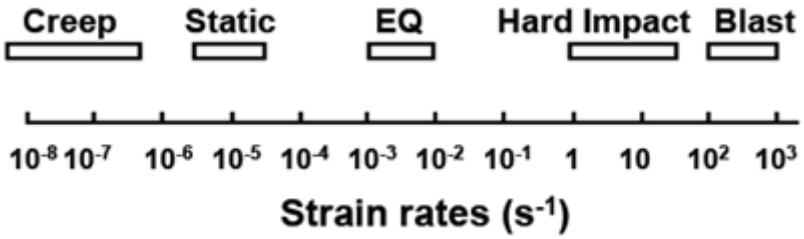

Figure 2.5: Range of strain-rates for different types of loads (Bischoff and Perry, 1991)

A large amount of test data has been collated to establish Dynamic Increase Factors (DIF), which are the ratios of the dynamic strength to the static strength, for different

materials. The DIF is a common and useful method which allows strain-rate dependent material properties to be included in analytical models. Test data for the DIFs of concrete in compression is shown in Figure 2.6a. Similar data has also been collated for concrete in tension and is shown in Figure 2.6b. It can be seen from these two figures that a wide variation in the data exists. Specific equations for the DIF as a function of strain-rate can only be determined by curve fitting of the experimental data. In the case of concrete, in both compression and tension, the relationship is approximated as bi-linear.

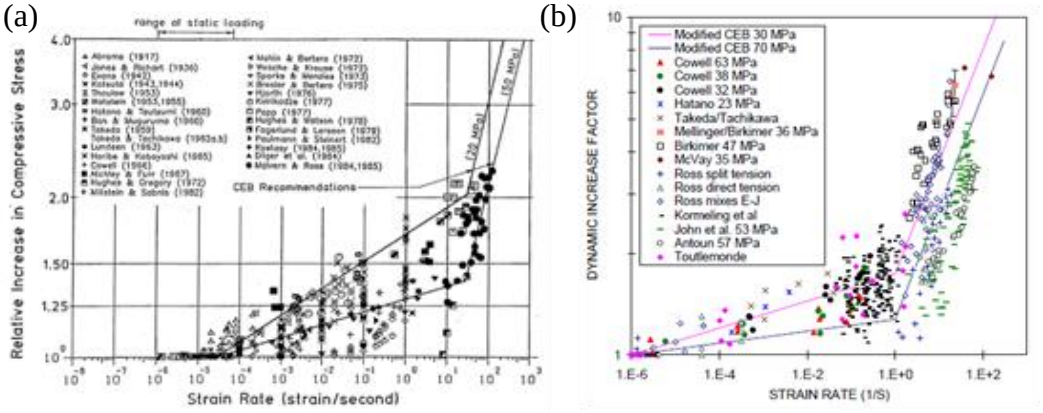

Figure 2.6: DIF for concrete: (a) in compression (Bischoff and Perry, 1991) and (b) in Tension (Malvar and Ross, 1998)

Similar results have been collated for steel by Malvar (1998) for the behaviour of US ASTM A615 bars with increasing strain-rates shown in Figure 2.7. Grade 60 steel has a yield strength of 60 kips per square inch (approximately 410 N/mm^2).

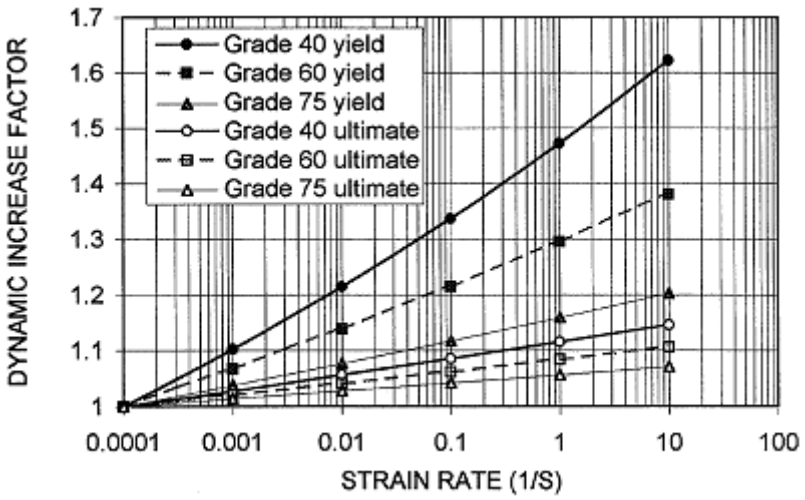

Figure 2.7: DIF for yield and ultimate stress of ASTM A615 steel reinforcing bars (Malvar, 1998)

It has been reported (Bischoff and Perry, 1991) that no agreement has been reached on the effects of strain-rates on the Young's Modulus, the critical compressive strain at maximum stress and the ultimate strain at failure in concrete. It is therefore generally assumed that high strain-rates have no effect on these characteristics, although some authors oppose these claims (Fu *et al.*, 1991a).

The strain-rate dependent increases in the strength of steel and concrete can have a significant effect on the moment capacity of a reinforced concrete member. As an example, Soroushian and Obaseki (1986) determined that the section capacity of a typical RC beam could increase by 25% when the strain-rates increased from a quasi-static rate of $5x10^{-6}$ s^{-1} to a rate of 0.05 s^{-1} which was stated as typical in earthquake situations. Razaqpur *et al.* (2009) went one step further when investigating blast effects on RC columns. It was shown here that when the strain-rate increased from what they considered a quasi-static rate of $1x10^{-7}$ s^{-1} to a rate of 1000 s^{-1}, the maximum moment capacity would theoretically increase by 250% and the energy absorbing capacity by 350%. However, these rates of straining are only encountered due to the propagation of waves which occurs significantly faster than a member can deform. In reality it is only the longitudinal straining that will enhance the strength of the materials and this would not reach the rates investigated by Razaqpur *et al.* (2009).

To date no simplified method for determining the varying rate of straining during the response of a member is available, although some FE packages can include this. Thus

constant, yet conservative values for the DIFs (Krauthammer *et al.*, 1994; Cormie *et al.*, 2009) are usually employed. To overcome this issue Chapter 6 presents a simplified analysis technique that provides an accurate method for calculating strain-rates in a dynamically loaded member and allows the direct application of these in the analysis through material DIFs. The aim of this is to provide an improved method for predicting the peak displacement of flexurally deforming RC members.

2.2.2. Shear/flexural failure transition

The apparent gain in flexural strength is not without its drawbacks. Many authors have shown that as the rate of loading increases substantially above the quasi-static rate, the failure mode of a concrete beam or column can change from a ductile flexural mode to a brittle shear mode. Fu *et al.*, (1991b) reports on this observation in quasi-static and impact tests carried out by Takeda *et al.*, (1977). Similar results have been shown by John and Shah (1990). In this study plain concrete beams were cast, into which a notch was cut on the tension side (Figure 2.8, X indicates the distance of the notch from the support). Successive three point bending tests were carried out under both quasi-static and impact loads in which the position of the notch was advanced from the centre towards the supports. It was shown that when the notch was located in a certain region between the support and the load the beam failed in flexure under the quasi-static load but in shear under the impact load (compare static and impact behaviour when $X = 1\frac{1}{8}$ in Figure 2.8), which indicates the increased brittleness at higher rates of loading.

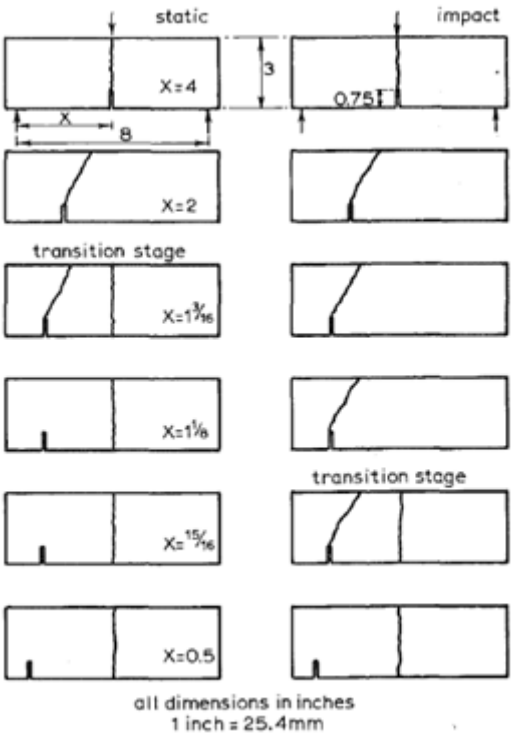

Figure 2.8: Influence of the notch location in determining failure mode in static and impact tests (John and Shah, 1990)

Similar results have also been shown by Magnusson *et al.* (2010) and Kishi *et al.* (2002), who investigated the behaviour of beams without shear reinforcement. Kishi *et al.* (2002) varied the shear span to investigate the effect of different static flexural to shear capacity ratios. One particular specimen, designed with a ratio of just greater than unity (1.03), deformed flexurally at low impact velocities but was shown to fail in shear at higher velocities. This can be seen in Figure 2.9b.

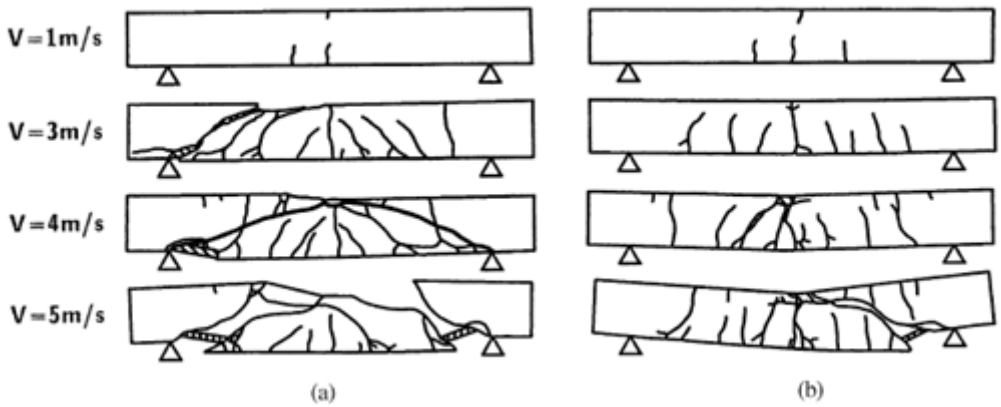

Figure 2.9: Crack patterns from beams tested with varying impact velocity with shear to moment capacity ratios of: (a) 0.64 and (b) 1.03 (Kishi *et al.*, 2002)

The transition to a brittle failure mode at high loading rates is highly undesirable in structural members that must withstand blast loads, as significantly less energy is dissipated and residual capacity is minimal. Tests carried out at the University of California in San Diego (UCSD) (Rodriguez-Nikl, 2006) showed how columns designed to US codes for non-seismic regions failed in a brittle shear manner under simulated blast loading (Figure 2.10). Columns that fail in this manner display no residual strength which can lead to progressive failure of structures.

Figure 2.10: Brittle shear failure of blast loaded column (Rodriguez-Nikl, 2006)

An explanation of this phenomenon has yet to be widely agreed. However, the issue is clearly important particularly in the assessment of RC columns which are often only designed to withstand nominal transverse loads. One explanation from Bertero *et al.* (1973) and reported upon by Fu *et al.* (1991b) was that the only significant effect of high strain-rates was to increase the moment capacity and that the effect on the shear capacity is negligible. However, this appears contradictory to the commonly held view that shear is essentially a tensile mode of failure and that concrete subjected to high rate tensile loading can reach DIFs of the order of 7, significantly higher than concrete in compression (Malvar and Crawford, 1998). Investigating the dependency

of the shear capacity of a member on strain-rates falls outside the scope of the current project but should be addressed in future research.

The most recent development in this field has been made by Cotsovos *et al*. (2008) who have attributed the increase in strength and change in failure mode under impact situations to the role that inertia forces play in a wave dominated response. They suggest that under impact loads a finite time is required for the force to propagate from the point of impact to the supports. During this initial phase of the response it was suggested by Cotsovos, that the dynamic force from the impact is resisted by the inertia of the beam. This is demonstrated from the impact force, inertia force and reaction forces recorded during tests carried out by Saatci and Vecchio (2009a), which are shown in Figure 2.11. From this it is clear that the reactions do not experience the impact force until around 2 ms after the initial impact.

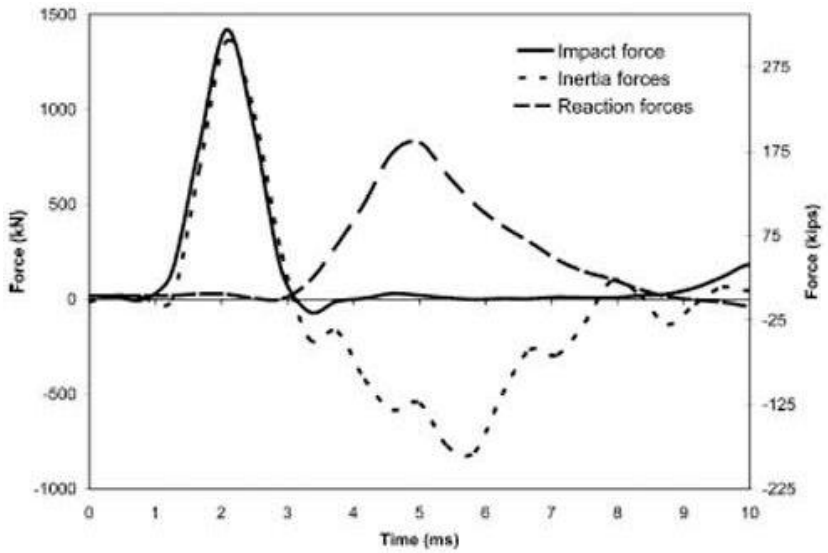

Figure 2.11: Change in forces with time for a point impact load on a RC beam (Saatci and Vecchio, 2009a)

Saatci and Vecchio (2009a) went on to show how including the inertia forces when plotting bending moment and shear force diagrams could have a significant effect on the peak demand, shown in Figure 2.12 (where, α, is the ratio of the inertia force to the impact force, which Saatci and Vecchio showed was initially close to unity)

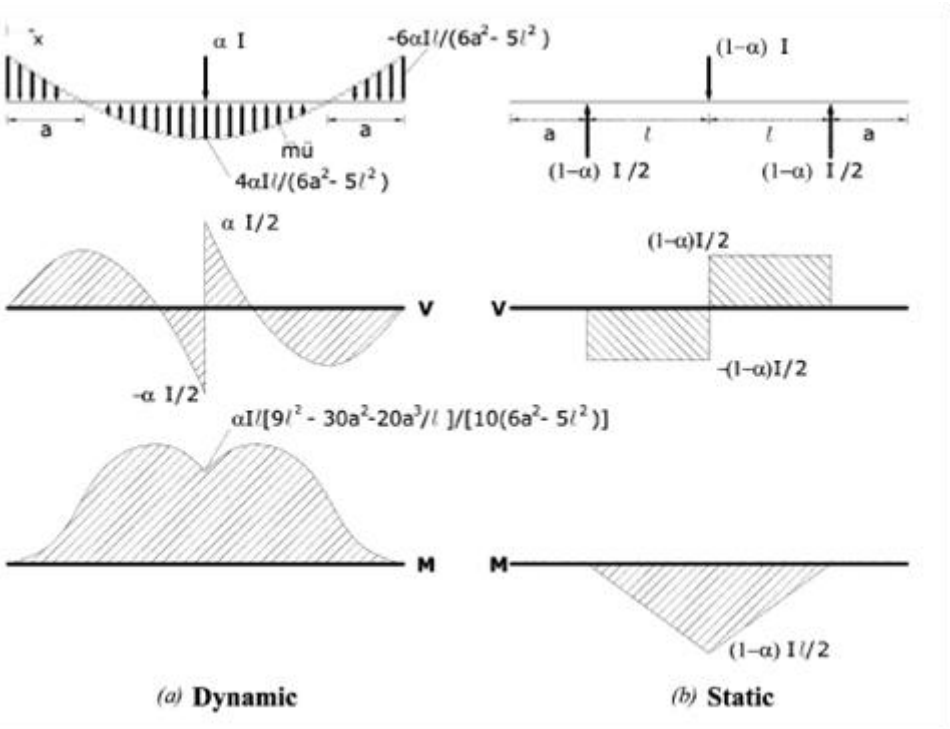

Figure 2.12: Dynamic and static bending moment and shear force diagrams with the inclusion of inertia forces (Saatci and Vecchio, 2009a)

By including the inertia force, through the ratio α, the peak bending demand reduces whilst the peak shear demand at the point of impact remains constant, when compared with the quasi-static predictions, as can be seen in Figure 2.12. Saatci and Vecchio presented a simplified formula for determining this reduction in the peak bending moment demand. Results from this showed that for tests carried out on beams with a clear span of 3 m, the maximum moment predicted for the dynamic case when inertia effects were included and the reaction forces were zero, was 0.437*I*, where *I* in this case is the impact force, which varies with time. For quasi-static conditions the peak bending demand for a simply supported beam with a point load would be 0.75*I*. It is therefore apparent that this theory predicts the peak bending demand under impact conditions initially to be almost half that of the quasi-static case for the same force. It can similarly be shown that under the same conditions the peak shear demand would remain constant for both the impact and quasi-static cases, given by $I/2$. This could therefore provide some rationale for the observed change in failure mode between static and impact loading and also the increased capacity of the section which has been found experimentally. A major drawback in the direct application of this theory

is that the time varying impact force must be known, which is difficult to determine, given its dependency on a wide range of factors. The analysis also only considers the situation when inertia from the deformation of the whole beam contributes to the behaviour. However, at the time the whole beam has responded, the impact force would have been experienced by the supports so assuming the reactions to be zero is not necessarily valid.

Cotsovos *et al.* (2008) presented the results of a numerical study which attempted to explain the increased short term load carrying capacity of a member under impact. The work is similar to that presented by Saatci and Vecchio (2009a) but avoids some of the drawbacks in the work discussed above. Cotosvos *et al*. introduced the concept that the response was dictated by an effective length which was dependent on the propagation of a shear wave from the point of impact. This approach was based on empirical observations from simply-supported beams impacted at mid-span, which showed that cracks could form on the top surface of the beam, indicating a hogging moment. These cracks form when the moment, M_{cr} is given by:

$$M_{cr} = f_t bh^2 / 6 \tag{2.6}$$

where f_t is the tensile strength of concrete (not including strain-rate effects), b is the width of the section and h is the depth.

The load corresponding to the first cracking can be estimated as:

$$M_{cr} = P_d L_{eff} / 8 \tag{2.7}$$

where L_{eff} is the effective length and P_d is the impact force in Cotsovos's work. The effective length is related to the distance travelled by the shear wave, travelling at velocity, u_w, which is assumed to propagate from the impact point. L_{eff} is given by:

$$L_{eff} = 2u_w \Delta t_c \tag{2.8}$$

and P_d is given by:

$$P_d = \dot{P} \Delta t_c \tag{2.9}$$

where $\dot{P}$ is the loading rate and Δt_c is the critical time at which the first crack will appear. The purpose of this method is to determine the critical time (Δt_c) at which a tension crack forms in the top surface. If the critical time is shorter than the time it takes the shear wave to reach the support then the response is wave dominated and failure will be concentrated in a central region close to the point of impact. Substituting equations 2.8 and 2.9 into equation 2.7 gives an expression for Δt_c as:

$$\Delta t_c = \sqrt{\frac{4M_{cr}}{\dot{P}u_w}} \tag{2.10}$$

Assuming that the impact load rate, $\dot{P}$, is known and by using the shear wave velocity, u_w, the effective length can be determined. Once the effective length is known this can be used in a static analysis to calculate the maximum dynamic force, which in turn allows the shear and bending moment demands to be found.

This method was carried out by Cotsovos *et al.* (2008) through numerical simulation, which meant that the rate of loading ($\dot{P}$) was a user defined parameter. However, as discussed above in relation to the work of Saatci and Vecchio (2009a), predicting this rate of loading in advance is difficult as it depends on many parameters, including the impact velocity, the stiffness of the member and local effects in the contact region between the impactor and the member. Cotsovos *et al.* (2008) proposed that the rate of loading could be estimated from the ratio of the member's static load carrying capacity (P_{max}) to the load duration (equation 2.11), which was assumed to be equal to the natural period for the member, *T*.

$$\dot{P} = {P_{\max}}/{T} \tag{2.11}$$

The justification for considering the natural period to be equal to the load duration is not clear. This equation also assumes that the loading rate is constant throughout the response which will not be the case in reality. It is therefore clear that whilst the work of both Cotsovos (2008) and Saatci and Vecchio (2009a) provides a tentative explanation for the observed behaviour of tests, further work is still required in this area to develop a more readily applicable theoretical model.

A further important issue raised in the work of Cotsovos (2008) was the use of the shear wave speed in determining the effective length, at a given time (equation 2.8), which is commonly quoted as:

$$u_w = \sqrt{\frac{G}{\rho}} \tag{2.12}$$

where, *G* is the materials shear modulus and ρ is the density of the material. For concrete this equation yields a wave speed in the order of 2300 m/s. If it is assumed that it is this form of wave that carries the force from the point of impact to the supports then this value should be in agreement with data obtained by Saatci and Vecchio (2009a) in Figure 2.11. However, this data indicates that the reactions experience the impact force 2 ms after the initial impact which, given that the distance

between impact point and supports is 1.5 m, suggests a wave speed of only 750 m/s. This result appears to suggest that the dominating propagating wave is not a shear wave but a lower velocity wave, such as a flexural wave.

It is also suggested in research carried out by Vermorel *et al.* (2009), who investigated the role of waves on the impact response of thin plates, that the wave speed shows a dependency on the impact velocity. The following relationship was derived between the wavefront velocity of transverse waves and the impact velocity, using a one-dimensional model:

$$\frac{\bar{U}}{c} = \left(\frac{V}{\sqrt{2}c}\right)^{2/3} - \frac{5}{6}\left(\frac{V}{\sqrt{2}c}\right)^{4/3} + \mathcal{O}((V/c)^2) \tag{2.13}$$

where, $\bar{U}$ is the wavefront velocity, c is the longitudinal wave speed in an elastic medium, V is the impact velocity, with the remaining terms in the order of $(V/c)^2$. This finding is contradictory to that of Jones (1989) who investigated impact on metal structures. Jones suggested that under impact a plastic hinge would develop under the point of impact at $t = 0$ and two hinges would propagate the disturbance towards the supports. Jones suggested that the velocity of the propagating plastic hinge ($\dot{\xi}$) could be determined from equation 2.14:

$$\dot{\xi} = \frac{12M_0(M+mL)}{MV_0mL} \tag{2.14}$$

Where M_0 is the plastic moment capacity of the section, M is the weight of the impacting mass, m is the weight per unit length of the section and L is the length of the section. This relationship appears to suggest that higher velocity impacts will actually cause the plastic hinge (and disturbance) to propagate more slowly. However, Jones (1989) was unable to provide experimental data to validate this relationship unlike Vermorel *et al.*, (2009). It is clear though that further research is required in this area, especially considering the disparity in the wave speed used by Cotsovos (2008) and that determined experimentally by Saatci and Vecchio (2009a). These issues will be discussed in greater detail in Chapter 4 where the relationship between impact velocity and wave propagation velocity will also be discussed further.

2.2.3. Stress waves

Under severe dynamic loads the role of stress waves on the response of a member becomes increasingly important. These events occur over very small time periods, in

the region of microseconds, and for this reason in quasi-static situations, stress waves are irrelevant.

The phenomenon of stress waves is incredibly complex owing to the many different types of wave that can be considered and the role of the geometry of a member. The primary wave types considered here are waves which travel parallel to the direction of the load (longitudinal waves) and waves that travel perpendicular to the direction of the load (transverse and flexural waves), all of which are highlighted in Figure 2.13. Research in the role of these types of waves on a structure's response has been limited as researchers have tended to focus on more global issues regarding a member's response.

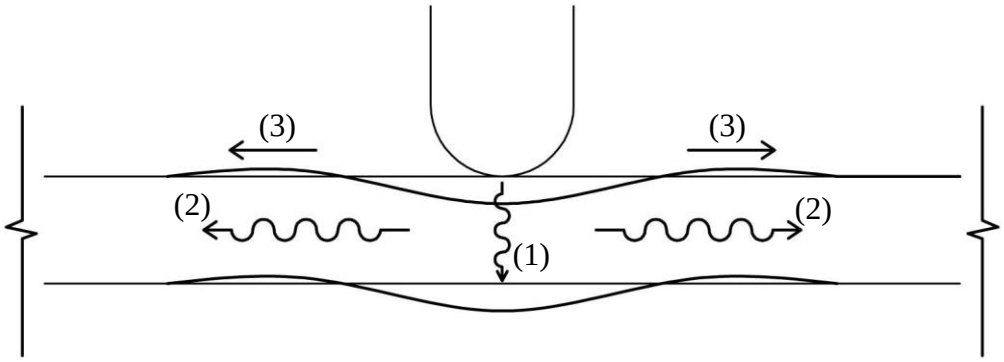

Figure 2.13: Stress waves resulting from structural impact: (1) longitudinal waves, (2) Transverse waves, (3) Flexural waves

Stress waves form at boundaries where large discontinuities exist. In impact situations flexural waves can be shown to propagate outward from the point of load application (Graff, 1975). In these situations transverse waves (also referred to as shear waves) are also known to propagate from the point of impact (Doyle, 1997). Cotsovos *et al.* (2008) was one of the first researchers to strongly consider the role of transverse waves in the impact response of RC members. This work, discussed previously, treated the impact problem as a shear wave dominated response which was linked to the increase in load carrying capacity under impact situations. These concepts will be developed in later chapters as a technique for predicting the response mode of RC members primarily to impact situations.

Research carried out by Olsson (2000) on the impact of composite plates showed that for very short duration loads the response is dominated by dilational through thickness

waves (these waves would cause spalling in RC members), for short duration loads the response is dominated by flexural waves and when the load duration is longer the response effectively becomes quasi-static (Figure 2.14). Under short duration loading it was shown by Olsson (2000) that the load will have significantly reduced by the time the boundaries experience the force as the impacting mass is forced to undergo very rapid deceleration. It was also shown by Olsson that during small mass impacts, the load, deflection and strains at the point of impact are out of phase indicating that the response is wave dominated, whereas for high mass impacts all three are in phase. Similar findings were also suggested by Arbrate (1991) who showed that where the contact duration is large, flexural waves can travel back and forth many times before the contact ends, and the plate behaves in a quasi-static manner. If the flexural waves have insufficient time to reach the boundaries then damage becomes more localised and the response is wave controlled. For intermediate conditions the response is much more complicated.

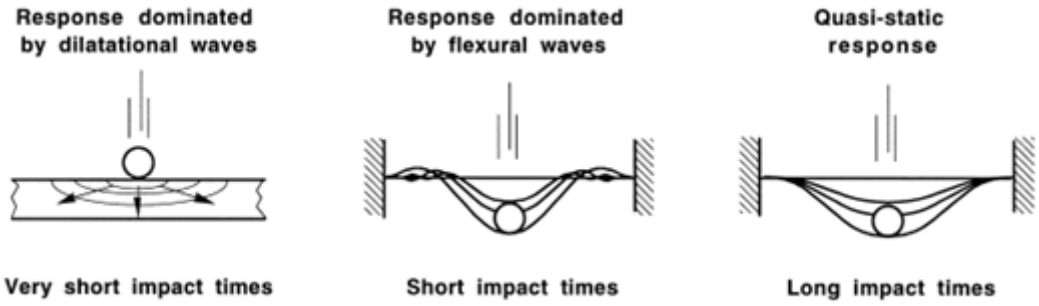

Figure 2.14: Response of composite plates to different duration loads (Olsson, 2000)

Through thickness longitudinal waves that lead to rear face spalling are generally not severe in impact situations although they have been observed in some tests (May *et al.*, 2006). However, in blast situations the role of through thickness waves in causing spalling of concrete is much more prevalent (Lu and Xu, 2004; Hao *et al.*, 2008) and the propagation of concrete fragments formed on the rear face of a member can be very harmful to the occupants of a building (Cormie *et al.*, 2009).

2.3. Methods of analysis/Design manuals

Analysing structures subjected to severe impulsive loads has received a great deal of attention over many years and a number of methods are currently employed which are

discussed below. The majority of these are concerned with predicting the peak displacement of members rather than areas of highest moment and shear force (and hence failure behaviour) which was first outlined by Biggs (1964). The primary reason for this is that the complicated dynamic response, combined with the incredibly short periods over which the forces act and strain-rate effects make the moments and shear forces difficult to accurately determine. It is therefore most common to specify hinge rotations or deflection limitations in design manuals e.g. (TM5-1300, 1990). This also gives some indication that the focus of design is commonly on achieving a ductile response.

2.3.1. Blast

The most widely quoted and used design manual for the blast design of structures is TM5-1300 (1990) (Ngo *et al.*, (2007)) . This manual first appeared in 1946 and was subsequently revised in 1990. The most recent update suggests structures should be analysed using the equivalent single degree of freedom (SDOF) method, which follows on from the work of JM Biggs (1964). This technique converts the real structural system into a single degree of freedom equivalent system by applying factors to the load, stiffness and mass (Figure 2.15). These factors are determined by equating the work done, strain energy and kinetic energy of the real and equivalent system with values dependent on the stage of the response and the member type. Cormie *et al*. (2009) provides all the factors along with a complete description of how they are determined. The equivalent system can then be solved according to Newton's equations of motion, with the damping force ignored. The model is established to determine the peak displacement of a salient point (usually the mid-point of a beam or column) and the factors applied to the real system take this into account. Once the real system has been converted to an equivalent one, ductility ratios can be established based on the level of safety required (TM5-1300, 1990). This procedure has inherent conservatism built into the analysis due to the assumption of a single mass with one mode of vibration, treating the load as an idealised triangular impulse and ignoring damping. This conservatism makes the SDOF approach appealing for the initial design of new buildings where the higher levels of conservatism would be acceptable. However, in some cases where existing structures are being analysed a greater

accuracy in the solution may be required which may make the SDOF approach unsuitable.

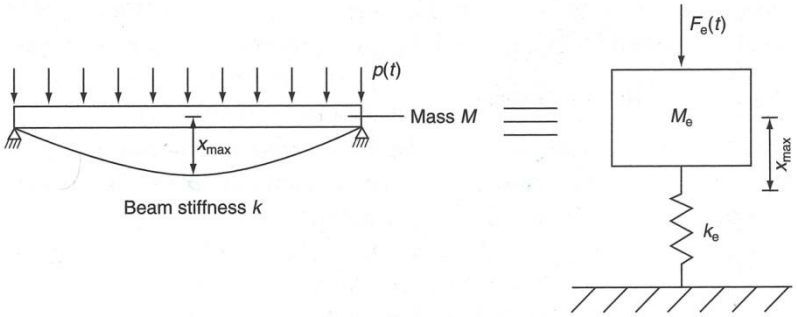

Figure 2.15: Real and equivalent SDOF system (Cormie *et al.*, 2009)

A number of methods have been developed based on the results of SDOF analyses to predict the response of structural configurations to given loading conditions. The most commonly used are pressure-impulse curves which take account of the blast pulse shape to determine the response (Abrahamson and Lindberg, 1976; Li and Meng, 2002). A more recent development in this field is the safe stand-off approach developed by Byfield and Paramasivam (2014). This approach makes use of the scaled distance, Z, determined by Hopkinson to predict the likely damage for a given structural configuration. This approach is particularly useful when designing barrier systems.

Tables are often used to find the load and mass transformation factors for the SDOF approach for a given structural configuration with assumptions made regarding the material behaviour, which determines the resistance function. Some concerns have been raised with regards to the accuracy of the method for anything other than the most simple cases (El-Dakhakhni *et al.*, 2009; Razaqpur *et al.*, 2009; Rodriguez-Nikl *et al.*, 2009). Particular issues encountered where the validity of this technique has been questioned include:

- Accuracy for predicting shear failures
- Selection of the most suitable resistance function, which is essentially an arbitrary decision with no scientific justification. It has been shown experimentally that in some cases less scientifically rigorous methods can actually be more accurate (Rodriguez-Nikl *et al.*, 2009)
- Overall accuracy of predicting the peak displacements

- Simplification of loading conditions
- Failure to accurately include issues such as strain-rate effects, spalling due to stress waves and inertia effects as a result of the gross simplifications employed

In response to some of the issues raised, efforts have been made to improve the methods of analysis. This has increasingly led to the development of complicated finite element packages. Commercially available packages such as CONWEP and LS-DYNA have all been used for this purpose, although many others are available (Ngo *et al.*, 2007). However, given the complex nature of the response and the limitations that finite element packages have for modelling reinforced concrete, a high level of skill is required to develop an accurate model (Ngo *et al.*, 2007). These limitations were also discussed in a recent publication by Crawford and Magallanes (2010). An example taken from this paper, highlighting the potential pitfalls of the modelling choices, is shown in Figure 2.16. The results highlight how different models for concrete used within the FE analysis can predict vastly different responses. The response of a member to an actual blast load is shown on the left of Figure 2.16 with four different responses from finite element models shown alongside it. As can be seen from this figure, the predictions vary dramatically depending on the concrete model chosen. For this example the K&C model for concrete was the only one developed specifically for blast loads, although the CSCM and BD model were also capable of including rate effects in concrete. Given these concerns finite element packages have not been used in this research.

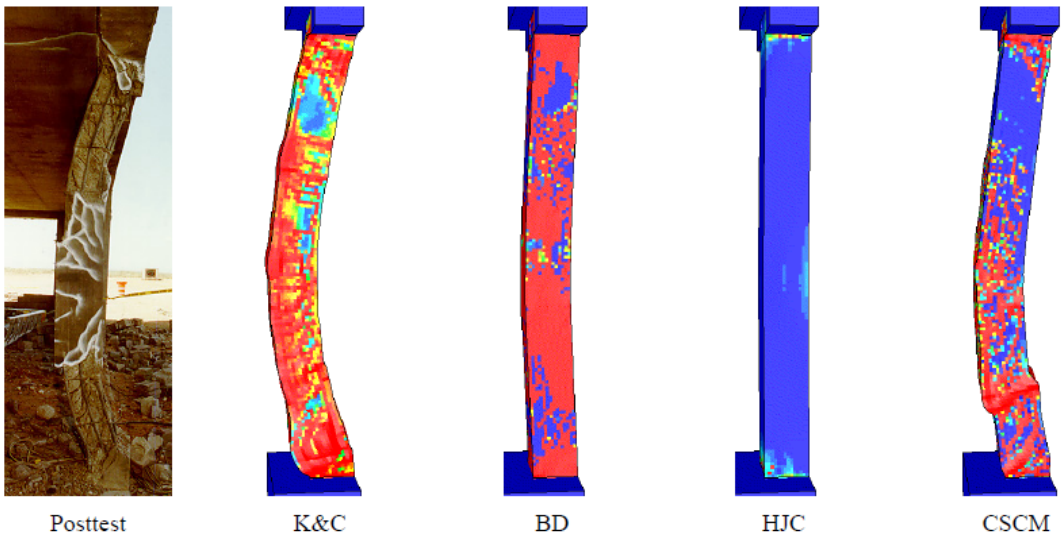

Figure 2.16: Variation in predicted response of RC column to blast load with different FE models (Crawford and Magallanes, 2010)

2.3.2. Impact

The most common design situation where impact is considered is in vehicle collisions with bridge piers. In these situations the UK's Highways Agency recommends applying conservative loads determined from experimental testing and carrying out a quasi-static analysis (Highways Agency, 2004). This technique ignores many important dynamic effects which affect the structural response to impulsive loads, such as the transition in failure mode and strain-rate effects which have been described previously. Morevoer, the loads employed may be grossly conservative leading to inefficient design solutions.

Research in this field can be divided into three primary areas: analytical modelling, experimental testing and numerical simulations. Given the concerns raised previously over the ability of numerical models to analyse these dynamic situations for reinforced concrete, these will not be discussed further. Analytical models have most commonly taken the form of single or multi degree of freedom models (Comite euro-international du beton, 1988; Lee *et al.*, 1983; Bischoff *et al.*, 1990). However, more recently Cotsovos (2008) has presented a solution to determine the peak load carrying capacity of an RC member based on wave and inertia considerations, as outlined previously (section 2.2.2). By far the most common goal of the analytical research presented has been to predict the equivalent impact force which can then be used in a quasi-static analysis. No analytical solutions currently exist which allow the full time

varying nature of the applied load to be determined within the analysis and employed directly to predict the demands acting on the structure. Only by doing this would it be possible to include in the solution a full representation of dynamic behaviour such as inertia and strain-rate effects.

A number of experimental studies have been conducted largely with the aim of providing test data for the development of semi-empirical design equations, e.g. Kishi *et al.*, (2002). Further to this, research carried out by Silva *et al.*, (2009) and Tachibana *et al.*, (2010) has attempted to provide experimental data to aid in the development of performance based design criteria. This work is very much in its infancy owing to the gaps in the theoretical understanding and the lack of data to corroborate analytical results with. However, with improved analytical models this situation should improve.

An investigation into the behaviour of reinforced concrete filled FRP tubes (CFFTs) to both blast and impact loads was carried out by Qasrawi (2014). It was shown that under impact loads the energy absorbing capacity of GFRP tubes could increase by over 1000% compared to traditional RC members. Qasrawi also developed a non-linear SDOF model for impact which included a non-linear resistance function. This resistance function allowed strain-rates to be included in the analysis and was derived from the experimental data obtained by Qasrawi. Because of this it showed good agreement with the experimental data. It is not clear however, whether the same accuracy would be shown for other tests with parameters outside the range of those tested by Qasrawi. The primary advantage though of this work is the focus on simplified methods which are more applicable to a design situations.

2.4. Strengthening existing structures

Where analysis shows a structural member to be deficient, one option available to engineers to improve the response is through retrofitting with fibre reinforced polymers (FRPs). This technology was first applied in Switzerland to strengthen bridges (Teng *et al.*, 2002) in quasi-static applications. However, more recent research has shown that the same technology could have potential applications for strengthening structures against blast and impact loads.

To date, much of the research on the use of FRPs for these applications has tended to focus on proof of concept rather than optimisation of the retrofitting arrangement,

which may still be several years away. A comprehensive review of the main experimental studies for blast resistant applications has been provided by Buchan and Chen (2007). This review paper summarised the main studies on the retrofit of beams, slabs, walls and columns. The following discussion will focus primarily on the strengthening of columns which are most relevant to the current study and where the success of retrofitting has been best demonstrated.

The exact retrofit configuration will depend on how a member is structurally deficient and on the objectives of retrofitting. For load bearing columns the primary objective will always be to prevent brittle shear failures, maintain structural integrity and increase ductility. Secondary objectives may include limiting deflections to reduce P-Δ effects and preventing dangerous concrete fragmentation. Preventing brittle shear failures can be achieved by wrapping FRP around the column with the fibres aligned in the transverse direction (Rodriguez-Nikl, 2006; Crawford *et al.*, 2001; Muszynski and Purcell, 2003). Rodriguez-Nikl (2006) was able to show that with just two layers of transversely wrapped CFRP, the brittle shear failure of RC columns subjected to blast loads could be avoided and a ductile response achieved.

Reducing the peak deflections requires that the stiffness of the member and moment capacity are increased. This can be achieved with longitudinal FRP strips attached to the tension face of the member. This type of retrofit has been researched less widely in the context of columns, as increasing the moment capacity without increasing the shear capacity would increase the likelihood of premature shear failures. It is also likely that the FRP strips would debond before they contributed significantly to the capacity of the member. These problems could be avoided by using transverse wraps in union with longitudinal strips but the benefits of this system have not been conclusively demonstrated (Rodriguez-Nikl, 2006).

To date, FRP design manuals such as TR55 (2012) or ACI 440 (2002) have not included meaningful design guidance for strengthening structures against blast or impact loads. Crawford *et al.*, (2001) proposed some guidelines for strengthening columns, based on analysing the member's response as a SDOF system. These proposals therefore incorporate the limitations relating to the use of a SDOF system which were described previously. Further to this, dynamic material properties are not utilised and the peak shear demand is derived from the flexural demand. This assumes that the dynamic forces are equal to the quasi-static forces an assumption which has already been shown to be incorrect. The development of more rational design

guidelines for strengthening existing structures is a major issue that future research should aim to address.

Less research has been undertaken on the applications of FRP to strengthen columns against impact loads. However, the UK's Highways Agency has published design guidelines for strengthening bridge piers with FRP (Highways Agency, 2002). In these guidelines the members capacity is checked against a quasi-static force, applied transversely. This has the obvious drawback of neglecting the many important dynamic effects discussed previously but is claimed to be a conservative solution and avoids the need for a full and complex dynamic analysis. Suter and Chang (2001) were able to show the significant improvements possible in the response of members to large impacts. It was shown that the kinetic energy dissipated in a ductile manner could increase between two and four times for retrofitted members depending on the number of layers of FRP used and the specific orientation. This improvement was largely due to an increase in the moment capacity caused by the additional longitudinal reinforcement. However, the confinement of the concrete and associated higher failure strain also contributed to the improved behaviour.

2.5. Conclusion

The above discussion on the literature on this subject has provided a broad overview of this field and addressed a number of areas where further work is required. It is the aim of this thesis to investigate the most important aspects in these areas. The key areas outlined from the literature review and addressed in subsequent chapters are therefore:

- The transition in failure mode observed in impact tests.
- Incorporating the apparent gains in strength of materials as the rate of loading increases into the analysis methods.
- A more accurate analytical model for predicting the peak response of RC columns deforming flexurally.

The theoretical models developed in this project are derived using fundamental principles to both understand the key parameters affecting the behaviour and provide engineers with solutions that can readily be employed in practice.

Developing an understanding in the first two areas will greatly aid in the assessment of existing structures which may be at risk from blast or impact loads. This will enable engineers to effectively develop retrofit strategies.

3. Preliminary Experimental testing

3.1. Introduction

It was outlined extensively in the literature review how the response of RC columns can differ significantly as the rate of loading increases above that associated with static loads. Understanding and fully appreciating issues such as strain-rate effects, the role of inertia forces and the transition between failure modes as the rate of loading increases is an essential aspect of this work. At the outset of this project no methods for carrying out appropriate experimental testing existed at the University of Bath. Therefore, in order to validate any theoretical work, arrangements were made to devise a test method that could be used here in Bath.

It was decided that impact testing would be the most suitable test method, given the resources available. Carrying out real blast tests requires specialist sites and the costs are usually prohibitive.

This chapter outlines the design and construction of an impact rig in the Structures Laboratory at the University of Bath. A discussion on observations made from bedding in tests and the development of suitable data acquisition techniques is also presented.

3.2. Design and construction of impact test rig

A number of systems have been employed throughout the world to test structural elements under high rate loading. High rate servo-hydraulic rams, pendulum impact, drop hammer impact, blast simulation and actual blast testing are some of the most commonly used techniques (Bischoff and Perry, 1991). In order for this project to provide useful test data for validation of the theoretical work it was elected that a suitable technique for testing members under high rate loading be devised. Given the limited financial resources of this project and the limitations of lab space for new equipment, it was decided that a drop hammer system would fulfil the core requirements in the most cost effective manner. The primary requirements set out for the design were:

- The ability to conduct tests safely. Given the large amount of energy involved with impact testing this was the primary concern for the design

- Durability so that the rig would remain a permanent piece of equipment for the laboratory
- Adaptability so that a range of impact velocities and masses could be used. An impact energy capacity of 7 kJ was selected as the maximum safe operating limit for the rig given practical constraints of height, size and maximum lifting capacity
- The maximum allowable height within the laboratory was around 5 m. However, this was reduced to around 4.4 m in order to leave space for lifting the rig into position
- Effective instrumentation. The requirement was to provide a clear line of sight to the test specimen so that the response could be recorded with high speed video cameras
- To take up as small amount of space as possible so that the labs could still function fully.
- Be demountable in order to be moved safely if required
- A safe method for releasing the drop mass.

3.2.1. Chosen Design

Drawings and photos of the final design are shown in Figure 3.1 and Figure 3.2. The final design features a free falling mass which runs between two channel sections which provided effective confinement to the mass. The rear channel rests on the floor and is fixed to the strong wall of the lab while the other comes down to a ‘goal-post’ support arrangement where the load is transferred laterally. This allows specimens to be placed under the rig and videoed without obstruction. The impacting mass was also constructed from channel sections with an open centre, allowing additional steel block masses to be added as desired. A steel nose was mounted on the base of the falling mass as the point of impact. This nose was designed to be interchangeable, giving the finished design further flexibility. The mass was attached to a pulley with a quick release snap shackle which could be operated from the ground at a safe distance. The key aspects of the design are discussed in more detail below.

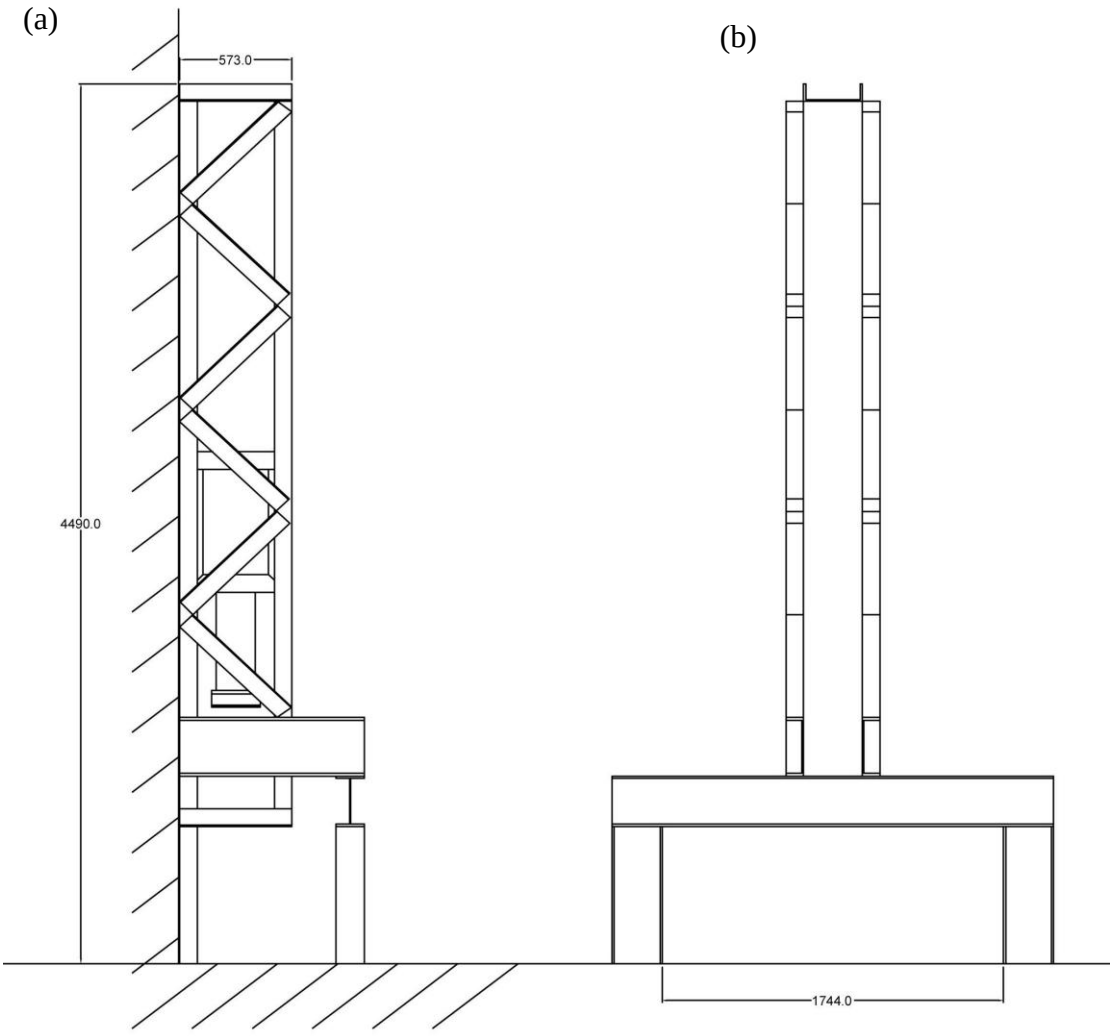

Figure 3.1: (a) Side elevation and (b) front elevation of impact rig design

Figure 3.2: Finished impact rig

Guide system/safety

To ensure safe operation the test rig was designed so that the mass would run inside two fixed channel sections and be completely contained. This containment was important for ensuring that the mass could fall safely without endangering people in the vicinity of the rig. This system was also chosen so that the channel sections would provide a constant guide within the tolerances of the design, allowing for a predictable impact zone. A view looking down the length of the channels is shown in Figure 3.3. This figure shows the two channels, left and right, and the four steel bars used as guide rails for the falling mass. It was intended that the mass would not be removed from inside the channels regularly, although this operation can be achieved by removal of brackets at the bottom of the channel sections, which can be seen in Figure 3.4.

Figure 3.3: Photo looking down the length of the impact rig showing the four bars used to guide the falling mass

Figure 3.4: Bottom brackets which prevent the impacting mass from falling out and act to arrest the motion of the falling mass, allowing safe operation

Velocity arrest

The worst design load was perceived to be for the impacting mass to be laden to its maximum weight and accidentally released from the top with no specimen to impact. The bottom plates where therefore designed to withstand the force generated in this

case. It could also be the case that if an impacted specimen suffered significant deformations, a premature or a brittle failure, then the plates would arrest the momentum of the falling mass. To limit the potential damage that this may cause to the test rig, a system to gradually reduce the velocity of the falling mass was devised. The problem was first solved by placing four high stiffness springs at the bottom which rested on the brackets. The brackets were bolted to the channel sections with four bolts on each side acting in single shear. To prevent the springs from being ejected unsafely upon impact, a set of four steel rods running the length of the channels, were placed within the inside diameter of each spring (shown in Figure 3.5). The springs then rested on a rubber pad (Figure 3.6) which would dampen out the oscillations in the spring.

Figure 3.5: Springs used to arrest the motion of the falling mass shown coiled around the steel guide bars which run the length of the rig

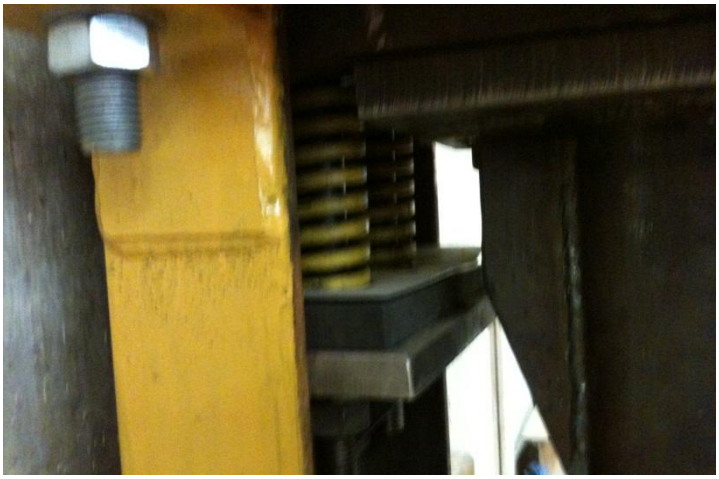

Figure 3.6: Springs resting on rubber pad

During initial operation it was found that when the springs were engaged to arrest the motion of the falling mass a significant number of rebounds resulted due to the lack of damping within the springs and structure. To overcome this issue the springs were replaced with a series of rubber pads stacked on top of one another. In subsequent tests these proved much more effective in damping out the rebounds of the mass.

Providing a clear line of sight of the specimen

Recording of high speed video footage was intended to be the primary means of data acquisition; therefore it required that the specimen could be observed without obstruction. This issue was complicated by the requirement to transfer any loads carried through the vertical channels safely to the ground. For the case of the rear channel, which was attached to the wall, this was not an issue as the arrangement allowed this channel to bear directly onto the ground. However, the front channel could not bear directly onto the ground without obscuring the specimen behind it. Despite a truss arrangement designed to transfer loads from the front to the rear it was also thought sensible to provide an alternative load path for the forces. The final design solution was to construct a ‘goal-post’ type arrangement where the load from the channel was directed onto a transfer beam which was supported by two short columns either end. The columns were mounted on base plates which could be secured to the laboratory strong floor for stability.

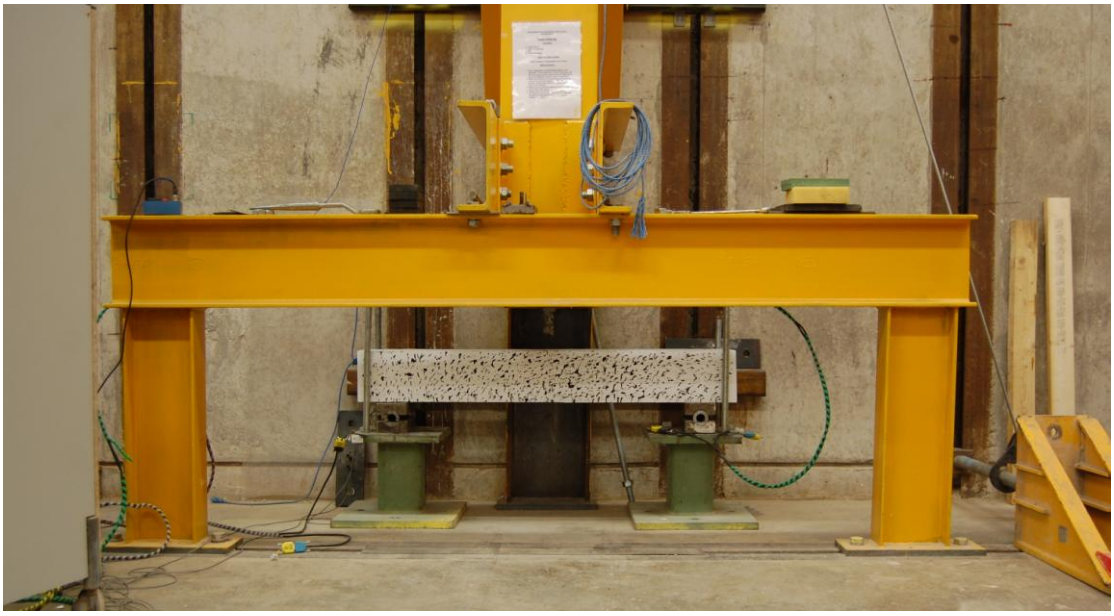

Figure 3.7: Front view of transfer beam and supporting post arrangement used to allow unobstructed views of the test specimen

Mass and variable nose

In order to have as much flexibility as possible in terms of loading characteristics, a simple method for altering the impact mass was devised. Given the shape and size of the impact mass module a maximum clear drop height of around 2.2 m was possible. In order to fulfil the target impact energy of 7 kJ the weight of the impacting mass would have to be around 360 kg. The impacting mass frame unit was constructed from small channel sections welded into a box shape as shown in Figure 3.8. Within this box shape, steel blocks could be stacked on top of one another and bolted down. The required 360 kg weight limit could then be achieved by stacking up to eight of the steel blocks (each weighing 30 kg) within the impacting mass frame, which, including the nose section, weighed 120 kg.

A particularly important issue for the operation of the rig was that the impacting mass should run smoothly between the channel sections. It is likely that this could have been achieved through suitable clearance between the channel section and the impacting mass. However, it was considered that the potential impacts and friction between the mass and channels could have led to issues with durability and the reliability of the results. These issues were resolved by mounting roller bearings around the impact mass frame. A much smaller tolerance was therefore required, which avoided the issues described above.

Figure 3.8: Impact mass frame unit during construction

Figure 3.9: Impact nose section mounted on mass frame

The nose section was constructed from a thick walled square hollow section with plate steel welded on each end (Figure 3.9). The nose was bolted securely in place to allow it to be interchanged if necessary. On the end of the nose section an interchangeable ‘tup’ was secured through a single embedded screw. The ‘tup’ which would impact the test specimen was hemispherical in profile, but could be changed if necessary.

Quick release/pulley system

The pulley system used to hoist the impact mass to the desired height was controlled through a winch at ground level (Figure 3.10). The winch cable passed over a cylindrical bar at the top of the rig and down between the channel sections to attach to the impacting mass (Figure 3.11a and b).

Figure 3.10: Winch used to lift the impacting mass

Figure 3.11: (a) Steel bar with cable threaded over it and (b) cable running up and over the bar

Various methods were considered to achieve a rapid release of the impact mass. The final solution selected was a quick release snap shackle (Figure 3.12). Alternatives considered included electromagnetic systems where a current is applied to open the catch. However, the snap shackle was considered to be both safer and simpler to operate. The pull cord used to operate the shackle was threaded out over the top of the rig next to the pulley cable.

Figure 3.12: Quick release snap shackle

Additional features

Overall stability of the frame was provided through a combination of diagonal bracing, to connect the two channels, and transverse sections mounted to the rear channel to secure the whole rig to the laboratory strong wall.

To allow for the frame to be moved, a pair of box sections were welded between the channel sections, one each side, so that the whole frame could be lifted by a fork lift truck and moved.

3.2.2. Construction and 'bedding in' tests

Construction was carried out over a period approximately 6 weeks starting in January 2011 with the help of the lab technicians. On completion of construction of the impact rig, preliminary tests were carried out. These tests were not intended to provide test data that would be used for validation of models outlined in later chapters or development of theoretical work. Rather they were intended to test the safe operation of the impact rig, develop best practice for conducting tests and confirm the suitability of the data acquisition methods which are discussed in detail below.

To carry out the ‘bedding in’ tests, two beam specimens were cast. Both were identical with a width of 110 mm, depth 160 mm and 1000 mm span. Longitudinal reinforcement was provided in the bottom by two 10 mm diameter steel bars which had a measured yield strength of 560 N/mm^2, with 20 mm cover. Transverse shear reinforcement was provided by 3 mm steel stirrups spaced at 100 mm centres, with a measured yield strength of 770 N/mm^2. The flexural capacity was predicted to be approximately 10 kNm and the shear capacity of the specimen was predicted to be 32.5 kN, according to BS8110. The force to cause a shear failure was therefore approximately 65 kN and the force to cause a flexural response was approximately 40 kN, assuming that the load was applied at the mid-span. This indicated that a flexural response was more likely.

Test 1

The first specimen was impacted at mid-span with a mass of 150 kg released from a height of 2.3 m, giving an impact energy of 3380 Joules. The series of images shown in Figure 3.13 are taken from a high speed camera which recorded at a rate of 2000 frames per second (fps).

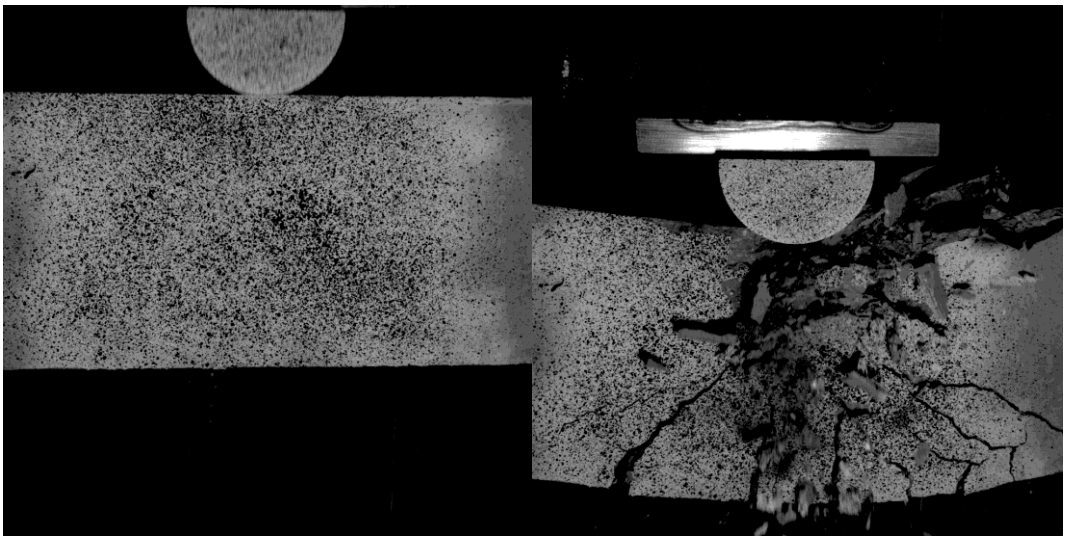

Figure 3.13: High speed images from test 1

It can be seen from the post-test photo (Figure 3.14) that the specimen displayed a flexural response with the majority of the deformation occurring over a localised central region. The impacting energy was insufficient to cause snapping of the

reinforcement. Significant spalling of crushed concrete can be observed in the region directly below the impacting mass.

Figure 3.14: Test 1, post test

A post-test assessment of the specimen revealed cracks approximately 400 mm from the impact location on the top face of the specimen (Figure 3.15). These cracks indicate that at some point in the specimen's response, part of the top surface of the specimen was in tension. This finding had been reported by other researchers (Silva and Lu, 2006) and was discussed in the literature review in Chapter 2 and represents a widely observed feature of impact tests which is not found in quasi-static situations.

Figure 3.15: Location of hogging cracks in relation to the impact location

Test 2

As the first specimen displayed a clear flexural response it was decided that the second specimen would be used to investigate the effect of increasing the shear

demand had on the response of the specimen. This was achieved by applying the load at the quarter-span which increases the shear demand whilst reducing the flexural demand for a given force. The load was applied by dropping 150 kg from a height of 2.3 m.

Problems with the high speed video equipment meant that the event was not captured. However, it can be seen from the post-test photo (Figure 3.16) that brittle shear failure occurred in this test and a catastrophic failure resulted. The catastrophic failure can be attributed to issues with the anchorage of the steel, but nonetheless, failure of this nature proved useful for testing the capacity of the mass arresting system described previously. The engagement of this system would ideally be avoided, however, this test revealed it to function adequately without damage to the rig.

A final assessment of the damaged beam once again revealed hogging cracks formed on the top surface, with the first occurring approximately 350 mm from the point of impact as can be seen in Figure 3.16. Given the very rapid and catastrophic failure of the specimen it can be concluded that these cracks form at a very early stage of the member's response, prior to failure.

Figure 3.16: Hogging cracks in test 2

3.3. Data acquisition

To a large extent, the ability of the impact rig to produce useful results requires suitable techniques for data acquisition. The high speed nature of the events significantly complicates matters in this respect. As previously mentioned, the ability

to capture the behaviour using a high speed camera was considered to be the primary requirement. In addition to this, further trials were carried out using load cells and accelerometers to capture other features of a member's response. Below is a description of the various methods employed for data acquisition and of how the acquired data could be employed in the analysis.

3.3.1. High speed camera

Given the incredibly short periods of time over which the majority of the behaviour occurs the use of a high speed camera is invaluable for understanding the behaviour of a specimen under impact loading. Providing a clear and unobstructed viewing 'window' to the specimen was essential in this respect. Frame rates for high speed cameras typically start at around 2000 frames per second (fps) and can reach up to 100,000 fps. However, at these speeds the resolution is considerably reduced and lighting becomes difficult. The response of a concrete beam was predicted to occur over a period of approximately 30 ms (Silva *et al.*, 2009) therefore a minimum frame rate of 2000 fps would provide a suitable number of images to see the most important dynamic features.

The use of a high speed camera also provides the potential to use digital image correlation (DIC) analysis. This technique allows strains to be calculated by observing the distortion of a random speckled pattern on the surface of a member. The accuracy of the results depends on the resolution of the camera and fineness of the speckle pattern. Trials with this technique were carried out during the 'bedding in' tests described previously. The left hand image of Figure 3.13 shows the speckled pattern applied to the surface over the central region of test specimen 1.

Images from the DIC analysis showing the principal strains for test 1 are shown in Figure 3.17. Challenges were encountered in using the propriety software to analyse the images captured. The primary reason for this was the blurring of the images, which suggests that the frame rate selected was too low. However, increasing this further would have led to a reduction in the size of the images requiring a compromise to be made. The software was also incapable of analysing more than one distinct region. Therefore, on forming shear cracks, only one region between cracks could be analysed. This issue could potentially be resolved through improved software. Given these challenges and the limitations of employing the DIC it was decided that data

acquisition would not depend on this. It will later be shown that data from DIC did prove useful in determining the changing deflected shape during the initial response of the member when using a suitably wide frame. As the technology develops the accuracy of the results obtained using this technique will improve, giving additional data that could be used in the analysis.

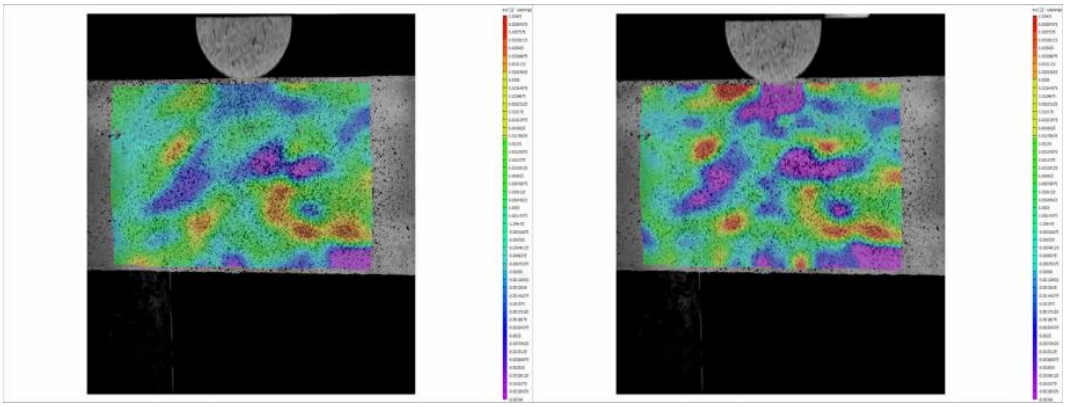

Figure 3.17: Principle strains produced from DIC analysis software

3.3.2. Load Cells

Determining accurately the reaction forces generated in an impact event presents a number of challenges. However, the results can be useful for comparison with theoretical work. Standard load cells usually have an internal inertia which makes them incapable of responding rapidly enough to detect the time varying forces in impact situations. High rate load cells are available but the cost is prohibitively high given the budget constraints of this project.

It was therefore decided that load cells would be constructed for the purpose of this project from tubular steel which, when loaded would deform slightly due to the applied force. The deformation generates strains which can be measured with strain gauges and recorded at a suitably high rate to determine the forces. A section schematic of this principle is shown in Figure 3.18 and a photo showing one of the two load cells constructed can be seen in Figure 3.19.

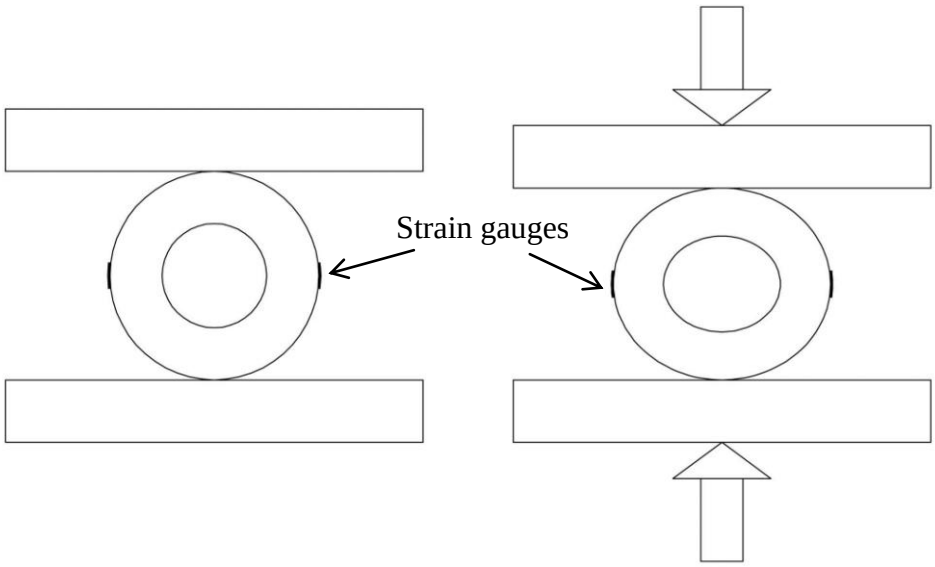

Figure 3.18: Load cells constructed for high speed reaction force measurement

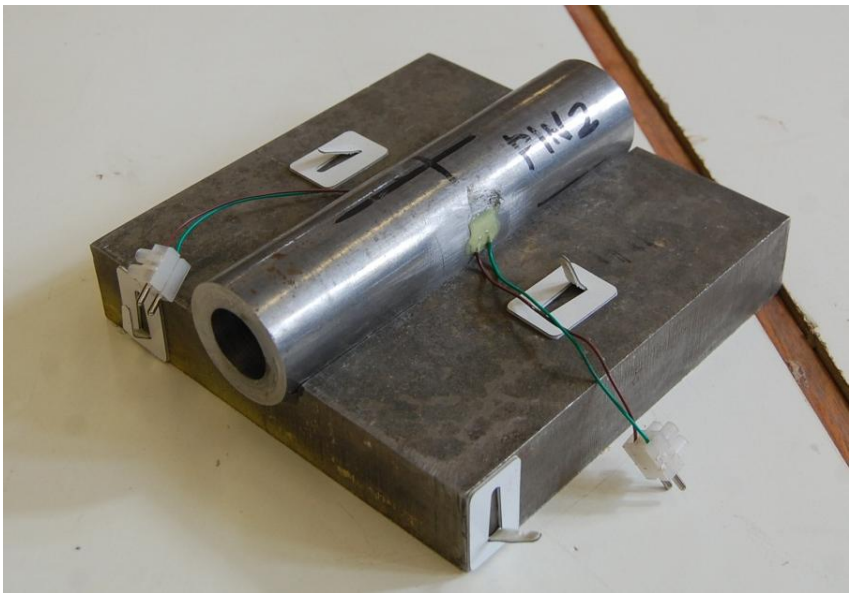

Figure 3.19: Photo of one of the two load cells

Calibration of the load cells was required so that strains measured dynamically could be equated to forces for use in the analysis. The strain gauges used were type FLA-2-11, manufactured by Tokyo Sokki Kenkyujo Co., Ltd. and had a gauge length of 2 mm and a gauge factor of 2.11. During their calibration the pin load cells were compressed via a calibrated static load cell. As the load cells could only be calibrated quasi-statically, it would be expected that the dynamically measured strains would slightly under predict the impact force due to strain-rate effects. However, quantifying this under prediction was not possible.

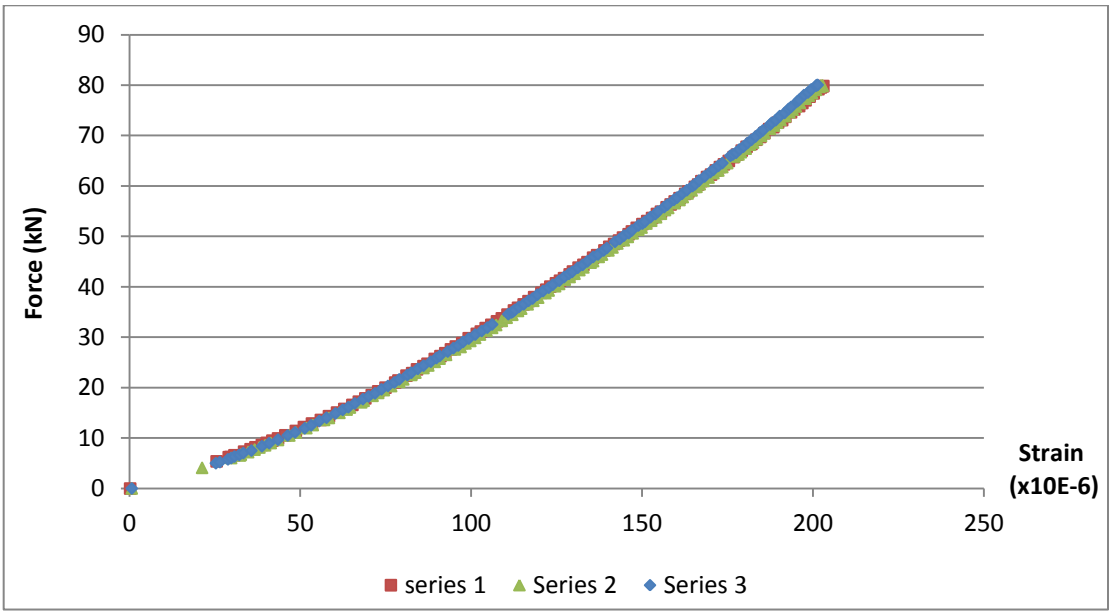

Figure 3.20: Load cell 1 calibration test results

The load calibration graph showing the relationship between the applied force and the strains measured for load cell 1 can be seen in Figure 3.20. Based on curve fitting, the relationship between the measured micro-strain (x10^{-6} ε) and the applied force (F, units kN) was determined as:

$$F = 0.044\varepsilon^{1.416} \quad (3.1)$$

When compared with the experimental data this relationship gave an R^2 value of 0.997.

For load cell 2 the calibration graph is shown in Figure 3.21. It was found that the data was best represented by the following expression:

$$F = 0.297\varepsilon^{1.081} \quad (3.2)$$

The R^2 value for this equation is 0.999. The difference in the two equations (3.1 and 3.2) is purely down to the curve fitting algorithm used in Microsoft Excel.

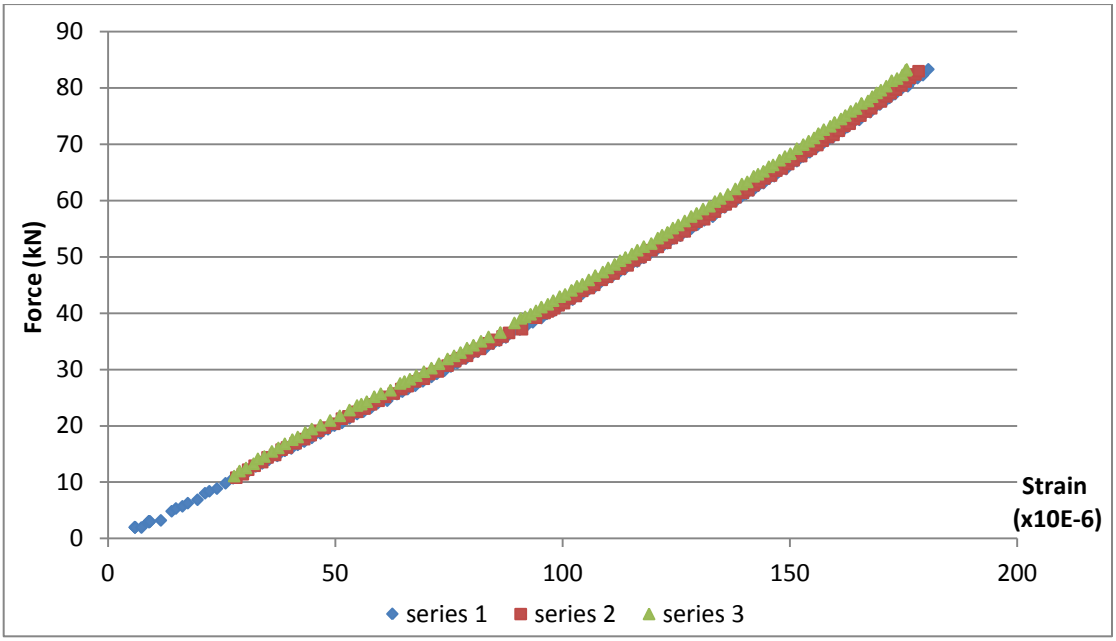

Figure 3.21: Load cell 2 calibration test results

Recalibration of the load cells was carried out after certain tests where damage had been sustained to the load cell. This is discussed where relevant in later chapters.

3.3.3. Accelerometers

Accelerometers were also used to provide additional data, these were mounted on the impacting mass in order to record the impact acceleration and hence, calculate the impact force. The data would also be useful in recording accurately the time at which the impact first occurred. Initially only 30g accelerometers were available. Typical data obtained using these accelerometers is shown in Figure 3.22, with data recorded at a sample rate of 10,000 Hz. The absence of data points above 30g indicates that the maximum capacity of the accelerometer was surpassed. In order to attempt to overcome this limitation, a 500g accelerometer (model 353B04) from PCB Piezotronics was employed in subsequent tests.

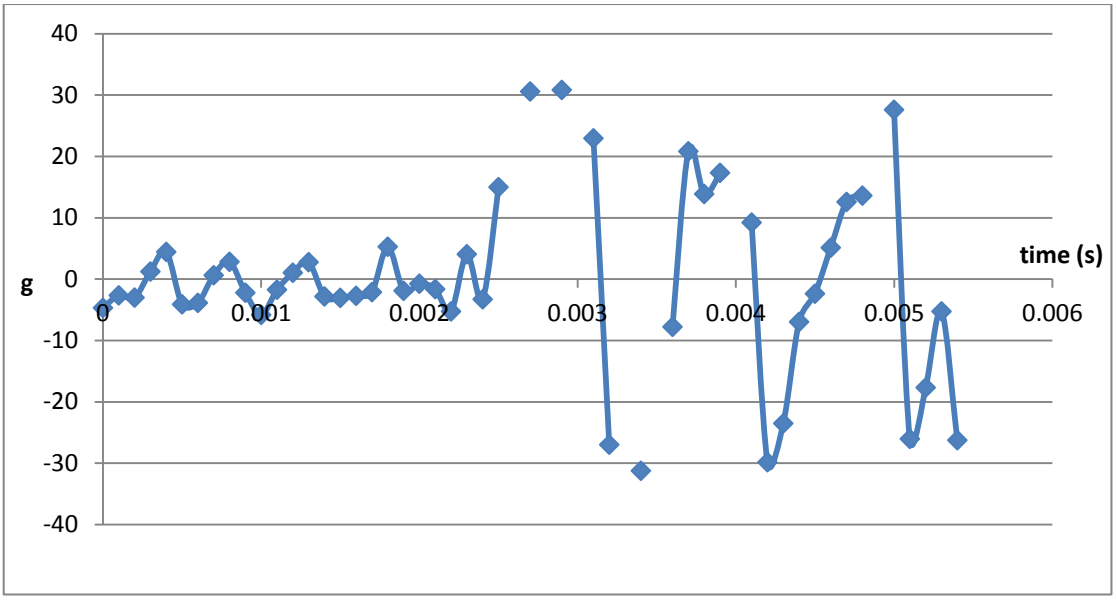

Figure 3.22: Data from impact test recorded with 30g accelerometer

3.3.4. Data logger

In order to capture data from the load cells and accelerometer with suitable accuracy it is important to use a sample rate which is sufficiently high. T simple rule of thumb often employed is that the sample rate should be twice the highest frequency of data expected. Since the frequency of the data was not known prior to testing therefore, initially, a sample rate of 10,000 Hz (the maximum possible with the equipment available at the time) was used. However, this was found to lack the precision required to accurately capture the strains from the load cells and the data from the accelerometer.

To overcome this limitation a new data logger was obtained capable of sampling at a much higher rate. Over one channel the new logger was capable of sampling at a rate of 500,000 Hz, although this reduces as the number of channels being utilised increases. This increased frequency was found to be more accurate for recording the time at which impact occurs, although high frequency background noise was still picked up.

3.4. Conclusion

Given the challenges of obtaining reliable and useful test data, to validate theoretical models, the development of an appropriate method for conducting tests was seen as an important step. This chapter has outlined the design and construction of suitable test

apparatus enabling experimental data to be collected, which was used extensively in the remainder of the study. This chapter has also described in detail the development of suitable data acquisition techniques which were developed with the aid of the preliminary experimental work described in this chapter. This process allowed the limitations of the test setup to be appreciated at an early stage and suitable modifications and developments to be made where appropriate.

The following chapter will outline the development of a theory to explain and predict some of the key observations made by other researchers. Following this, validation of the theory is achieved using test results obtained using the impact equipment described in this chapter.

4. Predicting failure mode of impulsively loaded RC members

This Chapter outlines the development of a new model to predict the failure mode of RC members (beams and columns) subject to impact loads. This work is in response to the literature review which highlighted that the rate of loading appears to have a significant influence on the failure mode. This chapter begins by outlining the empirical basis for the proposed model before developing the actual theoretical model, which is based on solving the equation of motion numerically over a number of time-steps. Following this is a detailed parametric and sensitivity analysis. The Chapter concludes with a discussion on the benefits and limitations of the model. The main findings from this Chapter are presented in Isaac *et al.* (2013).

4.1. Introduction

It has been shown by a number of researchers that for increasing impact velocities, the failure mode of reinforced concrete beams and columns can alter. Where a member would respond in a desirable ductile flexural mode under low-rate or quasi-static loading, as the impact velocity exceeds a certain threshold, the failure mode can become brittle and catastrophic (Kishi, *et al.*, 2002, Magnusson *et al.*, 2010).

Due largely to the complexity of the behaviour there is currently no widely accepted theory to explain this observation, despite the potentially serious consequences of brittle failures for the built infrastructure.

Providing a solution to this problem has gained more interest in recent years with a number of researchers making use of numerical modelling to try to better understand this complex problem (Cotsovos *et al.*, 2008 and Saatci and Vecchio, 2009b). However, the accuracy of many of these models is limited due to the lack of a strong theoretical understanding of the problem and a reliance on user defined parameters which are difficult to know *a priori* or replicate in reality.

This chapter presents the development of a new analytical model which provides a theoretical explanation for the observed transition in failure mode. This work develops the concept described by Cotsovos *et al.* (2008) which suggests that the behaviour of RC members subjected to impact loads is dominated by a wave phenomenon which results in a shortened effective length for the member and therefore alters the relative shear and flexural demand. The work presented in the

current chapter addresses some of the assumptions made by Cotsovos *et al.*, (2008) in their numerical modelling. This includes the assumption that the wave from an impact propagates at the speed of a shear wave and the dependence of their solution on a constant loading rate, which is different to the impact velocity. Using a loading rate is convenient for numerical modelling, however, it is difficult to predict in actual impact tests owing to its dependence on a number of factors, including, but not limited to, the impact velocity, and the local and global stiffness of a member. For this reason the analytical solution proposed in the following sections does not feature any dependency on the loading rate, instead predicting the impact force by solving the equation of motion over a series of small time increments.

This concept of the increasing effective length was first proposed by Cotsovos *et al.*, (2008) to explain the formation of hogging cracks on the top surface of an impacted member. These were alluded to previously in the literature review and were also observed in the preliminary experimental work, described in section 3.2.2. An example of this phenomenon is shown in Figure 4.1.

Figure 4.1: Post test photo of test specimen 14D-U-I showing hogging cracks at the quarter span on the top face of a specimen impacted at mid-span

It was also observed by Cotsovos *et al.* that as the rate of loading increases these hogging cracks formed closer to the point of impact. From these observations Cotsovos *et al.* concluded that the behaviour was attributable to a wave propagating from the point of impact. Evidence of this behaviour was confirmed through experimental testing carried out by Saatci and Vecchio (2009a) who were successful in measuring the time-delay between an impact occurring at the mid-span and the supports experiencing this force. From their experimental work, Saatci and Vecchio showed that the force propagated from the point of impact to the supports at an average velocity of around 750 m/s for an impact velocity of 8 m/s on a beam of depth 410 mm spanning 3000 mm. This is significantly lower than the shear wave velocity considered by Cotsovos *et al.*, which was approximately 2350 m/s.

Outlined in the current chapter is a detailed discussion of the force propagation velocity, which includes the results of experimental testing, carried out as part of this project in an attempt to measure the propagation velocity. The development of this concept and the experimental work carried out to understand this feature in more detail is one of the key aspects of this thesis. This parameter then forms the basis of the proposed analytical model presented below which is used to explain why higher velocity/lower mass impacts cause more brittle failures than lower velocity/higher mass impacts, despite equivalent input energies. The chapter concludes with a sensitivity analysis and discussion which is aimed at assessing the validity of the assumptions made in the model and areas where further research is required.

4.1.1. Force propagation velocity

From the available literature it would appear that Saatci and Vecchio (2009a) were some of the first researchers to provide data on the velocity with which the force from an impact propagates to the supports. This was achieved using an accelerometer on the impacting mass and load cells at the supports, data from which was logged simultaneously at a high rate, an example of which is shown in Figure 4.2.

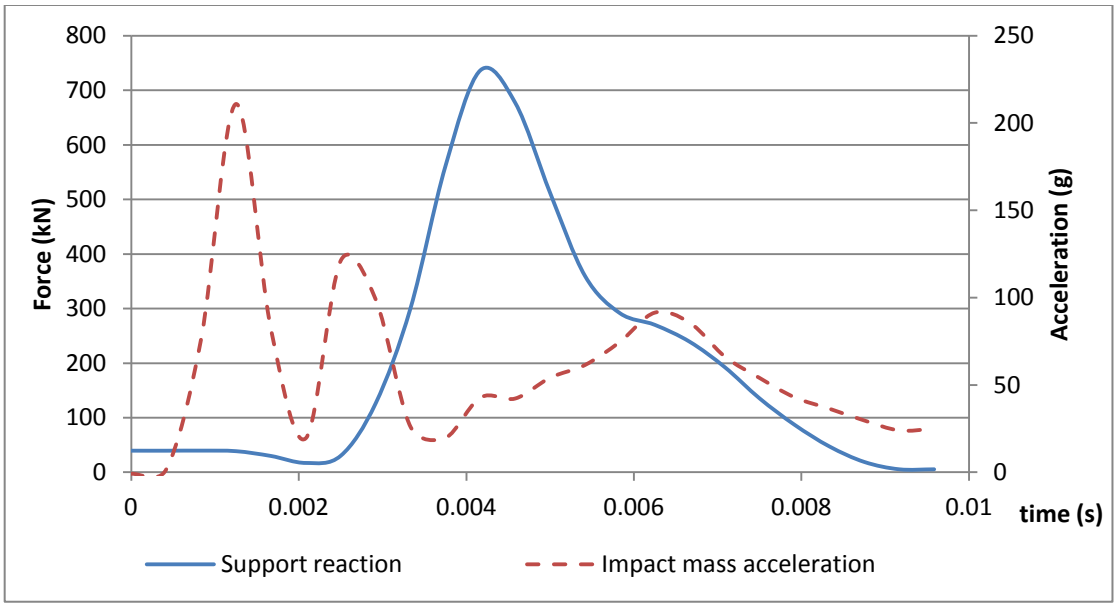

Figure 4.2: Data from Saatci and Vecchio (2009a) highlighting the time delay from the point of impact to the force reaching the reactions

Due to the limited data on the velocity at which a disturbance propagates from an impact, a number of tests were carried out as part of this research project to measure this phenomenon in a similar method to that of Saatci and Vecchio (2009a). Impact tests were instrumented with an accelerometer mounted to the impacting mass and strain gauged pins, acting as load cells, placed at the supports, as described in Chapter 5. By sampling these at a suitable rate it was possible to measure the time lag between the impact occurring and the supports experiencing the force from which the average force propagation velocity could be calculated. A summary of the results from these tests is given in Table 4.1. A more detailed description of these tests is given in later chapters.

Table 4.1: Summary of test results

Specimen Ref	Impact velocity V_{imp} (m/s)	Impact mass M_{imp} (kg)	Span, L (mm)	Depth, h (mm)	L/h	Force arrival time, t_a (s)	Force propagation velocity, μ (m/s)
4B-U-I	4	360	1000	200	5	0.0007	714
7B-R-I	6.3	210	1000	200	5	0.0006	833
8B-R-I	5	360	1000	200	5	0.0007	714
10C-U-I	6.7	150	1700	170	10	0.00293	286
12D-U-I	6.5	150	1700	170	10	0.00248	343
13D-U-I	6.5	150	1020	170	6	0.00078	654
14D-U-I	6.5	150	2210	170	13	0.00438	252

Data collected from the high speed images was also used in digital image correlation (DIC) software (geoPIV) to track the propagation of the deformation from the point of impact; this gave an alternative method for measuring the deformation propagation velocity. To make use of this system a series of images of the entire specimen were recorded at a rate of 3000 frames per second. Each image was subdivided into a number of reference frames which are shown in Figure 4.3 and the motion of the speckle pattern through a particular reference frame was tracked between images.

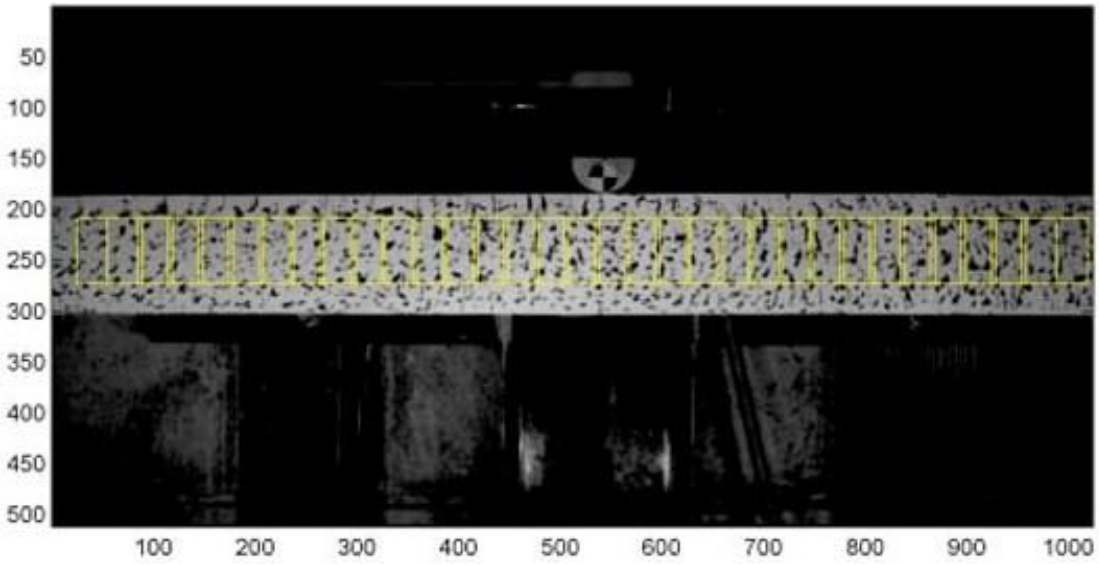

Figure 4.3: Division of specimen 14D-U-I into reference frames for DIC analysis

The relative displacement of the speckle pattern was then calibrated against a known geometric length to give actual displacements, from which the deformed shape was determined by plotting the displacement at each known coordinate along the members length. The first four deflected profiles of specimen 14D-U-I (described in Chapter 5) are shown in Figure 4.4. These profiles show clearly the propagation of the deformation and how the deformed length of the member increases with each time-step. This provides further evidence to support the effective length theory of Cotsovos *et al.* (2008). The results also provide a further source of data for measuring the force wave propagation velocity which can be used to corroborate the data from the load cells and accelerometer. Data obtained using this method for specimen 14D-U-I is included in Figure 4.5.

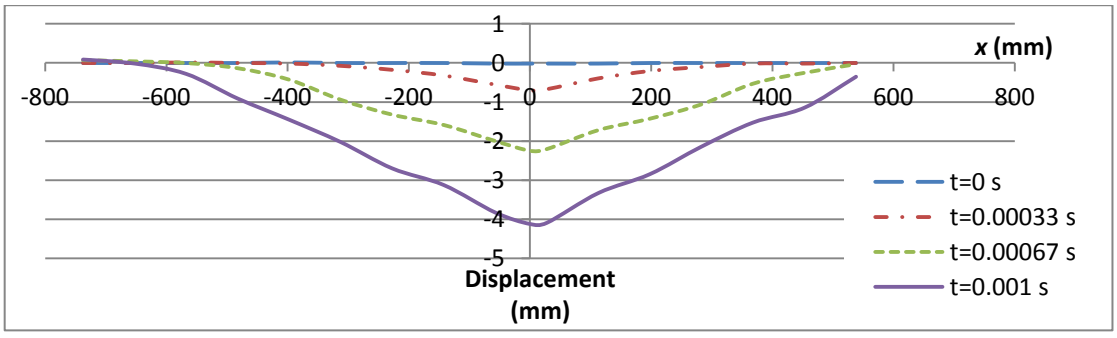

Figure 4.4: Deflected shape profiles for specimen 14D-U-I

Preliminary tests appeared to indicate that the force propagation velocity had a dependency on the span/depth (slenderness) ratio of a particular member. Due to the infancy of this work it was not clear which other parameters may affect the force propagation velocity, therefore, it was decided that efforts at this stage would be best focused on the span/depth ratio rather than covering other parameters in less detail. For this reason the majority of tests were carried out at a constant impact velocity of 6.5 m/s.

Data from the tests that measured the average force propagation velocity (Table 4.1) are plotted along with the DIC data for specimen 14D-U-I in Figure 4.5. The DIC results from specimen 14D-U-I were used as this was found to be easiest to measure the propagation from. This was done by measuring the increase in the effective length between frames. As the frame rate was known, the velocity with which the disturbance propagated could be easily calculated. A logarithmic best fit line was found to produce the best correlation with the data (R^2 = 0.89), which is given by equation 4.1:

$$\mu = -648 \ln\left(\frac{Span}{Depth}\right) + 1884 \tag{4.1}$$

where, μ, is the force propagation velocity.

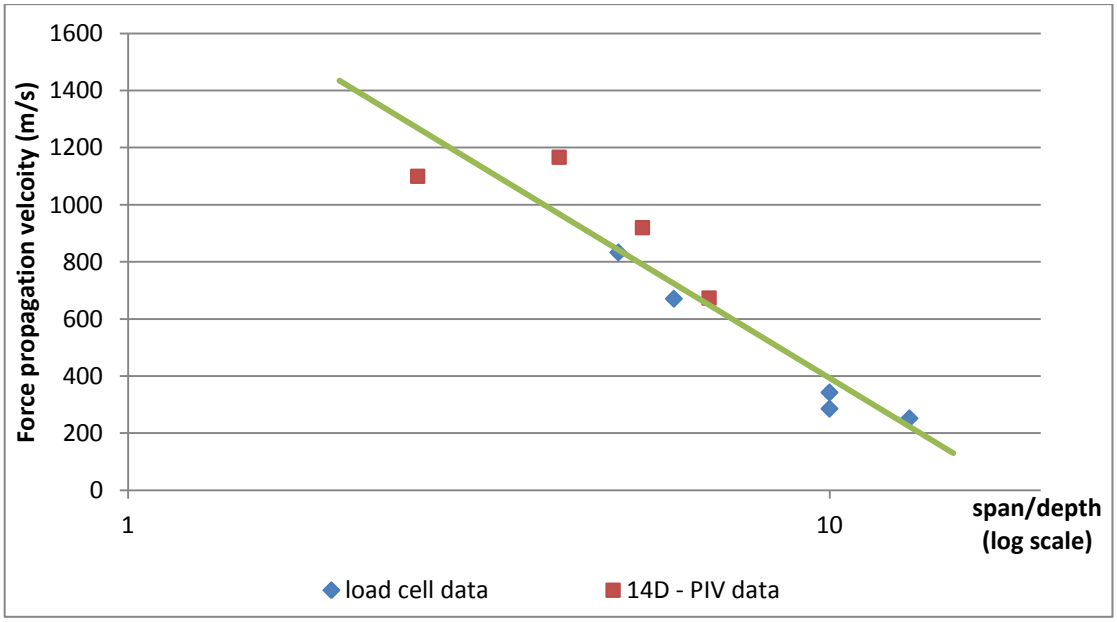

Figure 4.5: Variation in average force propagation velocity with increasing span/depth ratios (plotted on a logarithmic axis)

The results from the load cell data, outlined in Figure 4.5, demonstrate a clear relationship between the force propagation velocity and the slenderness of a member. This behaviour is supported by the propagation velocities determined from the DIC analysis on specimen 14D-U-I (also plotted in Figure 4.5). From this it can clearly be seen that the propagation velocity reduces as the slenderness of the member increases. It is not clear from the data whether for extremely small span/depth ratios the propagation velocity would approach the shear wave velocity, which is approximately 2500 m/s for concrete. However, for the practical range of span/depth ratios encountered in reality, it is clear that it does not.

Of the tests outlined in Table 4.1, 4B-U-I, 7B-R-I and 8B-R-I were the only tests carried out at different impact velocities on specimens with the same dimensions. The results for these are shown in Figure 4.6. Plotted alongside this data are the error bars which indicate the potential variation in the propagation velocity based on the sampling rate in these tests, which was just 10,000 Hz (data from the other tests was recorded at either 100,000 Hz or 150,000 Hz).

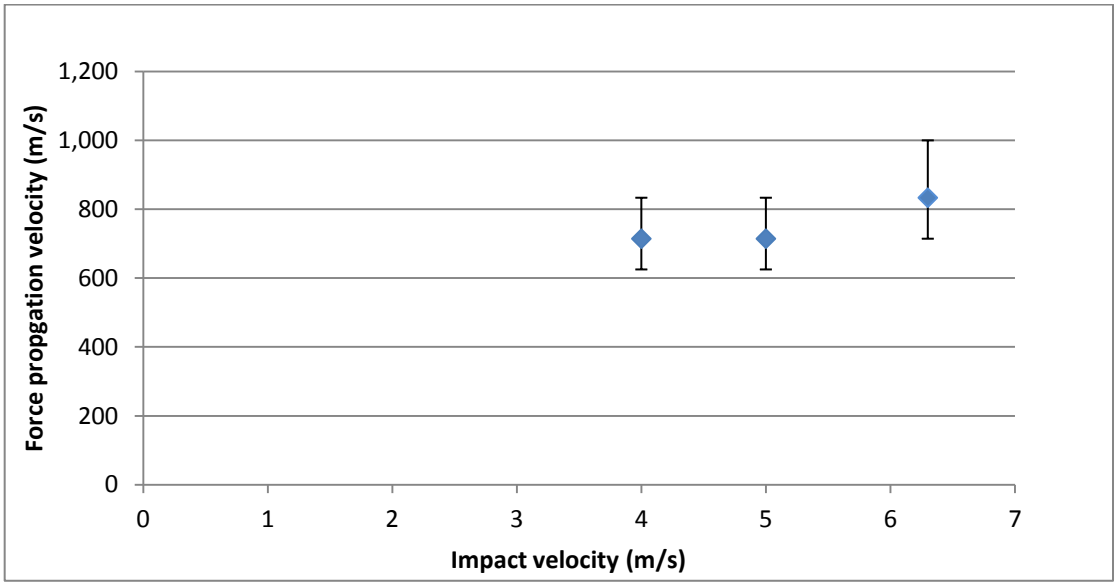

Figure 4.6: Relationship between impact velocity and force propagation velocity for members with same dimensions

Due to the limited sample size it is not possible to prove a conclusive relationship between the impact velocity and the force propagation velocity. However, as discussed in the literature review, a relationship between the impact velocity and the velocity with which waves propagate was found in tests carried out on thin elastic

sheets by Vermorel *et al.* (2009). The results from these tests are shown in Figure 4.7 which demonstrate that the wave front velocity ($\bar{U}$) increases as the impact velocity (V) increases. Whilst it is apparent that the behaviour of thin plates and concrete members is different, it may be expected that such a relationship would be found if more tests were carried out. However, due to the limited data on this parameter, the sensitivity analysis presented in Section 4.4 does not include any modification to the force propagation velocity for changing impact velocity.

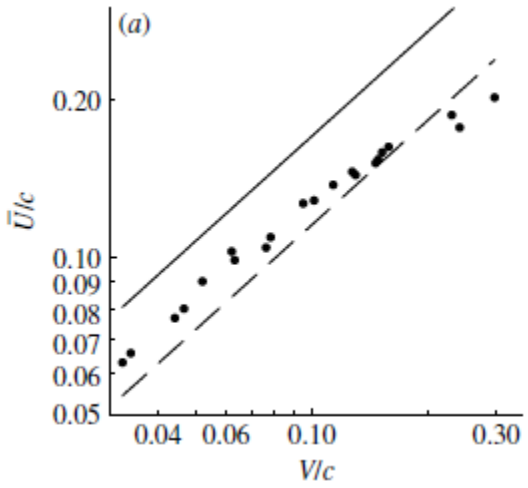

Figure 4.7: Relationship between wave front velocity ($\bar{U}$) and impact velocity (V), Vermorel *et al.* (2009)

From the data presented in Figure 4.5 it is shown that the propagation of the force from the point of impact is heavily dependent on the span/depth ratio of a member. It is shown that as the force propagates outward, and the effective length increases so the velocity reduces. The effective length makes up one of the key parameters for the model outlined below, enabling the time-dependent mass and stiffness of the member to be determined.

4.2. Development of analytical model for point load impact

Accurately modelling the initial force acting on a member subjected to a concentrated impact load can be complicated due to issues such as wave phenomena, plastic deformation, axial loading in compression members and strain-rate effects. Observations from impact tests carried out on concrete structures suggest that initially

the majority of deformation is caused by localised crushing in the contact zone, however, over a very short time the velocity of the impacted member increases and a period of conjoined motion between the impacting mass and the member occurs. After reaching the peak displacement (velocity of impacting mass and specimen are both zero) some elastic rebound occurs before the motion of both the member and the impacting mass eventually stops. The period of motion covering the conjoined motion, right up to the peak displacement being reached is covered in Chapter 6, this chapter only discusses the very initial motion where significant inertia forces develop.

Due to the complicated response, the current analysis technique attempts to approximate the response as a two degree-of-freedom (2DOF) system. In this approximation, spring stiffness's are considered to vary with time and damping is ignored. The validity of these assumptions is discussed below. The use of a simplified approach is beneficial in terms of demonstrating the importance of treating the behaviour as being dominated by a wave phenomenon and demonstrating the key observed features of a member's response.

A further simplification of the model is that it is assumed that the member is not subjected to axial loads.

The basic equations describing the forces acting on a member are given by equation 4.2 and 4.3. Equation 4.2 differs from the usually encountered static case by including inertia effects which would not be encountered under quasi-static load conditions.

$$2Q = -P(t) + \int m \frac{\partial^2 u}{\partial t^2} \partial x \tag{4.2}$$

$$\frac{\partial M}{\partial x} = Q \tag{4.3}$$

where Q is the shear force at the boundaries of the effective length (which is related to the stiffness), $P(t)$ is the impact force (which varies with time, as discussed below), m is the mass per unit length, x is the distance from the point of impact, u is the displacement in the direction of the impacting mass, t is the time and M_0 is the moment at $x = 0$. Equation 4.2 is essentially the equation of motion for a single degree of freedom system. A modification is made to this for the time dependency of the impact force P which itself does not vary spatially but is described by a second equation of motion which relates to the local force in the contact zone.

At each time-step it is assumed in the model that the member has an effective length (L_{eff}). In subsequent time-steps the effective length increases as the force propagates from the point of impact. This is highlighted in the diagram shown in Figure 4.8

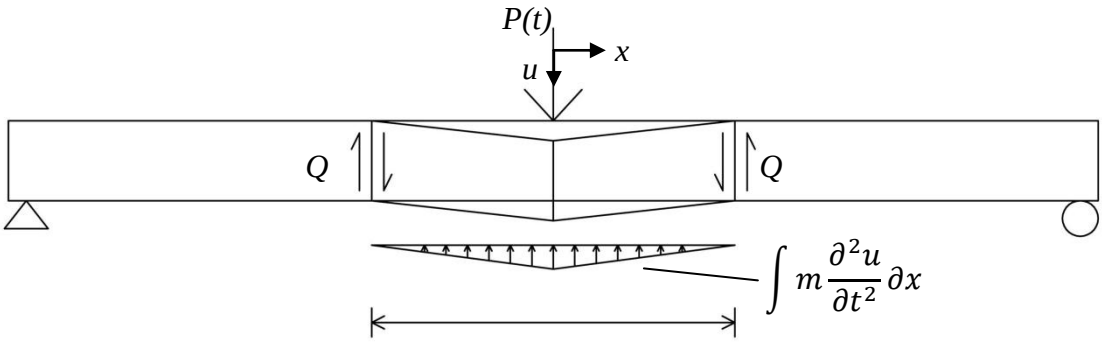

Figure 4.8: Diagram of forces acting on a member at a particular time-step for an effective length, L_{eff}, which has 'experienced' the force during impact event

The proposed model relates the diagram in Figure 4.8 and equations 4.2 and 4.3 to an idealised system of two masses (impacting mass and member mass) and two springs (contact zone stiffness and the member's bending stiffness) which are connected in series (Figure 4.9). The impacting mass (M_m) and the stiffness of the contact zone (k_c) are assumed to remain constant with time, but the mass and stiffness of the member, M_b and k_b respectively, are considered to vary with time as the effective length increases.

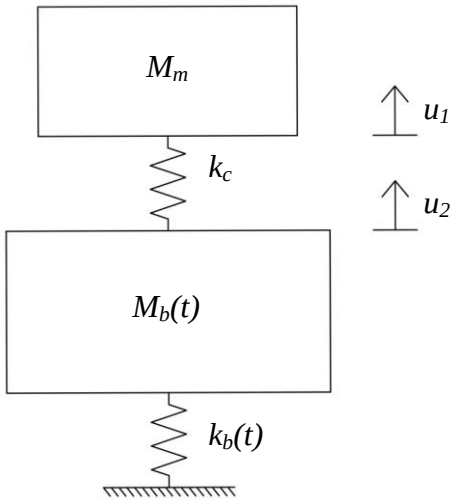

Figure 4.9: Two degree of freedom model used in analysis

The motion of the impacting mass and member can be determined by solving the two equations (4.4 and 4.5) for this system simultaneously at a particular time-step, which relate to equations 4.2 and 4.3.

$$\Delta F_{imp} = \Delta F_c \tag{4.4}$$

$$\Delta F_{imp} = \Delta F_{ine} + \Delta F_b \tag{4.5}$$

where, F_{imp} is the impact force caused by the deceleration of the impacting mass, F_c is the force due to localised compression in the contact zone, F_{ine} is the inertia force from the acceleration of the impact member and F_b is a ratio of the bending and shear stiffness of the impacted member depending on the effective length. Equations 4.4 and 4.5 are both written in terms of the change in force (Δ) for convenience when solving iteratively, however, they could equally be written as the total force. The method for determining each of these forces is outlined in detail below.

In a normal constant system these equations could be solved using a direct numerical integration method such as the Wilson-theta or Newmark method. However, due to the variation in the mass and stiffness of the member with time these methods require an additional iteration loop in order to solve the equations. This is described in Section 4.2.6.

On solving both equations simultaneously at each time-step, the analysis can proceed to the next time-step and the equations of motion solved again. By solving these equations, the impact force is determined along with the distribution of inertia forces along the member, from which, the overall bending and shear demand on the member at a specific time can be found (section 4.3.2).

One difficulty often encountered in dynamic situations is that the time varying impact force must be known prior to the analysis being carried out; however, this is overcome in the proposed model by employing the force propagation concept and determining the impact force at each time-step. Therefore, in order to carry out the analysis, only the properties of the member, the impacting mass and impact velocity need to be known. This approach makes it possible to determine the forces acting on a member during the first few milliseconds of its response, during which time, as will later be shown, the peak shear force acting on the member occurs.

4.2.1. Impact force

Given the variation in the mass and stiffness of the member, an iterative approach is required at each time-step to satisfy equations 4.4 and 4.5 simultaneously. It is assumed in the current formulation of the model that the impacting mass is rigid. The impact force is therefore dependent only on the deceleration of the impacting mass. Situations in which the impacting mass can deform require knowledge of the deformation characteristics of the mass for the analysis to proceed. These situations are not considered in the scope of the current work.

To begin the analysis it is necessary to assume that the impacting mass comes into contact with the member and the velocity decreases, leading to a small deceleration, $\ddot{u}_1$. Equations 4.4 and 4.5 are solved for the change in force at each time-step as opposed to the total force (although solving for the latter would be equally simple). The change in impact force (ΔF_{imp}) at a time-step, i, is therefore given by equation 4.6:

$$\Delta F_{imp} = M_m.\left(\ddot{u}_{1,i} - \ddot{u}_{1,i-1}\right) \tag{4.6}$$

It is clear that the solution for the change in the impact force is dependent on the assumed deceleration of the impacting mass. To achieve the correct solution to equations 4.4 and 4.5 simultaneously, this assumption may need to be re-iterated. The need for re-iterating the solution makes the analysis procedure best suited to a numerical program with inbuilt goal seeking solvers, this is discussed in more detail in Section 4.2.6.

4.2.2. Contact zone force

Failure to include the local stiffness in the contact zone effectively implies that the material is incompressible. Due to the effective length concept, this assumption would result in the model predicting an initial impact force that tends to infinity with decreasing length of time-step. As concrete is clearly not an incompressible material and has a finite stiffness it is important to include these effects in the analysis to avoid this problem.

The local stress state arising from the impact of a rigid body on another is complex, as outlined by Johnson (1985). Therefore, for the development of the proposed model, as a simplifying assumption, the relationship for a quasi-static case of local contact is

used. A further extension to this would be to include dynamic material properties based on strain-rates, an area which is discussed in greater detail below.

The change in the force in the contact zone (ΔF_c) is given by equation 4.7:

$$\Delta F_c = k_c(\Delta u_1 - \Delta u_2) \tag{4.7}$$

where, Δu_1 is the change in contact zone displacement, Δu_2 is the change in displacement of the member at the location of the impact and k_c is the stiffness of the contact zone. The contact stiffness is taken from the work of Johnson (1985) for the contact between cylinders and is given by equation 4.8:

$$k_c = \frac{\pi E_2 b}{(1-\upsilon_2^2)[2\ln(2h/a)-\upsilon_2/(1-\upsilon_2)]} \tag{4.8}$$

where E_2 is the Young's Modulus of the concrete, b is the width of the member (which can be considered as the breadth of the cylinder, Figure 4.10), υ_2 is the Poissons ratio for the concrete, h is the depth of the member. In this formulation, a, is half the width of the contact zone, which is shown diagrammatically in Figure 4.10 and is given by equation 4.9, from Roark's formulas (Young and Budynas, 2002).

$$a = 0.8\sqrt{pK_D C_E} \tag{4.9}$$

where p is the contact force per unit length (F_{imp}/b), K_D is the diameter of the impacting mass which is assumed to be cylindrical. C_E is given by equation 4.10:

$$C_E = \frac{1-\upsilon_1^2}{E_1} + \frac{1-\upsilon_2^2}{E_2} \tag{4.10}$$

where, υ is the Poisson's ratio and E is the Young's Modulus, with subscripts 1 and 2 referring to the impactor and specimen respectively.

From equations 4.8 and 4.9, it can be seen that the contact zone stiffness, k_c is dependent on a number of factors which may not be explicitly known, such as the diameter of the impacting point, K_D. It is also apparent that the equation for the width of the contact zone is dependent on the impact force which will change with each time-step.

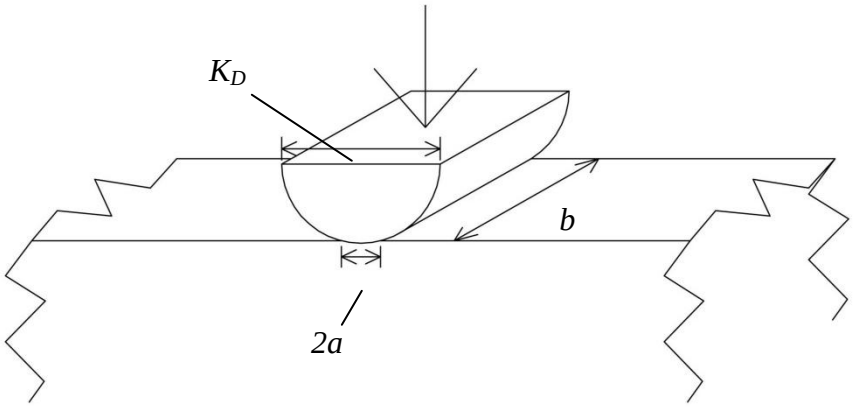

Figure 4.10: Diagram of contact zone

Due to the variation in the contact zone stiffness and its dependency on a number of factors, a sensitivity analysis has been carried out in section 4.4.2 to investigate the importance of this parameter on the predicted behaviour.

Using equation 4.7 assumes that the contact zone behaves as a linear elastic material. In reality this will not be the cases due to plastic flow and strain hardening. The exact material response under impact is complicated and little is known accurately about it. The diagram shown in Figure 4.11 was presented by Bischoff *et al.* (1990) and qualitatively indicates the relationship between the resistance of concrete to localised crushing. This figure indicates that the material's behaviour is initially linear elastic followed by a period of plastic flow before hardening occurs. Without quantitative data it is not possible to model this behaviour accurately so the simplified assumption of linear elasticity has been made for the purposes of the model developed here.

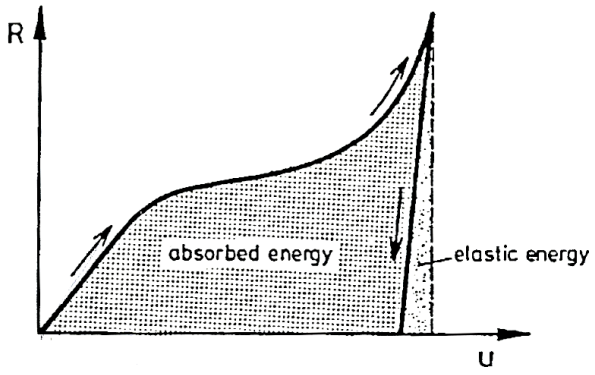

Figure 4.11: Contact zone behaviour model (Bischoff *et al.*, 1990)

4.2.3. Inertia force

The inertia force is the result of the rapid acceleration of the member. An important feature of the assumed effective length is that the member can only deform over this length. Outside of the effective length the member's displacement is zero and hence it has no inertia. It would be expected that the deflected shape would be related to the dominant mode of deformation. When the effective length is short this would be mainly through shear but when the effective length is longer this would change to a flexurally dominated mode. To simplify the analysis procedure the deflected shape is assumed here to vary linearly as indicated in Figure 4.8 and given by equation 4.11. In reality modelling both of these phases would present the ideal case, however, it will later be shown that the precise nature of the deflected shape has little bearing on the inertia force so the added complication of modelling both is unwarranted. A full comparison of the two is given in the sensitivity analysis in section 4.4.3.

With the coordinate system at the centre of the beam for convenience, it can be shown that the transverse displacement, u_2, of the member at a distance, x, from the centre is:

$$u_2(x,t) = \beta\left(1 - \frac{\mathrm{x}}{\mathrm{L_{eff}}}\right) \tag{4.11}$$

where, x is the distance from the centre, t is the time, L_{eff} is a function of t and β is a factor that is varied so that the total displacement of u_1 and u_2 at the point of impact is equal to the distance through which the impacting mass has moved.

The inertia force is determined by dividing the member into a number of segments. The displacement of the centroid of a segment at a location x for the i^{th} time-step is found from equation 4.11 from which the acceleration is found by differentiating twice with respect to time. In the current formulation rotational inertia is ignored. Due to the use of the time-step procedure, explicitly differentiating equation 4.11 is not necessary, instead the central difference method can be employed to find the solution.

The change in the inertia force, $\Delta f_{ine,seg}$ of each segment for a given time-step, i, is given by equation 4.12:

$$\Delta f_{ine,seg} = m_{seg}\left(\ddot{u}_{\mathrm{seg},i} - \ddot{u}_{\mathrm{seg},i-1}\right) \tag{4.12}$$

where, m_{seg} is the mass of a segment and $\ddot{u}_{seg}$ is the acceleration of a segment. The total change in the inertia force is then determined for each time-step by summing the forces of each individual segment:

$$\Delta F_{ine} = \sum f_{ine,seg} \tag{4.13}$$

4.2.4. Stiffness force

The final term from equation 4.5 that is left to discuss is that relating to the stiffness of the member. It was outlined above that for short effective lengths it would be expected that shear deformations would dominate. Due to the dependency of the inertia term on the time-step, modelling the transition in the dominant deformation mode to determine the inertia force leads to unwarranted complexities. However, for the case of the stiffness force, which is also dependent on the assumed deflected shape, but not the time-step, the solution can be set-up to be a combination of the shear stiffness and the flexural stiffness, with one dominating over the other depending on the effective length. The shear and flexural stiffnesses are given by equations 4.14 and 4.15. The relationship between the effective length and the shear or flexural stiffnesses is also shown graphically in Figure 4.12. This indicates that for effective lengths smaller than a certain threshold (in this example approximately 900 mm), the flexural stiffness is higher than the shear stiffness and therefore deformations will be through a shear mode. The precise length at which the transition in the dominant deformation mode occurs can be found by equating and rearranging equations 4.14 and 4.15.

$$k_{b,s} = \frac{\kappa GA}{L} \tag{4.14}$$

$$k_{b,f} = \frac{192EI}{L_{eff}^3} \tag{4.15}$$

where, *G* is the shear modulus of the concrete, *A* is the cross sectional area (assumed crack in accordance with the second moment of area), κ is the shape factor for shear, *I* is taken as the cracked second moment of area for a transformed section and *E* is the Young's Modulus for the transformed material

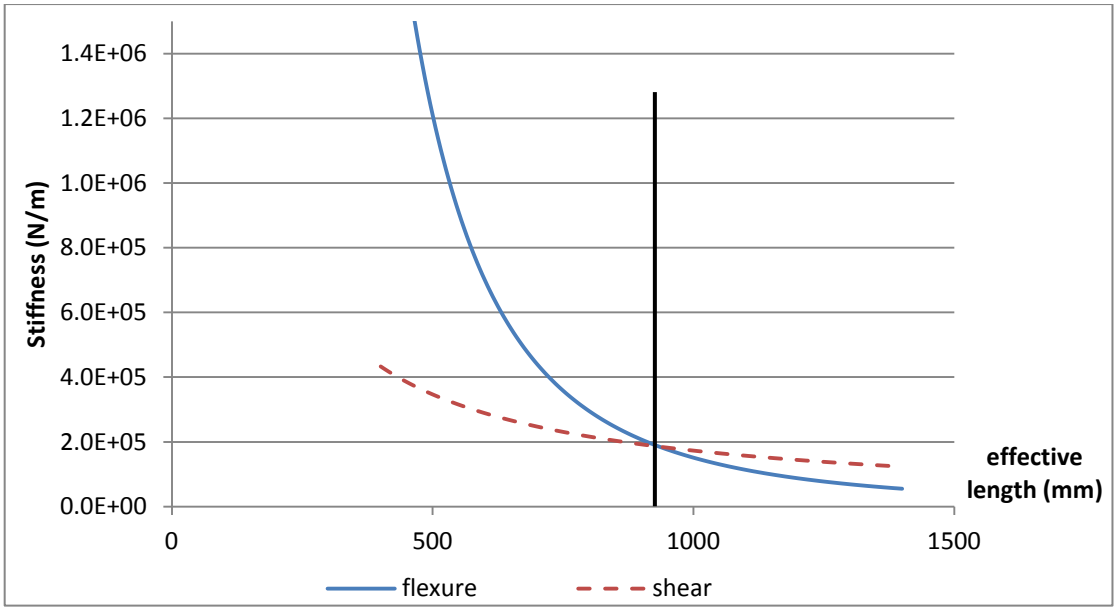

Figure 4.12 Shear and bending stiffness variation with increasing effective lengths

The change in the stiffness force (ΔF_b) at a time-step is given by equation 4.16:

$$\Delta F_b = k_b.\left(u_{2,i} - u_{2,i-1}\right) \tag{4.16}$$

where $u_{2,i}$ is the displacement of the member at the point of load application, at the i^{th} time-step and k_b is dependent on the relative bending and shear stiffness of the member which is dependent on the effective length. For a given effective length the term, $k_b \Delta u_2$, can be considered to be made up of two components based on the shear and bending stiffness:

$$k_b \Delta u_2 = k_{b,f} \Delta u_{2,a} + k_{b,s} \Delta u_{2,b} \tag{4.17}$$

where, $\Delta\left(u_{2,a} + u_{2,b}\right) = \Delta u_2$. It is clear from this relationship that when the bending stiffness is significantly greater than the shear stiffness then deformation through shear will dominate the response and vice versa.

4.2.5. Time step and effective length

The equations of motion outlined above are solved over a series of small time increments which allows an iterative procedure to be employed. The time-step is also important in determining the effective length of the member which is used to find the bending stiffness of the member and its effective mass.

To simplify the analysis procedure a constant time-step is used when solving the equations of motion, from which the effective length is determined from the best fit line for the experimental data shown in Figure 4.13, which is given by equation 4.18:

$$\frac{Effective\ length}{depth} = 167t^{0.466} \tag{4.18}$$

where, *t*, is the time at a given time-step. This relationship has been determined by curve fitting data obtained from impact tests where the impact velocity was approximately 6.5 m/s in all cases.

In order for this relationship to be applicable for an impact of any velocity it is suggested here that the above relationship is multiplied by a factor (Ψ) determined from equation 4.19 which is based on the data shown in Figure 4.6. The limitations in the use of this factor have been discussed previously.

$$\Psi = 0.065V_{imp} + 0.576 \tag{4.19}$$

where V_{imp} is the impact velocity.

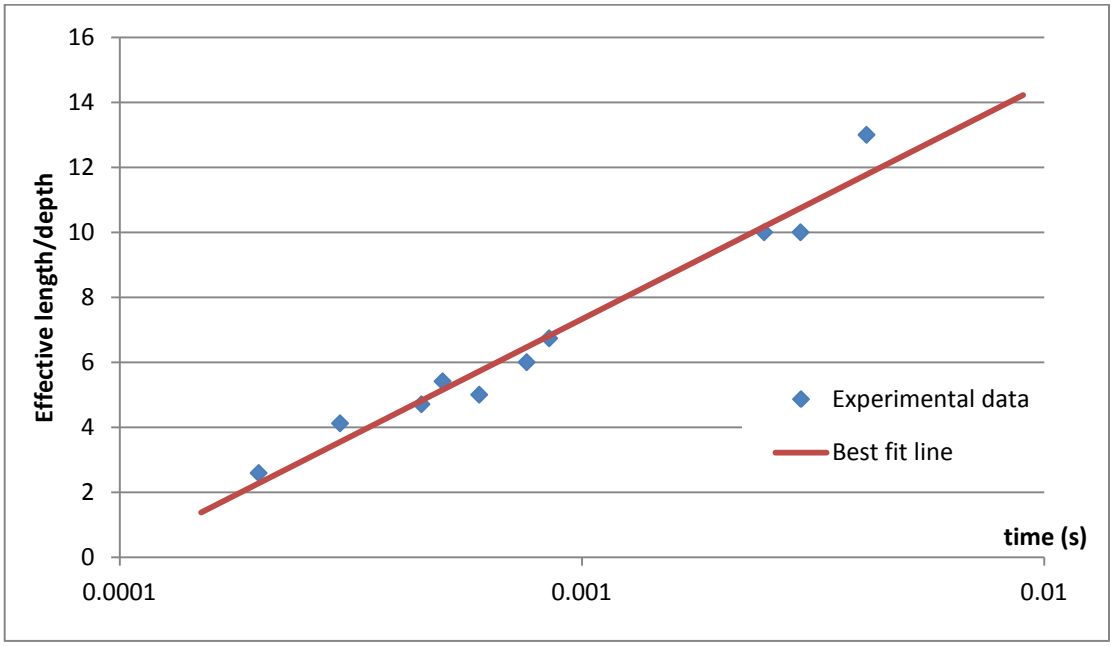

Figure 4.13: Variation in effective length/depth ratio with time for impact velocity of 6.5 m/s

Although the solution is unconditionally stable, refinement in the results can require some iteration to achieve the required accuracy. Small time-steps come at the cost of increased computational time but a value in the order of 1/500th of the total response time (which is usually in the order of 10-30 ms) has been found sufficient. A

sensitivity study on the influence of the time-step on the results from the model is given in section 4.4.4.

Upon knowing the effective length at each time-step, the bending stiffness and mass of the member can be found which is used to solve the equation of motion at the specific time-step can be determined.

4.2.6. Solving the equations of motion

In order to determine the solution for the motion of the impacting mass and member, equations 4.4 and 4.5 must be solved simultaneously. These equations can be rewritten in full as:

$$M_m \Delta \ddot{u}_1 = k_c(t) \Delta u_1 \tag{4.20}$$

$$M_m \Delta \ddot{u}_1 = M_b(t) \Delta \ddot{u}_2 + k_b(t) \Delta u_2 \tag{4.21}$$

Due to the variation with time of the mass and stiffness of the member, these equations cannot be solved explicitly. Therefore the simplest solution is to solve these equations iteratively. The displacement, u, velocity, $\dot{u}$, and acceleration, $\ddot{u}$, of the impacting mass and member are all related through the central difference method, which is shown in equations 4.22 and 4.23 for the velocity and displacement:

$$\dot{u}_{i+1} = \dot{u}_i + \frac{\Delta t}{2}(\ddot{u}_i + \ddot{u}_{i+1}) \tag{4.22}$$

$$u_{i+1} = u_i + (\Delta t\, \dot{u}_i) + \frac{\Delta t^2}{4}(\ddot{u}_i + \ddot{u}_{i+1}) \tag{4.23}$$

As the initial displacement, velocity and acceleration are known, it is possible to calculate the velocity and displacement of both the impacting mass and member in the subsequent time-step simply by estimating the acceleration, $\ddot{u}_{i+1}$ (both the impacting mass and member have their own independent equations for velocity and displacement, however, as they are identical they are written here only once).

The initial estimation for the acceleration used to determine the velocity and displacement in equations 4.23 and 4.22 must be such that equations 4.20 and 4.21 are solved simultaneously. This ensures that at each time-step there is only one solution for the change in acceleration of the impacting mass and member.

4.3. Results

On achieving a solution for equations 4.20 and 4.21 for the given number of time-steps used in the analysis, the distribution of forces and velocity/displacement profiles can be used to predict the initial behaviour of an impact loaded member.

4.3.1. Forces and velocities

Figure 4.15 shows the forces that are initially generated from the impact of a 150 kg mass travelling at 6.5 m/s on a simply supported RC member spanning 2200 mm with cross section dimensions of 170x170 mm and an EI value of 7.9×10^{11} N/mm^2.

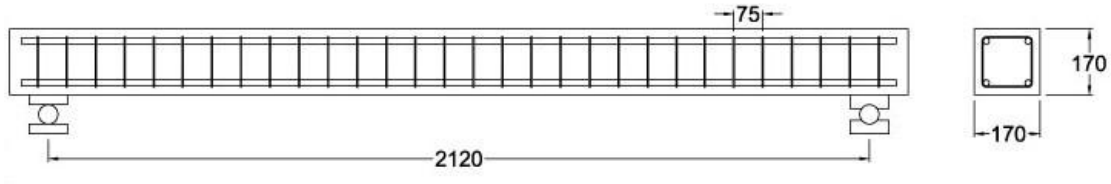

Figure 4.14: Dimensions of specimen used in the parametric study

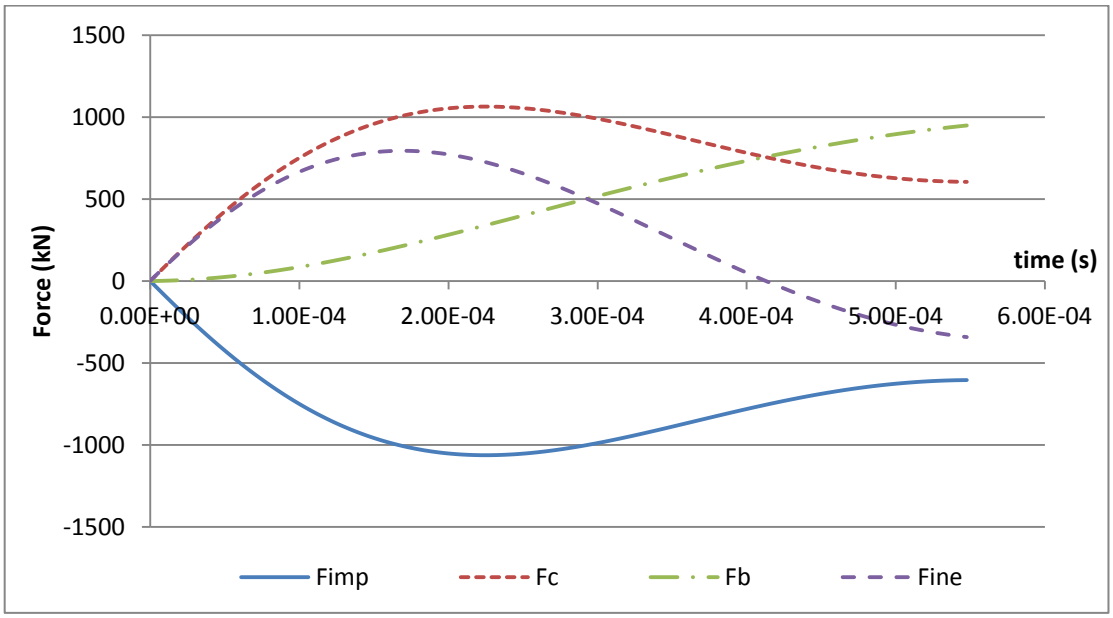

Figure 4.15: Example of the variation in forces acting on a centrally impacted member

It is indicated in Figure 4.15 that the force from the impact is initially resisted by the inertia force, however, over time the stiffness force increases and the inertia reduces. From equation 4.4, $\Delta F_{imp} = \Delta F_c$, therefore these lines are mirrors of one another, as

shown in Figure 4.15. The variation in the velocity of the member at its mid-span and the impacting mass are shown in Figure 4.16. This indicates that the velocity of the member is actually predicted to exceed the impacting mass velocity suggesting that at a certain point the two will become separated or that the contact spring will start to extend rather than contract. This is discussed in greater detail below.

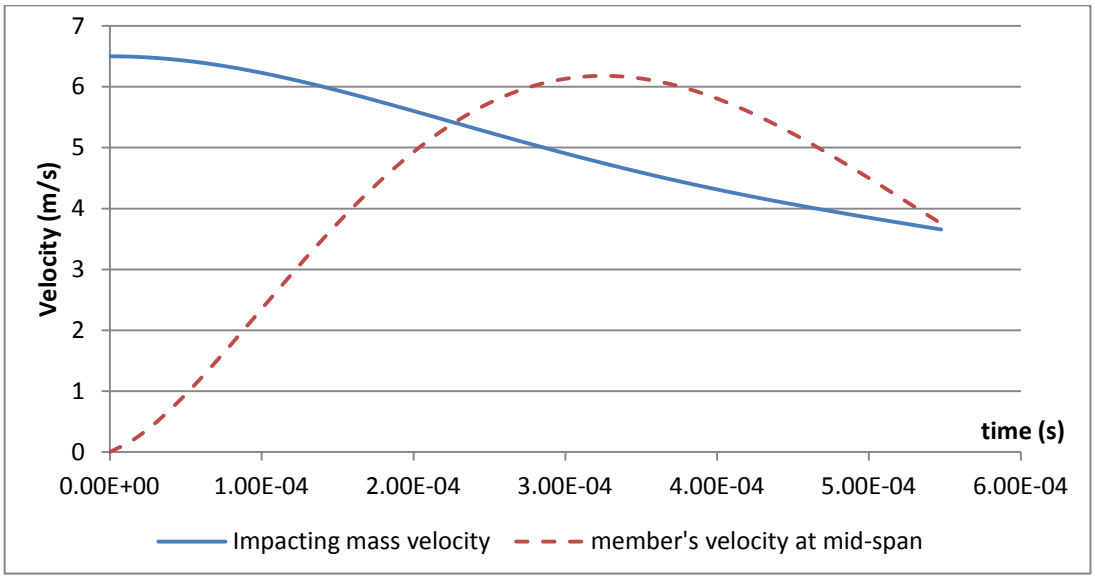

Figure 4.16: Predicted variation in velocity of impact mass and member

4.3.2. Bending moments and shear forces

By using the above procedures to solve the equation of motion for each time-step the distribution of forces acting on a member at any given time can be readily determined. Using these forces it becomes a relatively simple procedure to plot the bending moment and shear force diagrams for each time-step. These moments and shear forces represent the structural demand. The failure mode of the specimen can be determined if the section's capacity is known, although this is not covered in the current work.

Bending moments are plotted at discrete time-steps assuming a member with fixed-fixed end conditions and making use of the principle of superposition to combine the moments from the impact point load with those from the inertia forces. This assumes that the member is behaving elastically in the early stages. A plastic analysis is beyond the scope of the current work. Example results for the time varying shear forces and bending moments acting on a member are shown in Figure 4.17.

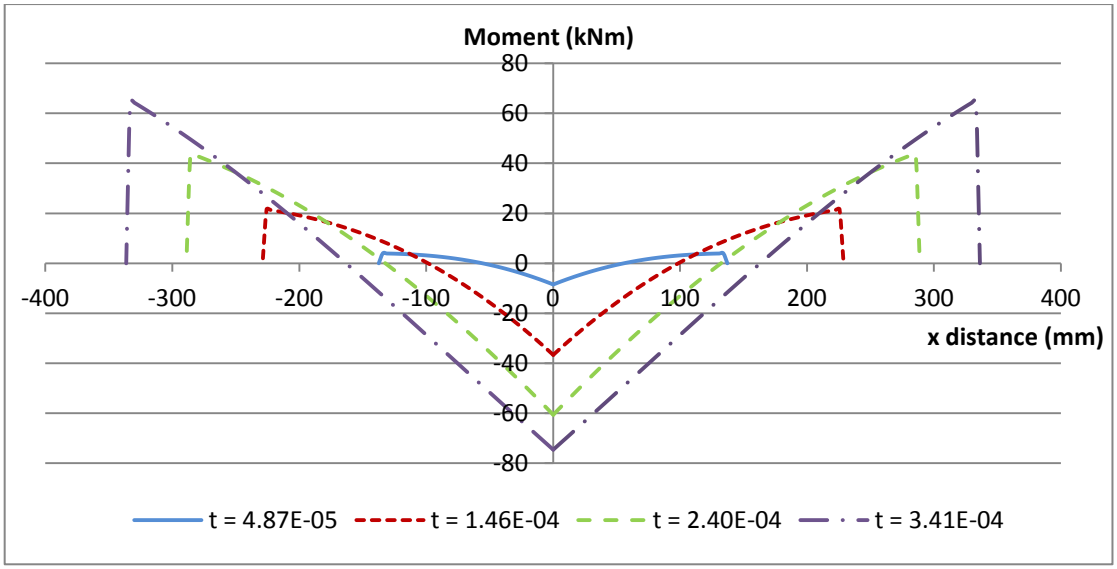

Figure 4.17: Variation in bending moment diagram for full beam with time (impact at origin)

The curved shape of the bending moment profiles (Figure 4.17) indicates that initially the inertia force has a strong influence on the predicted bending demand. Over time, as the inertia component of the force equilibrium reduces and bending stiffness dominates, the shape of the bending moment profile becomes the same shape as seen for fixed beam subjected to a central point load.

The formation of travelling plastic hinges at the boundaries of the effective length is not considered in this section but is discussed in more detail in section 4.4.5. It is interesting to note that both hogging and sagging moments are predicted by the model due to the assumption that the member is behaving as a fixed beam with a reduced length. This provides an indication as to why the test photo in Figure 4.1 showed cracks forming on the top surface of the member.

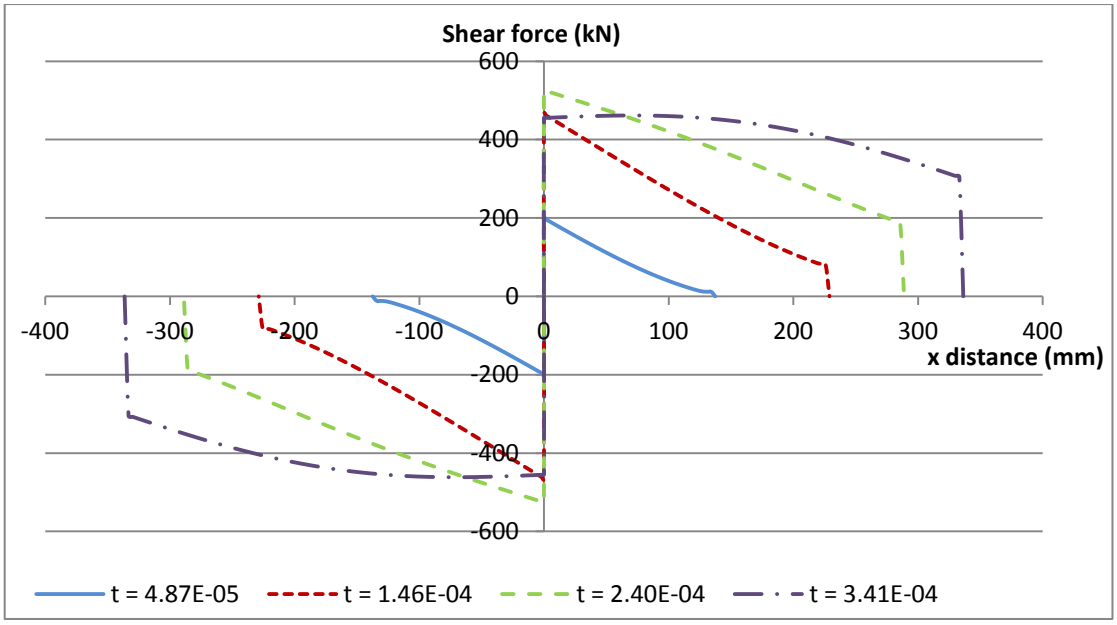

Figure 4.18: Variation in shear demand for full beam with time (impact at origin)

Results for the predicted time varying shear forces are shown in Figure 4.18. Initially the shear force increases rapidly with the maximum occurring at the centre where the impact occurs. Over time, as the effective length increases and the bending stiffness force begins to dominate the response, the peak shear force no longer occurs at the point of impact, as can be seen at $t = 3.41 \times 10^{-4}$ in Figure 4.18. It can also be seen that when this begins to occur the shape of the shear force diagram tends towards that of the quasi-static shape for a central point load.

4.4. Parametric study/Sensitivity analysis

The assumptions made in the formulation of the analytical model described above have been outlined in general. However, to investigate fully the effect of these assumptions and demonstrate the potential of the model, the following section details the results of a parametric study and sensitivity analysis. This study has been conducted assuming a member with the dimensions shown in Figure 4.14 and the properties outlined in section 4.3.1. The impact mass was taken as 150 kg unless otherwise stated and the impacting nose was cylindrical with a diameter of 90 mm. These dimensions and impact characteristics relate to specimen 14D-U-I which was shown in Table 4.1 to have an average force propagation velocity of 252 m/s and a force arrival time at the supports of 0.00438 seconds.

Given the high forces expected it was assumed from the outset that the section would be cracked and hence the second moment of area for a cracked section was employed where relevant. In situations where an axial force was present, this assumption may need revising due to compression effects. However, this is not relevant to the range of tests carried out in this study.

4.4.1. Mass/velocity ratios

One of the primary aims for the development of the proposed model was to provide a theoretical explanation for the observed experimental behaviour that higher velocity impacts can cause more brittle failures in RC than lower velocity ones.

To demonstrate this the following parametric study was carried out by predicting the impact forces and peak shear demand for three different ratios of impact mass and velocity in which the kinetic energy was kept constant at approximately 3200 joules. It was assumed that the force propagation velocity followed the relationship given in Section 4.1.1, with no modification made for the impact velocity.

The relationship between the impact mass/velocity and the predicted impact force is shown in Figure 4.19, with the relationship between the impact mass/velocity and the predicted shear demand shown in Figure 4.20.

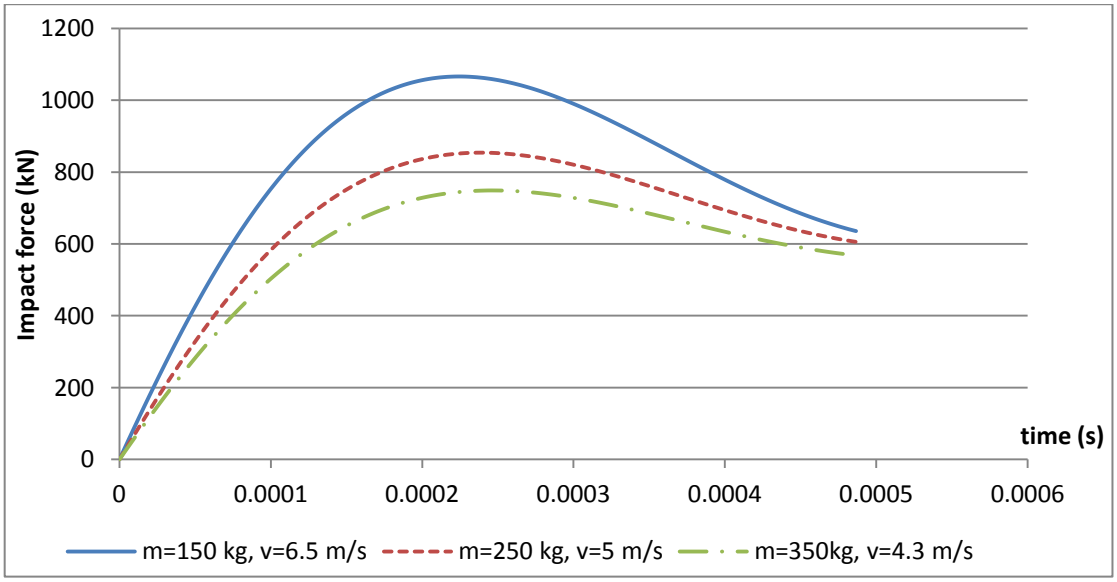

Figure 4.19: Relationship between impact mass/velocity and predicted impact force

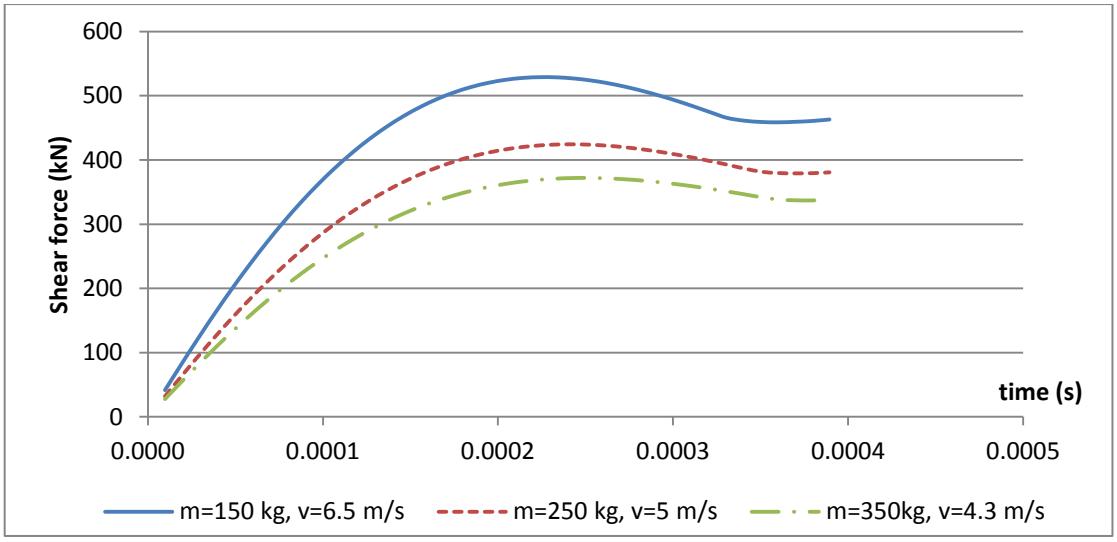

Figure 4.20: Predicted peak shear demand for impacts with different mass/velocity ratios

Figure 4.19 indicates that the impact force is predicted to increase as the impact velocity increases and the mass reduces. The same trend is shown in Figure 4.20 for the predicted shear demand. These results give a clear indication as to why higher velocity, lower mass impacts would cause more brittle failures than lower velocity, heavier mass impacts. Demonstrating these trends in the predicted shear demand for impacts of different velocities is an important development in this field and provides a clear theoretical basis for the behaviour outlined in the introduction to this chapter. However, this does not consider the effect of increasing loading rates on the shear *capacity* of the member. Whilst a study of this falls outside the scope of the current work a discussion on this aspect is given in section 4.5.2.

4.4.2. Contact zone stiffness

The contact zone stiffness was shown in section 4.2.2 to be dependent on a range of parameters including the diameter of the head of the impacting mass (K_D), the impact velocity and material properties which may exhibit strain-rate dependent behaviour. In addition to this, the precise load-displacement behaviour of the contact zone in impact situations is not well understood (Figure 4.11). Given these issues the following sensitivity analysis was carried out to determine the influence of the contact zone stiffness on the predicted demand. In order to simplify this analysis and understand the effect of the contact zone stiffness on the behaviour it was elected to apply a constant stiffness value for each time-step of the analysis, removing the dependency

on the impact force. Given the indicative nature of the sensitivity analysis it is considered that this assumption is acceptable.

The sensitivity analysis was carried out by varying a theoretically determined value of k_c = 1.4x10^9 N/m (as determined from equation 4.8, section 4.2.2), over a range of +/- 50% (7.1x10^8 N/m to 2.1x10^9 N/m). The effect that this has on the predicted impact force is shown in Figure 4.21.

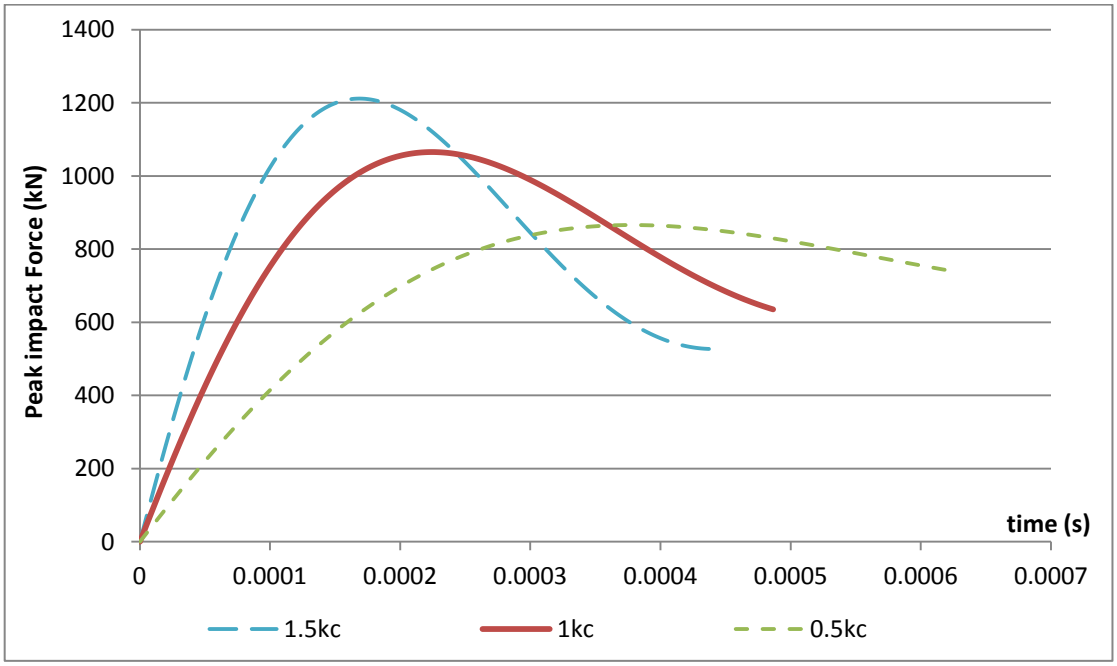

Figure 4.21: Predicted impact forced for different contact zone stiffnesses

Figure 4.21 indicates that the peak impact force is highly dependent on the contact zone stiffness and that for a stiffer contact zone the peak force is reached earlier but decays more quickly. It is indicated in Figure 4.22 that reducing the contact stiffness by around 50% from the base value results in a reduction in the predicted peak impact force by around 19%.

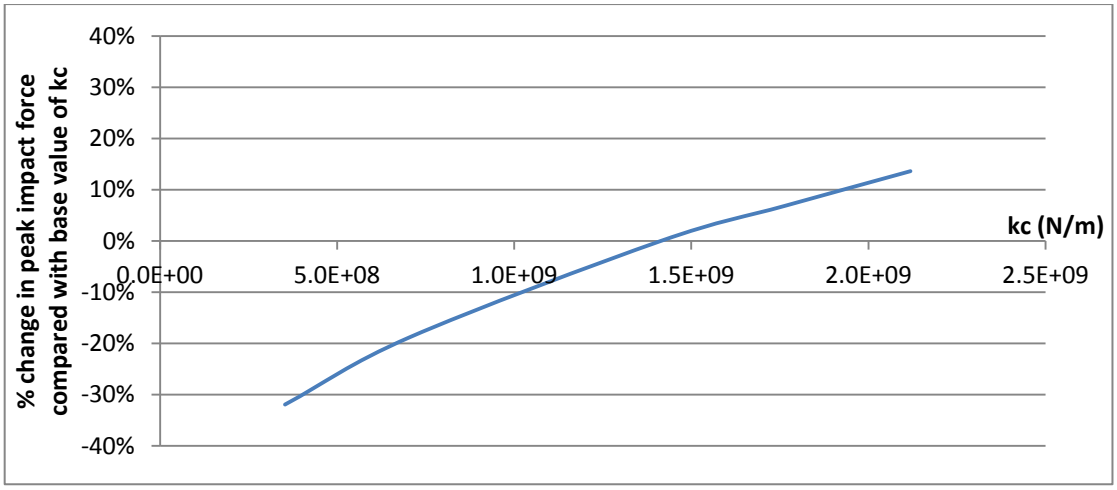

Figure 4.22: Percentage change in peak impact force for different contact zone stiffnesses from a mean value of $1.4x10^9$ N/m

More important for determining the response of a member subjected to an impact load is the predicted shear demand. By varying the contact stiffness within the same range as above, it can be shown that the peak shear demand has a similar dependency on the stiffness. Increasing the stiffness by around 50% results in an increase in the predicted peak shear demand by around 13%, whereas decreasing it by around 50% results in a decrease in the peak shear demand by around 18%.

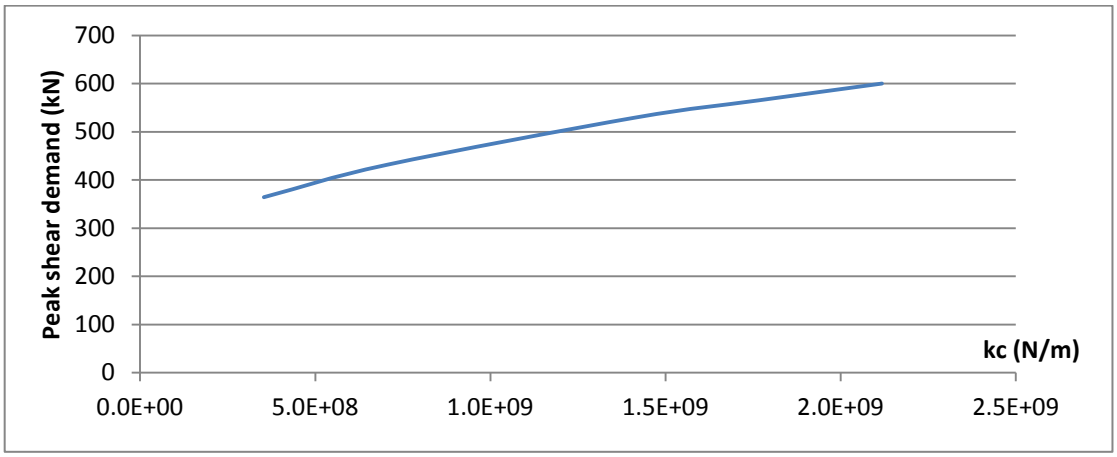

Figure 4.23: Predicted peak shear demand for different contact zone stiffnesses

It is clear from the dependency demonstrated in Figure 4.21 and Figure 4.23 that the contact zone stiffness plays an important role in determining the forces which the member is subjected to.

A final and interesting point to note on this subject is the variation caused by the change in contact zone stiffness to the predicted velocity of the impacted member. This is shown, compared with the velocity calculated from the DIC data for the test being modelled in this sensitivity analysis (14D-U-I), in Figure 4.24. It is clear from this figure that 0.25kc gives the closest approximation between the predicted velocity and the actual velocity from the test data, this is likely a function of the various idealising assumptions made in the model.

Due to the assumption of linear elastic behaviour for the contact zone stiffness, more energy would be stored elastically for a given displacement when the stiffness is higher. From this explanation it can clearly be seen why assuming a higher stiffness in the contact zone causes the velocity of the impacting mass to decrease more rapidly. In reality, being able to model accurately the stiffness of the contact zone would result in improved predictions for the behaviour but this is beyond the scope of the current work.

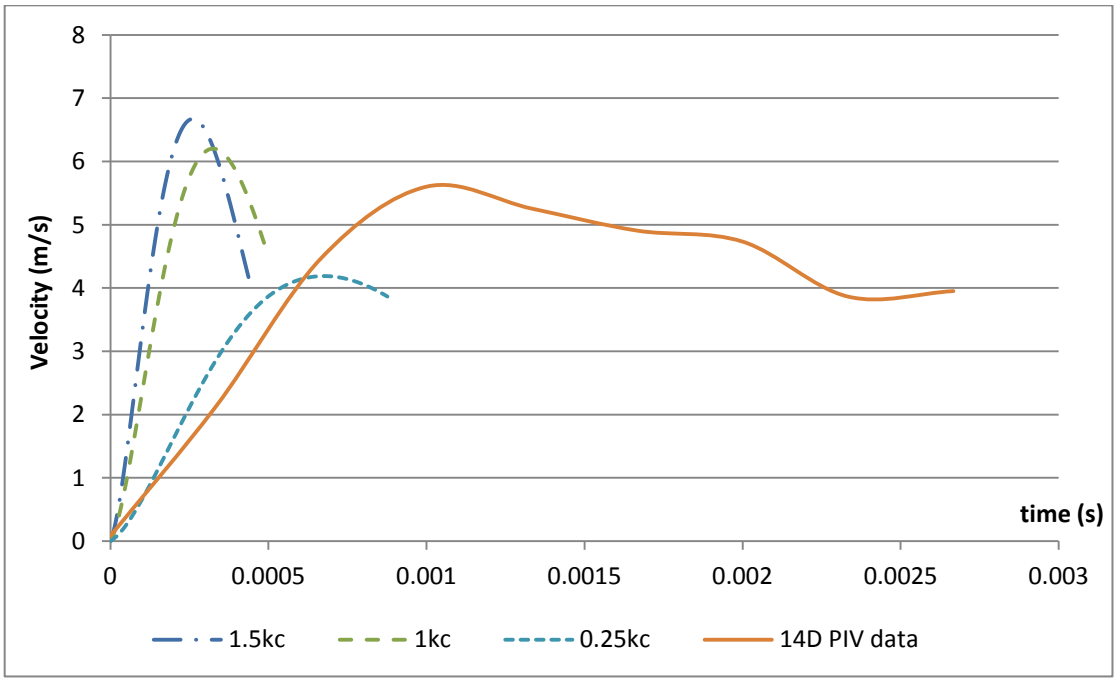

Figure 4.24: Variation in predicted peak velocity of mid-span of impacted member with different contact zone stiffnesses, compared with experimental data

4.4.3. Deflected shape

In the formulation of the model described above, the inertia profile is determined by assuming an assumed linear deflected shape. It was discussed in section 4.2.3 and indicated in Figure 4.4 that due to the short effective length of the member it would be expected to deform initially in a shear mode but that a transition may occur to a flexural mode as the effective length increases, where the deflected shape of the two modes is different. To validate the assumption of a linear deflected shape another model was set-up in which the inertia forces were determined assuming the displacement varied along the effective length by the shape given for an Euler beam in bending, the equation for which is given by:

$$u_2(x,t) = \beta\left(\frac{x^3}{12} + \frac{L_{eff}^3}{192} - \frac{L_{eff}x^2}{16}\right) \tag{4.24}$$

where, x is the distance from the centre, t is the time, L_{eff} is a function of t and β is a factor that is varied to give the correct displacement at the centroid.

From Figure 4.25 it can be seen that changing the assumed deflected shape from a flexural shape to a linear profile makes no difference to the predicted impact force. This result would be expected given the iterative procedure outlined above to determine the variation in forces.

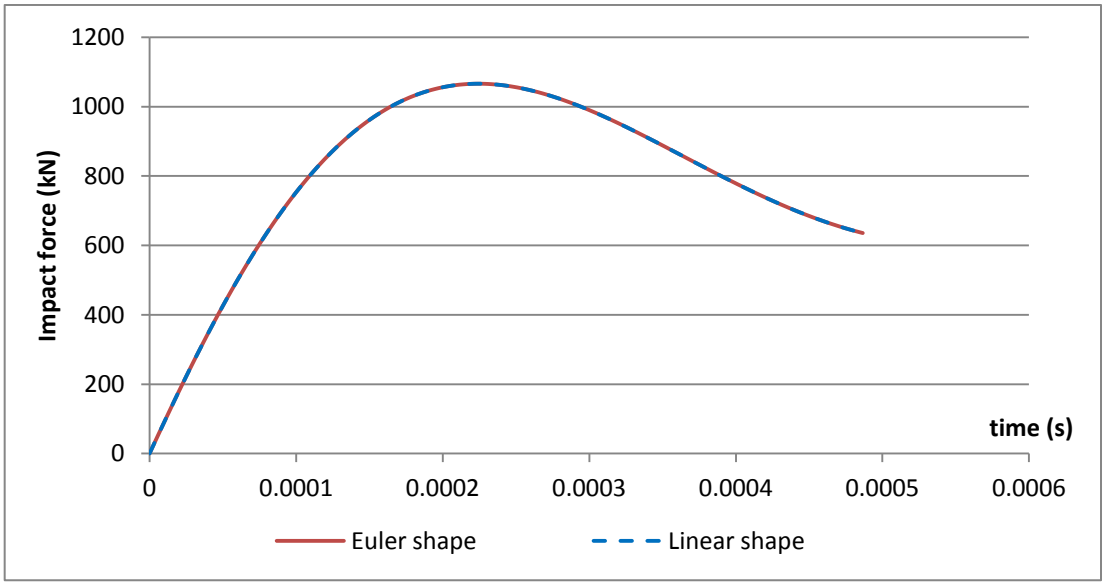

Figure 4.25: Variation in Impact force with time for linear and Euler assumed deformed shapes (lines are coincident)

It would be expected that the main difference in using different deflected shapes in the model would be to change the distribution of inertia forces in the member due to the different accelerations between the two shapes at a given location. This change can be seen from the shear force diagrams shown in Figure 4.26 (only plotted for right hand side due to symmetry).

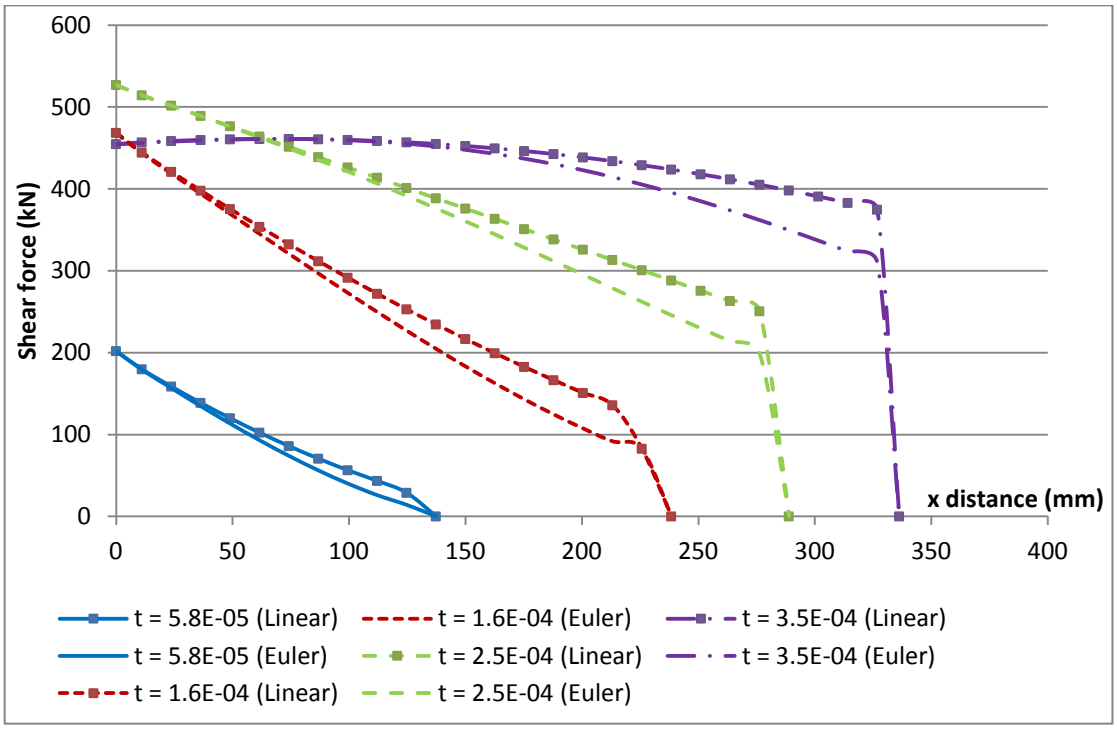

Figure 4.26: Variation in shear demand with time for flexural and linear assumed deformed shapes

The variation in the shear force diagrams is relatively minor and the peak shear force for each assumed shape is the same. From Figure 4.25 and Figure 4.26 it can be seen that the assumed deformed shape has no effect on the impact force and little effect on the shear demand. It can also be shown that the assumed deformed shape has no effect on the bending demand predicted by the proposed model. As the primary focus of the proposed model is to predict whether shear failure occurs prior to flexural failure, as this has been shown to be the most catastrophic failure mode, it can be concluded that the assumed deformed shape has no bearing on the failure mode that would be predicted.

4.4.4. Time-step

It was outlined in the development of the model that the equation of motion is solved over a series of small time increments. In explicit methods of direct integration, where the equation of motion is solved over a series of time-steps, the solution is conditionally stable based on the size of the time-step. The proposed model is based around an iterative approach which does not suffer from the same time-step dependency. In addition to this the use of graphical outputs provides an easy method for checking instability. Despite the theoretical lack of dependency of the solution to the time-step, it is useful to demonstrate this through a sensitivity analysis by varying the time-step duration over a range of approximately 100%.

Shown in Figure 4.27 is the variation in the predicted peak impact force and inertia force when the time-step used in the analysis is increased by 100% (from $3.5x10^{-6}$ seconds to $7x10^{-6}$ seconds). This figure indicates that increasing the time-step by around 100% leads to a reduction in the predicted peak impact force of 1%. The effect on the peak inertia force is slightly more noticeable with a 100% increase in the time-step causing a 2.5% reduction in the peak inertia force predicted.

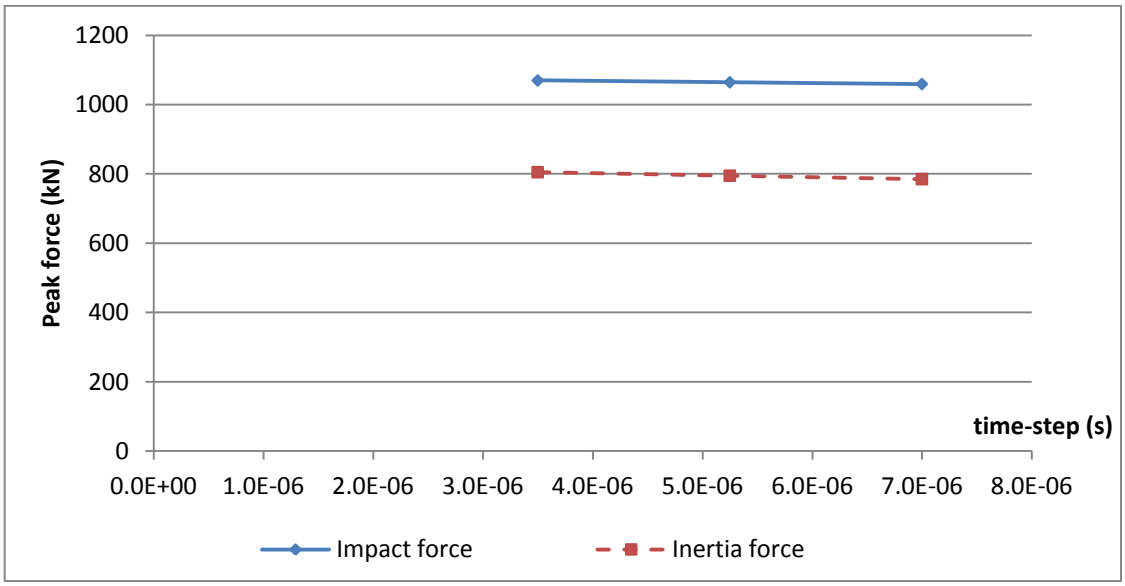

Figure 4.27: Variation in impact force with time for different changes in effective length between analysis steps

It can also be shown that the predicted peak shear demand reduces by around 1% when the time-step is increased by 100%. This shows that, provided the time-step remains in a suitable range (as outlined in section 4.2.5), then the solution is stable.

4.4.5. Plastic hinge formation

It is implicitly assumed in the proposed model that the moment demand at the edge of the effective length as the force propagates does not exceed the plastic moment capacity of the section. However, in reality, given the large forces that are expected, the plastic moment capacity might be exceeded and a plastic hinge would form. This would then be expected to propagate as the force from the impact propagates to the supports. The formation of plastic hinges at the boundary of the effective length would affect the predicted impact forces. If plastic hinges form then the change in stiffness force, ΔF_b, for subsequent time-steps would be zero. The second part of the equation of motion (equation 4.5) would therefore change to equation 4.25:

$$\Delta F_c = \Delta F_{ine} \tag{4.25}$$

To investigate the effect of plastic hinges forming on the model outlined above, the model was first modified so that there was no stiffness term, which corresponds to a situation in which the plastic hinge has formed at the onset of the analysis, this is termed 'plastic'. An intermediate, 'elastic-plastic' model was then developed whereby the plastic hinge was assumed to have formed at some point during the analysis. The time at which the hinge was assumed to have formed was determined from analysis of the bending moment diagram for the elastic model. It was assumed that the hinge would form when the moment at the boundary of the effective length at a given time-step exceeded the quasi-static plastic moment capacity of the section. This assumption ignores the enhancement in the capacity due to strain-rate effects but is acceptable for the purposes of the current discussion. A more detailed discussion on the dynamic capacity of a section is given below.

The results for the predictions of the forces acting on the member for the elastic-plastic model are shown in Figure 4.28. It can be seen that the plastic hinges form just before 0.0002 seconds, after which the stiffness force is assumed constant. The sharp transition causes a minor kink in the inertia force but overall the model appears stable when this assumption is included.

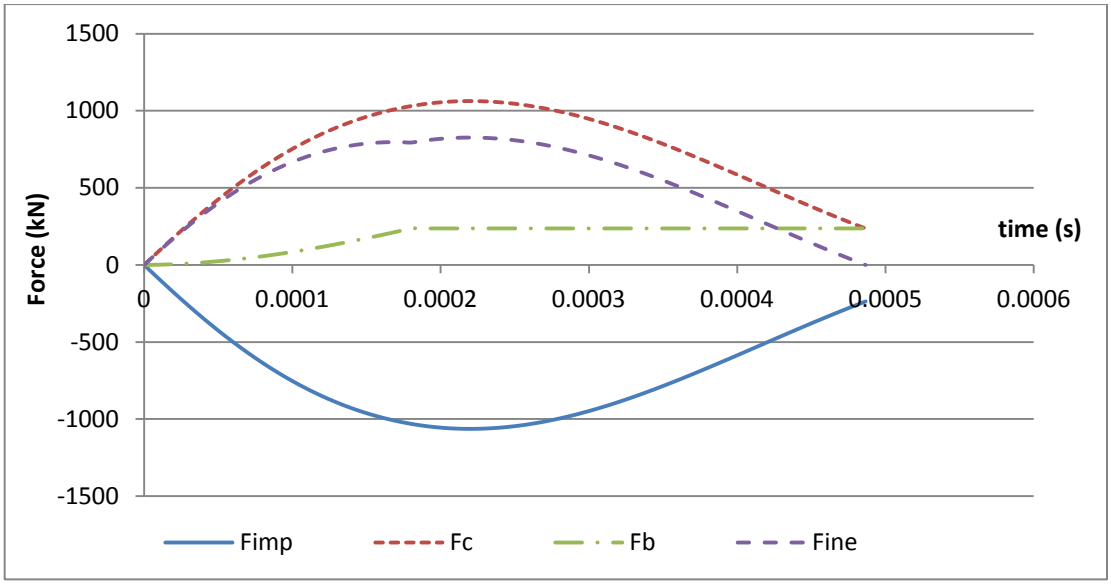

Figure 4.28: Forces acting on a member assuming elastic-plastic behaviour

The results for the impact force and inertia force predicted with the three different models are shown in Figure 4.29. From the initial analysis it was found that the quasi-static moment capacity would be exceeded at around 0.185 milliseconds after the impact occurred. This time was therefore used in the elastic-plastic model to determine when ΔF_b became zero. It can be seen that this time happens to coincide quite closely with the peak force being reached. It can therefore be seen that the differences between the peak impact force for the elastic and elastic-plastic model are negligible but the force decays more rapidly in the elastic-plastic model. The inertia force predicted in the elastic-plastic model is seen to increase above the elastic model's value at around 0.185 milliseconds and begins to reduce at a later time than the elastic model. It can also be seen that the predicted peak impact force for the fully plastic model is less than that in the other two models and that the impact forces and inertia forces are coincident for the plastic model, as would be expected given the assumption that ΔF_b is zero throughout.

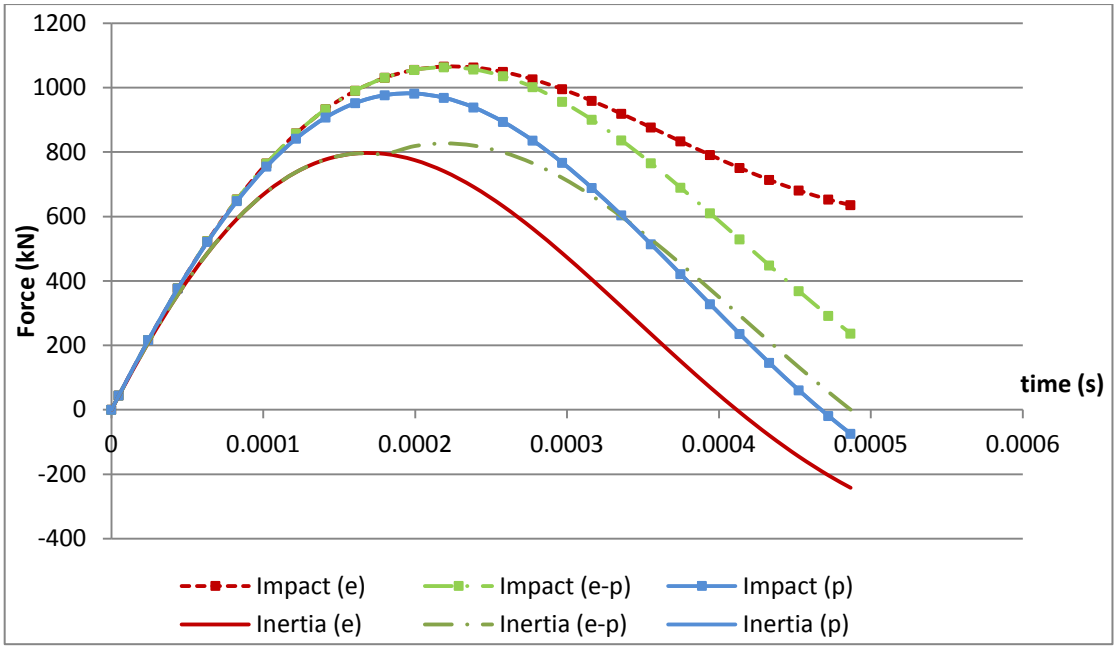

Figure 4.29: Impact and inertia forces for elastic (e), elastic-plastic (e-p) and plastic (p) models (note: forces from plastic model are coincidental)

It is interesting to note from Figure 4.30 the variation in the predicted shear force diagram due to the use of different bending stiffness models. It can be seen that the fully plastic model (blue lines, square markers) predicts zero shear force at the boundary of the effective length for a given time. This contrasts with both the elastic and elastic-plastic models which both show finite shear forces at the boundaries (as would be expected). Comparing the boundary values for the elastic and elastic-plastic model between times t = $2x10^{-4}$ seconds and t = $3x10^{-4}$ seconds shows that the shear force for the elastic model continues to increase. However, as it is assumed that a plastic hinge has formed in this time then the shear force at the boundary of the elastic-plastic model cannot increase further and is hence constrained to a value of around 120 kN in this case.

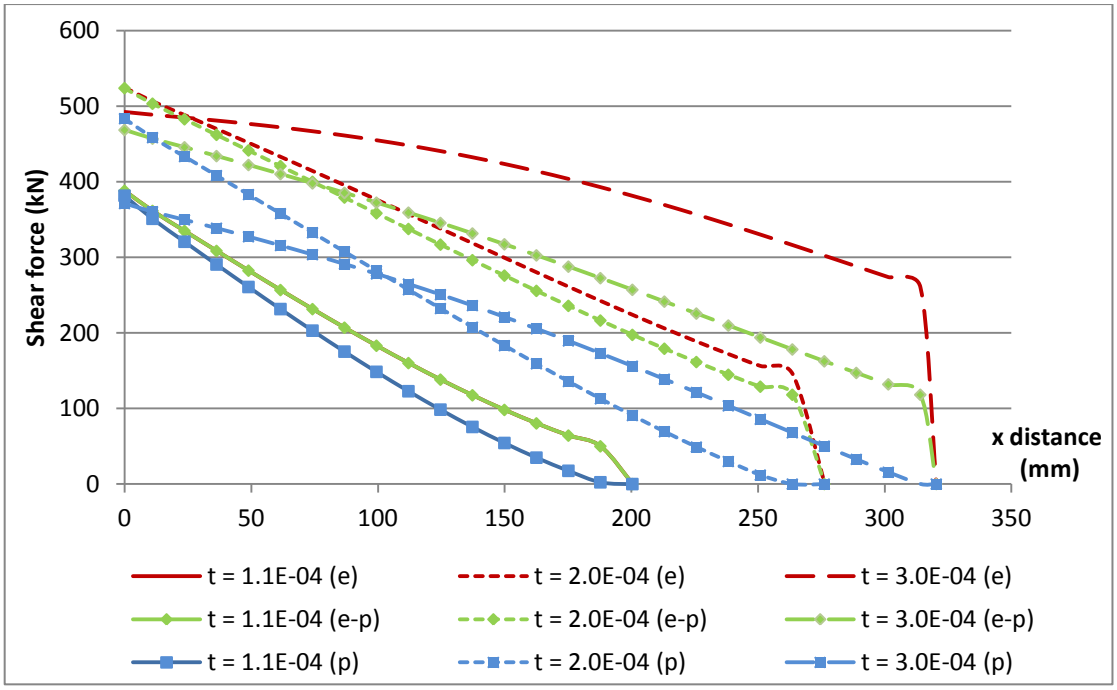

Figure 4.30: Shear force diagram for elastic (e), elastic-plastic (e-p) and plastic (p) assumed stiffness models (shown only for half member due to symmetry)

While comparison of the predicted shear force diagrams for different models are useful, it is perhaps more informative to consider the effect that the different models have on the variation of the maximum shear force with time. This is shown in Figure 4.31 and indicates that the predicted peak shear demand for the elastic and elastic-plastic models is the same, which is due to the plastic hinge forming around the time the peak force is reached. Consistent with the results for the predicted impact force shown in Figure 4.29, it can be seen in Figure 4.31 that the predicted shear force for a perfectly plastic model is lower than the elastic and elastic-plastic models by around 8%.

It can also be seen from Figure 4.31 that the shear force in the elastic model begins to increase again after 0.0003 seconds. This rise is due to the assumptions of linear elasticity in the contact zone which causes the impacting mass to separate from the member. This is a function of the modelling assumptions and would not occur in reality.

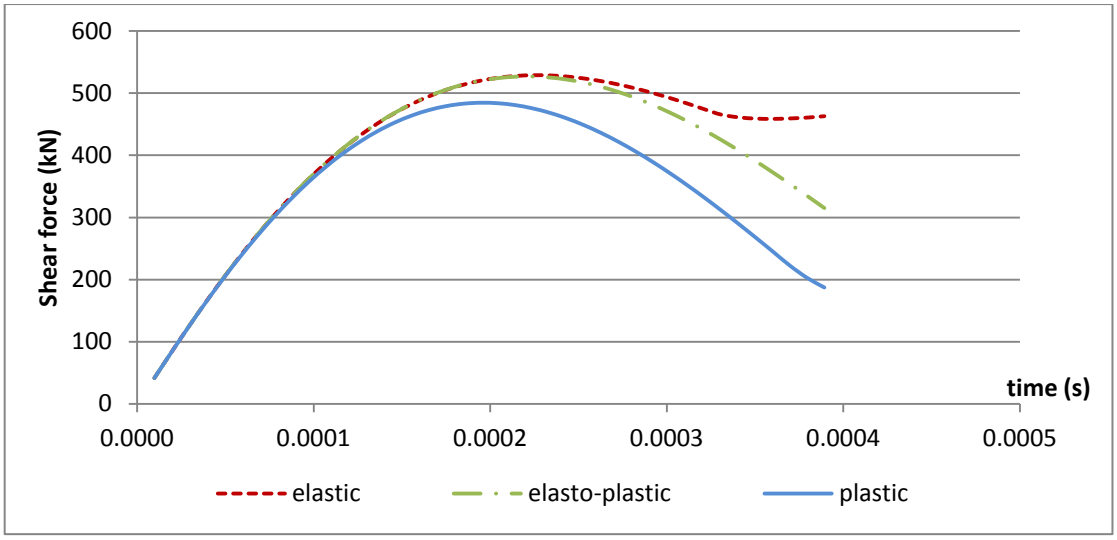

Figure 4.31: Shear demand for elastic (e), elastic-plastic (e-p) and plastic (p) models

The results outlined above indicate that the material behaviour plays an important role in the solution for the theoretical response. It is not unreasonable to expect a plastic hinge to form at some point in the analysis, prior to the force propagating to the supports, due to the extremely high forces encountered.

A potential difficulty may be encountered in actually predicting when the hinge will form which is discussed in more detail below.

4.5. Discussion

Formulation of the model outlined above requires a number of assumptions to be made regarding the complex behaviour, some of which may require further refinement in future. However, in the current form, the model is able to demonstrate and predict many of the most important experimentally observed dynamic phenomena qualitatively.

Discussed in this section are areas where the proposed model could be developed further and where the current limitations lie. Particularly important to this is the discussion on determining the section's capacity as well as the sensitivity shown by the model to the contact zone behaviour and plastic hinge formation.

4.5.1. Force propagation velocity

Due to limited resources the impact tests discussed in section 4.1.1 were carried out mainly on members with similar geometric properties. The primary variable

investigated was the slenderness, the results shown in Figure 4.5 and Figure 4.13 indicate that this parameter had a major effect on the propagation velocity. The limited literature available in this field also suggested that the impact velocity would influence the response (Vermorel *et al.*, 2009). The relationship between the slenderness and the force propagation velocity indicates that the waves are dispersive which is consistent with the characteristics of flexural waves. It is apparent that further experimental research is required in this field where different geometries and impact velocities should be assessed before addressing other issues that might affect this parameter. To this end, theoretical or numerical modelling may play some role in indicating the parameters which are likely to govern the propagation velocity.

It is also interesting to compare the experimental data with the theoretical prediction for the plastic hinge propagation velocity proposed by Jones (1989), given in equation 2.14. The relationship derived by Jones (1989) was intended for metallic structures exhibiting high levels of plasticity. However, given the limited theoretical data available in this field it is considered informative to plot the theoretical values determined from equation 2.14 against the experimental values determined in this research project (Figure 4.32). This indicates that for low span/depth ratios Jones's theory has reasonable agreement with the experimental data. However, at large span/depth ratio the velocity is significantly above the experimentally determined velocity.

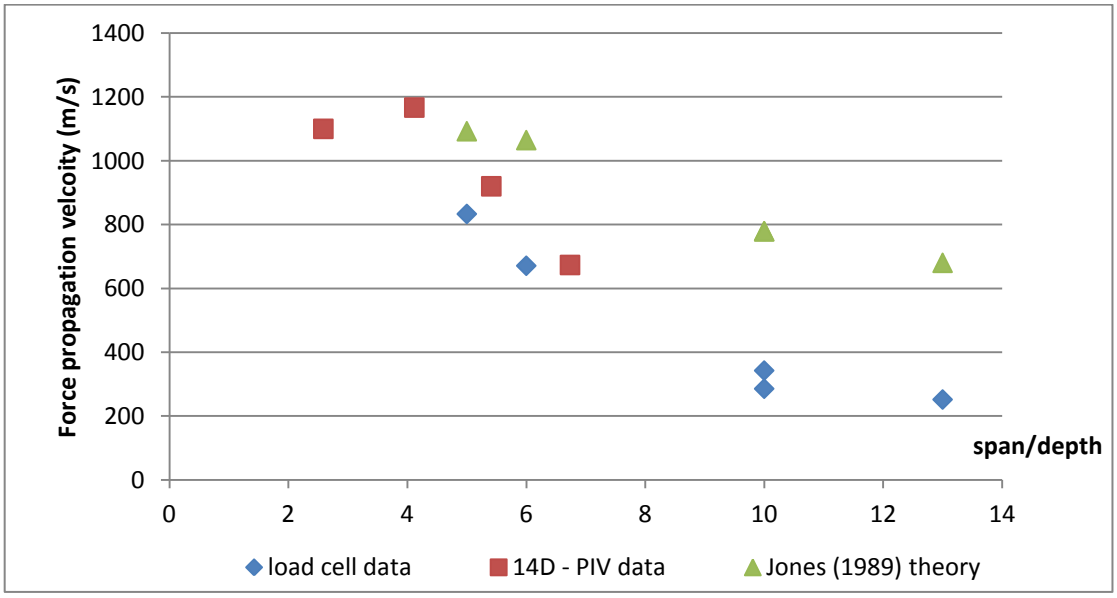

Figure 4.32: Force propagation data presented alongside Jones (1989) theoretical plastic hinge propagation velocity

It was discussed in the literature review that the relationship proposed by Jones (1989) predicts that higher velocity impacts would lead to plastic hinges propagating more slowly. The experimental results showing the effect of impact velocity on force propagation velocity (given in Figure 4.6) is shown in Figure 4.33 compared with theoretical predictions from Jones (1989). This clearly shows that the theoretical predictions follow the opposite trend compared with the experimental data. Given that Vermorel *et al*., (2009) also showed that the force propagation velocity increased with increasing impact velocity it may suggest that the relationship proposed by Jones (1989) is not appropriate in this situation or maybe incorrect.

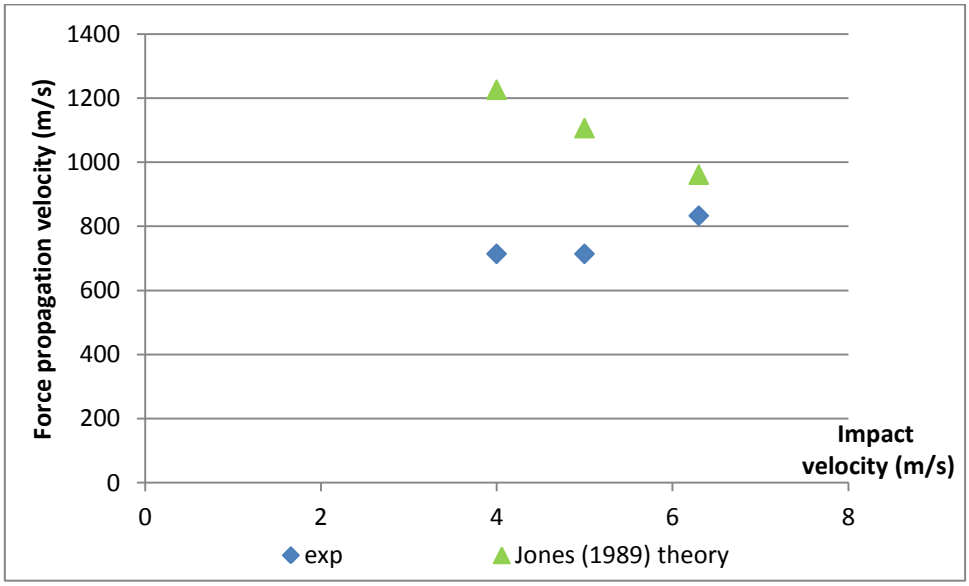

Figure 4.33: Experimental results for the effect of impact velocity on the force propagation velocity compared with Jones (1989) theory for plastic hinge propagation velocity

4.5.2. Section capacity

The model outlined above uses a novel approach to predict the dynamic *demand* on a structural member. However, only by comparing this with the *capacity* can the failure mode of a member be determined. Predicting the dynamic capacity falls outside the scope of the current work although it is informative to consider in some detail how the current work could tie in with this.

It was outlined in the literature review that dynamic effects, mostly strain-rate effects, can have a significant influence on the strength of materials and the capacity of a

section (e.g. Bischoff and Perry, 1991, Fu *et al.*, 1991b, and Malvar and Ross, 1998). In this respect, the majority of research has been conducted into the effect of high strain-rates on the flexural capacity of a member and little has been written on the effects of the dynamic material properties on the shear capacity of a member.

In order to accurately predict the failure mode using the model it is crucial that the dynamic shear capacity is known. It has been shown that shear failures in dynamically loaded members tend to occur at a very early stage in the loading (Krauthammer *et al.*, 1994). Also, as shear is a brittle failure mode, it is apparent that if the shear capacity is exceeded then shear failure will occur regardless of the flexural capacity. This is highly undesirable as there is limited residual capacity in members which have failed in shear and in the case of load bearing columns this could lead to structural collapse.

A potential further application of the model is to determine the strain-rates in a given section at a given time. As the full time varying demands on a member are known from the analysis it would be relatively simple to use these to determine the rates of straining in a section, although this would require assumptions such as plane sections remaining plane to be made. Assuming that suitably accurate methods for predicting the strain-rate dependent section properties exist, it would then be relatively simple to predict the capacity of a section from which the failure mode could be more accurately predicted.

Applying strain-rate effects to the moment capacity is usually simpler than in shear (Soroushian and Obaseki, 1986) as the effects of strain-rates on the shear capacity are currently poorly understood, which could be considered directly related to the wide range of shear theories that currently exist. To this end the modified compression field theory of Vecchio and Collins (1986) may present some possibilities for including dynamic material properties, particularly to the tensile strength of concrete which is used explicitly in the model. Despite this work falling outside the scope of the current project there are a number of interesting dynamic features observed that would influence the shear capacity. An example of this is the crack angle which has been shown to steepen for higher velocity impacts. By considering a simple shear model such as the variable truss model such as in Eurocode 2 it can be seen that the crack angle has a strong influence on a section's shear capacity. A further feature of the effective length concept is that it might suggest a certain minimum length is required for a shear crack to form. It has been shown that the crack angle steepens as the

impact velocity increases (CEB, 1988), which suggests that the effective length is important in this respect.

In addition to this is the consideration of the increased stiffness due to reduced cracking in the presence of an axial compressive force. The axial force may inhibit the development of tensile cracks in the concrete which suggests that the gross second moment of area could be more suitable than the cracked section proposed in section 4.2.4. Due to limitations in the testing it is not possible to comment further on whether an axial force could have an effect on the force propagation velocity and this should be investigated in the future. Further to this, secondary effects such as compressive membrane action are not considered, but it is recognised that these may be considerable.

4.5.3. Contact zone behaviour

A consequence of the proposed formulation of the model is the dependency of the predicted forces on the contact zone stiffness, as outlined in section 4.4.2.

The proposed model and contact zone stiffness relationship assume what is termed a 'hard' impact i.e. the impactor is incompressible. For a situation such as a steel mass impacting a material such as concrete, this assumption is reasonable. However, if 'soft' impacts were considered then the behaviour of the impactor would become more important and the term for k_c would be replaced by a term relating to the load-deformation response of the impacting mass. Figure 4.34 indicates diagrammatically the difference between hard and soft impact.

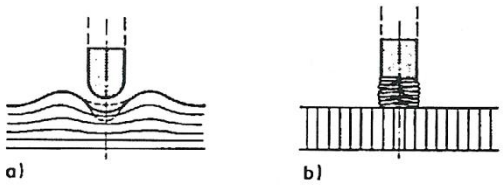

Figure 4.34: Diagrammatic representation of hard (a) and soft impacts (b) (Bischoff *et al.*, 1990)

An accurate knowledge of the load-deformation relationship for the contact zone would avoid the need for the proposed assumption regarding the stiffness. A general qualitative relationship for the contact zone stiffness was shown by Bischoff *et al.*

(1990) and shown in Figure 4.11. It is apparent that the assumption of a linear elastic contact zone stiffness is a limitation of the proposed model and a load-deformation relationship more closely related to that shown by Bischoff would be more suitable. Despite this limitation it is still evident that the model is capable of predicting many of the most important dynamic features observed experimentally and the importance of including the wave propagation type phenomenon when considering the response is clearly demonstrated.

4.5.4. Energy conservation

Although not expressed explicitly in the formulation of the model, an assumption made is the conservation of energy at each time-step. The initial kinetic energy from the impacting mass is converted to kinetic and strain energy in the member, as it deforms, and strain energy in the contact zone. In reality energy will be dissipated in other modes, including heat loss, plastic effects, micro-cracking of the concrete away from the contact zone and sound, which would have an effect on the predicted forces acting on the member. One way to include these additional energy dissipation modes would be through a damping term, although this would need further theoretical work along with additional experimental testing to determine specific parameters. It is due to this assumption of linear elastic springs that the velocity of the member is predicted to exceed the velocity of the impacting mass.

By currently not accounting for additional energy dissipation modes in the form of a damping term causes the predicted impact forces to be higher than would be observed in reality. Because of this the predicted velocity of the impacting mass decreases more rapidly than would occur in reality, as demonstrated in Figure 4.24.

By comparing different values for the contact zone stiffness, k_c, it is indicated in Figure 4.35 that when k_c is reduced, the rate at which energy is converted to elastic strain energy (reduction in 'KE mass') is less and the velocity of the member does not exceed that of the impacting mass to the same extent (Figure 4.36). Reducing the stiffness of the contact zone to 25% of the theoretically determined value causes the peak velocity to be reached when the velocities of the impacting mass and column are approximately equal. This contrasts with the behaviour when the theoretically determined higher value for the contact zone stiffness is used. Figure 4.36 shows that the member's velocity reaches a peak after the velocities of the mass and the member

are equal. This suggests that for higher contact zone stiffnesses, energy is transferred from the impacting mass to the member more quickly, which would be expected.

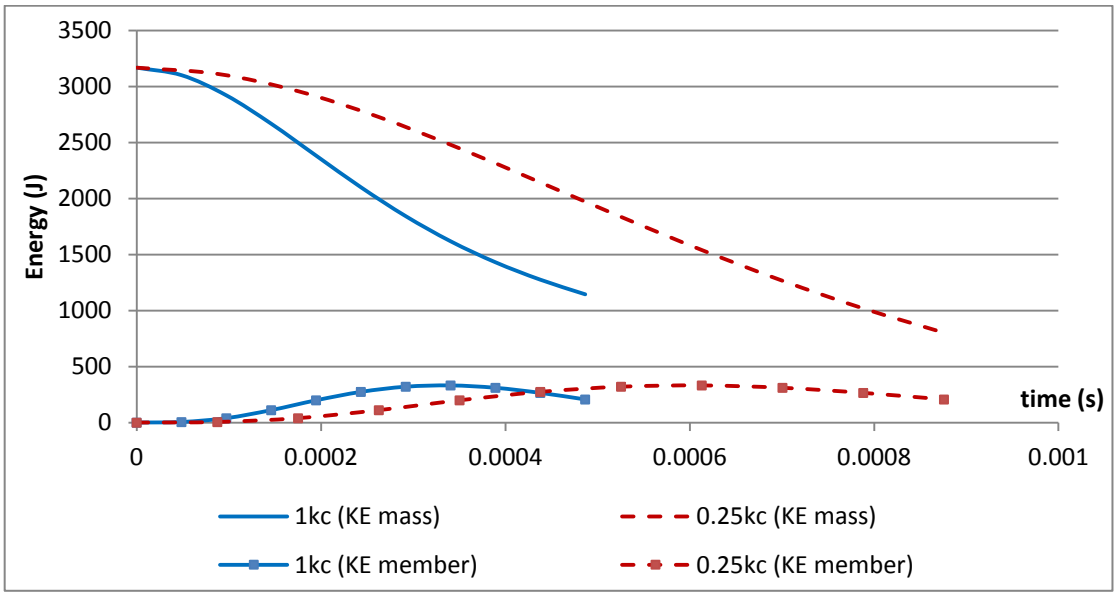

Figure 4.35: Predicted change in kinetic energy of impacting mass and member during impact

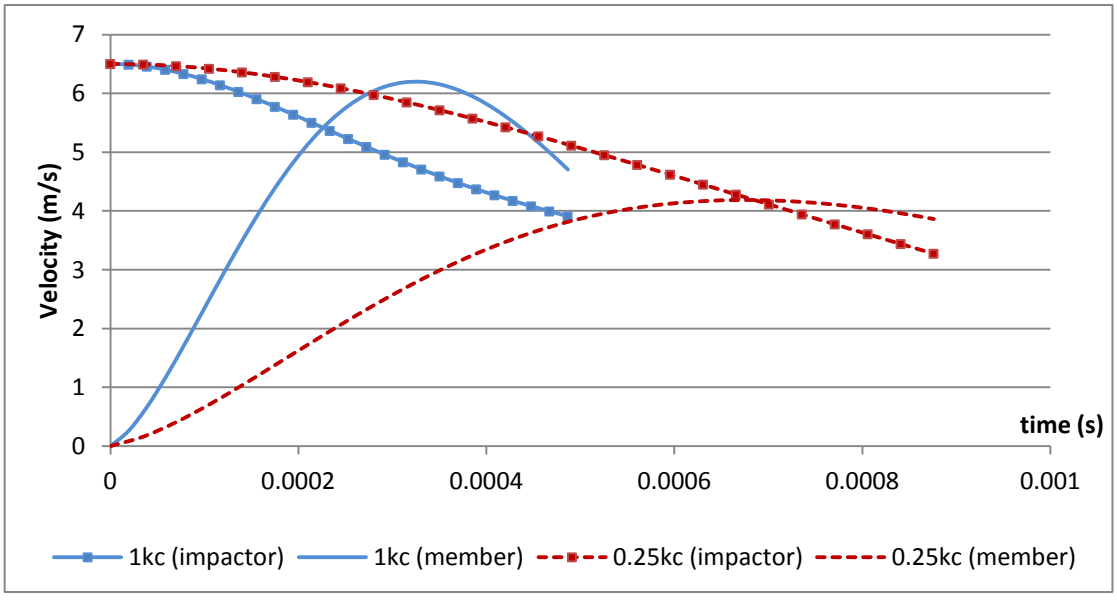

Figure 4.36: Velocity profiles for impactor and member for different k_c ratios

Experimental observations of tests carried out on RC members suggest that the member's velocity does not in fact exceed that of the impacting mass. This is most likely attributable to the complex energy dissipation process in the contact zone and other methods of energy dissipation which are not included in the model. However,

impact tests between an aluminium impactor and beam carried out at much higher velocities by Pierron *et al.* (2010) showed that the velocity of the member at the point of impact could exceed the impactor's velocity and separation would occur for a brief time.

Accurately accounting for the precise methods of energy dissipation is beyond the scope of the current work. These losses may occur through the micro-cracking of concrete, higher rate stress wave phenomenon and losses through heat and sound. It was suggested by Kishi *et al.* (2002) that anywhere between 40%-60% of the impact energy could be lost and would not be used to do useful work (actually causing deformation of the member). Given the magnitude of these losses an appreciation of the modes through which energy is lost is important in terms of understanding the conservativeness in the predictions for the forces from the model outlined.

4.5.5. Formation of plastic hinges

Included in section 4.4.5 was a detailed discussion on the formation of plastic hinges and how these affect the predicted results. It was discussed that predicting the formation of these hinges presented some difficulty. However, it was shown that inclusion of these effects would alter the predicted response by causing the impact force to be resisted purely by the inertia of the member after the hinges form.

In section 4.4.5 the formation of the hinges in the elastic-plastic model was assumed to occur when the moment at the boundary of the effective length exceeded the quasi-static plastic moment capacity. The moments were determined from the forces found from the elastic analysis, as discussed in Section 4.3.2. The potential drawback of determining the moments in this way is that it assumes that the forces predicted through the elastic analysis are correct. An alternative option for determining the time at which the plastic hinge forms is by assuming a plastic hinge length and estimating the curvature from the displacement (a similar method to that presented in Chapter 6 to determine the peak displacement). Once the curvature exceeds the yield limit, then a plastic hinge will form. The potential drawback of this method is that it relies on the proposed model predicting the displacements accurately and that it uses an assumed plastic hinge length.

Once plastic hinges are predicted to form it is assumed that they will travel along the member with the same velocity as the impact force wave propagation and will thus

reach the supports at the same time. This same assumption was employed by Jones (1989) which was discussed in the literature review and in Section 4.5.1.

4.6. Conclusion

Outlined in detail above is a new model to predict the forces acting on a reinforced concrete member in the initial stages of its response to an impact load. Experimental testing indicates that a finite time exists between the impact occurring and the reactions experiencing the force. This concept has formed the basis of the outlined model. By including this concept and solving the equations of motion at a number of finite time-steps, the full time varying forces acting on a member can be predicted. Of particular importance to dynamic situations is the ability of the model to show that the forces generated from a low mass/high velocity impact are greater than those from a high mass/low velocity impact for identical kinetic energies, leading to a more brittle failure mode.

The sensitivity analysis carried out indicated the influence of some of the key assumptions employed in the model on the predictions for the forces acting during an impact. In this respect the most important parameter was shown to be the contact zone stiffness. The assumed deflected shape used to find the inertia forces and the time-step employed in the numerical integration was shown to have a limited effect on the predicted results.

Future work in this area may look to address the dependency of the solution on the contact zone stiffness as well as consider in more detail the implicit assumption that energy (strain and kinetic) is conserved in the system. It was discussed above how previous research has shown that this is not the case and energy is lost through many other modes besides crushing of the concrete and strain energy due to the member's deformation. Many of these additional energy dissipative modes are difficult to quantify. However, by failing to include all of these energy losses and employing the assumption of conservation of energy it is likely that the impact force will be over predicted. Therefore, comparing the model quantitatively with data remains difficult.

The model was intended to only predict the demand on the member due to the impact forces. A problem still exists in relating these to the dynamic capacities of the member. This is due largely to a lack of research on the dynamic shear capacity of RC members. Some authors have claimed that the quasi-static strength and dynamic

strength are identical in shear; however, this is still yet to be proven categorically and further research is still required. On top of this is the issue of steepening shear cracks which have been shown to develop at higher impact velocities (CEB, 1988). Given that the time dependent shear forces and bending moments are known it may be possible to use these to determine strain-rates which could then be employed to determine the dynamic capacity of a member.

It should also be noted that the tests performed to determine the force propagation velocity have not included an axial load. It is not clear what affect an axial force would have on the force propagation velocity. It may however, be expected that an axial force would have an effect on the dynamic capacity of a member by reducing the cracking and this would need to be considered when predicting the failure mode. There is also the potential that it may affect the overall behaviour by altering the angle at which shear cracks form.

The following chapter presents the results of experimental testing aimed at demonstrating many of the most important dynamic features of impact events predicted by the proposed model.

5. Experimental testing and validation

Outlined in Chapter 4 was the development of a new model to predict the initial demand on an impact loaded RC member. This work has developed from observations made in preliminary experimental work which shows that a finite time exists between the impact occurring and the reactions experiencing the force. Presented in this Chapter is a detailed discussion of these tests and the important observations that link this data with the theoretical work presented previously.

5.1. Introduction

It has been discussed in previous chapters that the lack of experimental data in this field makes it difficult to fully appreciate the range of parameters that affect the response of an RC member to impact loads. In many cases this lack of data makes validating theoretical models a challenge. In response to these issues a programme of impact testing was carried out to investigate the influence of a range of parameters, which are reported on below.

Described in Chapter 3 was the design and construction of an impact test rig commissioned for this research program. All impact tests discussed in the current chapter were carried out using this rig.

It was intended that the experimental testing would provide additional data on the force propagation velocity whilst also enabling further validation of the theoretical work outlined in Chapters 4 and 6 whilst also providing data to validate the proposed models. Finally, it was intended that specific parameters outlined from the analytical work could be examined and their contribution to the behaviour of a member established.

Discussed in the current chapter are the results of series A, C and D specimens. Series B specimens are discussed in Chapter7.

5.2. Specimen description

All tests were performed on horizontally arranged reinforced concrete members with a transversely applied load. These members had a symmetrical longitudinal reinforcement arrangement of two bars top and bottom and the quantities of steel were typical for a column, although no axial load was applied in any of the tests in order to

simplify the test arrangement. Concrete cover for all specimens was 20 mm. The primary aim of the experimental investigation was to demonstrate the reduction in ductility of the response as the loading rate increases. In all cases two or more identical specimens were cast. It was intended that within each set at least, one specimen would be tested under a hydraulically applied quasi-static load. A summary of the main properties of each specimen is given in Table 5.1 and the loading characteristics in Table 5.2. The convention for labelling specimens is outlined in Figure 5.1.

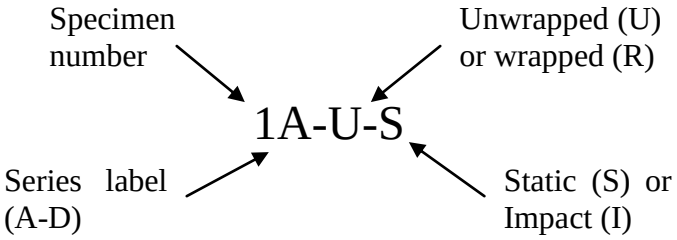

Figure 5.1: Specimen labelling convention

Table 5.1: Properties of test specimens

	Dimensions			Longitudinal reinforcement	Transverse RF		
Specimen reference	Length (mm)	Width (mm)	Depth (mm)	Bar dia (mm)	Bar dia (mm)	Spacing (mm)	Concrete cube strength (N/mm^2)
1A-U-S	1300	110	200	12	3	75	28.8
2A-U-S	1300	110	200	12	3	75	28.8
3A-U-I	1300	110	200	12	3	75	30.7
4A-U-I	1300	110	200	12	3	75	30.7
5B-U-S	1300	110	200	12	4	115	31.1
6B-R-S	1300	110	200	12	4	115	37.3
7B-R-I	1300	110	200	12	4	115	43.5
8B-R-I	1300	110	200	12	4	115	43.5
9C-U-S	1900	170	170	16	3	90	49.5
10C-U-I	1900	170	170	16	3	90	57.0
11D-U-S	1900	170	170	16	3	75	42.7
12D-U-I	1900	170	170	16	3	75	37.0
13D-U-I	1260	170	170	16	3	75	49.7
14D-U-I	2320	170	170	16	3	75	48.3

Table 5.2: Testing arrangement

Specimen reference	Type	Span	Impact mass (kg)	Target impact velocity (m/s)
1A-U-S	Static	1000		
2A-U-S	Static	1200		
3A-U-I	Impact	1000	120	6.26
4A-U-I	Impact	1000	300	3.96
9C-U-S	Static	1700		
10C-U-I	Impact	1700	150	6.5
11D-U-S	Static	1700		
12D-U-I	Impact	1700	150	6.5
13D-U-I	Impact	1020	150	6.5
14D-U-I	Impact	2210	150	6.5

5.3. Material testing

Tests were carried out where appropriate to determine the relevant quasi-static strength of the materials which allowed the quasi-static section capacity to be determined. The properties of reinforcing steel for each of the bar sizes used are shown in Table 5.3. Tests were carried out on concrete cubes on the day of testing to determine the mean compressive strength, with a minimum of 2 cubes tested; the results for these are shown in Table 5.1.

Table 5.3: Properties of reinforcing steel

Bar dia (mm)	Yield Stress	Ultimate stress	Ultimate strain
3*	770	800	5%
4*	660	750	3.1%
12	560	650	15%
16	530	600	14.2%

*3mm and 4 mm both smooth bar

5.4. Testing arrangement

All specimens were simply-supported and the load was applied at mid-span. Specimens were supported on a pin and a roller to prevent any possible arching action which may enhance the strength of the member. It was decided that achieving a consistent level of end fixity between all the tests would be difficult and this may have affected the results, therefore the simply-supported arrangement was chosen, although this is not strictly representative of columns. It was also considered, based on the theory outlined in Chapter 4, that the support conditions should not alter the dynamic behaviour as, during wave propagation, it is assumed that the member behaves as if its boundaries are fixed for the given effective length. Testing arrangements also made it difficult to apply an axial load to the specimens, which might be expected to enhance the shear and bending capacity of the member. As comparisons are made between specimens, provided that the test arrangement is kept consistent, the omission of an axial load is not considered significant for the purposes of this investigation.

In the case of impact tests, load was applied through a vertical free falling mass, unless stated otherwise. In the case of quasi-static tests loads were applied through a hydraulic jack connected to a strong frame.

Data acquisition for the quasi-static tests was of the form of linear variable differential transducers (LVDTs) to measure displacements and a load cell to measure the applied load. For the impact tests, data was acquired through a high speed camera and an accelerometer. Efforts were made to try and record the reaction forces with load cells made specifically for this project (as described in Chapter 3). However, high frequency vibration issues meant that in many tests this data proved inconclusive in terms of giving an accurate value for the reaction force, although it did prove invaluable for measuring the arrival time of the force, from which the force propagation velocity could be found.

A detailed discussion and analysis of the behaviour of each test specimen is given below. Predictions for the quasi-static capacity of the section in shear and bending were made in accordance with BS8110, using measured material properties and neglecting material partial safety factors.

5.5. Set A specimens

As outlined in Table 5.1, specimens in set A were cast with an identical reinforcement configuration. It was therefore expected that all specimens would exhibit similar behaviour under the same loading conditions. Figure 5.2 shows the reinforcement layout, details of which are also given in Table 5.1. The reinforcement configuration means that the moment capacity and shear resistance were expected to be around 18.9 kNm and 45.7 kN respectively. Of the four specimens, 1A-U-S and 2A-U-S were tested under quasi-static loading and 3A-U-I and 4A-U-I were tested under impact loading.

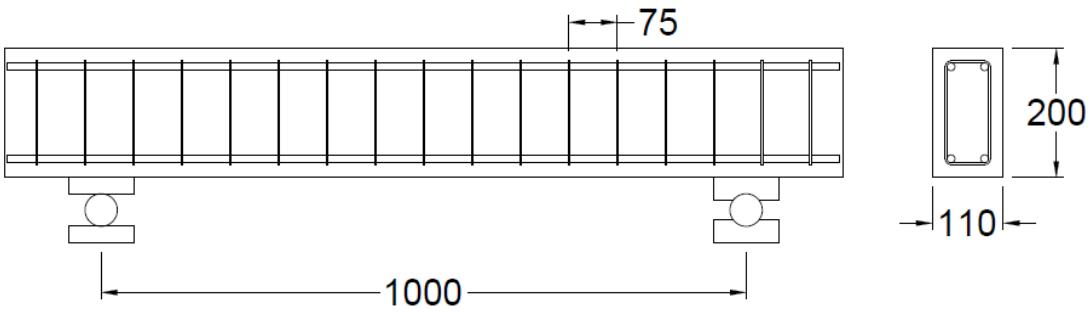

Figure 5.2: Reinforcement arrangement in set A specimens

5.5.1. Specimen 1A-U-S

Specimen 1A-U-S was tested under quasi-static three point bending with a clear span of 1000 mm. The specimen was expected to reach its plastic moment capacity at a peak load of 74.8 kN. Figure 5.3 indicates that the intended response was not achieved and the specimen had a severe lack of ductility, which can also be seen from the photo in Figure 5.4, showing that the specimen failed in shear with a major crack forming on the pin side.

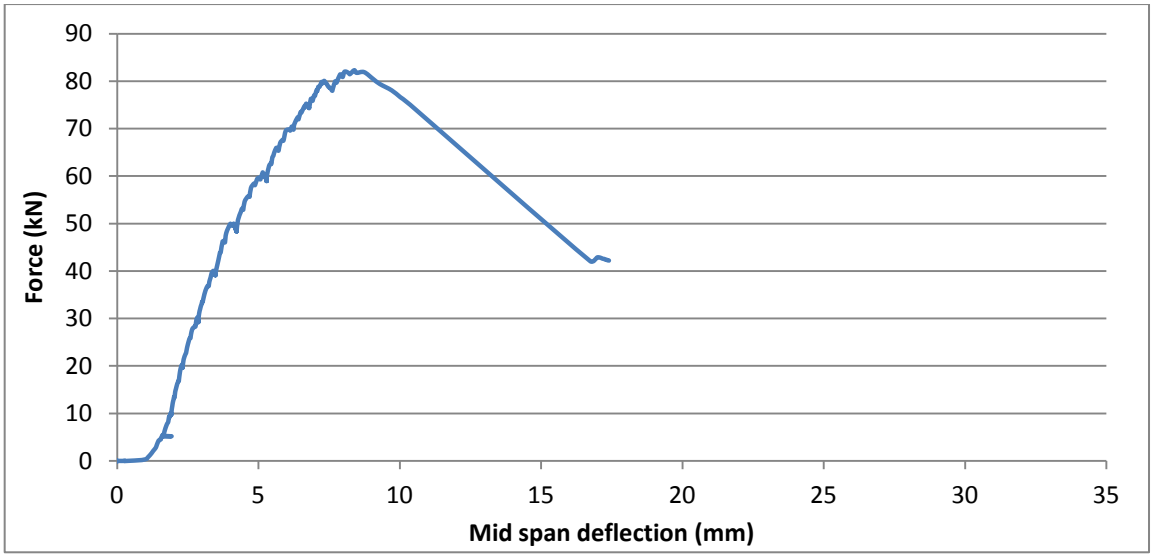

Figure 5.3: Load-deflection graph for specimen 1A-U-S

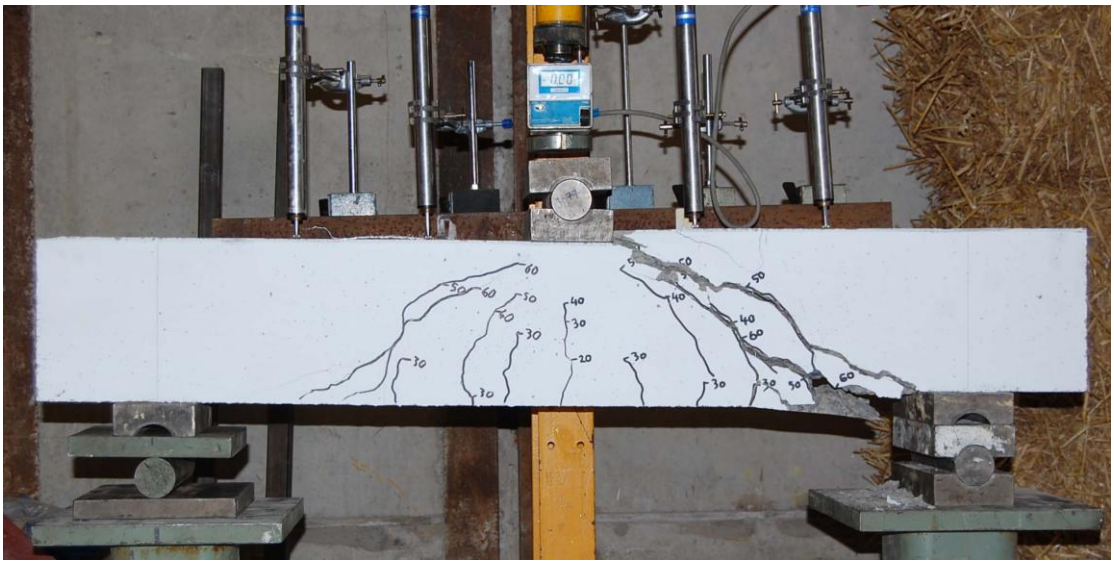

Figure 5.4: Ultimate failure of specimen 1A-U-S

The substantial difference between the failure mode seen in reality and that expected from the analysis suggested problems with the analysis. The theoretical shear capacity for the section according to BS8110 was 45.7 kN. However, the results indicate that the actual capacity was around 41.1 kN. The failure of the specimen to reach its full moment capacity may be attributable to the low a/d ratio of 2.5. Kani (1964) presented the results from a range of tests that showed for a/d ratios in the region of 1.5-4.0 the full flexural capacity was not achieved, with the worst results occurring at exactly 2.5.

Given these findings it was decided that specimen 2A-U-S would be tested under a quasi-static load with an increased span. This was intended to move the dimensions away from the shear valley and promote a flexural response.

5.5.2. Specimen 2A-U-S

Given the issues raised in the behaviour of specimen 1A-U-S, the span in test 2A-U-S was increased to 1200 mm. Making this alteration would cause the moment demand to increase whilst the shear demand would remain constant. Results shown in Figure 5.5 indicate that specimen 2A-U-S had significantly more ductility and obtained a plateau in the load-deflection response, suggesting the full moment capacity was achieved at a load of 70 kN. The image shown in Figure 5.6 indicates that the ultimate failure mechanism was through diagonal shear. This shows that a purely flexural response had still not been achieved. The predictions for the capacity of the member suggested that the full moment capacity would be achieved at a load of 62.3 kN whilst shear failure would not occur until a load of 91.4 kN was reached, although based on the results from test 1A-U-S, a load of 82.2 kN would be considered more realistic. Figure 5.5 indicates that a flexural response was actually achieved at a load of around 70 kN with failure once again occurring on the side of the specimen with the pin support (Figure 5.6). This suggests the actual moment capacity was 21 kNm which is around 11% higher than the theoretical moment.

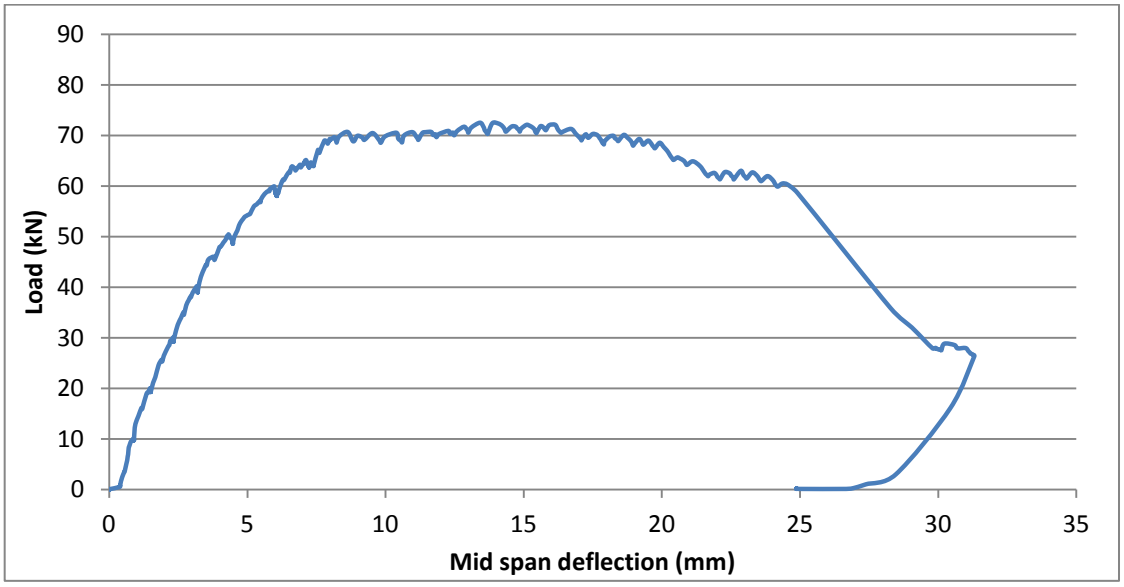

Figure 5.5: Load-deflection graph for specimen 2A-U-S

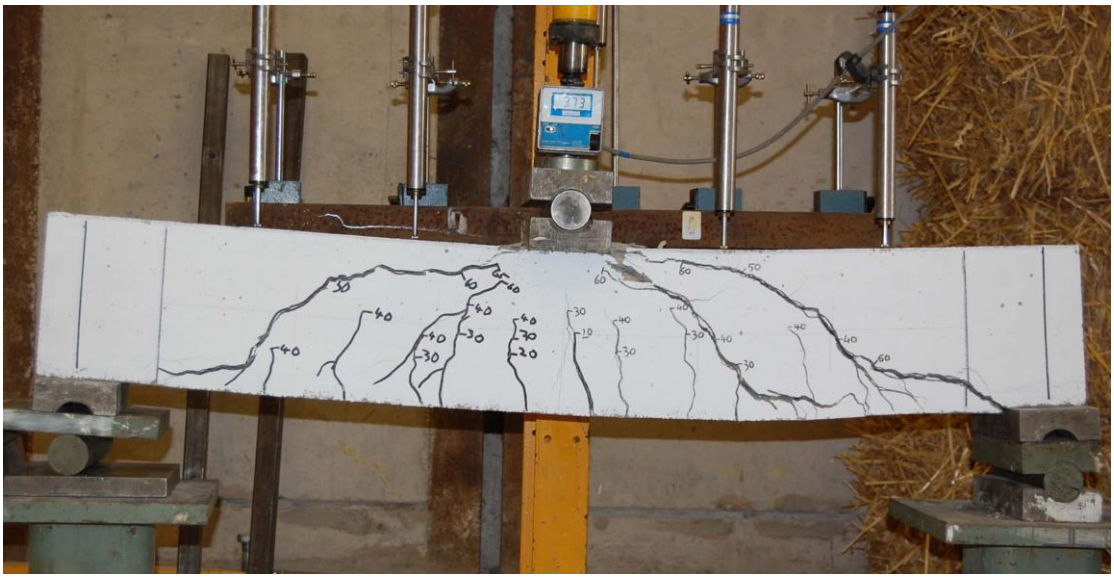

Figure 5.6: Ultimate failure of specimen 2A-U-S

Following on from the results obtained in tests 1A-U-S and 2A-U-S specimens 3A-U-I and 4A-U-I were tested under impact loads. Despite failing to fully obtain the flexural behaviour desired from tests 1A-U-S and 2A-U-S these tests would provide valuable data that could be used to validate the theoretical work outlined in Chapter 4. The loading conditions for each of the tests were selected such that the impact energy was constant between the tests, but the mass and impact velocity were varied. It was intended that these tests would demonstrate the observation that a lighter mass travelling faster causes a more brittle failure than a heavier mass travelling slower for the same kinetic energy. As discussed in Chapter 4, these tests also provided data for the force propagation velocity.

5.5.3. Specimen 3A-U-I

Specimen 3A-U-I was impacted with a falling mass weighing 120kg dropped from a height of 2 m. This gives an impact velocity of approximately 6.3 m/s and a kinetic energy at impact of approximately 2350 joules. High speed video footage of the event was recorded at 2000 fps with a resolution of 1024 x 512. The sequence of images in Figure 5.7 shows the response of the specimen in the first 10 ms. Attempts were also made to record the impact force with an accelerometer and the reaction forces with

custom made load cells. However, problems with the data acquisition meant that these readings proved unreliable and are therefore not reported.

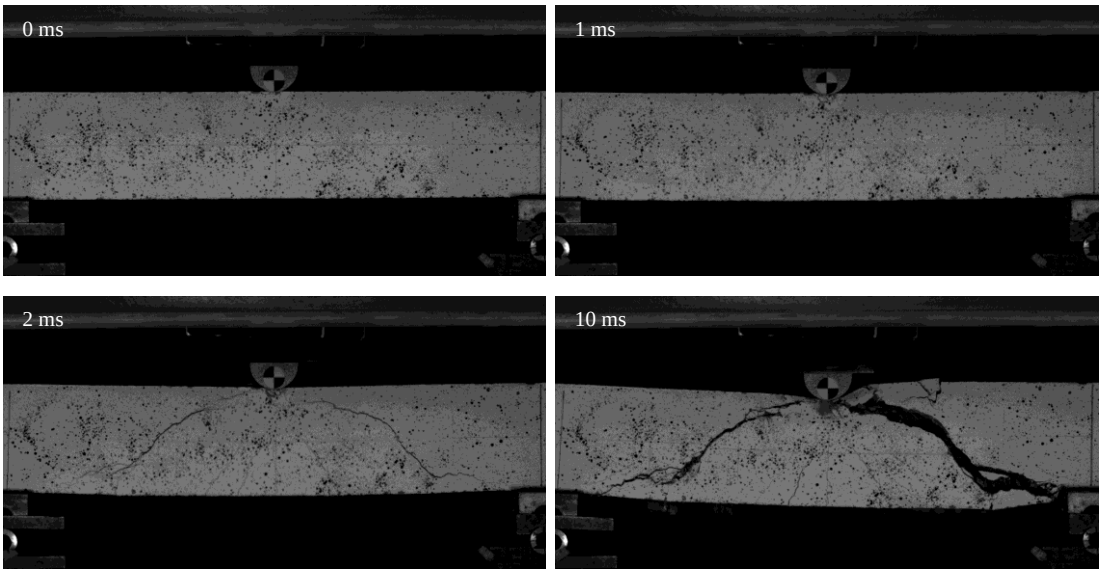

Figure 5.7: Images showing response of specimen 3A-U-I captured with high speed camera

Specimens were again tested with a clear span of 1000 mm. It is shown from the high speed photos in Figure 5.7 that a shear wedge forms with catastrophic shear cracks forming on both sides with almost no flexural cracking present.

Digital image correlation (DIC) analysis on the speckled pattern seen on the surface of the specimen also confirmed the observation of a shear cone forming in the central region of the member. The deformation profiles shown in Figure 5.8 indicate that up to 0.0015 s the deformation follows a flexural shape. However, at 0.002 s it can be seen, by the discontinuity in the curve, that shear cracks have formed at approximately +/- 200 mm on both sides. After this time it is clear that the deformation of the central region is separate from the ends indicating that shear has occurred.

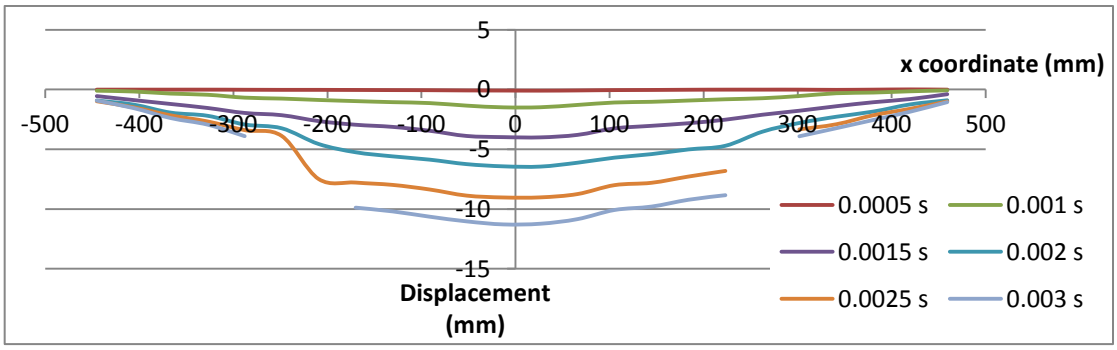

Figure 5.8: Time varying deflected profiles from DIC analysis for specimen 3A-U-I

An interesting feature observed in the behaviour of the specimen was the presence of a hogging crack around 210 mm from the point of impact (Figure 5.9). This phenomenon was discussed in Chapter 4 with the theoretical model predicting this behaviour due to the assumption that the member initially behaves as a fixed ended member with a reduced effective length. However, under quasi-static loading this would not be encountered as the top surface would always be in compression.

Figure 5.9: Hogging crack in specimen 3A-U-I

5.5.4. Specimen 4A-U-I

The impact characteristics of test 4A-U-I were varied such that the kinetic energy was the same but the mass and velocity were different. For this reason it was decided to drop a mass of 300 kg from a lower height of 0.8 m, which would result in an impact velocity of 4 m/s and the impact energy would be 2350 joules. Data was acquired through a high speed camera which captured images at a rate of 3000 fps (Figure 5.10). Data was also acquired from a 30g accelerometer attached to the impact mass and via load cells at the supports. These were all sampled at a rate of 10,000 Hz.

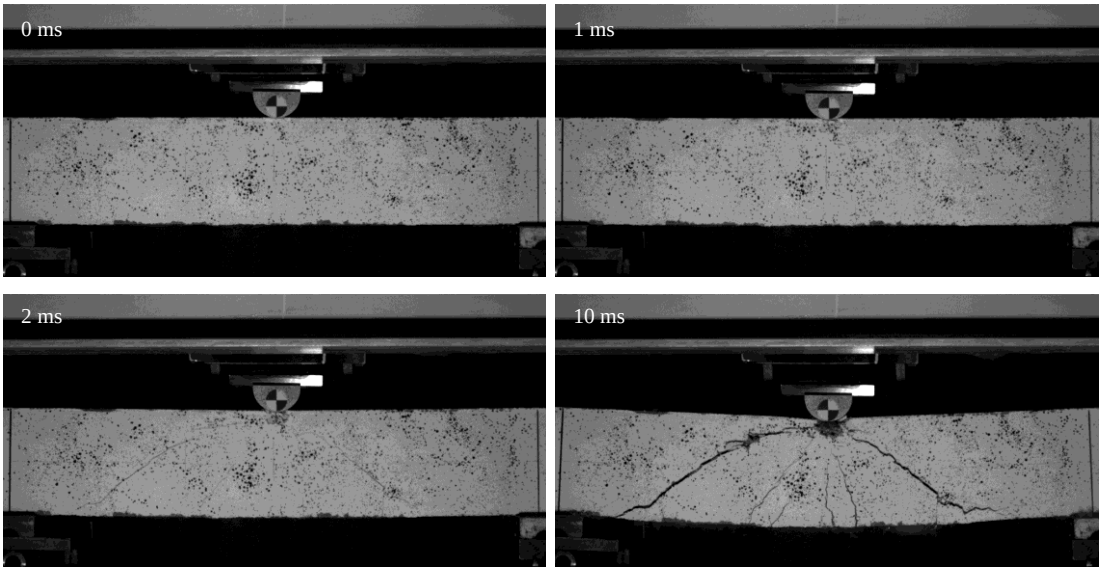

Figure 5.10: Images showing response of specimen 4A-U-I captured with high speed camera

It can be seen from Figure 5.10 that specimen 4A-U-I exhibited very little ductility, failing at a very early stage in shear. Hairline shear cracks can be seen from around 1 ms after impact but become much clearer after 2 ms, particularly on the left hand side. Similar results are also obtained from DIC analysis carried out on the speckled pattern applied to the surface of the specimen. The deformation profiles calculated using this analysis are shown in Figure 5.11. These appear to indicate that up to around 0.002 s the member was still deforming in a flexural shape. However, after this point the deformation of the central region increases by a greater amount indicating that shear cracks have formed. The results also highlight the fact that a shear wedge has formed and that the crack angle on the right hand side is steeper than on the left.

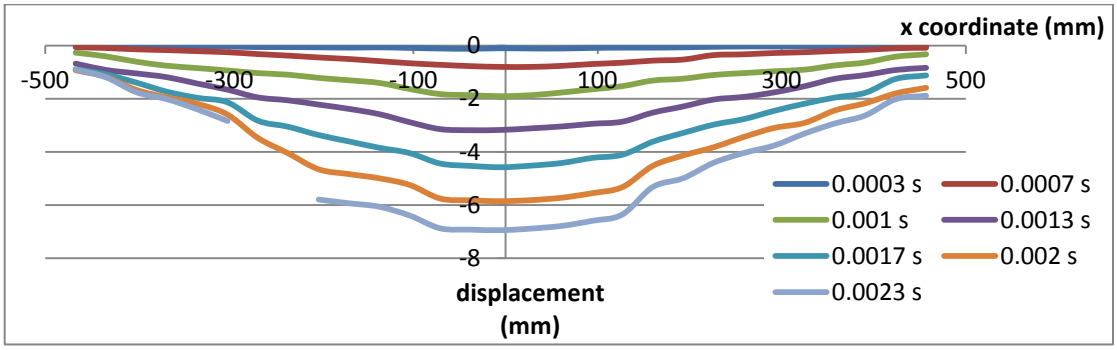

Figure 5.11: Time varying deflected profiles from DIC analysis for specimen 4A-U-I

Data from the accelerometer and right hand reaction load cell is shown in Figure 5.12. Unfortunately due to damage sustained during the test, the data set is incomplete and not usable in terms of measuring the full time varying reaction forces. In addition to this the 30g accelerometer was insufficient to record the peak acceleration and hence the peak force at impact. However, the data did prove useful in terms of measuring the lag between the time of impact and the support experiencing a reaction force. From Figure 5.12 this time lag is approximately 0.0007 seconds. As the distance from the load to the support was 0.5 m, this suggests the deformation wave propagated at an average velocity of approximately 714 m/s. Due to the sampling rate the time measurement is only accurate to within 0.0001 second and, therefore the force propagation velocity has a relatively high margin of error of between -12% to +16.6%.

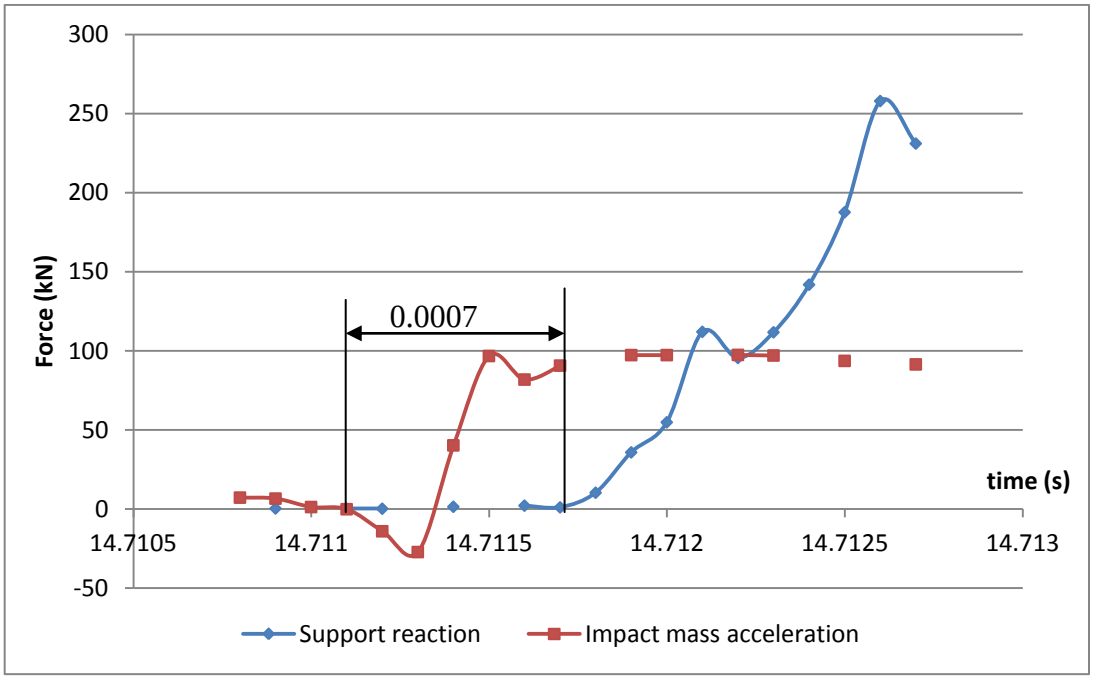

Figure 5.12: Accelerometer and load cell data for the initial response of specimen 4A-U-I

Similarly to specimen 3A-U-I, a hogging crack also formed in specimen 4A-U-I approximately 230 mm from the point of load application.

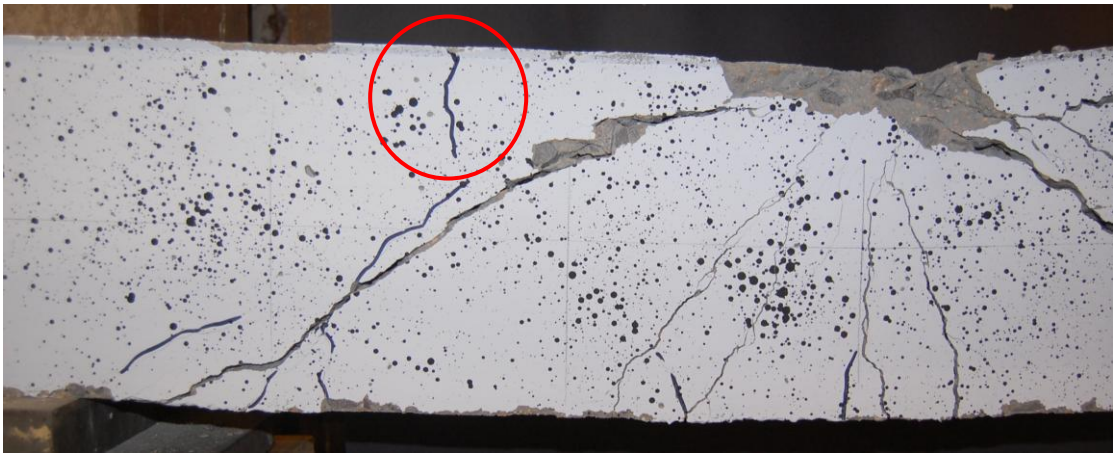

Figure 5.13: Hogging crack in specimen 4A-U-I

5.6. Set C Specimens

Specimens 9C-U-S and 10 C-U-I were designed to compare the dynamic response of an impact loaded member (10C-U-I) with the quasi-static behaviour of a member (9C-U-S). Figure 5.14 shows the dimensions and reinforcement arrangement of set C specimens. The reinforcement arrangement was expected to give the member a moment resistance of 28.5 kNm and a shear capacity of 51.9 kN (i.e. flexural and shear failure loads of 67 kN and 104 kN respectively).

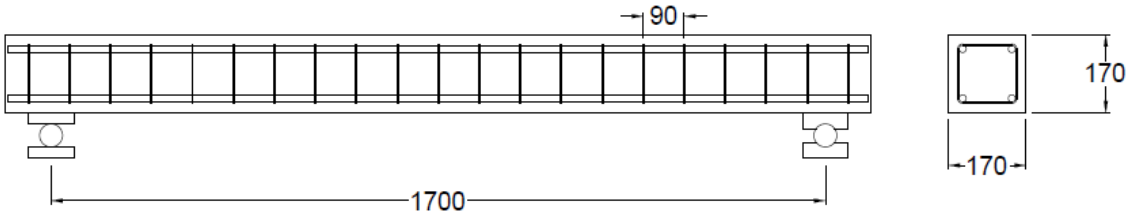

Figure 5.14: Reinforcement arrangement in set C specimens

5.6.1. Specimen 9C-U-S

Specimen 9C-U-S was tested under a centrally applied quasi-static point load. The clear span for the test was 1700 mm.

Shown in Figure 5.15 is the load deflection plot from the test. These results indicate a high level of ductility was achieved in the test and that the full flexural capacity was reached at a load of around 70 kN, indicating that the moment resistance was around

29.8 kNm. This compares well with the theoretical moment capacity of 28.5 kNm. The energy dissipated in the specimen up to failure can also be estimated from the area under the load-displacement graph (Figure 5.15) and equates to approximately 3100 joules, the graph also reveals that this is mostly by plastic straining which would be expected in a flexurally deforming member.

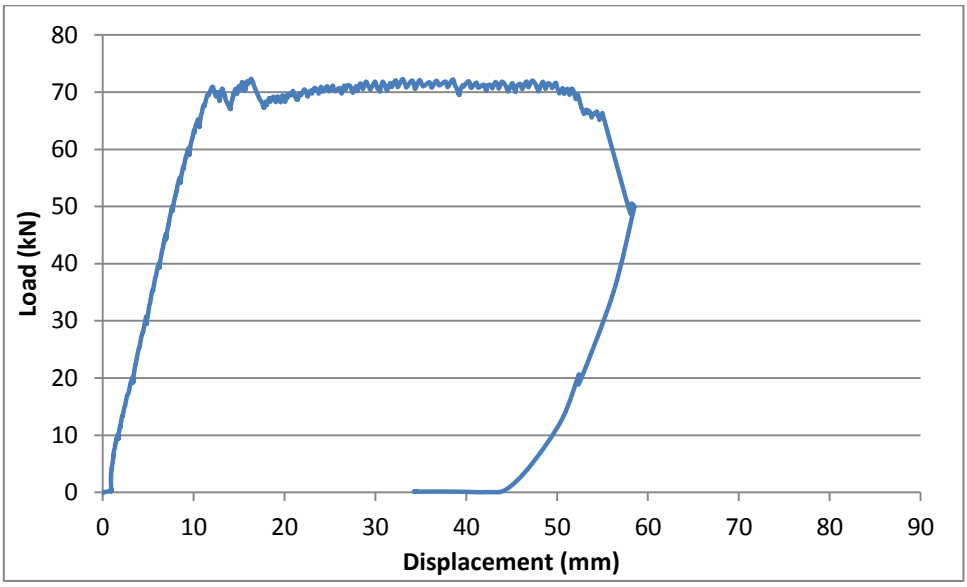

Figure 5.15: Load deflection for specimen 9C-U-S

Final failure, however, occurred through a diagonal tension failure indicating a flexural/shear type response of the member. The displacement of the specimen at failure was approximately 50 mm. Figure 5.16 indicates that up to a load of approximately 45 kN no diagonal cracks were present. However, from Figure 5.17 it can be seen that diagonal cracking dominated the ultimate failure.

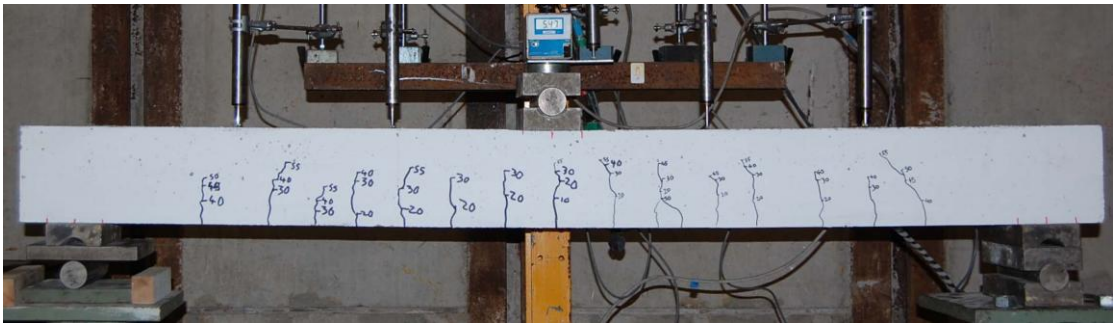

Figure 5.16: Crack patter for specimen 9C-U-S at 45 kN

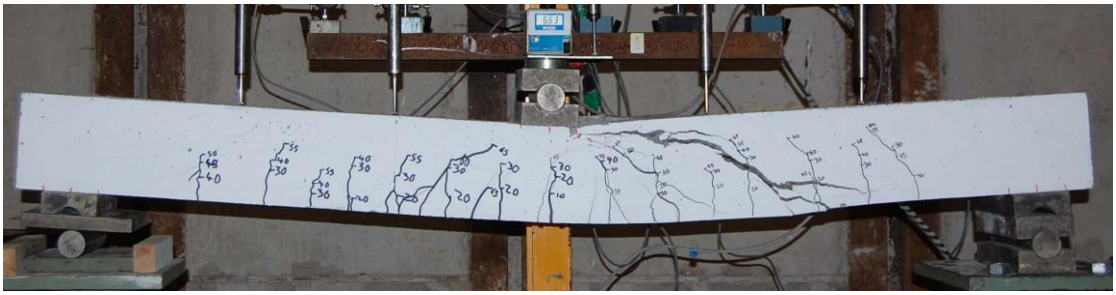

Figure 5.17: Crack pattern for specimen 9C-U-S at failure

5.6.2. Specimen 10C-U-I

It was desired that Specimen 10C-U-I would be tested at the maximum impact velocity achievable with the impact rig which was 6.5 m/s. It was determined from test 9C-U-S that the energy dissipated as strain energy was approximately 3100 joules. Using this dissipated energy as a guide for the sections ductility capacity a mass of 150 kg was selected for the impact. The impact event was recorded with a high speed camera at a frame rate of 3000 fps. A 500g accelerometer (rather than the 30g accelerometer used previously) and the custom built load cells were also used for data acquisition and were sampled at a rate of 150,000 Hz. The test setup is shown in Figure 5.18.

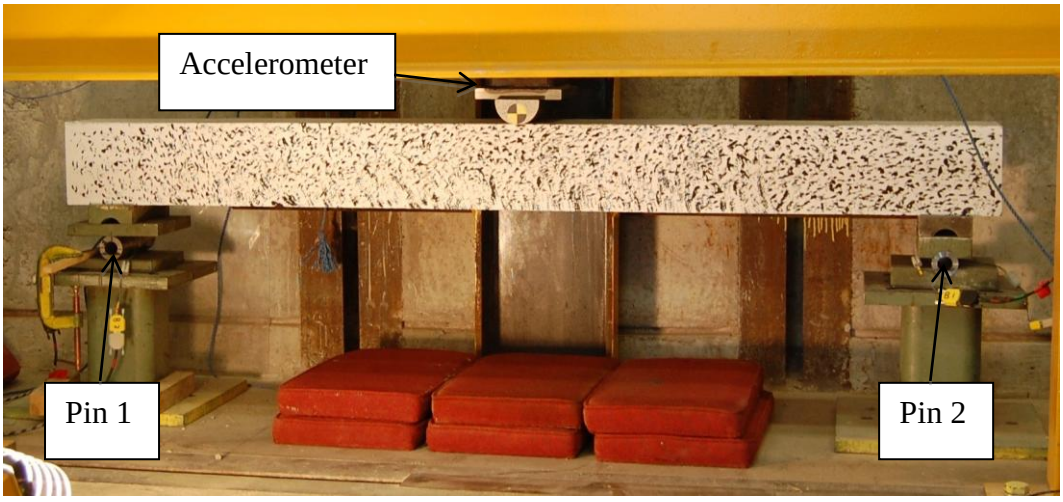

Figure 5.18: Impact test set up

Shown in Figure 5.19 are high speed images of the member's deformation up to the peak deflection which occurred 13.3 ms after impact. The peak deflection reached

was 43 mm. These images clearly indicate that a plastic hinge has formed at the point of impact.

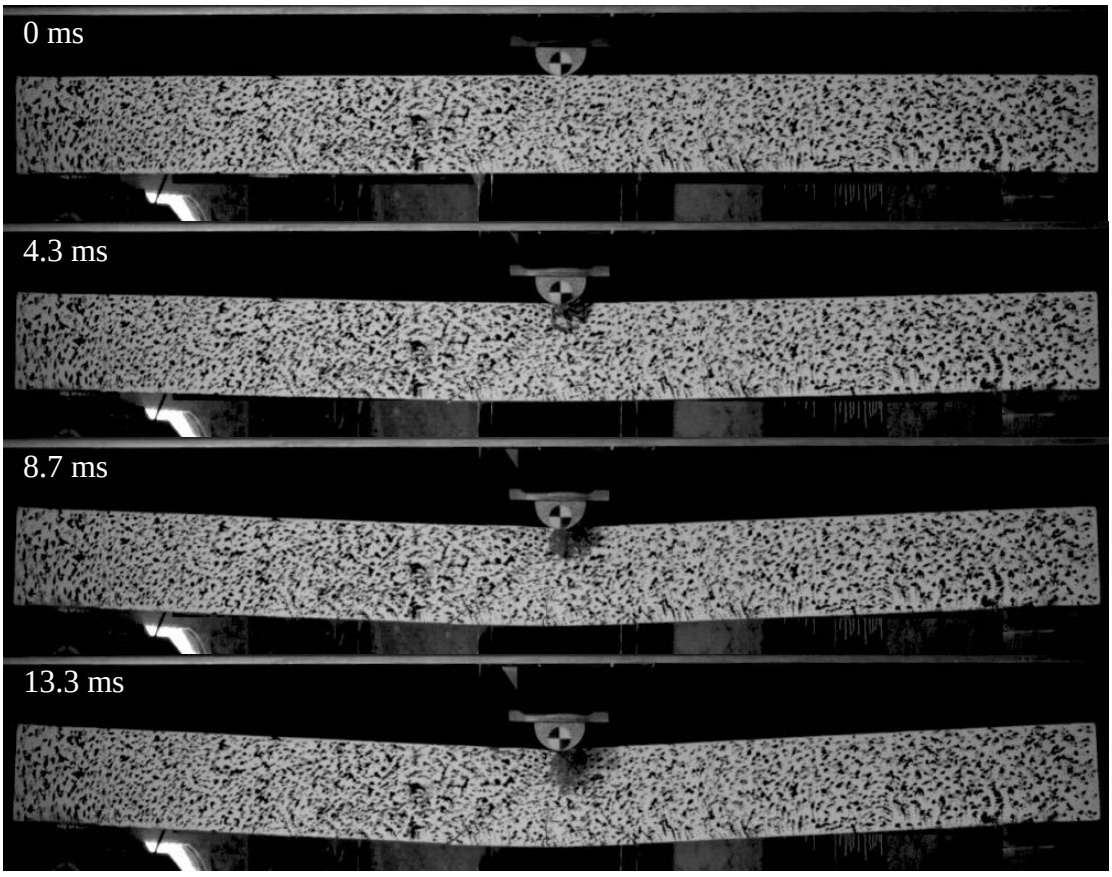

Figure 5.19: Images from high speed camera for specimen 10C-U-I up to peak deflection

The images shown in Figure 5.19 indicate that a flexural response was achieved with little visible evidence from these high speed photos of shear cracks forming.

DIC analysis carried out to plot the change in the deflected profile of the member during impact is shown in Figure 5.20 and appears to show that the overall response was through bending. It is evident that shear deformations occur at a location of x=+/-250 mm 0.0017 s after impact, as shown by the deformation profiles from the DIC data in Figure 5.20. The propagation of the deflected profile can also be clearly seen between 0.0003 s and 0.0013 s which provides further evidence for the basis of the model outlined in chapter 4.

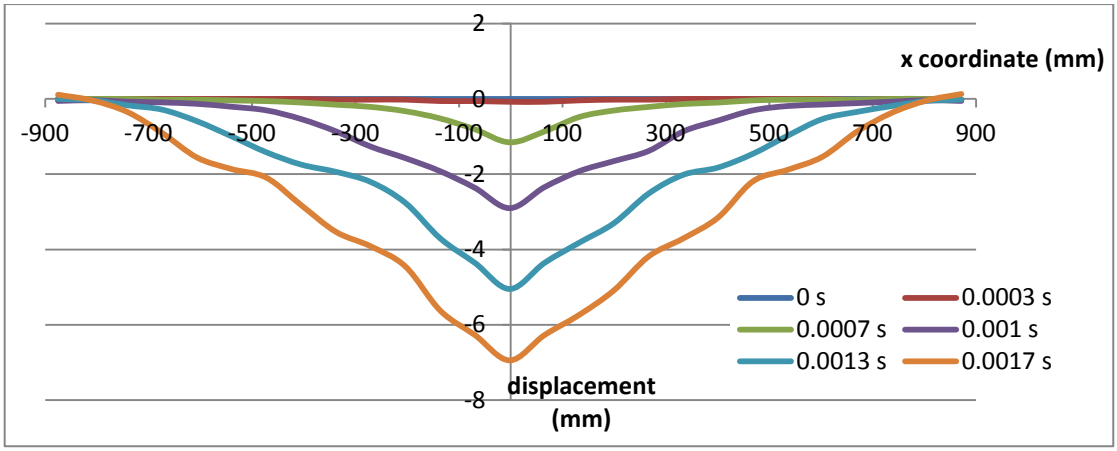

Figure 5.20: Time varying deflected profiles from DIC analysis for specimen 10C-U-I

As outlined above, data was also acquired through an accelerometer mounted to the impacting mass and from load cells at each support, which were sampled at a rate of 150,000 Hz. The primary aim of this data acquisition was to measure the force propagation velocity, the importance of which has been described previously in relation to the theoretical work. From Figure 5.21, the delay between the time of impact and the supports reacting can clearly be seen. This shows that the initial impact occurs at around 837 ms after data logging began with the right hand load cell (pin 2) reacting 2.5 ms later and the left hand load cell (pin 1) reacting 3 ms after the initial impact. As the load was applied centrally and the span of the member was 1700 mm, the force propagation velocity is calculated to be between 280 and 340 m/s.

Unfortunately, the data in Figure 5.21 appears to show that the accelerometer exceeded its 500g capacity which would indicate that impact force was initially greater than 735 kN. However, it is also possible that high frequency ringing which is seen in frequencies over 20,000 Hz (Doyle, 1997) may have affected the data. There is also a large discrepancy between the data recorded from both load cells which suggests that this data cannot be relied upon for predicting the forces which act on the member. This difference may have been caused by the load cell at the roller side being free to slide out whereas the pin at the other end was restrained.

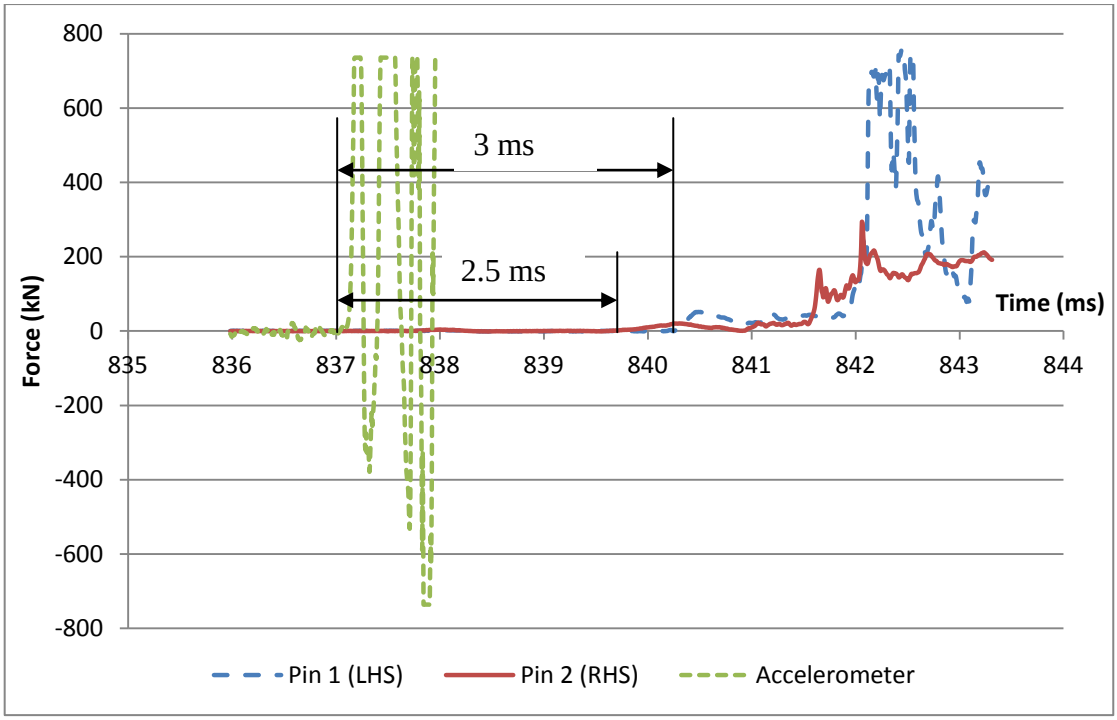

Figure 5.21: Combined load cell and accelerometer data for specimen 10C-U-I

The cracks seen on the specimen post-test reveal a flexural/shear type response (Figure 5.22). Cracks can be seen to have formed radially outwards from the point of impact and also diagonally around the quarter span (which would normally be associated with a shear failure). The radial cracks may also indicate the formation of a shear plug in the specimen, although it is clear that this has not developed fully as the impact was not sufficiently large. These observations appear to be consistent with the deformation profiles plotted from the DIC analysis in Figure 5.20 which indicate that some shear deformation had occurred. It can also be seen that hogging cracks have formed on the top surface approximately 440 mm from the impact point on the right side of Figure 5.22 and 500 mm from the impact point on the left side.

Figure 5.22: Post-test crack pattern for specimen 10C-U-I

5.6.3. Set C Behaviour comparison

The crack patterns shown in Figure 5.17 and Figure 5.22 contrast significantly. It can be seen from Figure 5.16 that under quasi-static loading a significant number of flexural cracks form prior to ultimate failure and these cracks form almost perpendicular to the longitudinal direction. In contrast cracks in specimen 10C-U-I can be seen to have formed radially from the impact point. It is clear from Figure 5.17 that ultimate failure in specimen 9C-U-S has occurred through the formation of a single diagonal crack. This differs from the response of specimen 10C-U-I where it can be seen that symmetrical diagonal cracks have formed (Figure 5.22) but further from the centre of the member than in specimen 9C-U-S. It is also clear that no failure has resulted from the applied load. Not visible in Figure 5.22 are cracks which have formed on the top surface of specimen 10C-U-I, which are shown in Figure 5.23. These cracks indicate that at some stage in the member's response the top surface in these areas was in tension which contrasts with the quasi-static behaviour observed where the top surface is always in compression. However, it is consistent with the behaviour of a fixed end beam as outlined in the theoretical work presented in Chapter 4.

Figure 5.23: Hogging cracks in specimen 10C-U-I

The peak displacement of specimen 9C-U-S was found to be around 50 mm at failure. In specimen 10C-U-I the peak displacement was slightly smaller at around 43 mm. The impact energy was selected to be identical to the energy dissipated in the quasi-static test, therefore it may have been expected that the deflections would be similar. The results would therefore appear to indicate either that energy is lost in the impact event or that the flexural capacity increases due to strain-rate effects (or both).

5.7. Set D Specimens

Set D specimens were designed with the same longitudinal reinforcement as set C. However, the spacing of the transverse shear reinforcement was reduced in set D from 90 mm to 75 mm. Increasing the shear capacity further would ensure that a ductile response is achieved. This change in reinforcement arrangement was expected to increase the shear resistance from 51.9 kN in 9C-U-S to 55.4 kN. The specimens were tested with the same setup as set C, with 11D-U-S tested under quasi-static loading and specimens 12D-U-I, 13D-U-I and 14D-U-I tested under impact loading. The specimens were again designed as columns with symmetrical reinforcement, the layout of which is shown in Figure 5.24.

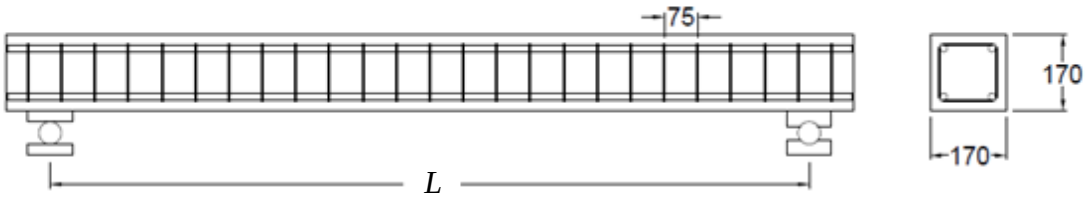

Figure 5.24: Reinforcement arrangement in set D specimens

5.7.1. Specimen 11D-U-S

Specimen 11D-U-S was tested under quasi-static 3-point bending with a centrally applied point load. The specimen had a clear span of 1.7 m.

Results from the load-deflection graph are shown in Figure 5.25 which indicate that yielding occurred at a load of 75 kN and the peak load achieved was close to 80 kN. This suggests that the actual moment capacity at yield was around 31.9 kNm which is slightly higher than the design capacity of 28.1 kNm. The peak deflection achieved in the specimen prior to failure was 80 mm.

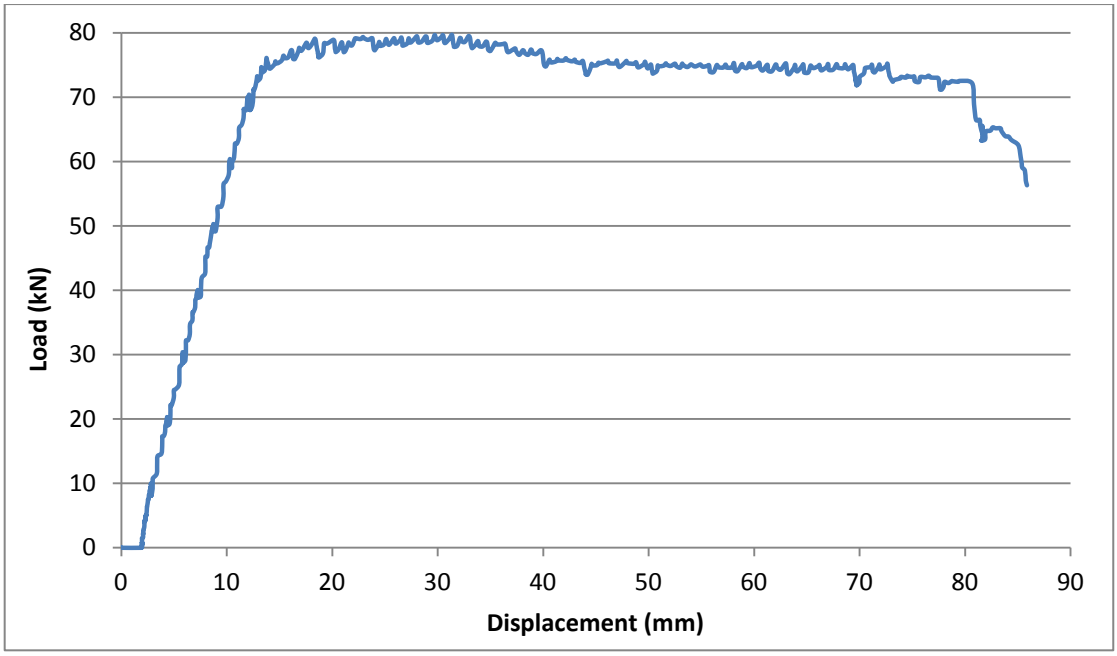

Figure 5.25: Load deflection for specimen 11D-U-S

Failure of specimen 11D-U-S occurred firstly through crushing of the concrete in the compression zone (Figure 5.26) followed ultimately by the formation of a diagonal crack (Figure 5.27). Softening due to the effects of crushing in the compression zone was seen to start occurring at a displacement of around 36 mm.

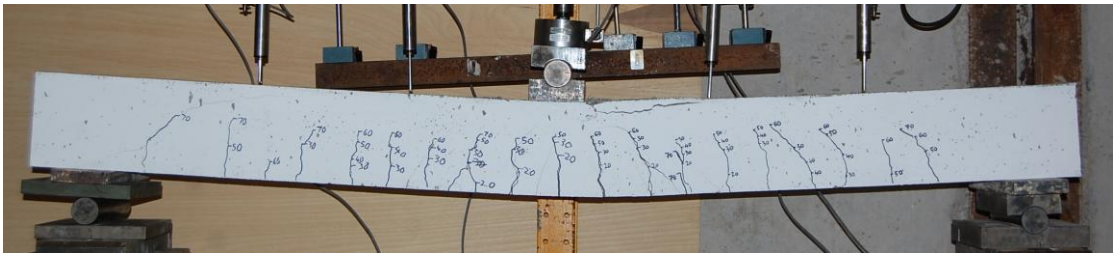

Figure 5.26: Specimen 11D-U-S at the onset of crushing in the compression zone

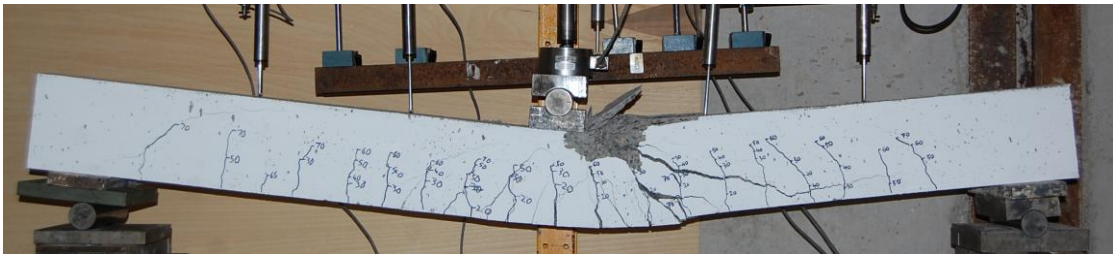

Figure 5.27: Specimen 11D-U-S at ultimate failure

The behaviour seen in specimen 11D-U-S represents a considerable improvement in ductility when compared with specimen 9C-U-S. The primary difference between the two specimens was the reduction in link spacing from 0.64d to 0.54d. This had a significant effect on the member's behaviour and allowed a much greater amount of strain energy to be dissipated.

5.7.2. Specimen 12D-U-I

Specimen 12D-U-I was tested under the same loading as specimen 10C-U-I, with a 150 kg mass impacting at a velocity of 6.5 m/s giving an impact energy of 3100 joules. The impact event was filmed with a high speed camera at 3000 fps and data from load cells and the accelerometer were sampled at 150,000 Hz.

The response of the member was very similar to that of specimen 10C-U-I as shown in Figure 5.28. The peak deflection of the member occurred 13 ms after the initial impact and was approximately 41 mm.

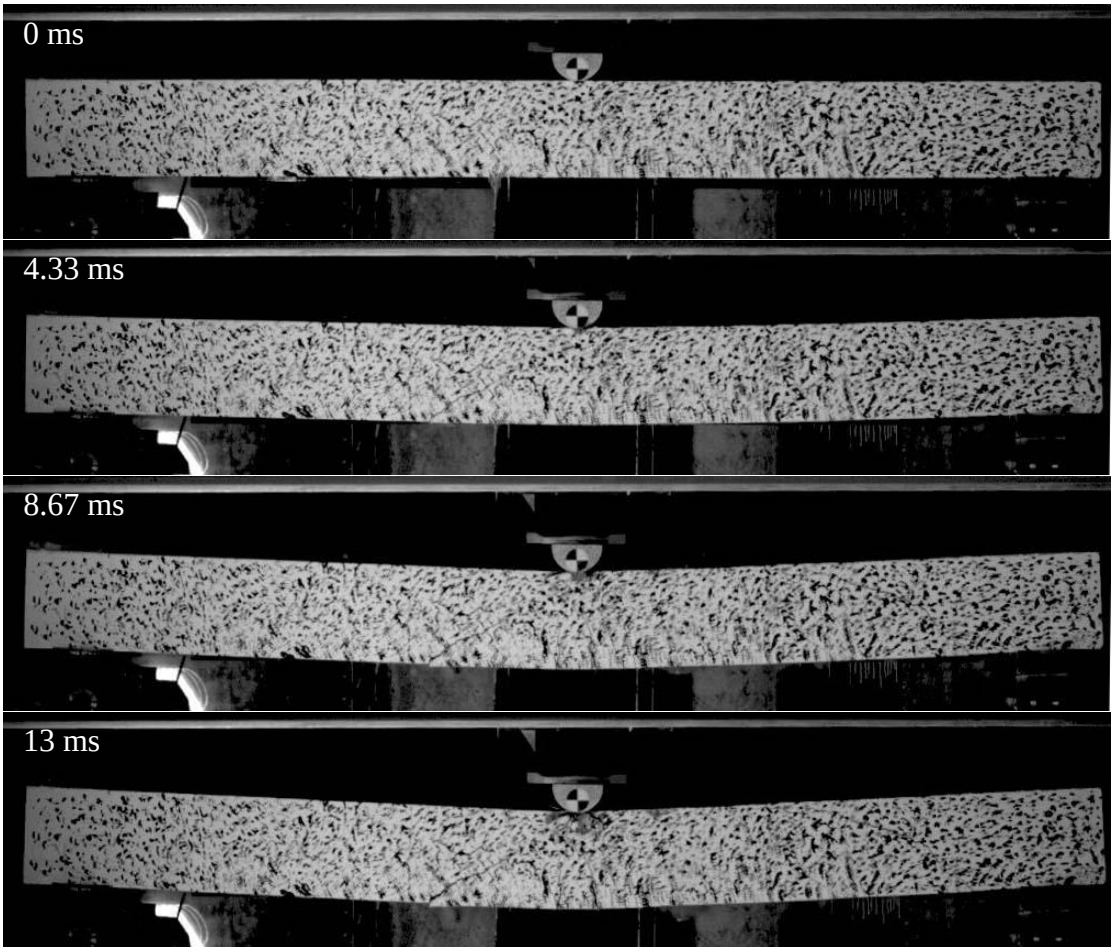

Figure 5.28: High speed images showing response of specimen 12D-U-I up to peak displacement

The images recorded with the high speed camera appear to show the formation of a shear crack on the left hand side between 8.67 ms and 13 ms (Figure 5.28). This would appear to be confirmed by the DIC analysis carried out to track the change in the deformation profile as the member is impacted, shown in Figure 5.29. It appears from this that a discontinuity arises in the displacement of the central portion of the member at around 0.001 s (seen at x = +/-150 mm), which may be due to the formation of a central shear plug. The DIC analysis once again appears to confirm the presence of the wave type phenomena associated with the propagation of the displacement from the point of impact to the supports.

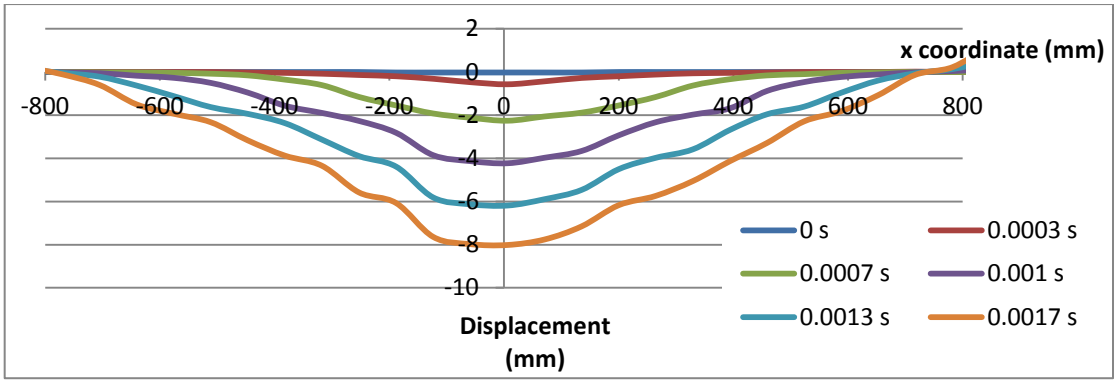

Figure 5.29: Time varying deflected profiles from DIC analysis for specimen 12D-U-I

The data for the first few milliseconds of the response is shown in Figure 5.30. This clearly indicates the time lag between the impact occurring and the load cell supports experiencing the force. It can also be seen that there is a slight time difference between pin 1 and pin 2 experiencing the force, which was also seen in other tests. Taking this time difference into account it is possible to calculate the force propagation velocity to be between 245-280 m/s.

Of the tests where both load cells functioned correctly it was found in each case that the pin support shows a change in force before the roller support. This suggests that the roller may have been pushed out by the wave prior to being loaded, although the time difference is very small.

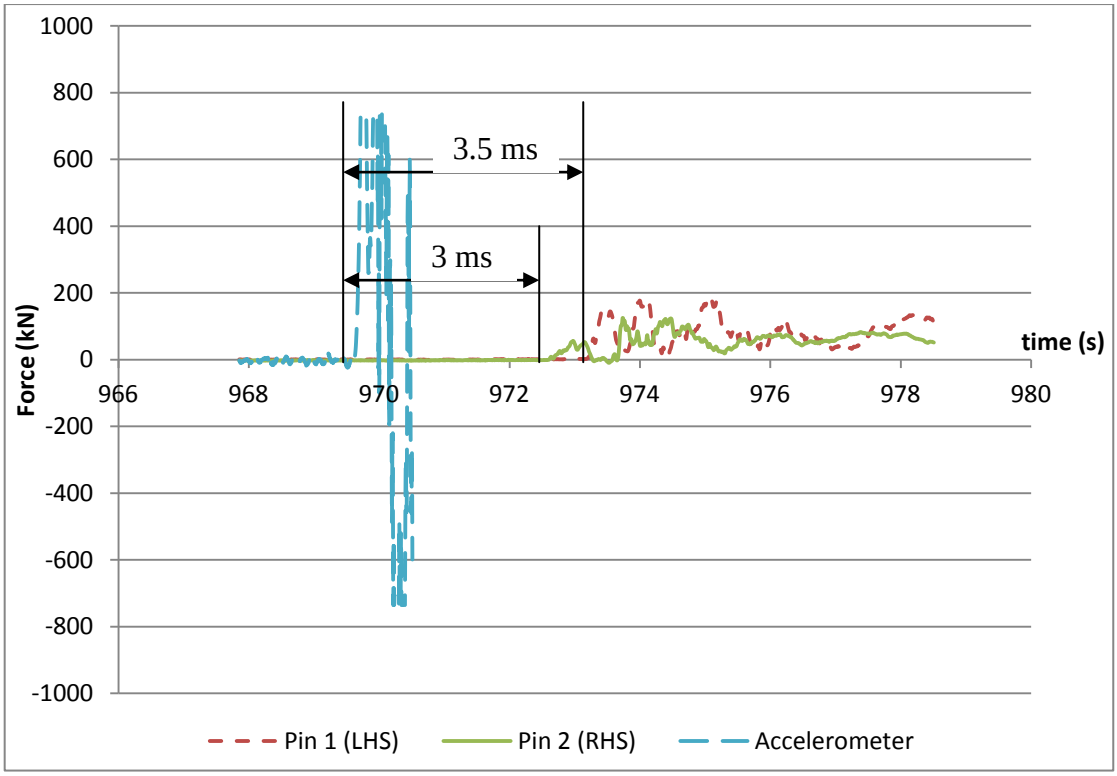

Figure 5.30: Combined load cell and accelerometer data for specimen 12D-U-I

The data from the accelerometer shown in Figure 5.30, again appears to indicate that the accelerometer exceeded its capacity and the maximum impact force was greater than 700 kN. However, once again, it is not clear whether this is the result of high frequency vibration or actually indicates that the impact force exceeded 700 kN. The positive and negative fluctuations in the data are, however, indicative of vibrational issues and for this reason it is not considered that the data can be used to reliably predict the impact force.

The data from the load cells indicates clearly the time of the initial impact. The load experienced by both load cells at this time is relatively consistent with pin 1 experiencing a peak force of 210 kN and pin 2 experiencing a peak force of 150 kN. The data also reveals some oscillations which again appear to indicate a wave type phenomenon which dominates the force-time response.

The post-test assessment of the crack pattern on the back face (Figure 5.31) indicates a flexural/shear response of the member without a complete failure occurring. It can be seen that flexural cracking has occurred at the centre of the member and shear cracks have started to develop towards the supports. The crack pattern also appears to

concur with the deformation profiles determined from the DIC analysis shown in Figure 5.29, which show a shear discontinuity forming after 0.001 s at +/- 150 mm.

Figure 5.31: Post-test crack pattern for specimen 12D-U-I

In addition to this, hogging cracks were also observed to have formed on the top surface of the member, as shown in Figure 5.32. This behaviour would not be encountered in quasi-static situations and can thus be attributed to inertial effects in the member's response. It should also be pointed out that these cracks are not connected to the shear cracks.

Figure 5.32: Hogging cracks in specimen 12D-U-I

5.7.3. Specimen 13D-U-I

All specimens in set D were designed with identical cross-section dimensions and reinforcement arrangements (both longitudinal and transverse). To provide additional data regarding the variation in the force propagation velocity with different span/depth ratios, the span of 13D-U-I was reduced to 1020 mm, giving a span/depth ratio of 6. In order to effectively isolate the importance of this parameter the same impact mass (150 kg) and velocity (6.5 m/s) used in test 12D-U-I were used here. Once again data was recorded using a high speed camera recording 3000 fps and a data logger recording at 100,000 Hz. Attempts were also made in this test to apply piezoelectric pressure transducers to the underside of the beam. These were propped on foam

blocks which were considered soft enough not to affect the response mode whilst also allowing the pressure transducers to work effectively. This arrangement can be seen at the quarter span on the left hand side in Figure 5.33. It was considered that these transducers would provide additional data to measure the force propagation velocity.

The sequence of images in Figure 5.33 show the response of the member from the time of impact up to around 12.3 ms. These clearly show that a brittle shear failure has occurred. The quasi-static shear capacity was calculated, using BS8110, to be 55.4 kN and the maximum moment capacity was recorded in test 11D-U-I to be around 34.0 kNm. This suggests that under quasi-static conditions the load to cause a shear failure would be 110.8 kN and the load required to reach the plastic moment capacity would be 133.3 kN indicating a shear failure was inevitable.

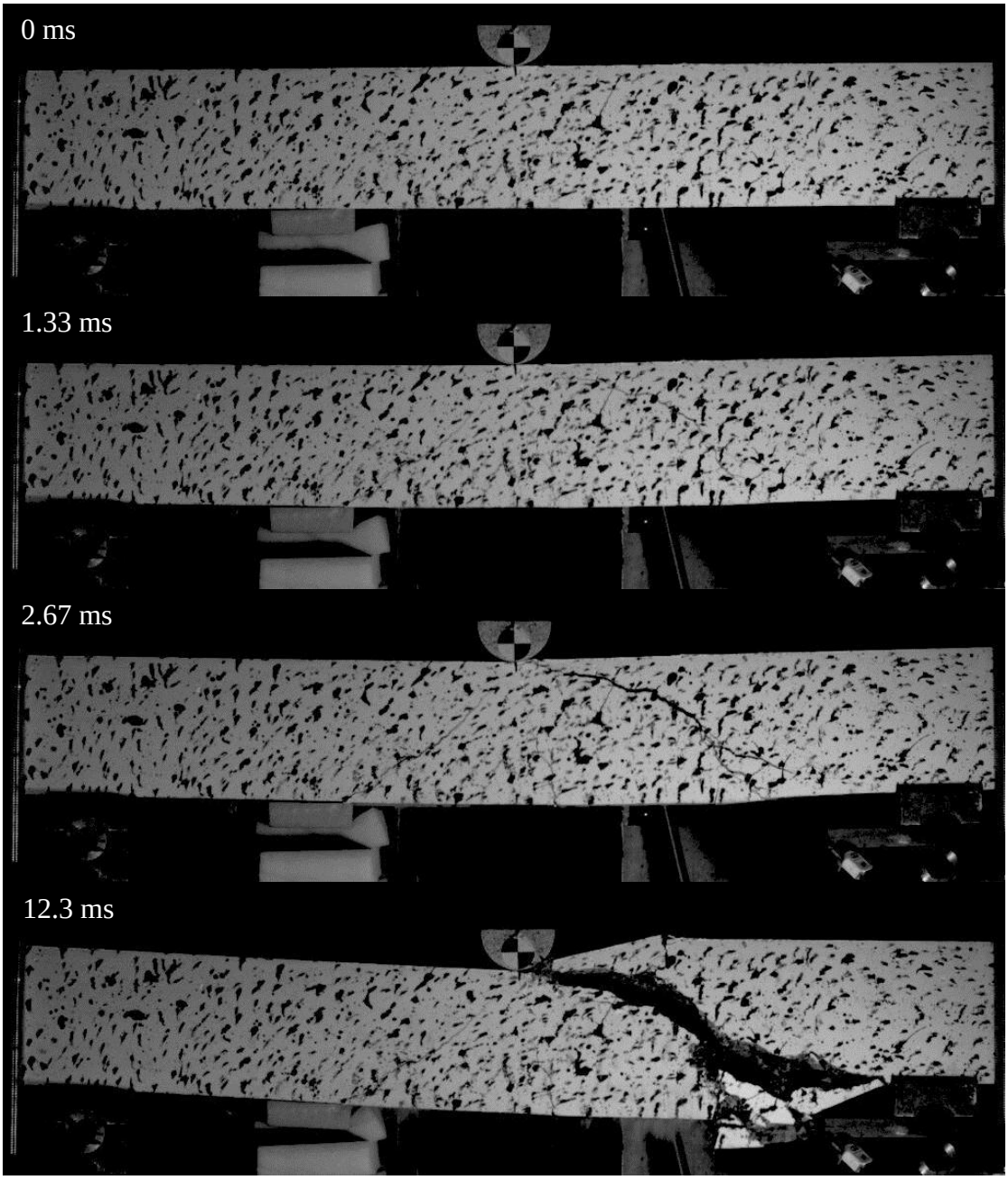

Figure 5.33: High speed images showing response of specimen 13D-U-I up to peak displacement

Results from previous tests (3A-U-I and 4A-U-I) would suggest that a shear cone would have been expected to form in this test with large shear cracks forming on each side. It is clear from the image taken at 2.67 ms (Figure 5.33) that while a shear crack has formed on the left hand side, failure has only occurred on the right hand side. It is likely that this is a result of the arrangement supporting the pressure transducer pad which restricted the movement of the left hand side. Due to the perceived effect the

prop had it was decided not to use this type of arrangement in future tests, with the data obtained from this also proving inconclusive.

The effect of this prop can also be seen from the DIC analysis on the deforming shape shown in Figure 5.34 from which the shear deformation (and failure) of the central region can clearly be seen.

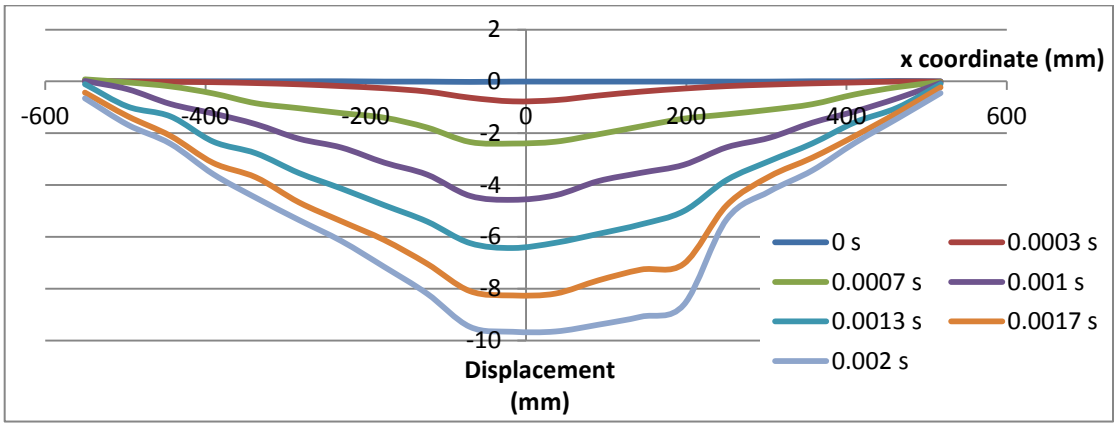

Figure 5.34: Time varying deflected profiles from DIC analysis for specimen 13D-U-I

Data showing the initial response of the support load cells and the accelerometer is presented in Figure 5.35. The time lag between impact and the left and right hand reactions experiencing the force was 0.00078 seconds and 0.00085 seconds respectively. This indicates the force propagated at a velocity of between 654 m/s and 600 m/s. There also appears to be a wide discrepancy between the peak force recorded from the accelerometer and from the load cells. In the initial positive phase of the accelerometer's response it would appear that the force did not exceed the maximum capacity of the accelerometer which suggests the impact force was around 600 kN. However, the oscillations seen in the accelerometer data would appear to indicate high frequency vibrations were experienced.

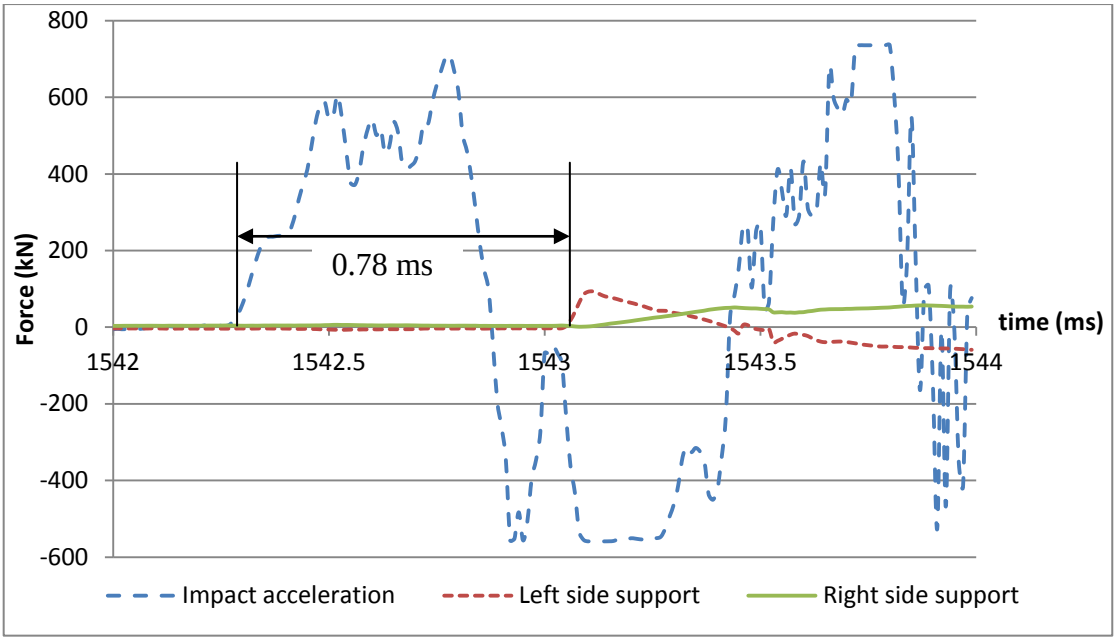

Figure 5.35: Combined load cell and accelerometer data for specimen 13D-U-I

5.7.4. Specimen 14D-U-I

Specimen 14D-U-I was also designed to provide additional data on the relationship between the span/depth ratio and the force propagation velocity by testing a much higher ratio of a/d. Impact was again provided by a falling mass weighing 150 kg which was intended to reach a peak velocity of 6.5 m/s at the point of impact. The specimen was intended to span 2210 mm, giving a span/depth ratio of 13.

Due to the increased span compared with the other specimens in set D, the quasi-static load required to cause the plastic moment capacity to be reached was now estimated to be around 61.5 kN based on the results from test 11D-U-I. The quasi-static load for shear failure was again estimated to be 110.8 kN based on the BS8110 design standard.

Images recorded using a high speed camera at 3000 fps are shown in Figure 5.36. Due to the length of the member it was not possible to fit the whole member in the shot without compromising resolution which would have adversely affected the accuracy of the DIC analysis shown in Figure 5.37. The images appear to show the formation of a shear cone which first forms approximately 2 ms after the impact occurs, although this is difficult to see given the resolution of the photos. The time at which the shear crack first forms is confirmed by the DIC analysis which suggest that shear discontinuity occur around +/- 400 mm from the origin on each side at 0.0017 s. The

DIC analysis can also be used to measure the peak displacement of the member which can be shown was around 46 mm, occurring around 18.7 ms after impact.

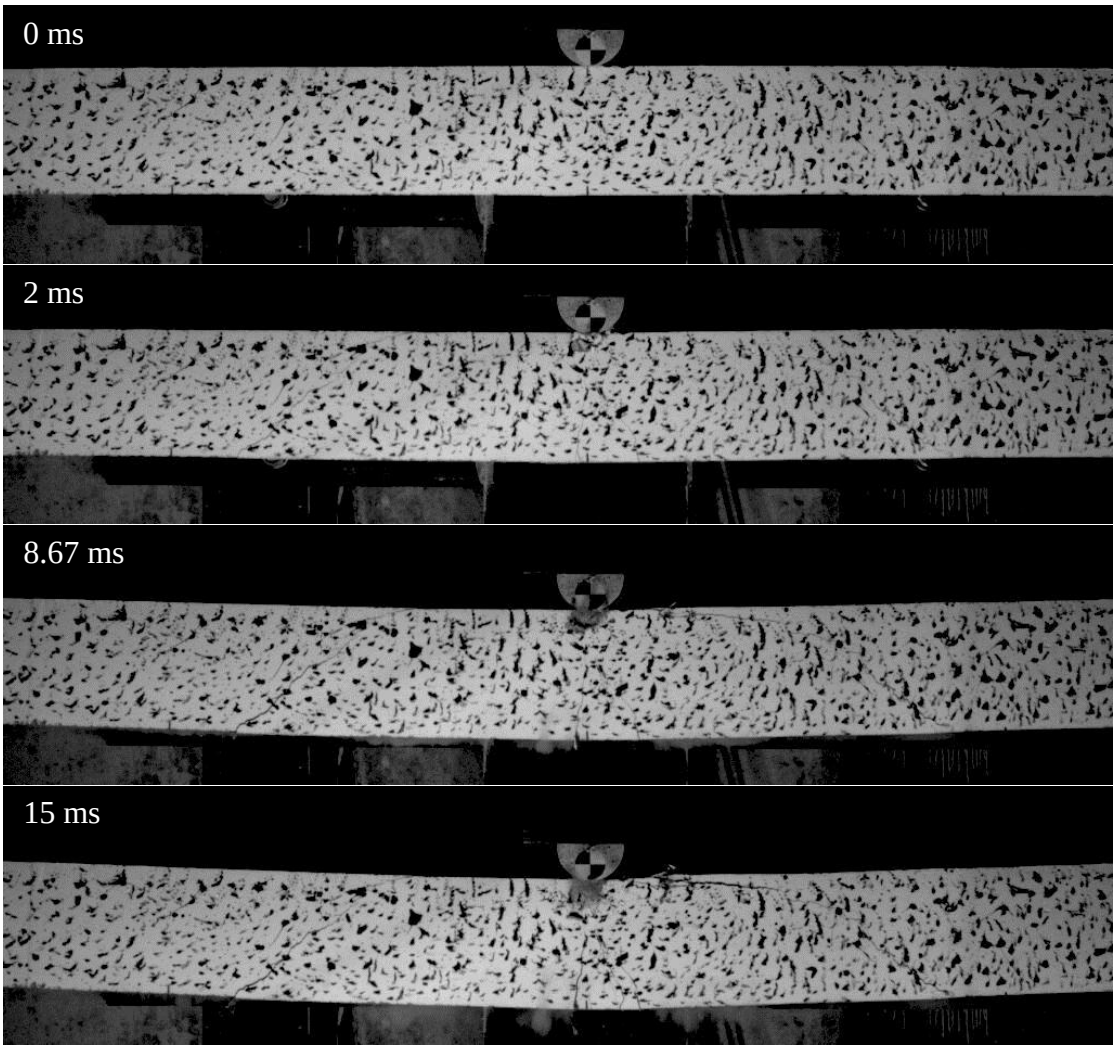

Figure 5.36: High speed images showing response of specimen 14D-U-I up to peak displacement

Given the behaviour observed in specimens 11D-U-I and 12D-U-I and the large difference in the load required for flexural and shear failure under quasi-static loads, such large shear cracks were not expected to form in this test. A full comparison of this behaviour is given below.

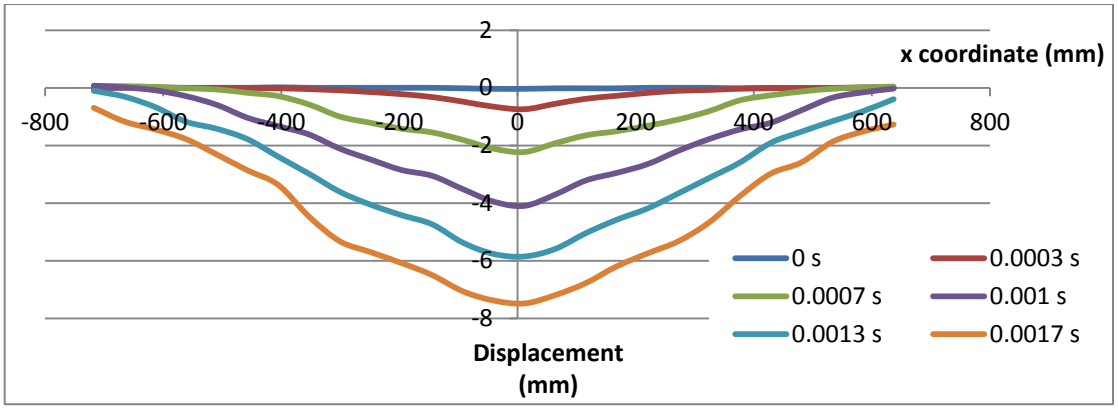

Figure 5.37: Time varying deflected profiles from DIC analysis for specimen 14D-U-I

Data was once again recorded from an accelerometer mounted to the impact mass and load cells at the support, which is shown in Figure 5.38. Due to damage sustained to the load cell during previous tests only the right side support provided useful data. This still indicates clearly the time lag between the impact occurring and the supports reacting around 4.4 ms later. This indicates that the average force propagation velocity for this specimen was around 250 m/s.

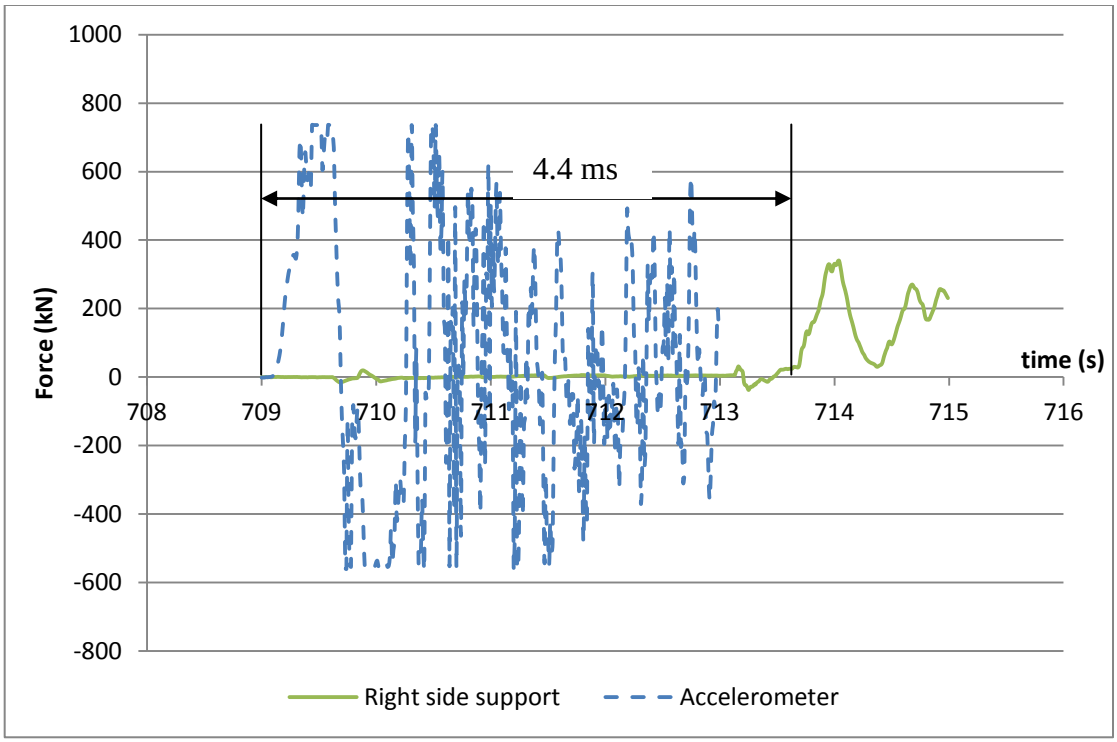

Figure 5.38: Load cell and accelerometer data for specimen 14D-U-I

An assessment of the crack pattern post-test (Figure 5.39) confirmed the formation of a shear cone in the central region, although once again, no complete failure was observed. Also observed were the presence of three hogging cracks spaced at 150 mm intervals on each side, the first of which occurred around 500 mm from the point of impact on both sides, these are shown more clearly in Figure 5.40.

Figure 5.39: Post-test crack pattern of specimen 14D-U-I

Figure 5.40: Post-test crack pattern of specimen 14D-U-I showing hogging cracks on top surface

5.7.5. Comparison of set D specimens

The specimens tested in set D exhibited a range of behaviour modes that were closely related to the span of the member and the test method. Specimen 11D-U-S clearly exhibited a flexural response, attaining its peak moment capacity before failing through crushing of the concrete. Specimen 13D-U-I failed through brittle shear, as was expected. Specimens 12D-U-I and 14D-U-I had perhaps the most interesting behaviour, exhibiting a flexural/shear response. This is perhaps best indicated in specimen 14D-U-I where a clear shear wedge formed. This behaviour contrasts with the behaviour that would be expected if the member was loaded quasi-statically, where, based on the behaviour seen in specimen 11D-U-S, a purely flexural response would be expected given the increased span. These results support the hypothesis that as the rate of loading increases so the failure mode tends to become more brittle.

5.8. Comparison of test data with theory

The primary motivation for carrying out the test programme outlined above was to provide data for validation of the theoretical work presented in Chapter 4. Discussed in detail below is a comparison of the theoretical predictions for the behaviour with the available test data. Due to limitations in the data acquisition methods it has proven difficult to provide definitive quantitative comparisons between the predicted impact forces and those measured. However, this does not restrict the model's ability to qualitatively predict many of the important dynamic phenomena and trends seen.

5.8.1. Set A specimens

Both specimens 3A-U-I and 4A-U-I were shown to fail catastrophically in shear under the actions of different impact loads and that failure occurred at a very early stage in the member's response. It is therefore clear that the shear capacity of the member was exceeded in both cases. Shown in Figure 5.41 are the predicted peak forces for each of the tests. Due to the lack of force arrival time data from test 3A-U-I the arrival time was determined by rearranging equation 4.18 with a modification made for the impact velocity according to equation 4.19. For specimen 4A-U-I the experimentally determined force arrival time of 0.7 ms was used in the prediction.

The predictions for the impact force (Figure 5.41) show that the higher velocity, lighter mass impact (3A-U-I) causes a significantly greater initial impact force than the lower velocity, heavier mass impact (4A-U-I). It is predicted that the peak impact force in specimen 3A-U-I would be around 910 kN and in specimen 4A-U-I would be around 590 kN. Unfortunately due to the low rating of the accelerometer used in these tests the results cannot be verified quantitatively. Over time the difference between the two reduces and it is predicted that at around 0.45 ms the impact forces are the same for each test. After this time it is shown that the predicted impact forces actually increase.

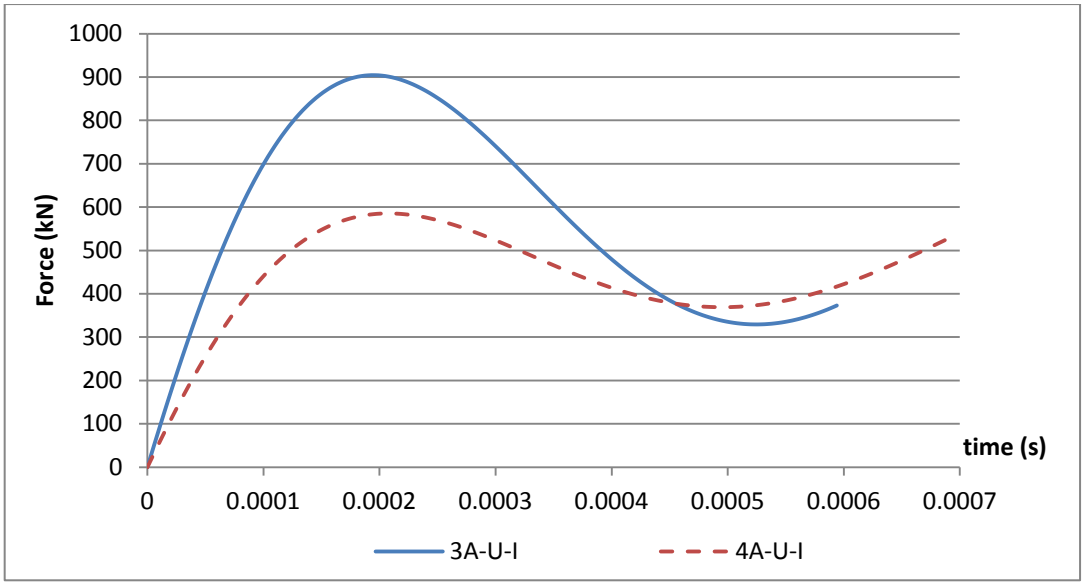

Figure 5.41: Predicted impact forces for specimens 3A-U-I and 4A-U-I

The increase in force is a result of the assumption of linear elastic behaviour in the contact zone which cannot predict the conjoined motion that occurs in reality. This problem is highlighted in the velocity-time profile for test 3A-U-I shown in Figure 5.42. This shows that the theory outlined in Chapter 4, predicts that the member's velocity will at some point exceed that of the impacting mass velocity suggesting that for a brief period the member will actually move away from the impacting mass (0.0002 – 0.0005 seconds). Following this, the velocity of the impacting mass once again exceeds that of the member which suggests the contact zone spring is being compressed again and the force increases. In reality this behaviour would not be expected and it has been commented on previously that for impacts involving concrete, the impacted member's velocity would not exceed the velocity of the impacting mass. Future work may look to address this inaccuracy by modelling more accurately plasticity effects and other energy loss modes especially in the contact zone.

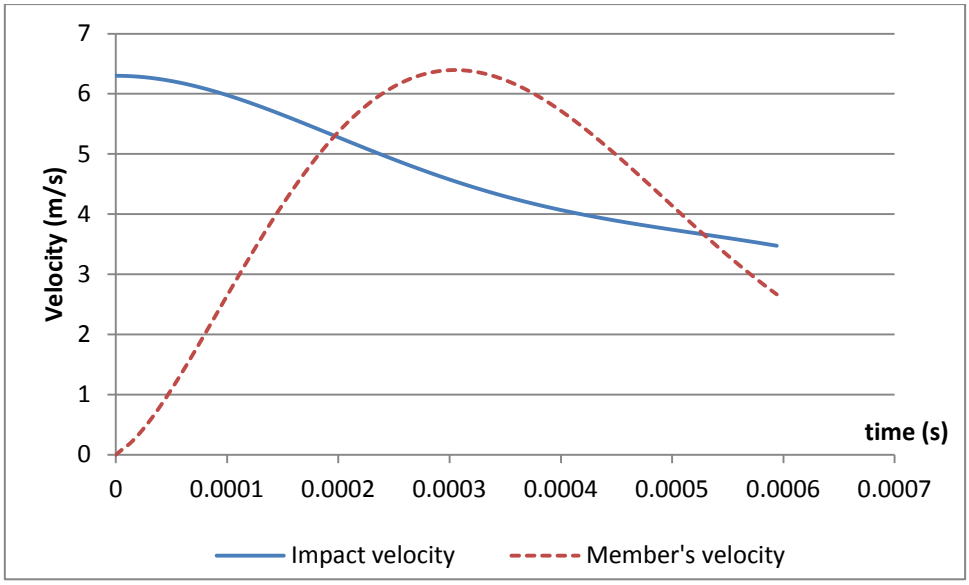

Figure 5.42: Velocity-time profile for specimen 3A-U-I

The predictions for the shear demand from each of the impact tests are shown in Figure 5.43. For both tests it is predicted that the shear demand will significantly exceed the experimentally determined static shear capacity (test 1A-U-S) of 41.1 kN for the duration of the analysis and shear failure will result in both tests. This is confirmed from the images taken from the high speed camera, shown in Figure 5.7 and Figure 5.10. The shear forces predicted in test 3A-U-I are significantly larger than those predicted in test 4A-U-I. It would therefore be expected that failure in this test would be more catastrophic. This again is confirmed by the images from the high speed camera which show that for specimen 3A-U-I (Figure 5.7) large shear cracks open with almost no flexural cracking, whereas, in specimen 4A-U-I (Figure 5.10) a greater degree of flexural cracking is seen in addition to the shear cracks.

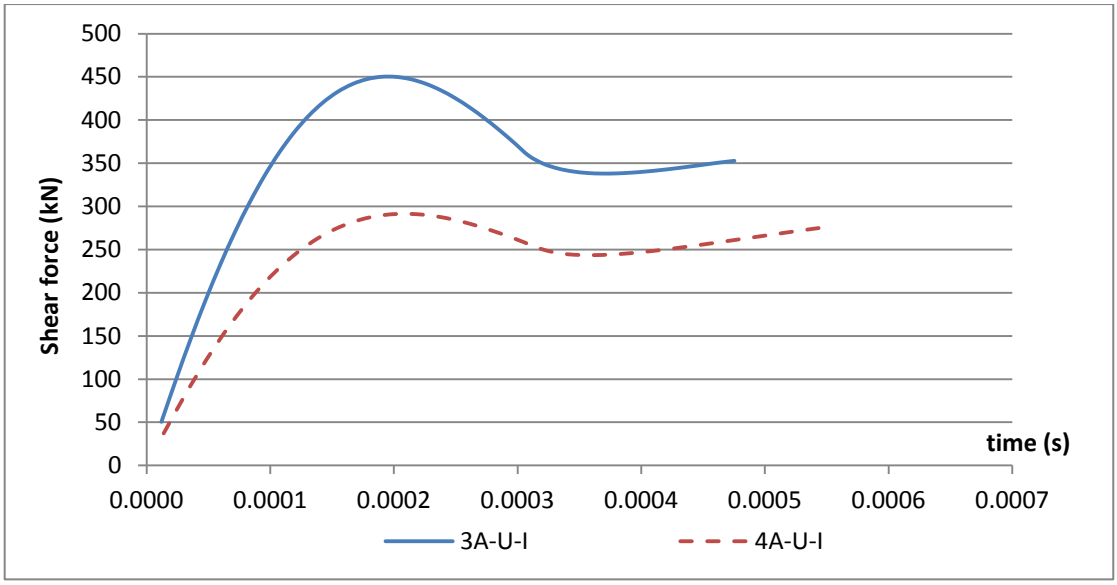

Figure 5.43: Predicted shear demands on specimens 3A-U-I and 4A-U-I

It was also suggested by Grady and Kipp (1985) that more brittle failures would result in cracks following a more direct path rather than the lowest energy path. The shear cracks that formed in both specimens 3A-U-I and 4A-U-I provided a good opportunity to test this theory by looking at cases of aggregate shear in the crack. Where failure was more brittle it would be expected that cases of direct shear through aggregate would be greater.

Although it was considered that this would provide only fairly rudimentary qualitative data, it would also provide a further opportunity to compare the behaviour of specimens 3A-U-I and 4A-U-I.

Assessment of the internal faces of the two shear cracks from specimen 3A-U-I revealed very little aggregate shear on the left hand crack but substantial amounts on the right hand crack, Figure 5.44 and Figure 5.45 respectively. Unfortunately quantifying this finding is difficult. In the case of the left hand crack only 1 instance of aggregate shear was observed, however in the right hand crack around 15 cases were seen, as indicated in Figure 5.45. This suggests that the right hand crack formed more catastrophically than the left which appears to be confirmed by the photos in Figure 5.7.

An analysis was also carried out on cases of aggregate shear in the cracks that formed in specimen 4A-U-I. This revealed that no cases of aggregate shear occurred. These results further support the assessment that specimen 3A-U-I failed in a more brittle manner than specimen 4A-U-I.

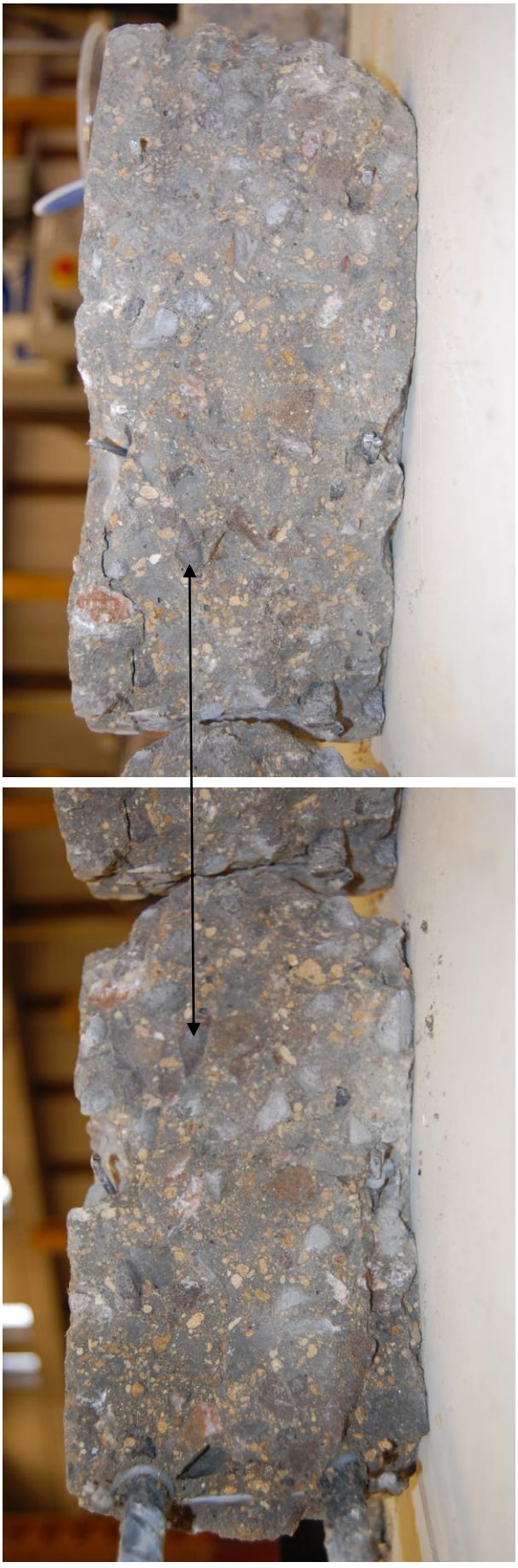

Figure 5.44: left hand shear crack face of specimen 3A-U-I with one observable case of aggregate shear

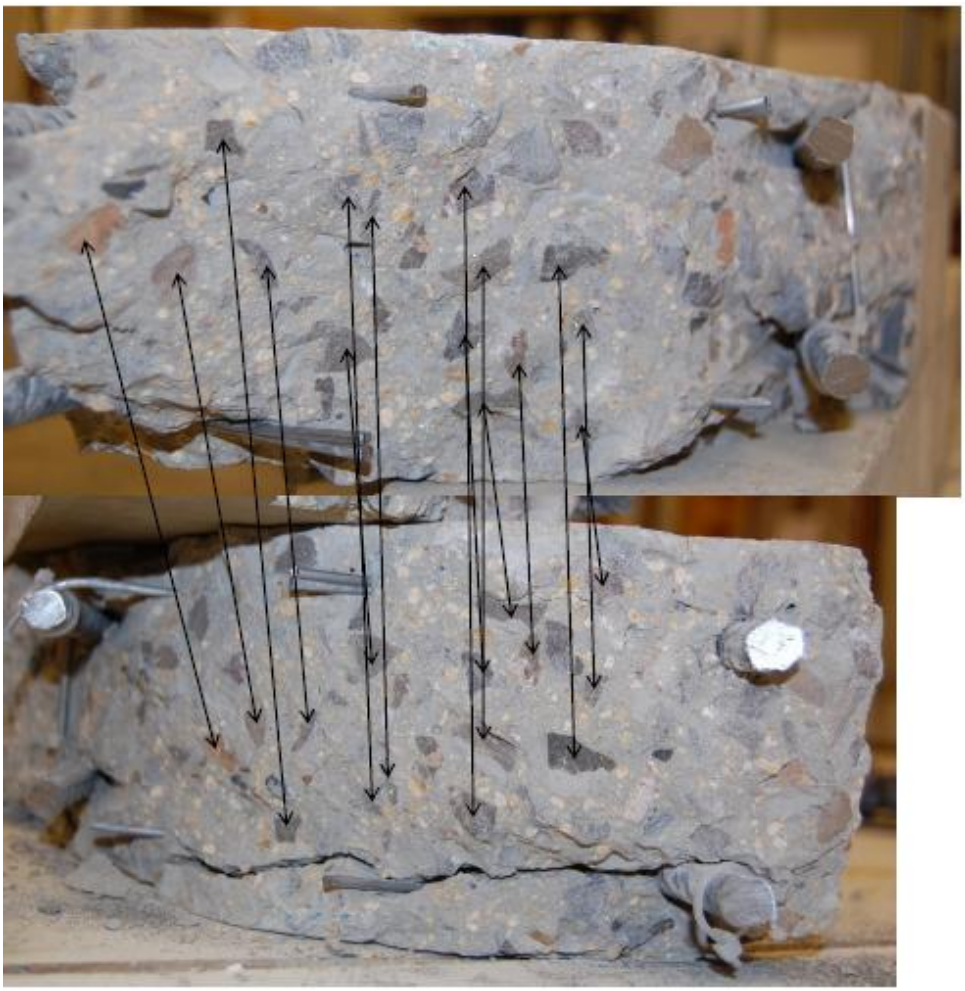

Figure 5.45: Right hand shear crack of 3A-U-I with sheared aggregate indicated by arrows

A final feature predicted in the theoretical model is the presence of hogging cracks on the top surface of the specimens. The predicted variation in the hogging moment with increasing effective length is shown for half the member in Figure 5.46. Also shown in this figure is the quasi-static cracking moment and an upper-bound cracking moment, which takes into account dynamic increase factors due to strain-rates. The strain-rates were estimated from the time-varying moment capacity, this was alluded to in section 4.5.2. It was found that rates of straining for the steel were in the order of 0.5 s^{-1}.

Cracking will begin to occur when the stress in the extreme fibre of a deforming member exceeds the tensile strength of the concrete (f_{ctm}) which can be estimated from equation 5.1 (EC2):

$$f_{ctm} = 0.3 f_{ck}^{(2/3)} \tag{5.1}$$

where f_{ck} is the characteristic compressive strength of a concrete cylinder. The cracking moment (M_{crack}) can then be found simply from the Engineer's equation:

$$M_{crack} = \frac{f_{ctm} I}{y} \tag{5.2}$$

Where, I is the gross second moment of area for a transformed section, as it is assumed that the section is initially uncracked, and y is the distance from the centroid to the extreme fibre. The value for the concrete tensile strength obtained using equation 5.1 represents a mean value. However Eurocode 2 gives the 95% fractile value as being up to 30% greater than the characteristic value. In addition to this strain-rate effects may also increase the strength of the concrete in tension which would increase the cracking moment of a section.

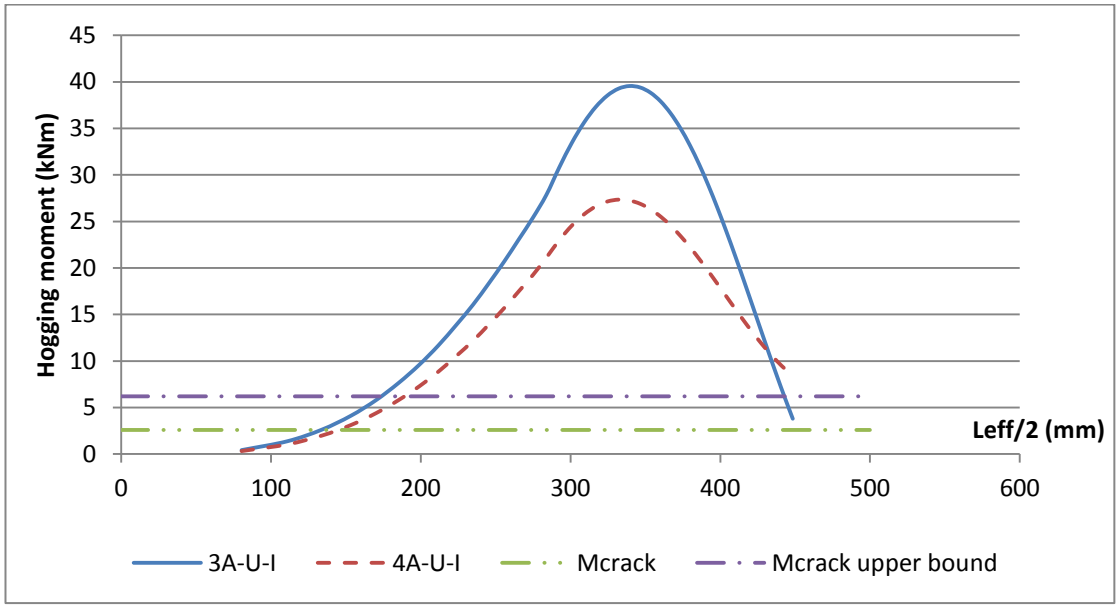

Figure 5.46: Hogging moment demand for specimens 3A-U-I and 4A-U-I

From Figure 5.46 it is possible to estimate the distance from the centre of the beam at which a hogging crack would be expected to first form. Assuming a mean quasi-static value for the concrete's tensile strength, it is estimated that a hogging crack will form at a distance of 130 mm from the point of impact in specimen 3A-U-I and 145 mm in specimen 4A-U-I. Using the upper bound value for the concrete's tensile strength which includes an estimate for the dynamic increase factor, the distance between the point of impact and a hogging crack increases to 170 mm and 190 mm in specimens 3A-U-I and 4A-U-I respectively. This compares with experimentally determined values of 210 mm and 230 mm in specimens 3A-U-I and 4A-U-I respectively.

Given the challenges outlined above with the data acquisition this theory provides a good opportunity to qualitatively compare the predictions for the behaviour with the test results. The under-prediction in the distance between the impact point and the hogging crack forming suggests that the hogging demand is over estimated. This may indicate that the impact force is over-predicted by the theory. This is most likely attributable to the assumption that energy is conserved in the impact. If the energy loss was taken into account, the peak impact force predicted would reduce and the hogging demand would increase more slowly, which would increase the predicted distance between the point of impact and the first hogging crack.

5.8.2. Set C and D specimens

The impact tests carried out on Set C and D specimens were all carried out under identical loading conditions of 150 kg impacting at 6.5 m/s. Results were obtained from each test for the force arrival time and the theoretical predictions discussed below make use of the measured values in each case, these are summarised in Table 5.4. Post-test photos of specimens 10C-U-I, 12D-U-I and 14D-U-I (Figure 5.22, Figure 5.31 and Figure 5.39) indicate that complete failure of the member has not occurred, despite the formation of shear cracks in each case. In contrast, specimen 13D-U-I, which had a much shorter span, failed catastrophically in shear.

Table 5.4: Force arrival times determined from experimental work used in analysis

Specimen reference	Force arrival time (s)	Average force propagation velocity (m/s)
10C-U-I	2.973E-03	343
12D-U-I	2.480E-03	286
13D-U-I	7.800E-04	654
14D-U-I	4.380E-03	252

Shown in Figure 5.47 are the theoretical predictions for the time varying impact force up to 0.0005 s. The results indicate that the peak impact force predicted for each test is fairly consistent which would be expected given that the impact characteristics are the same in each case. In each of these tests the accelerometer reached its peak capacity which suggested the peak impact force may have been greater than 700 kN, which is also predicted by the theoretical model shown in Figure 5.47. Future tests carried out should avoid this by using a higher capacity accelerometer.

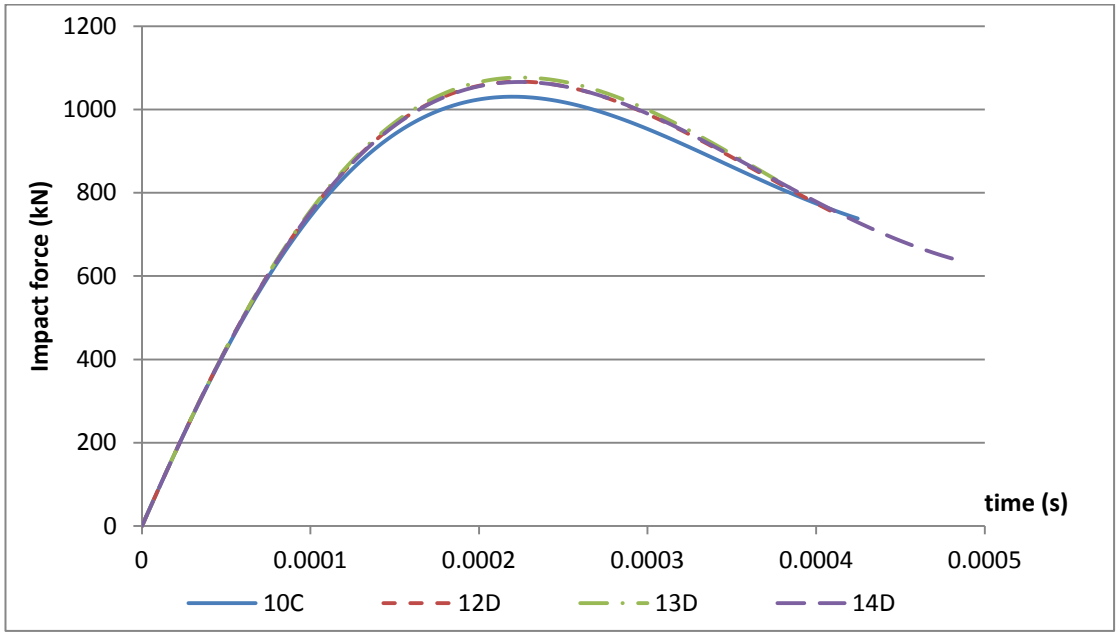

Figure 5.47: Theoretical impact force for specimens 10C-U-I, 12D-U-I, 13D-U-I and 14D-U-I

The predicted variation in the peak shear demand with time for series C and D specimens is shown in Figure 5.48. This indicates that the quasi-static shear capacity of 51.9 kN for specimen 10C-U-I and 55.4 kN for series D specimens was greatly exceeded. Post-test crack patterns and the DIC analysis indicate that in tests 10C-U-I, 12D-U-I and 14D-U-I shear cracks formed but that no overall failure occurred. This contrasts greatly with the behaviour of specimen 13D-U-I which failed catastrophically in shear. This is an interesting and important observation as it indicates that whilst all four specimens experienced approximately the same shear demand only the shortest specimen failed catastrophically in shear. This may suggest that the shear capacity of the section was sufficient to resist the high initial shear demand long enough in tests 10C-U-I, 12D-U-I and 14D-U-I for a more flexural response to occur but not in test 13D-U-I. In this test the impact force reached the reactions at a much earlier time due to the shorter span therefore, the shear demand had insufficient time to decay.

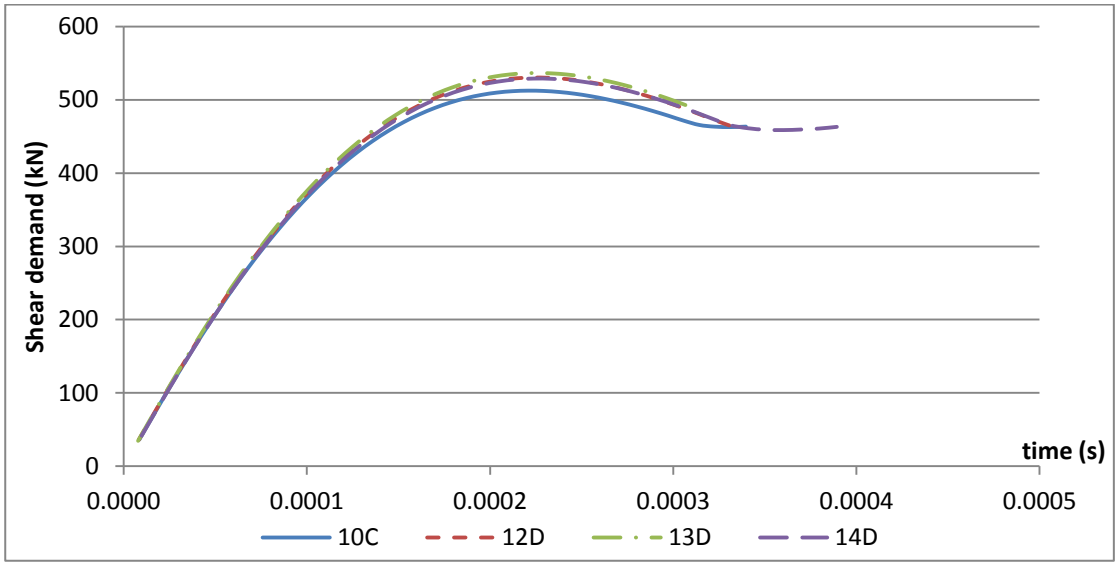

Figure 5.48: Variation in peak shear demand

Comparing the predicted shear demands with the shear capacity is complicated due to the effects of strain-rates and also relating the effective length concept to the capacity of a member. It would be expected that the shear capacity for small effective lengths would be much greater than when the effective length is large as the shear crack angle can reduce. As there are currently no dynamic models which include all of these effects it is difficult here to make direct comparisons. However, a qualitative assessment can be made.

Figure 5.48 shows that the shear forces are predicted to be fairly constant amongst all specimens but the post test analysis appears to suggest that 14D-U-I suffered a greater degree of shear cracking than the other specimens (Figure 5.22 and Figure 5.39). This appears to be confirmed by a comparison of the deformation profiles from the DIC analysis of specimen 14D-U-I and 10C-U-I at 0.002 seconds as shown in Figure 5.49, which shows a large discontinuity in the profile at +/- 400 mm caused by a shear crack forming.

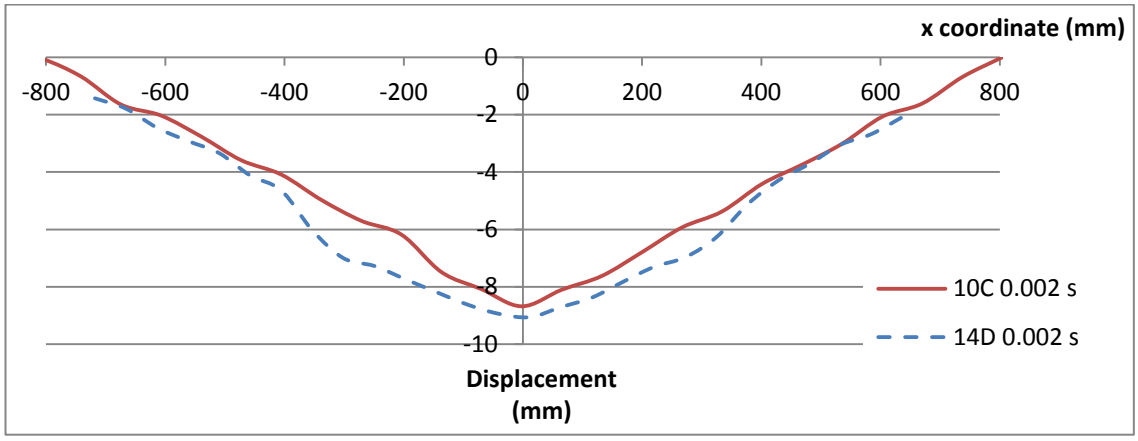

Figure 5.49: Deformed profiles of specimens 10C-U-I and 14D-U-I at t = 0.002 s

The results outlined in this section appear to indicate that either the impact force is over-predicted, which could be due to the assumptions regarding conservation of energy, or the section capacity is under-predicted, which may be related to conservative predictions for the dynamic material properties. Unfortunately the absence of additional data makes it difficult to ascertain which of these effects is the most important.

5.9. Conclusion

The experimental data presented in this chapter has proved conclusive in demonstrating the finite time between an impact occurring and the reactions experiencing this force. This data has been used extensively in developing the theory outlined in chapter 4. The results also give an indication as to why failures become more brittle with increasing impact velocities. Of particular interest here are the results of test 14D-U-I which clearly shows the formation of a shear wedge despite the high span/depth ratio. This is important because under quasi-static conditions a purely flexural response would be expected with no shear cracking, which highlights the importance of dynamic effects on the behaviour of RC members.

Unfortunately due to limitations in the data acquisition, forces obtained from the accelerometer and custom built load cells were less useful due to high frequency vibration. At the time of testing this could not be improved upon and would need to be addressed in future work in order to validate more accurately the theoretical predictions.

One aspect of data acquisition that worked well was the DIC. This data proved useful in plotting the changes in the deflected profiles as the member deformed under the impact

load and observing more accurately when shear cracks first formed and came to dominate the response.

Due to resources only a limited number of tests could be performed and focus was therefore given to measuring the force propagation velocity over a repeatable series. For this reason the simplest test setup was chosen and axial forces were omitted. Future work should aim to investigate what effect axial forces have on the measured force propagation velocity and the observed behaviour.

6. A new method for predicting the peak displacement of blast and impact loaded RC columns

Chapter 4 outlined the development of a new model for predicting the initial forces acting on a member which has been subjected to an impact load. The chapter showed that the predicted shear demand caused by a lighter/faster impact was greater than that caused by a heavier/slower impact. Presented in this chapter is the development of a new model to predict the peak displacement of members which respond flexurally. It can be considered that whereas Chapter 4 was more concerned with initial response and failure, this chapter is concerned with the overall response, assuming that shear failure has not occurred. Isaac *et al.* (2011 summarises the main results from this Chapter.

6.1. Blast response of FRP wrapped RC columns

A number of limitations have been identified as to the ability of the most commonly used method to accurately predict the peak displacement in flexurally deforming RC columns. This method, referred to as the single degree of freedom (SDOF) model (Cormie *et al.*, 2009, Biggs 1964.), is a widely used analysis technique owing to its simplicity and relative ease of implementation. However, the validity of the inherent simplifications have been questioned (Razaqpur *et al.*, 2009) and research has shown that in certain circumstances the predictions using this model can vary quite widely depending on the assumptions employed (Rodriguez-Nikl *et al.*, 2009). Alternatives to this approach have tended to be based on finite element modelling. However, significant questions have been raised over the validity of these predictions (Crawford and Magallanes, 2010).

It has also been shown that the predictions for the peak displacement of actual test results can be inaccurate (Rodriguez-Nikl *et al.*, 2009). Given the basis for the development of the SDOF model this result is not surprising. The method was originally developed for inclusion in design manuals (e.g. TM5-1300) to aid in the design of RC structures for military structures, such as munition storages. In these circumstances, over-predicting the response leads to an increased level of conservatism, which, given the massive variation in possible loading conditions leads to a safer design solution, although at the cost of lower material efficiency.

This section details the development of an improved method of analysis which takes into account the flexural deformation in a more realistic manner. The model is intended to address specific weaknesses of the SDOF model, whilst retaining, where possible, a relatively simple approach which is useful for design purposes. The primary areas addressed by the new model are:

- The accurate determination and inclusion of strain-rate effects, something which is currently not possible in the SDOF approach leading to over conservative estimates for material strengths.
- The avoidance of having to select an appropriate resistance function for the section, something which has been shown to lead to wide variation in the predictions from the SDOF model

6.1.1. Development of new model

The proposed model has been developed to analyse RC columns deforming flexurally and is predominantly intended for columns with sufficient shear capacity (e.g. with significant shear links or wrapped with fibre reinforced polymers (FRPs) in the transverse direction), where a flexural response is expected. Given this assumption, and that the column is rotationally fixed at both ends, a three hinge plastic failure mechanism is expected to form as indicated in Figure 6.1. The deformation of the member in this mechanism can then be analysed over a series of small time-steps in an incremental approach. The use of this approach makes it possible to accurately calculate strain-rates in the section and incorporate them directly, through dynamic increase factors (DIFs) in the analysis. It is also possible to take full account of the time varying nature of the applied load, avoiding the need for simplifying this to a triangular load – time history as is common in the SDOF approach (Cormie *et al.*, 2010). A few key assumptions are employed in the formulation of the model, the validity of which are discussed in detail below.

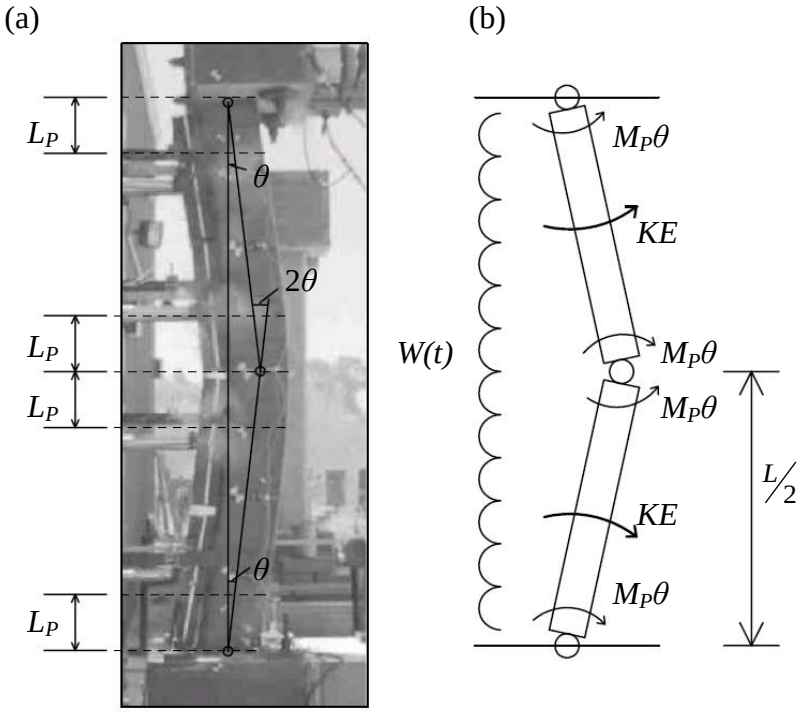

Figure 6.1: Plastic hinge assumption for flexurally deforming RC member with fixed end conditions

The method for determining the peak displacement through this new model is summarised in the flow diagram shown in Figure 6.2.

Implementation of the model first requires that the blast impulse be converted to kinetic energy, as discussed below. Assuming that the member deforms with rigid body rotations (Figure 6.1b) about the supports, the relationship between the rotational kinetic energy of the member and the impulse imparted by the blast load can be established. Considering half the length of the member (between the support and the centre point), the relationship between the rotational momentum and impulse is given by equation 6.1:

$$I_{half}\dot{\theta} = \int_0^t Q\, dt \tag{6.1}$$

where, $\dot{\theta}$ is the rotational velocity, Q is the moment about the end support caused by the force from the blast, which is given by equation 6.2,

$$Q = W(t).\frac{L}{2}.\frac{L}{4} = \frac{W(t)L^2}{8} \tag{6.2}$$

where, $W(t)$ is the time dependent force per unit length from the blast (assuming the blast pressure is uniform along the column length) and L is the length of the column. I_{half} is the moment of inertia for half the column taken about the support, given by equation 6.3:

$$I_{half} = \frac{\frac{M_{tot}}{2}\left(\frac{L}{2}\right)^2}{3} = \frac{M_{tot}L^2}{24} \tag{6.3}$$

where, M_{tot} is the total mass of the column. Substituting equations 6.2 and 6.3 into equation 6.1 gives:

$$\frac{M_{tot}L^2}{24}\dot{\theta} = \int_0^t \frac{W(t)L^2}{8}dt \tag{6.4}$$

Equation 6.4 can be rearranged and written in terms of the impulse per unit length (i_e) as:

$$i_e = \int_0^t W(t)dt = \frac{M_{tot}\dot{\theta}}{3} \tag{6.5}$$

and the rotational kinetic energy for half the column rotating about the support is given by:

$$\frac{KE_{tot}}{2} = \frac{I_{half}\dot{\theta}^2}{2} = \frac{M_{tot}L^2\dot{\theta}^2}{24\times 2} \tag{6.6}$$

where, KE_{tot} is the total kinetic energy for the whole column. By squaring equation 6.5 and substituting into equation 6.6, $\dot{\theta}$ can be eliminated. Since the impulse from the blast, i, is given by i_eL (the impulse per unit length multiplied by the total length), the total kinetic energy acquired by the column from the blast impulse can be finally expressed as:

$$KE_{tot} = \frac{3i^2}{8M_{tot}} \tag{6.7}$$

The primary assumption employed by the model is that the energy from the blast impulse (equation 6.7) is dissipated in localised plastic hinge regions. For a three hinge mechanism the energy dissipated (ED) by straining in the plastic hinges is given by equation 6.8:

$$KE_{tot} = ED = M_P(\dot{\varepsilon})4\theta \tag{6.8}$$

where $M_P(\dot{\varepsilon})$ is the strain-rate dependent plastic moment capacity of the section and 4θ is the sum of the rotations in the plastic hinges (Figure 6.1b). The model essentially determines θ based on the energy that is imparted to the member from the blast. However, due to the dependency of the moment capacity on the strain-rate the solution to equation 6.8 is non-trivial. Because of this, the solution is broken down into a series of small time increments. Within each time-step, Δt, which must be taken as a suitable fraction of the total response time expected, a hinge rotation, θ, is assumed. This assumption for the hinge rotation is an important step in the implementation of the

model, although its exact value can be found by iteration at a later stage. From the assumed plastic hinge length, L_p, which is indicated in Figure 6.1a, the curvature, χ, in the section can be determined which gives the strain profile. In accordance with the assumed time-step, the strain-rate profile can then be determined. Once the strain and strain-rate profiles are known a sectional method of analysis can be used to determine the moment capacity of the member at any stage of the response, taking into account DIFs. This technique for determining strain-rates and including the effect in the analysis overcomes one of the significant issues raised with alternative analytical models in that they are not able to account for strain-rate effects in the section accurately.

As both the plastic moment capacity and the energy dissipation have a dependence on the assumed hinge rotation, θ, it is necessary to include a method for validating the assumption employed and this is discussed in detail below (section 6.1.6).

The process of determining the full response is achieved by repeating the steps outlined above for a series of consecutive time-steps until all of the kinetic energy of the blast load has been dissipated through plastic straining in the hinge regions. The specific stages in the formation of the model are described in more detail below.

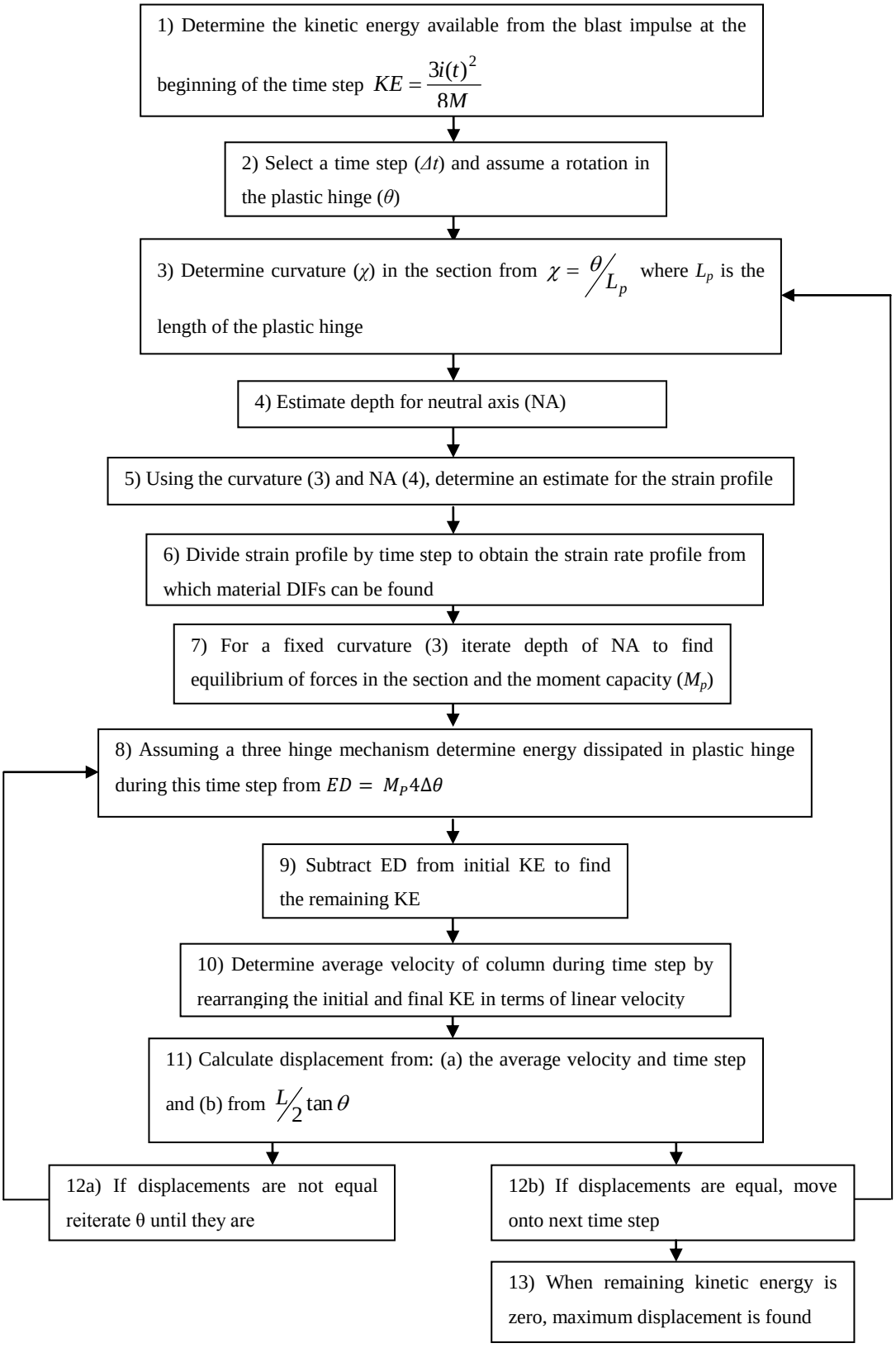

Figure 6.2: Flow diagram showing key stages in implementing new model

6.1.2. Plasticity theory and plastic hinges

Plastic analysis is used widely in design owing to its ability to accurately simplify ultimate limit state (ULS) structural problems and represent material behaviour accurately. Idealised plastic materials are characterised by having an initial elastic slope followed by a ductile plateau where the strain increases with no further increase in load carrying capacity. Mild steel is the most common material exhibiting this behaviour. Flexurally deforming reinforced concrete members have been shown to exhibit similar behaviour in their moment curvature response. If we assume that the materials behave as perfectly plastic and that no strain hardening occurs (an assumption that can be relaxed later in the analysis) then the moment-curvature response of the section will follow the general trend shown in Figure 6.3. This indicates that on reaching the ultimate moment capacity (M_u) the rotation in the plastic hinge increases for a constant moment. It has been shown (Haskett *et al.* 2009) that this rotation is confined to a specific region, forming a plastic hinge which has a finite length, L_P, as indicated in Figure 6.1a. This plastic hinge length is a key assumption employed in the proposed model, although the sensitivity to the chosen value will later be assessed through a parametric study.

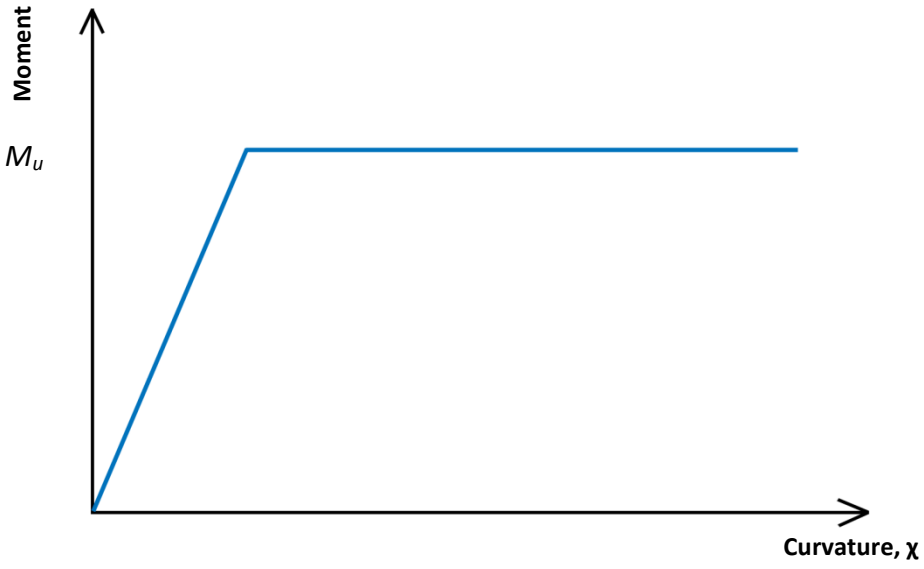

Figure 6.3: Elastic-perfectly plastic moment curvature response for RC member

The curvature in the section (χ) which, as described previously, can be used to find the strain and strain-rate profile in the section and hence the moment capacity, can be found from the hinge rotation (θ) and the plastic hinge length (L_P) through equation 6.9:

$$\chi = \theta / L_P \tag{6.9}$$

Equation 6.9 assumes that the curvature is constant over the length of the hinge. The model also assumes that hinges form from the outset of the analysis which allows the column to be treated as two rigid bodies (Figure 6.1b). This assumption is a necessity of the implementation of the model but given that large displacements are expected in these extreme situations, it is expected to make only a minor difference to the predicted response. Where hinge rotations are small and the curvature in the section is less than the plastic limit (Figure 6.3) then the moment capacity can still be found and used in equation 6.8, although this assumes that straining only occurs in the hinge region. Without this assumption equation 6.9 cannot be used.

6.1.3. Layered sectional analysis

Determining the moment capacity of the member at a given time-step from the curvature calculated using equation 6.9 can be achieved through a layered sectional analysis approach (Wu *et al.*, 2009) Other methods for determining the moment capacity of a section are available but this technique presents a number of advantages including the ease with which the analysis can be carried out using a relatively simple spreadsheet and the ability to easily include strain-rate dependent material properties for each layer of the section. This last point is potentially the most important of the benefits, given that both steel and concrete have been found to exhibit significant strength gains at higher loading rates (Bischoff *et al.* 1991, Fu *et al.* 1991b, Malvar and Ross, 1998).

The layered sectional analysis approach divides the cross section of a member into a number of layers of a finite thickness. Within each layer the stress (σ), strain (ε) and strain-rate ($\dot{\varepsilon}$) are all assumed to be constant for a given time-step, as indicated in Figure 6.4. It is assumed that plane sections remain plane throughout the response.

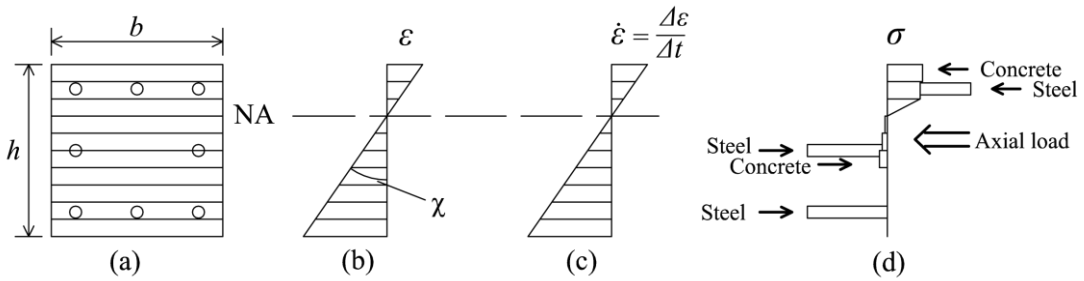

Figure 6.4: (a) Cross-section, (b) Strain profile, (c) Strain-rate profile and (d) Stress profile for a typical RC member in a sectional analysis.

Determining the exact strain-rate dependent moment capacity of a section requires the curvature in the section to be known from equation 4.9 and the depth of the neutral axis (NA) to be found. Keeping the curvature constant the neutral axis depth is iterated until equilibrium of forces is achieved, after which moments can be taken to determine the moment capacity. Strain-rates within each layer are determined simply from the change in strain for a given layer between time-steps divided by the time-step used in the analysis, as indicated in Figure 6.4c. Once the strain-rates are known, strain-rate dependent material strengths can be employed in the analysis as outlined below.

6.1.4. Dynamic increase factors

The strength of concrete and steel have both been shown to be dependent on the rate with which the material is strained. This strain-rate dependency is usually irrelevant in quasi-static loading situations. However, at the rates of loading experienced in blast situations these strength increases become more important and can make a significant impact on the capacity of a section for short duration loads. Research by Soroushian and Obaseki (1986) showed that at strain-rates of 0.05 s^{-1}, which would be typical in earthquake situations and represents a 100,000 times increase compared to a typical quasi-static loading rate, taken by Soroushian and Obaseki (1986) as 5x10-7 s^{-1}, the moment capacity of a RC member could increase by around 25%. In blast situations the rate of straining would be expected to be much higher and hence the increase in moment capacity would be even greater.

Dynamic increase factors (DIFs) were established as a convenient way to describe the increase in strength of materials with increasing strain-rates. A large quantity of research data has been compiled from dynamic tests on concrete to display the strain-

rate dependency of the material to both compressive and tensile loads. These are shown in Figure 6.5 (a) and (b).

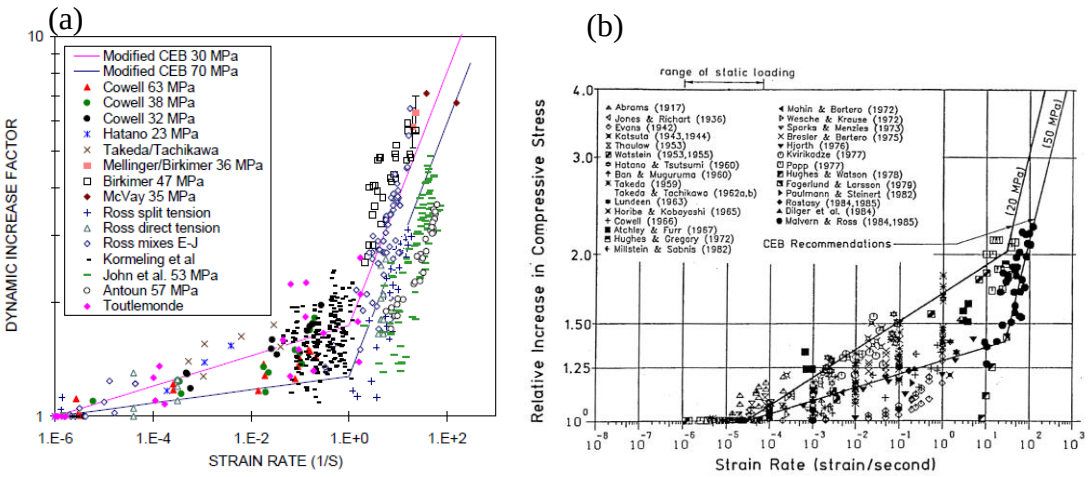

Figure 6.5: DIF for concrete in: (a) Compression (ref) and (b) tension (ref)

The relationship for concrete in tension has been included as research has shown that at high strain-rates, strength increases of up to 200% can be achieved (Malvar and Crawford, 1998). It is therefore proposed in the model that concrete in the tension zone be included in the layered sectional analysis up to a limiting strain of ε_{ft}, which is given by equation 6.10:

$$\varepsilon_{ft} = {f_{ct}}/{E_c} \tag{6.10}$$

where, f_{ct} is the strain-rate dependent strength of concrete, given by equation 6.11 and E_c is the quasi-static value for the concrete's short term Young's modulus. Fu *et al.*, 1991, reported that there was some dispute as to the effect of strain-rates on the Young's modulus of concrete, with some Authors claiming to have shown a small dependency whilst others showed no relationship. For this reason the quasi-static value is used in the current formulation.

The DIF relationships used in the model for concrete in tension and compression are given by equation 6.11 (a) and (b) and 6.12 (a) and (b) respectively. The DIF relationship for concrete in tension is based on the proposals by Malvar and Crawford, 1998:

$$\text{DIF} = \left(\frac{\dot{\varepsilon}}{10^{-6}}\right)^{\delta} \qquad \text{for } \dot{\varepsilon} \leq 1 \text{ s-1} \tag{6.11a}$$

$$\text{DIF} = \beta\left(\frac{\dot{\varepsilon}}{10^{-6}}\right)^{1/3} \qquad \text{for } \dot{\varepsilon} > 1 \text{ s}^{-1} \tag{6.11b}$$

where, $\dot{\varepsilon}$ is the strain-rate, $\log\beta = 6\delta - 2$, $\delta = 1/(1 + 8\,fcs/10)$ and f_{cs} is the static compressive cube strength of the concrete. The compressive DIF relationship is based on the CEB model (CEB, 1988) as reported by Bischoff and Perry, 1991:

$$\text{DIF} = \left(\frac{\dot{\varepsilon}}{30\times10^{-6}}\right)^{1.026\alpha} \qquad \dot{\varepsilon} \leq 30 \text{ s}^{-1} \tag{6.12a}$$

$$\text{DIF} = \gamma(\dot{\varepsilon})^{1/3} \qquad \dot{\varepsilon} > 30 \text{ s}^{-1} \tag{6.12b}$$

where, $\alpha = 1/(5 + 3f_{cs}/4)$ and $\log\gamma = 6.156\alpha - 0.492$.

The DIF relationship for steel used in the model is based on the work of Malvar (1998) who summarised tests carried out on ASTM grade reinforcing steel and proposed the DIF relationships for the yield and ultimate strength of steel shown in equations 6.13. Figure 6.6 shows the relationship for the DIF with increasing strain-rate.

$$\text{DIF} = \left(\frac{\dot{\varepsilon}}{10^{-4}}\right)^{\alpha} \tag{6.13}$$

where, when determining the increase factor for the yield stress, $\alpha = \alpha_{fy}$ and when determining the increase factor for the ultimate stress, $\alpha = \alpha_{fu}$ which are given by equations 6.13a and 6.13b respectively.

$$\alpha_{fy} = 0.074 - 0.04\frac{f_y}{414} \tag{6.13a}$$

$$\alpha_{fu} = 0.019 - 0.009\frac{f_y}{414} \tag{6.13b}$$

where, f_y is the static yield stress of the steel in N/mm^2.

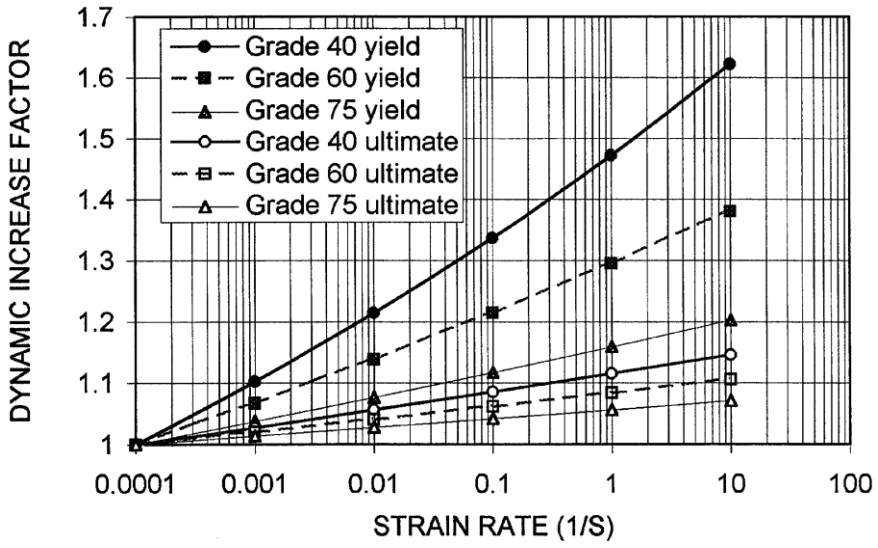

Figure 6.6: DIF for yield and ultimate stress of ASTM A615 reinforcing steel bars (Malvar, 1998)

6.1.5. Determining moment capacity

On determining the dynamic increase factor, the moment capacity can be calculated by iterating the depth of the neutral axis as described in section 6.1.3. The strain profile, based on the assumed depth of neutral axis and curvature allows the stress profile to be determined, assuming quasi-static Young's moduli for the steel and concrete. The force in each layer of concrete is given by equation 6.14:

$$F_{Co} = t_L b f_C(\varepsilon) DIF(\dot{\varepsilon}) \tag{6.14}$$

where t_L is the thickness of the layers in the sectional analysis, b is the width of the layer and $f_C(\varepsilon)$ is the concrete stress. The force in the steel is calculated from equation 6.15:

$$F_{St} = nA_S f_S(\varepsilon) DIF(\dot{\varepsilon}) \tag{6.15}$$

where, n is the number of reinforcing bars in a particular layer, A_S is the cross sectional area of each steel bar and $f_S(\varepsilon)$ is the stress in the steel. Once the steel has yielded the DIF is interpolated between the yield and ultimate dynamic increase factors. As stated previously, it is assumed that the Youngs modulus of both materials are strain-rate independent, therefore the stress-strain relationships employed in the model are those shown in Figure 6.7 (a) for concrete and (b) for steel.

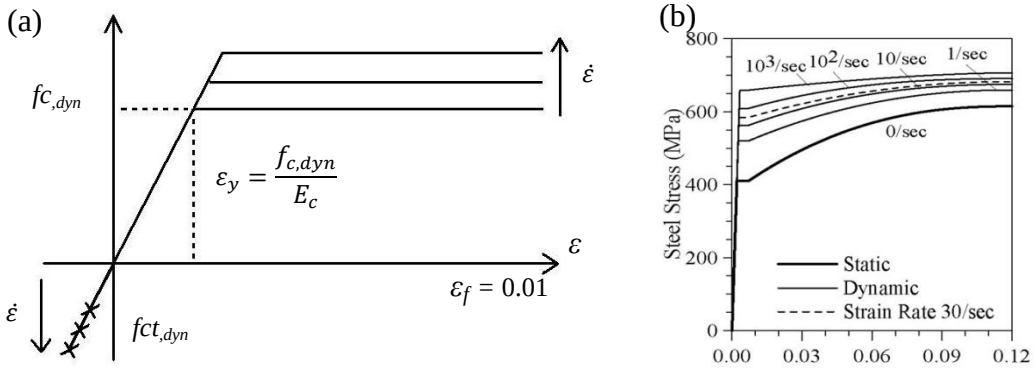

Figure 6.7: Stress strain relationships for (a) concrete and (b) steel with increasing strain-rate

From Figure 6.7 it can be seen that the failure strain of the concrete in compression has been taken as 1%. The value of 1% assumes that the column is wrapped with FRP which effectively confines the concrete (Concrete Society, 2012). To analyse the flexural response of unconfined members a failure strain of 0.0035 would be taken in the analysis. When a layer reaches the failure strain it is deleted from the analysis allowing a softening of the hinge to occur.

The depth of the neutral axis is iterated to obtain equilibrium of forces, as given by equation 6.16:

$$N = \Sigma F_c - \Sigma F_t \tag{6.16}$$

where, N is the axial force applied if the member being considered is a column, ΣF_c is the sum of the compressive forces for each layer and ΣF_t is the sum of the tensile forces for each layer, which can be determined from equations 6.14 and 6.15. In a state of pure bending, N would be set to zero. However, for axially loaded members this is not zero. The general variation of moment capacity with changing axial load is referred to as the *M-N* interaction diagram, which is shown in Figure 6.8.

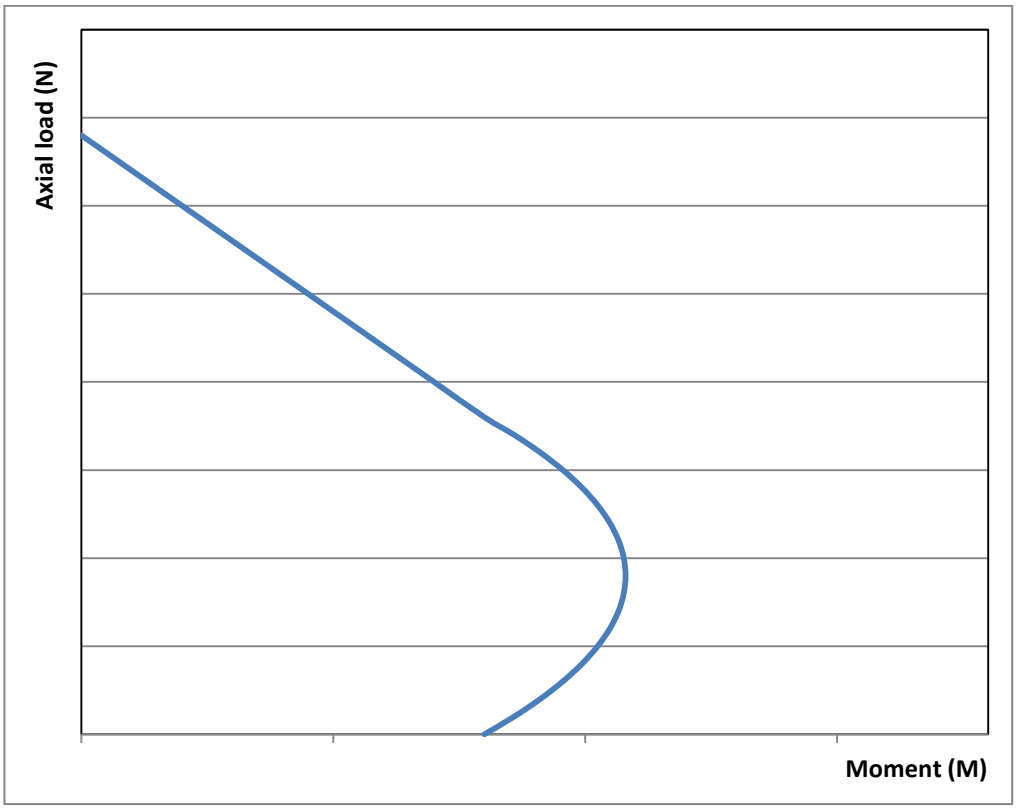

Figure 6.8: Generalised M-N interaction diagram for RC column

A detailed study on the effect of dynamic increase factors on the M-N diagram for an RC column was carried out by Soroushian and Obaseki (1986). A typical strain-rate dependent M-N diagram from this work is shown in Figure 6.9 which clearly indicates the enhancement in the axial strength and moment capacity which might be achieved by including the increase in material strengths due to strain-rate effects.

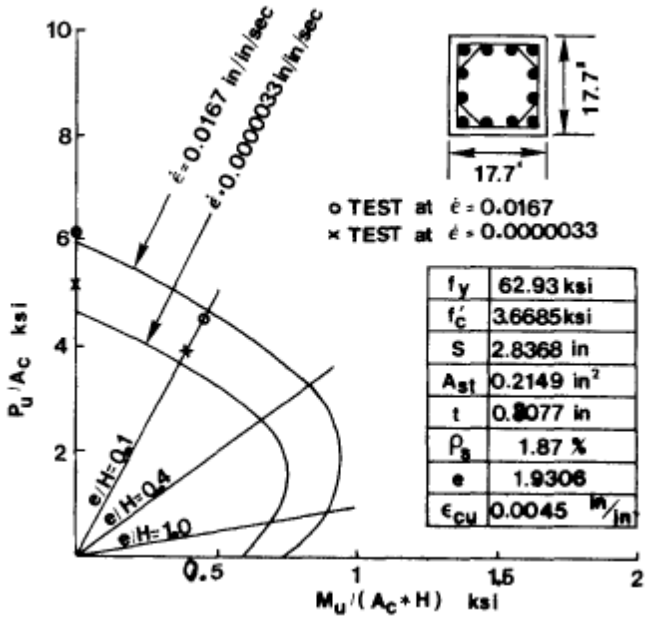

Figure 6.9: Strain-rate dependent moment-axial force interaction diagram for RC column (Soroushian and Obaseki, 1986)

The *M-N* interaction diagram shows that increasing the axial force from a state of pure bending (N = 0) causes the moment capacity of a member to increase initially, before reducing to zero as the axial capacity reaches a maximum. Considering equation 6.8, it can be seen that for a particular level of energy dissipation, increasing the moment capacity, M_p, would reduce the hinge rotation, θ, and hence the displacement predicted by the model.

The effect of the axial force on the response of columns to simulated blast loads was investigated briefly by Rodriguez-Nikl (2006). Two tests were carried out to ascertain the influence of the axial load. It was found that the column with an axial load suffered marginally less damage than the one without. Rodriguez-Nikl therefore suggested that the axial load does have an effect but the effect is relatively minor and tests conducted without an axial load are acceptable as column tests. It is clear that this issue deserves further investigation. A further issue to consider is that blast loads can cause uplift in the floor slabs, therefore relieving the compression load. By neglecting axial load, the solution would represent the worst possible design case (Byfield and Paramasivam, 2014).

6.1.6. Energy dissipation and validation of initial assumptions

By assuming a hinge rotation (θ) at a particular time-step, the moment capacity of the section and the energy dissipated can be determined as discussed previously. However, to ensure the correct solution has been determined it is necessary to validate the assumption for the hinge rotation at each time-step based upon conservation of energy. A novel method has therefore been devised to carry out this validation using the assumptions that have already been discussed.

The assumed hinge rotation is validated by determining the mid-span displacement of the member from the assumed hinge rotation and comparing it with the displacement during the time-step due to the change in kinetic energy of the member.

From the assumption of rigid body rotations the change in mid-span displacement during the n^{th} time-step can firstly be calculated from simple trigonometry as:

$$\Delta\delta_\theta = \frac{L}{2}\tan(\theta_n) - \frac{L}{2}\tan(\theta_{n-1}) \tag{6.17}$$

where L is the height of the member. Determining the displacement from the motion of the member, as kinetic energy is dissipated, requires a slightly more involved analysis.

It was discussed previously that the impulse from the blast causes the member to acquire kinetic energy, the acquisition of which will vary with time depending on the duration of the applied load. It is usually assumed that the pressure from the blast increases rapidly to the peak overpressure before decaying exponentially with time (Cormie *et al*., 2009), Figure 6.10a. From this relationship the time varying impulse can be found Figure 6.10b, from which the kinetic energy imparted on the member at the beginning of the time-step can be determined from equation 6.7. The initial kinetic energy (KE_{n-1}) at the start of the time-step can then be rearranged in terms of the rotational velocity ($\dot{\theta}$) from equation 6.6 which can in turn be rearranged into the linear velocity of the mid-point (v_{n-1}) of the member from equation 6.18:

$$v_{n-1} = \frac{L}{2}\dot{\theta} \tag{6.18}$$

During the time-step, kinetic energy is dissipated through plastic straining in the hinge regions. The kinetic energy at the end of each time-step (KE_n) is then given by:

$$KE_n = KE_{n-1} - \Delta ED_n \tag{6.19}$$

where subscripts *n-1* and *n* refer to the beginning and end of the time-step and ΔED_n is the energy dissipated during the time-step by the plastic hinges. The final kinetic energy at the end of the time-step can then once again be rearranged in terms of the member's mid-height linear velocity (v_n). Assuming that suitably small time-steps are chosen, the

average velocity of the mid-point (v_{av}) during the time-step can be approximated by equation (6.20):

$$v_{av} = \frac{v_{n-1} + v_n}{2} \tag{6.20}$$

From this, the change in displacement during the time-step can be calculated:

$$\Delta\delta_v = v_{av}\Delta t \tag{6.21}$$

It is important at this stage to recognise that the initial assumption regarding the formation of a three hinge mechanism allows the above prediction of the displacement to be made during the time-step using rigid body dynamics.

If the correct value for the hinge rotation was assumed then the change in displacement determined from equation (6.17) will be equal to that determined from equation (6.21). If they are not equal then the initial assumption for the hinge rotation must be iterated which will, in turn, require the neutral axis to be iterated to find the plastic moment capacity. By using this approach to validate the assumed hinge rotation, the accuracy of the strain-rate profile which has been used in the analysis can be confirmed, a key feature of the proposed model.

The process outlined above is subsequently repeated for additional time-steps until the kinetic energy of the column is zero. At the beginning of a given time-step the kinetic energy is taken as the final kinetic energy from the previous step combined with any additional kinetic energy from the blast impulse that is acquired by the member. The peak displacement of the member is finally determined, when the kinetic energy of the member reaches zero, by summing the displacements from each time-step. The time for the member to reach its peak displacement can also be determined by summing the time-steps.

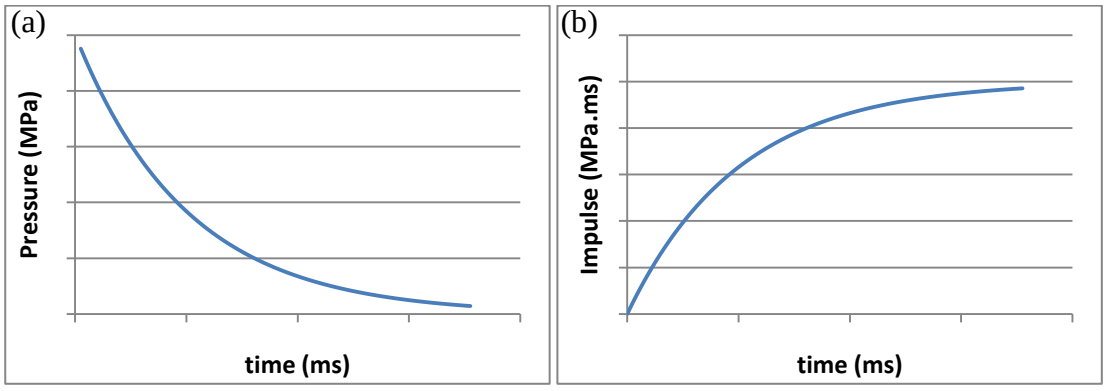

Figure 6.10: (a) Variation in blast pressure with time and (b) Variation in impulse with time

6.1.7. Results

There is a lack of publically available, reliable and useful test data reporting accurately the peak displacement of flexurally deforming RC members subject to blast loads owing to the difficulties associated with testing in this field. Rodriguez-Nikl (2006) provides the most useful test data via simulated blast tests carried out at the University of California in San Diego (UCSD). Simulated blast tests give engineers the opportunity to subject specimens to realistic blast loads through the use of high velocity hydraulic rams whilst also being able to accurately record data through high speed cameras as the member is not hidden in a fire ball. Of the tests carried out by Rodriguez-Nikl, only two specimens, both wrapped with FRP, displayed a true flexural response and are thus useful for comparison with the developed model. Full details of test 6 can be found in Rodriguez-Nikl (2006) and test 10 in Hegemier *et al.* (2007), where the test number refers to the referencing system used by Rodriguez-Nikl.

Both of these test specimens were rotationally fixed at the supports and had cross-sectional dimensions of 356×356 mm and a clear height of 3227 mm with a concrete cylinder strength of 45 N/mm^2. Longitudinal reinforcement was provided through 8 #8 (25 mm) ASTM A615 grade 60 longitudinal steel bars, and transverse reinforcement through #3 (10 mm) bars at 324 mm spacing. Clear cover was 38 mm. Externally applied CFRP transverse reinforcement had a tensile modulus of elasticity and rupture strength of 89 kN/mm^2 and 1544 N/mm^2 respectively. Test 6 employed two layers of Carbon FRP (CFRP) and Test 10 used six layers. In both cases, the CFRP wrap was sufficient to prevent shear failure, leading to the formation of plastic hinges, as the model assumes. A slight modification is required to the impulse given by Rodriguez-Nikl (2006) to take into account the different assumed deflected shapes. Rodriguez-Nikl (2006) presented a method for converting measured simulated blast pressures to impulses which assumed an Euler deflected shape for a fixed beam. However, in keeping with the theory presented in the current chapter this was modified to account for the assumed linear shape.

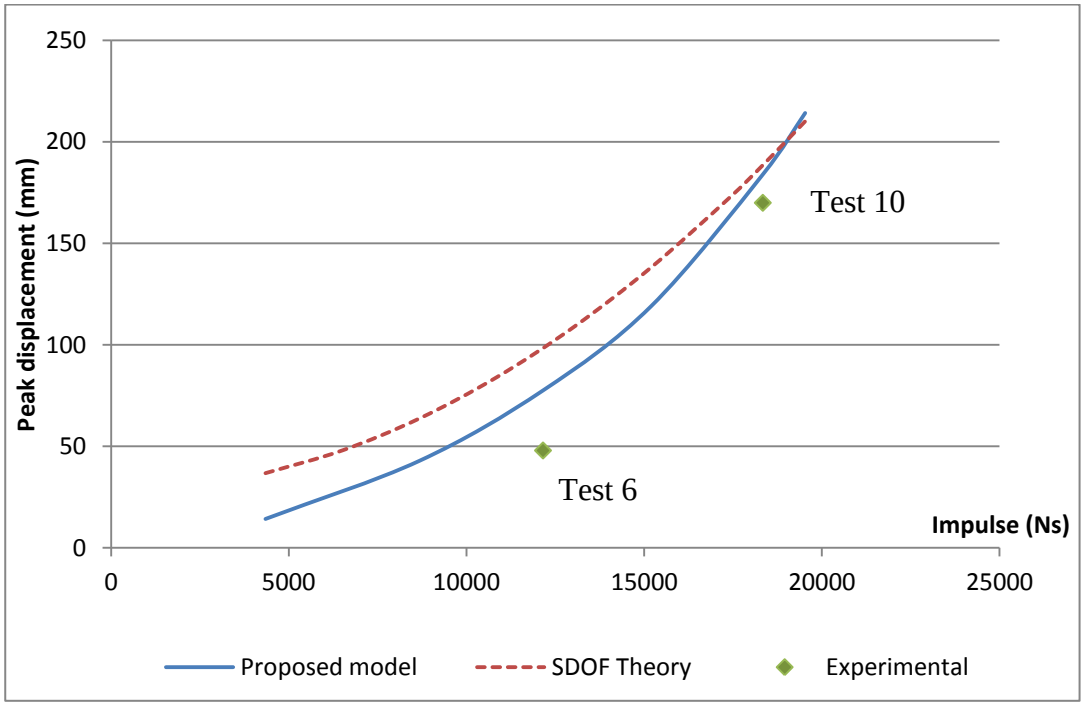

Figure 6.11: Graph showing the model predictions compared with a SDOF model (Cormie *et al.*, 2009) and experimental data (Rodriguez-Nikl, 2006 and Hegemier *et al.*, 2007)

It can be seen from Figure 6.11 that the proposed model provides a conservative over-prediction for the peak displacement of the test results. However the proposed model shows an improvement over the equivalent SDOF method, which is based on an elasto-plastic resistance function. The percentage error of the prediction of the higher impulse test (Test 10) is approximately 8% whereas the prediction for the lower impulse test (Test 6) is less accurate (around 60% greater than the measured result). It can also be seen that the trend from the proposed plasticity model better replicates the experimental data than the SDOF model, although it is clear that more data is required. Figure 6.11 also appears to indicate that the SDOF theory does not tend to zero. However, this is purely a function of using the elastic-plastic relationship which includes a predetermined elastic portion. In reality, for low impulse blasts, this elastic portion would be included differently (Cormie *et al.*, 2009).

It was expected that the proposed model would over-predict the response due to the assumption that all energy delivered from the simulated blast event is dissipated as strain energy. A future development of this model would be to ascertain the levels of energy that are dissipated in additional modes, such as micro-crack growth or concrete fragmentation for example.

6.1.8. Comparison with SDOF

Figure 6.11 indicates that the SDOF model, displays lower accuracy than the new model developed in this chapter. The predictions for the SDOF approach are based on the steps outlined in Cormie *et al.* (2009) which are derived for an elastic-perfectly plastic resistance function based on Eurocode 2. Alternative predictions for the peak displacement of test 10 were also derived using the SDOF model by Rodriguez-Nikl *et al.* (2009) using alternative resistance functions. The SDOF predictions produced by Rodriguez-Nikl (2009) used both an elastic-perfectly plastic (e/pp) and an elastic-plastic (e/p) resistance function. The elastic-plastic resistance function includes both strain-hardening and compression membrane effects which the elastic-perfectly plastic resistance function does not. Figure 6.12 shows the comparison between the experimental data for test 10, which had a peak displacement of 170 mm, three SDOF models with different resistance functions and the plasticity model described in the current chapter. It can be seen that some variation exists in the predicted peak displacement for test 10 when using the different resistance functions in the SDOF model. The difference between the predictions using the elastic-plastic and elastic-perfectly plastic resistance functions is around 23% (compared to one another). It can be seen that the idealised elastic-perfectly plastic (e/pp) SDOF prediction is the most accurate, despite not being the most realistic model of behaviour due to strain-hardening and compression membrane effects being neglected which underlines one of the concerns of the SDOF method. The new plasticity model presented in the current chapter is shown to be comparable to the SDOF predictions but avoids the necessity of arbitrarily selecting a resistance function.

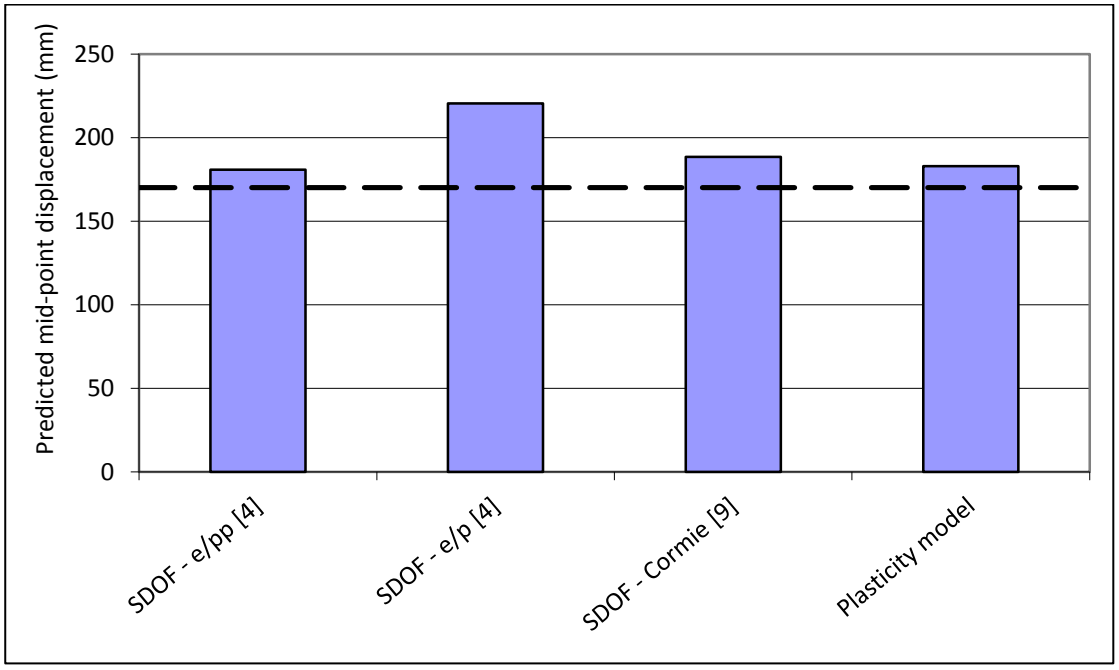

Figure 6.12: Comparison of predicted peak displacement of test 10 (dashed line, Hegemier *et al.*, 2009) with the three alternative SDOF predictions (Rodriguez-Nikl, 2009, and Cormie *et al.*, 2009) and the prediction from the new model

6.1.9. Effect of plastic hinge length

As described previously, the developed model requires the length of the plastic hinge to be estimated. For the purpose of the results shown in Figure 6.11 the plastic hinge length was taken as 0.75*h*, where *h* is the depth of the member. This value was based upon that used by Wu *et al.* (2009).

To investigate the sensitivity of this assumption a simple parametric study was undertaken to vary the plastic hinge length over a range and ascertain the effect this has on the predicted peak displacement. Figure 6.13 shows the effect on the predicted peak displacement of varying the hinge length between 0.65*h* and 0.85*h* (± 13.3% from 0.75h). This indicates that, over this range, the variation in the predicted peak displacement is just ± 1.9%. This low variation suggests that varying the plastic hinge length over a realistic range has a relatively small effect on the predictions.

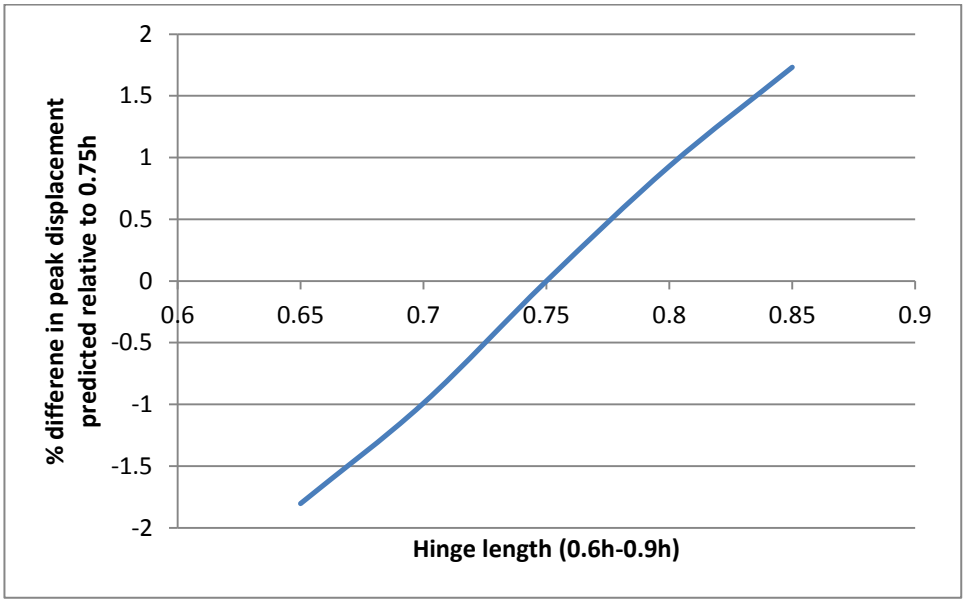

Figure 6.13: Effect of varying the plastic hinge length of the prediction for the peak displacement

6.1.10. Discussion

It can be seen from Figure 6.11 that the new model shows an improvement in predicting the peak displacement of flexurally deforming RC columns wrapped transversely with FRP over the SDOF model. Further comparison with alternative SDOF resistance functions (Figure 6.12) is also favourable for the new model. It is apparent from this figure that the selection of the resistance function has a significant influence on the prediction for the peak displacement using the SDOF approach.

The primary benefits of the new plasticity model are that it:

- Provides a method for accurately determining and implementing strain-rate effects in the analysis procedure
- Avoids the need to arbitrarily select a resistance function

It was discussed previously that the accuracy of predicting the higher impulse test, test 10 was greater than predicting the lower impulse test, test 6 (8% error compared to 60%). It is likely that this increase in the error is due to only considering straining in discrete plastic hinge regions. For large displacements the effect of this assumption is lessened but where the elastic portion of the response is more significant (when displacements are small) the influence will be greater. A plasticity model developed for impact situations by Jones (1989) to analyse the response of ductile structures suggested that when the ratio of the total strain energy to elastic strain energy was greater than 10

a purely plastic approach could be accurate to within 10%. It is therefore considered that a similar ratio would be applicable in the situations outlined in this Chapter. It is also stated in the UFC guidelines (2008) that where large displacements are expected the elastic and elasto-plastic ranges of response can be ignored and only the plastic behaviour need be considered.

The main assumptions of the proposed model are that plastic hinges have formed simultaneously from the outset of the deformation; that all of the supplied energy is converted to plastic strain energy in the hinges and that shear failure does not occur. As the model is primarily intended to analyse structures with large deformations, neglecting the elastic and elasto-plastic ranges of response is likely to be acceptable. The assumption regarding all the energy being dissipated in the plastic hinges is likely to be the biggest source of error in the model with additional energy dissipation modes such as the creation of new surface area in micro-crack growth, heat and sound also contributing to the behaviour.

The primary advantage of the proposed plasticity model over the equivalent SDOF method is the ease and accuracy in calculating strain-rates in the materials and the ability to directly apply these in the analysis, throughout the response period of the structure. It was alluded to by El-Dakhakhni *et al.* (2009) that no simple method exists for accurately calculating the strain-rates. This led Cormie *et al*. (2009) to suggest using constant values that are known to be conservative. The incremental approach of the current model overcomes this problem and allows accurate strain-rates to be determined relatively simply. A comparison between the moment capacity predicted using constant DIFs (as recommended in Cormie *et al.*, 2009) and using the model outlined above, where accurately determined variable strain-rates are used to find the actual DIFs, is shown for test 10 (Hegemier *et al.*, 2009) in Figure 6.14. These are also shown compared against the prediction for the quasi-static moment capacity. From this figure the effect that the strain-rates have on increasing the moment capacity is clear and the potential advantage of including a more accurate representation of the material's strength is apparent.

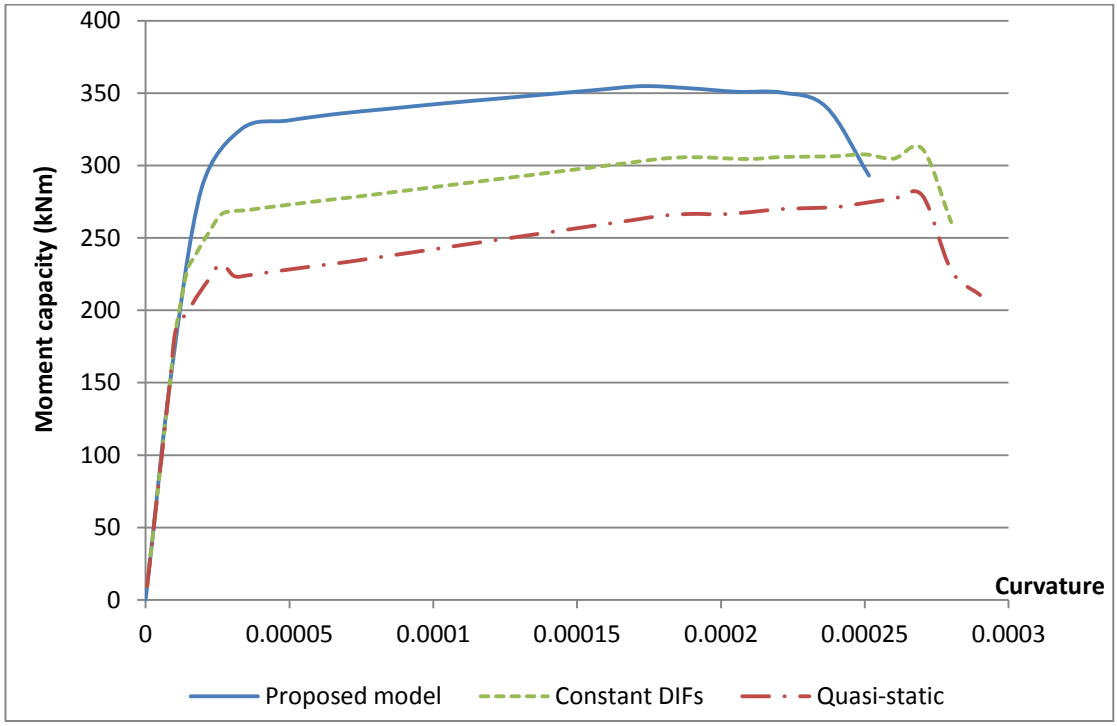

Figure 6.14: Comparison of moment-curvature response including and not including strain-rate effects for test 10 Hegemier *et al.* (2009)

6.2. Impact response of RC members

The model outlined in section 6.1 to predict the peak displacement of blast loaded members can be extended to predict the peak displacement of impact loaded members with a few modifications which reflect the different loading conditions.

The major benefit of the proposed model is the use of an energy based approach, assuming that the energy from the blast is dissipated through plastic straining in the hinge regions. This assumption, and the use of an iterative procedure, has made it possible to accurately determine strain-rates and predict the peak displacement to a reasonable accuracy, which in some cases was shown to be better than alternative approaches (Figure 6.11).

It was discussed that the model implicitly assumes conservation of energy which leads to an over prediction in the peak displacements. In reality some of the impact energy will be lost through other mechanisms of energy dissipation. In impact situations it has been shown that anywhere up to 50% of the impact kinetic energy can be lost (Kishi *et al.*, 2002; Tachibana *et al.*, 2010). The sources of these losses are difficult to quantify, with local crushing effects, heat and sound likely to contribute, as discussed by Gilardi and Sharf (2002).

Outlined below is a description of how the model described above for blast loading can be extended to predict the peak displacement of impact loaded RC members. This is followed by a discussion on methods to improve the accuracy of the predicted results which incorporates some of the work presented in Chapter 4.

6.2.1. Impact model outline

The model for impact situations follows the same principles outlined previously for blast situations. It is again assumed that in flexurally deforming RC members, energy is dissipated through straining in the plastic hinge regions. The initial kinetic energy which is dissipated as strain energy in the plastic hinge regions is given by equation 6.22.

$$KE_i = {}^1/_2 M_m V_{imp}^2 \tag{6.22}$$

where, M_m is the impact mass and V_{imp} is the velocity of the mass at the instant of impact.

It is once again assumed that the member undergoes a small displacement over a given time-step. Assuming rigid linear behaviour (Figure 6.15) it is possible to convert this displacement to a rotation, θ, in the hinge region. The hinge rotation can then be converted to a curvature by assuming a fixed length for the hinge region. The assumption for the plastic hinge length is the same as outlined previously for the blast model, which was discussed in detail in section 6.1.9.

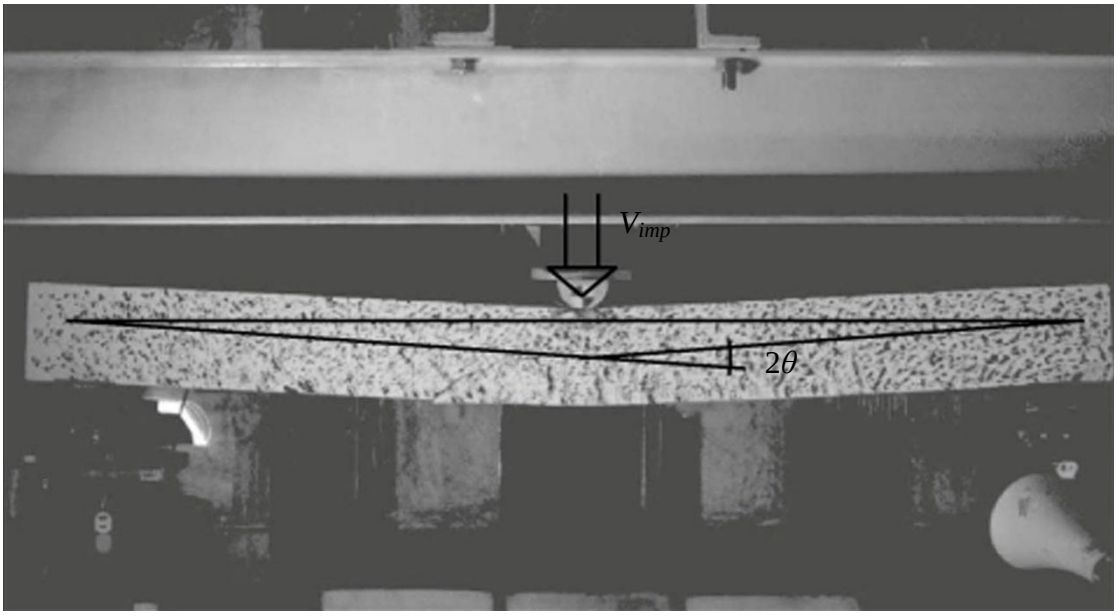

Figure 6.15: Linear deforming shape assumption

Upon knowing the curvature in the section, the moment capacity can be found using a standard method such as sectional analysis, as described in section 6.1.5. The energy dissipated (*ED*) during a particular time-step, *n*, for a simply supported member is then given as:

$$ED_n = M_P(\dot{\varepsilon}).2\Delta\theta \tag{6.23}$$

Where, $M_p(\dot{\varepsilon})$ is the strain-rate dependent moment capacity for the given curvature. It is assumed in this case that the member is pin ended (which reflects the test setup described in Chapter 5), therefore, the change in rotation, $\Delta\theta$, is multiplied by two. For cases of fixed end beams this would be replaced by a four.

The final kinetic energy (KE_n) of the impacting mass at the end of the time-step, *n*, is then given simply as

$$KE_n = KE_{n-1} - ED_n \tag{6.24}$$

where subscripts *n-1* and *n* refer to the beginning and end of the time-step and ED_n is the energy dissipated during the time-step.

The velocity ($V_{imp,n}$) of the impacting mass at the end of the time-step can then be found by rearranging the equation for kinetic energy which is the final kinetic energy given by equation 6.24.

$$V_{imp,n} = \sqrt{\frac{2KE_n}{M_{imp}}} \tag{6.25}$$

A check to ensure the correct initial assumption for the rotation can then, once again, be performed. Assuming that the deceleration of the impacting mass can be considered linear between time-steps the average velocity ($V_{imp,av}$) of the impacting mass can be found simply as:

$$V_{imp,av} = \frac{V_{n-1}+V_n}{2} \tag{6.26}$$

The change in displacement is then given simply as $V_{av}\Delta t$, from which the rotation can be calculated assuming rigid body rotations. If the initially assumed rotation is not equal to the rotation predicted from the average velocity then the initial value is iterated until the correct solution is found.

The time to reach peak displacement is typically in the order of 10-30 ms, depending on the magnitude of the impact, and a time-step in the region of 1/50 of this total response time has been found suitable for achieving accurate results.

As stated previously, use of this concept provides a convenient method for determining the strain-rates and applying them directly in the analysis through material DIFs.

6.2.2. Discussion and limitations of proposed model

Outlined above is the development of a simple plastic hinge model to predict the peak displacement of RC members subject to impact loads. Results showing the predictions for the peak displacement using the method are presented in Chapter 7 for flexural tests carried out as part of this research project.

A consequence of extending the proposed model developed for blast situations to impact situations is that they both suffer from many of the same limitations. Perhaps the most important of these limitations is the assumption of conservation of energy between kinetic and strain energy in the plastic hinges. In reality it is likely that energy is dissipated in a range of alternative modes that do not contribute to the overall displacement of the member. This was alluded to by Kishi *et al.* (2002) who stated that only between 40-60% of the energy supplied is used in causing the member to displace. The rest of the energy is lost in other modes which are difficult to quantify. Based on the work outlined in Chapter 4, crushing in the contact zone is perhaps the easiest of these modes to quantify, although including this through an elastic term suggests it is later recoverable which is not the case in reality.

As outlined in Chapter 4, the behaviour of the contact zone is difficult to predict due to the complex stress state that can arise and the variation in material properties at high strain-rates. Fully modelling this complex behaviour falls outside the scope of the current project. However, consideration of the velocity-time relationships for both the impacting mass and the member provides the potential for a simplified method to estimate this form of energy dissipation.

A typical velocity-time relationship predicted from the work in Chapter 4 is shown in Figure 6.16. To estimate simply the energy that is lost through crushing it is assumed that while the member's velocity is lower than that of the impacting mass, then crushing is occurring. Upon the impacting mass and the member attaining the same velocity ($V_{contact}$) it is then assumed that crushing has ceased and conjoined motion occurs, although as discussed previously in Chapter 4, due to the assumptions of linear elasticity, this does not occur in the model. The energy that is lost in crushing is then simply given as:

$$ED_{crush} = \frac{1}{2} M_m V_{imp}^2 - \frac{1}{2} M_{imp} V_{contact}^2 \quad (6.27)$$

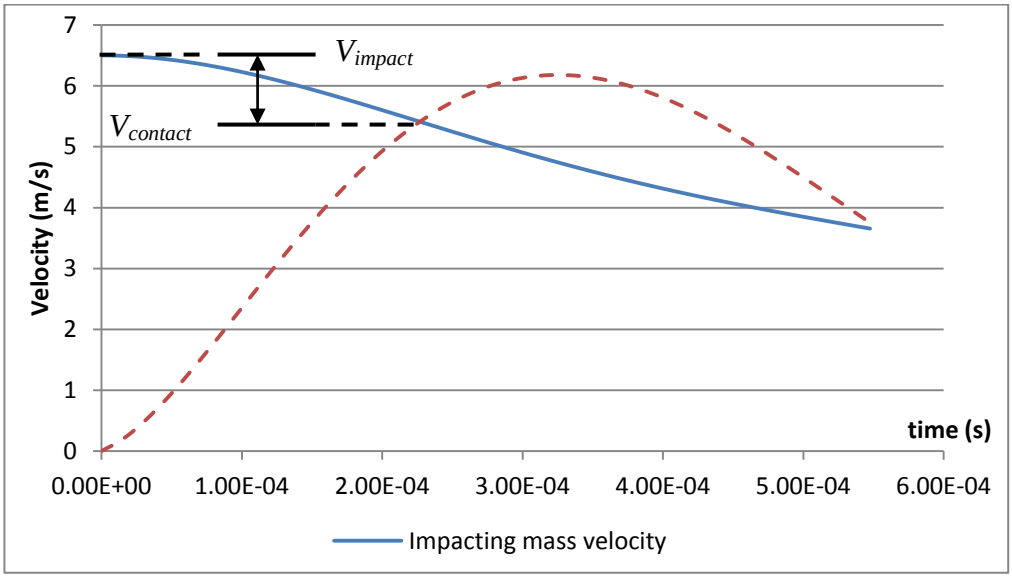

Figure 6.16: Typical velocity-time relationship for impact test predicted from theoretical work in Chapter 4

For the example graph shown in Figure 6.16, where the impact mass was 150 kg, the energy that is lost through crushing is in the order of 30% of the total energy supplied, suggesting that this mode is important to consider when improving the accuracy of the energy based approach outlined above. Due to the complicated behaviour of the contact zone, the use of simplified relationships is a potential limitation of using this method to predict the energy lost. However, it does provide a useful method for initially estimating this loss.

As the contact velocity is readily determinable from the model outlined in Chapter 4, a further simplification of the above model is to assume that $V_{contact}$ is the actual velocity at impact. This is used to determine the kinetic energy which is dissipated in the plastic hinges. This assumes that the energy lost through crushing is non-recoverable which is likely to be a realistic assumption. A small modification might be required to include the small displacement and kinetic energy acquired by the member in reaching the contact velocity. This could be determined quite simply from the model and would be relatively small given that the majority of deformation during this period is through crushing.

A further point of interest is how the above discussion on the energy dissipated in the contact zone could explain the differences in the peak displacement seen for flexurally deforming specimens tested with different mass and velocity ratios but identical kinetic energies. Shown in Figure 6.17 are the results of a series of impact tests on standard,

flexurally deforming, RC beams carried out by Tachibana *et al.* (2010). These results indicate that for identical kinetic energy impact events a lower velocity impact leads to higher peak displacements.

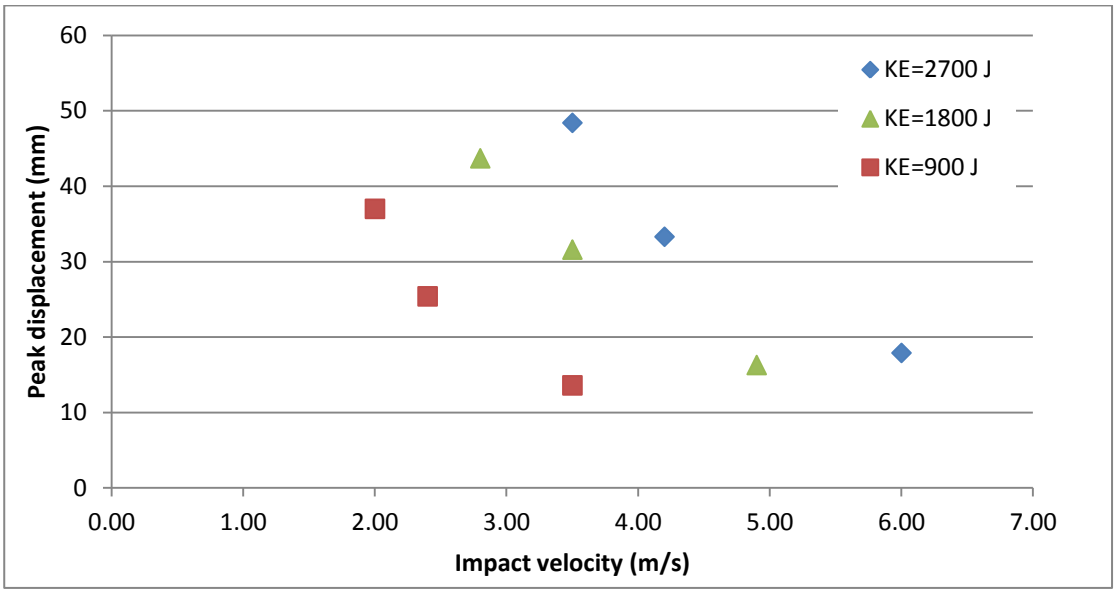

Figure 6.17: Relationship between peak displacement and impact velocity (Tachibana *et al.*, 2010)

Tachibana *et al.* (2010) were unable to provide a theoretical basis for this observed behaviour. However, the above discussion on the energy dissipated in the contact zone presents a possible explanation of this behaviour. By considering a simple parametric study on two impacts, one for a high velocity, low mass and the other for a low velocity, high mass it is shown that for higher velocity impacts more energy is dissipated in the contact zone. Considering the impact of a 150 kg mass at 6.3 m/s (Figure 6.18) and a 350 kg mass at 4.2 m/s (Figure 6.19), where the kinetic energy is 3000 joules for both, it can be shown that for the higher velocity impact approximately 31% of the energy is lost in the contact zone whereas in the lower velocity impact only 16% is lost (as determined from equation 6.27).

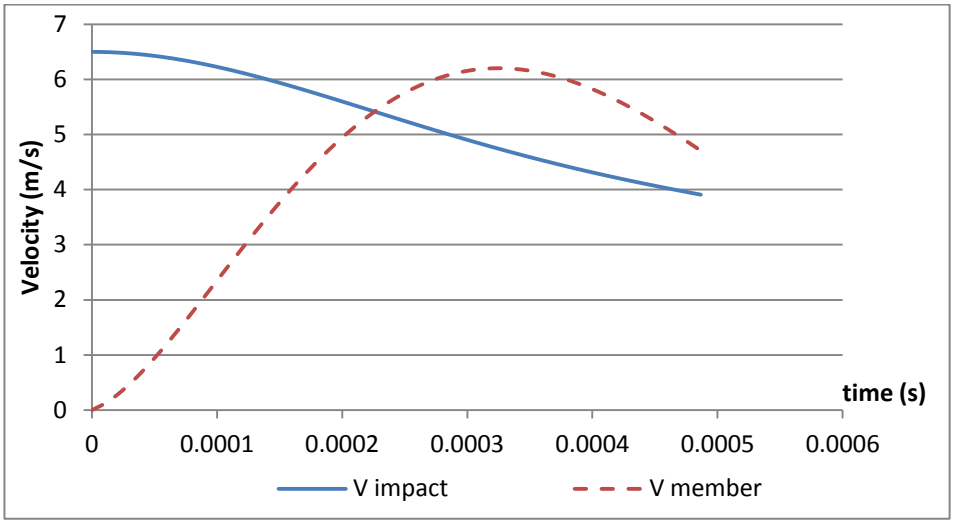

Figure 6.18: Velocity-time graph for impact of mass weighing 150 kg, (member properties are given in section 4.3)

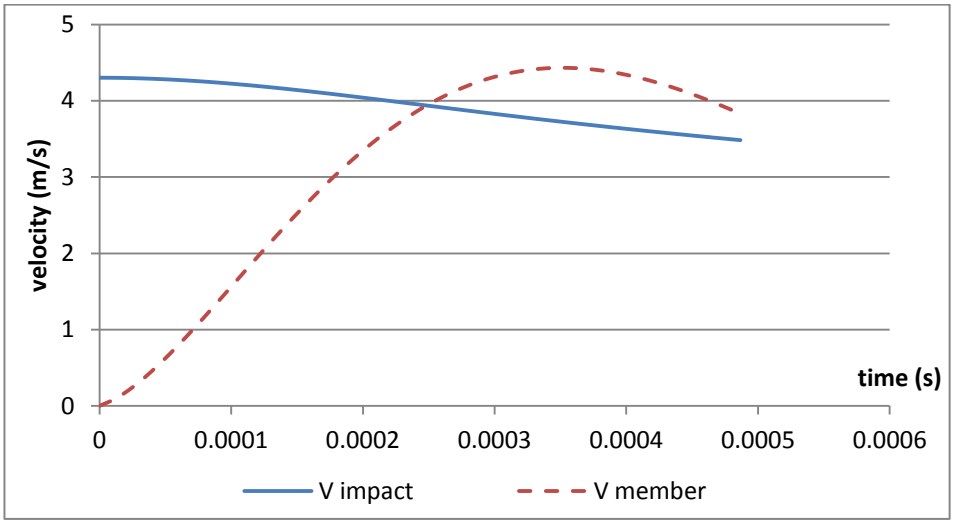

Figure 6.19: Velocity-time graph for impact of mass weighing 350 kg, (member properties are given in section 4.3)

These results suggest that for the higher velocity, lower mass impact more energy is dissipated in the contact zone which leaves less for deforming the member. Further to this it is apparent that strain-rates in the higher velocity impact test will be greater, resulting in an enhanced initial moment capacity and more energy dissipation for a given hinge rotation which again will reduce the deflection.

6.3. Conclusion

This chapter has presented a new model for predicting the peak displacement of a blast loaded RC member. It was also shown how this model could be extended to impact situations with only minor modifications.

The proposed model considers the conservation of energy in the system over a series of small time increments. This has a number of advantages, most important of which is the ability to accurately calculate and include material dynamic strength increases due to high strain-rates. It was also shown to be more accurate, in some cases, for predicting the peak displacement of blast loaded members compared to the more commonly used SDOF approach (Figure 6.11). The model inherently assumes that brittle shear failure is prevented, either through sufficient steel shear reinforcement or through additional FRP transverse reinforcement.

The assumption of conservation of energy is perhaps the biggest drawback of the proposed model. Due to the complexity of the response in both blast and impact situations, a full analysis of all modes of energy loss fall outside the scope of this work. However, to this end it was shown in section 6.2.2 that inclusion of the contact zone behaviour could provide a method for approximating some of the energy lost in an impact event. It was shown that the energy that was lost in the contact zone is greater for higher velocity impacts and can be as much as 30% of the total supplied energy.

Future work in this area should look at providing additional experimental data to validate the proposed model for blast situations whilst also focusing on understanding in more detail the various modes through which energy is lost in the system.

The following chapter demonstrates how even a small amount of additional FRP can have a significant influence on the behaviour of a member by preventing a brittle shear failure and allowing a flexural deformation to occur.

7. Strengthening structurally deficient members

Where analysis shows an existing structure to possess insufficient capacity to resist the design load from either an impact or explosion then two options are open to designers. Either the structure can be demolished and rebuilt or it can be structurally retrofitted. Economically it is almost always more desirable to retrofit a structure than to demolish it. To this end a number of methods have been employed to strengthen structures in a number of different ways. Most recently fibre reinforced polymers have emerged as the preferred method for strengthening. This chapter considers the application of this technology to strengthen structures predominantly against impact loads, for which tests were carried out as part of this project. The chapter also briefly discusses situations where the same technology has been successfully applied to retrofitting columns against blast loads.

7.1. Introduction

Fibre reinforced polymers (FRPs) have been used increasingly to strengthen RC structures in a number of ways including increasing the load bearing capacity of columns and the flexural or shear capacity of beams. This is largely due to their superior strength to weight properties when compared with alternative strengthening techniques such as steel jacketing. A vast amount of research has been carried out into the application of FRPs to improve the resistance of structures to quasi-static and seismic loads (TR55, 2012). To date, the application of these materials to strengthen against impulsive situations, such as blast and impact, is limited due both to a lack of understanding of the full dynamic behaviour of members subjected to these loads and a lack of test data. Where research has been conducted in retrofitting RC columns to withstand impulsive loads the advantages of these types of system have been demonstrated categorically in terms of preventing brittle shear failures and confining the concrete, which maintains the integrity of a section (Rodriguez-Nikl *et al.*, 2009).

The current chapter outlines how this technology has developed over the years for a range of applications. Following this is the main part of the chapter where the results of two experimental programs undertaken as part of this research project are presented. The first investigated increasing the shear strength of shear critical members through transversely applied CFRP strips. It was highlighted in the literature review and demonstrated from the tests in Chapter 5, that under high-rate loading, RC columns

have a propensity to fail in catastrophic shear. Therefore the application of FRPs to prevent shear failure is important with respect to the current project. Following this are the results of a separate experimental program which looked at the increase in the flexural capacity that could be achieved, again through transversely applied CFRP wraps. Transverse CFRP is not usually applied for this purpose; however, the results demonstrate that a significant improvement in the performance of an impacted member can be achieved. The final part of the chapter briefly discusses research that has been carried out in the application of this technology to blast situations.

7.2. Background

7.2.1. Structural applications (Teng *et al.*, 2002)

The origins of retrofitting structurally deficient RC members with fibre reinforced polymers (FRPs) can be traced to the mid 1980's at the Swiss Federal Laboratory for Materials Testing and Research (EMPA). The first application of this technology was to strengthen RC beams in flexure. However, over time the advantages of FRP retrofit systems to strengthen members in other ways developed, including shear strengthening of beams. It was found that if only the flexural capacity of a beam was increased then a brittle shear failure may occur rather than the desirable flexural mode. For beams, shear strengthening is commonly achieved through either side bonded strips or U wraps (Figure 7.1). Due to access it is usually not possible to provide a full wrap for beams; however, in rare cases where this is possible it is by far the most effective method (TR55, 2012).

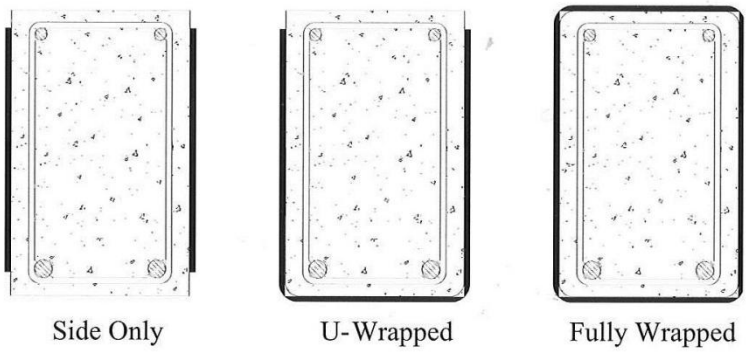

Figure 7.1: Shear strengthening options for RC beams: (a) Side plating, (b) U-jacketing, (c) Fully wrapped (TR55, 2004)

RC columns have in the past been strengthened to increase their axial load bearing capacity and their seismic performance. In both cases this is usually achieved by providing a full and continuous wrap of fibres transversely around the member. For axial strengthening the purpose of this is to provide confinement to the concrete. In seismic applications the primary purpose is to increase the ductility whilst also increasing the shear strength. It is this application of FRPs which has been employed by some researchers to strengthen columns to withstand transverse blast loads (Buchan and Chen, 2007). However, the application of this technology to impact situations has not been as comprehensively researched. The current chapter aims to address this issue.

7.2.2. Materials

Fibre reinforced polymers have been adopted for strengthening applications primarily due to their superior strength-to-weight ratios and corrosion resistance when compared to steel jackets which were used previously. This has a number of advantages, the most important of which is the easier installation due to the lightness and flexibility of the materials, and their durability which can lead to long-term maintenance cost savings.

There are three main fibre types used in structural retrofits. The most common are carbon (CFRP) and glass (GFRP), but aramid (AFRP) is also used in some instances due to its high toughness. Carbon is both the strongest and the stiffest of the three.

In order to strengthen a member, the fibres must be bonded effectively to the substrate. The fibres themselves are normally supplied either as a plate, where the fibres are already impregnated with resin and set, or as a cloth which is bonded to a member through a process known as wet lay-up. The wet lay-up approach is usually more common when wrapping columns as the cloth itself is flexible before the resin is applied which makes application easier and more efficient. In most cases the fibres are orientated uni-directionally so the properties are highly orthotropic, which must be considered when designing a retrofit system. For the applications considered in the current chapter the fibres are orientated in the transverse direction. It is this orientation which is most commonly used when shear strengthening members.

7.3. Experimental testing to increase the shear capacity

In order to demonstrate the benefits of shear strengthening an RC member to resist impact loads, a range of tests were carried out on retrofitted and unretrofitted RC

columns which are discussed in detail below. This section details the results of tests investigating the benefits of retrofitting in terms of increasing the shear capacity while Section 7.4 discusses the enhancement to the flexural capacity that can also be achieved.

7.3.1. Specimen description

Four specimens were tested in total as part of series B, with the dimensions, shear and bending capacity of the unretrofitted specimens identical to specimens 1-4 (series A) which were discussed in Chapter 5. This allows comparison to be made to these earlier tests where appropriate. The retrofitting consisted of strips of CFRP transversely wrapped fully around the member, which is discussed in greater detail below. A summary of the test program is presented in Table 7.1 and the concrete compressive strengths determined from cube tests at the time of testing are shown in Table 5.1.

Table 7.1: Test matrix for retrofitted members

Specimen Reference	Type	Retrofit	Span	Impact mass (kg)	Target impact velocity (m/s)
5-B-U-S	Static	N/A	1200		
6-B-R-S	Static	1 layer	1000		
7-B-R-I	Impact	1 layer	1000	210	6.5
8-B-R-I	Impact	1 layer	1000	360	5

From Table 7.1 it can be seen that specimen 5B-U-S was designed as the quasi-static control specimen. However, due to its similarities with specimen 1A-U-S, the span was increased so that the flexural demand would be greater. It was then intended that comparisons could be made between the behaviour of specimen 5B-U-S and 6B-R-S which were intended to demonstrate the improvement in performance caused by retrofitting. Specimens 7B-R-I and 8B-R-I were both tested under impact loads, which by comparing the behaviour of these specimens with specimen 6B-R-S would demonstrate the benefits of this type of retrofit system in impact situations.

A schematic drawing of the specimen's cross-section is shown in Figure 7.2. This can be compared with the cross-section of specimens 1-4 (series A) which is shown in Figure 5-1.

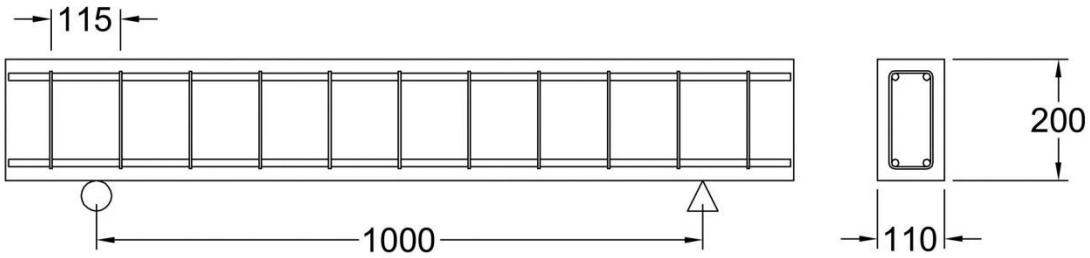

Figure 7.2: Longitudinal and transverse cross-section for set B specimens

The primary difference between the specimens in series A and series B is the size and spacing of the transverse reinforcement. For series A specimens 3 mm reinforcing steel with a yield strength of 770 N/mm^2 spaced at 75 mm was used whereas for series B specimens 4 mm reinforcing steel with a yield strength of 660 N/mm^2 spaced at 115 mm was used. Both sets of specimens were designed to have identical shear capacity according to BS 8110. Therefore the ratio $A_{sv}.f_y/s_v$ in both cases were selected to be the same, where A_{sv}, is the shear reinforcement ratio, f_y, is the yield strength of the steel transverse reinforcement and s_v is the transverse reinforcement spacing. Full details of the properties of the concrete members tested in series B are given in Table 5.1 with material properties given in Table 5.3.

7.3.2. Unretrofitted test

Test specimen 5B-U-S

Specimen 5B-U-S was designed to act as the unretrofitted quasi-static control specimen, which would enable a comparison to be made with the behaviour of the retrofitted specimens tested under quasi-static and impact loading. The results from the test would also give an accurate value for the ultimate moment of resistance of an unretrofitted member which could be used to design the retrofits.

The specimen was tested under three-point bending with the force applied at mid-span. Static design checks were carried out on the specimen to BS 8110 which predicted the moment capacity to be 18.7 kNm and the shear resistance to be 45.4 kN. This corresponds to a flexural failure load of 62 kN and a shear failure load of 91 kN suggesting the member would deform flexurally rather than failing in shear. The member was tested with a clear span of 1200 mm.

The load-deflection results from the test are shown in Figure 7.3. This plot indicates some ductility was achieved, which suggests the flexural capacity of the section was reached. The yield plateau is fairly short and photos in Figure 7.4 confirm that ultimate failure was through the formation of diagonal shear cracks. This suggests that the behaviour is a flexural/shear response rather than pure flexure or pure shear. The results from Figure 7.3 indicate that the flexural capacity was reached at a load of 73.3 kN, suggesting that the actual moment capacity of the section was 22 kNm. It was not clear why the experimental value for the moment capacity was around 17% higher than the theoretical value as actual measured material properties were used in the analysis.

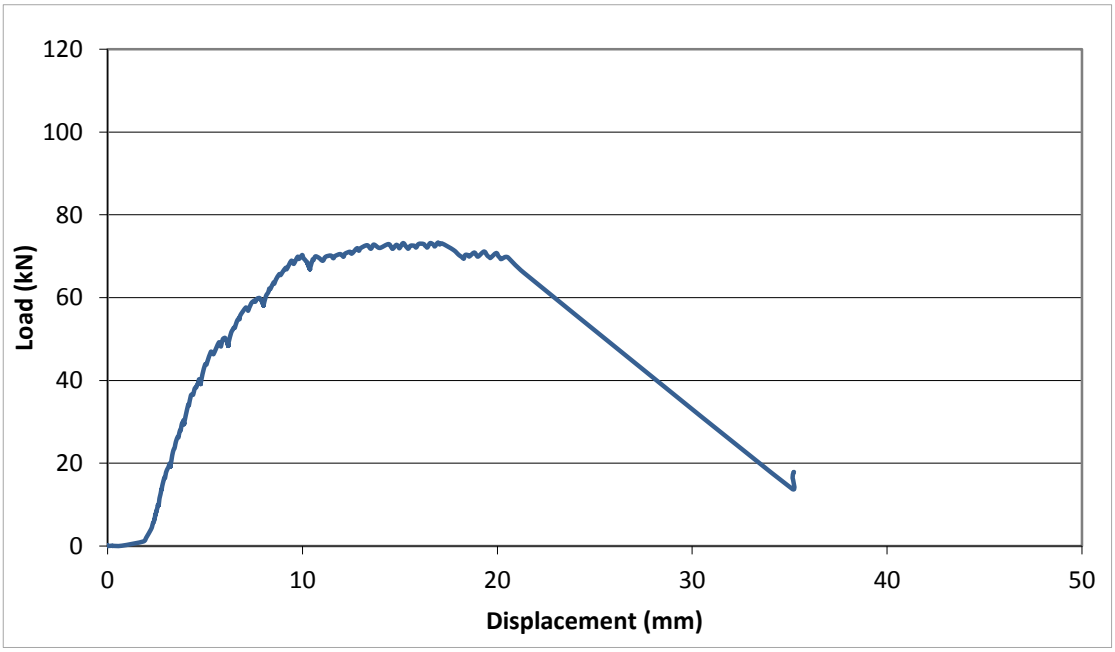

Figure 7.3: Load-deflection graph for specimen 5B-U-S

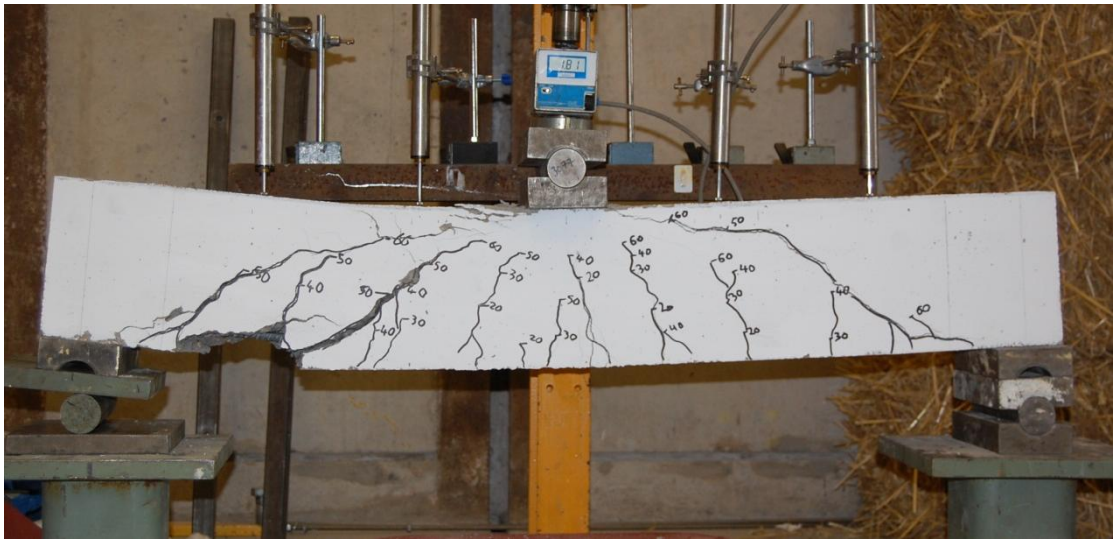

Figure 7.4: Ultimate failure of specimen 5B-U-S

7.3.3. Retrofitted tests

Design of retrofitting

In order to effectively design the transverse wraps applied to the remaining three specimens in set B, use was made of the results from specimens 1A-U-S, 2A-U-S and specimen 5B-U-S. Specimens in set A (1-4) were designed to have the same shear and moment capacity as specimens in set B (5-8). Specimen 1A-U-S was tested under quasi-static loading with a clear span of 1 m. The load deflection graph for this specimen (Figure 5-2) and the photo of the final failure (Figure 5-3) indicate that brittle shear failure has occurred prior to the ultimate flexural capacity being reached. The ultimate load achieved was 82.2 kN which indicates the actual shear resistance of the member to be 41.1 kN, which is lower than the design value of 45.4 kN.

The results from specimen 2A-U-S (Figure 5-4) indicate that the flexural capacity was reached and a ductile response was achieved up to final failure which is again shown to be through diagonal shear cracking (Figure 5-5). The ultimate load achieved in this test was 72.5 kN at a clear span of 1.2 m which indicates the moment resistance of the specimen to be 21.8 kNm. This result is almost identical to the moment resistance of specimen 5B-U-S. From these tests it can be concluded that the actual shear capacity is 41.1 kN and the moment resistance is 21.9 kNm.

These results are used below to design the FRP transverse strips that were applied externally to increase the shear capacity of the remaining three specimens in set B.

Design of the transverse strips was carried out in accordance with TR55 (2012). A carbon sheet was selected which could be cut to the desired strip width and bonded to the member with resin. The manufacturer's properties for the CFRP sheet are given in Table 7.2.

Table 7.2: CFRP fibre properties (Manufacturer's data)

Property	**Value**
Young's Modulus	214 kN/mm^2
Failure strain	0.0145
Nominal thickness per ply	0.16 mm

Coupon tests were also carried out (Collingwood, 2012) to validate the accuracy of the manufacturer's data. The results from these tests are shown in Figure 7.5 which indicate the ultimate failure strain of FRP strips depending on the number of plys.

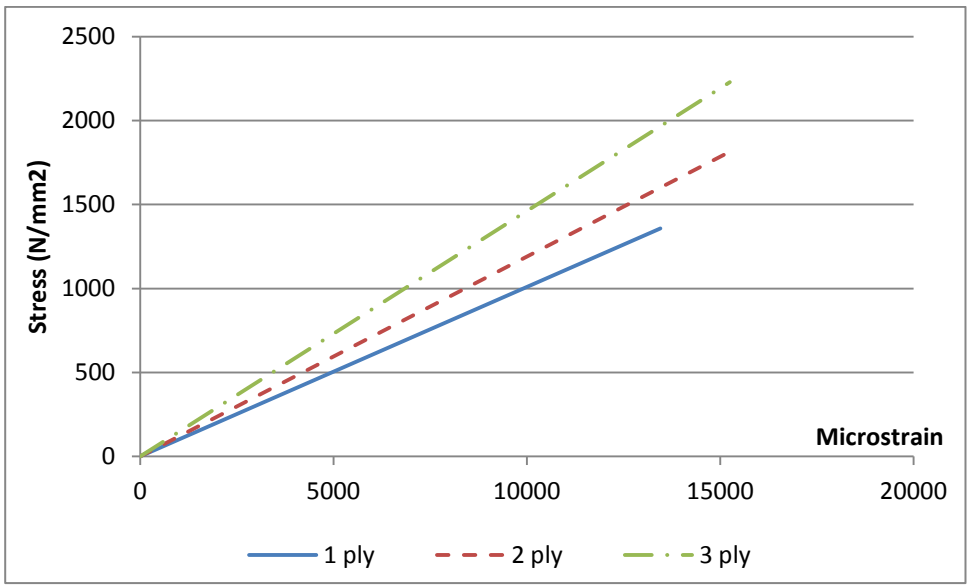

Figure 7.5: Coupon tests on CFRP (Collingwood, 2012)

TR55 (Concrete Society, 2012) gives the shear reinforcement of a member as:

$$V_R = V_c + V_s + V_f \tag{7.1}$$

where, V_R is the total shear resistance of a member, V_c is the contribution from the concrete, V_s is the contribution from the transverse steel and V_f is the contribution from the external FRP reinforcement. The additional shear capacity provided by the transverse CFRP, V_f, is calculated according to equation 7.3:

$$V_f = E_{fd}\varepsilon_{fse}\frac{A_{fs}}{s_f}(d_f) \quad (7.2)$$

A full description for what each parameter represents is given in TR55. The wrapping configuration selected in this case was discrete strips wrapped fully around at a uniform spacing of 115 mm along the length of the member. The retrofit requirement was then determined as a function of the strip width, b_f. The following values were used in equation 7.3.

E_{fd}	=	214,000 N/mm2	s_f	=	115 mm
ε_{fse}	=	0.004	d_f	=	170 mm
t_f	=	0.16 mm	n	=	0
A_{fs}	=	$0.32b_f$	β	=	0

ε_{fse} depends on a criteria of limiting effective strain which in this case was found to be 0.004. As it was intended that two layers of 0.16 mm CFRP would be used, the area, A_{fs}, is given as $0.32b_f$.

The Young's modulus was taken as the value obtained from the coupon tests shown in Figure 7.5. Substituting these values into equation 7.2 gives the following expression for the additional shear resistance provided by the FRP:

$$V_f = 0.404b_f \ \ kN/mm \quad (7.3)$$

The FRP strip width, b_f, was determined based on a selected factor of safety to ensure a flexural response under quasi-static loading as follows. All specimens were tested with the load applied centrally and with a clear span of 1 m, as this had been shown previously (specimen 1A-U-S) to fail in shear in unretrofitted members. Using the actual shear capacity and moment resistance of the member determined from the test program, it could be shown that the load required to cause shear failure in an unretrofitted member, P_s, was:

$$P_s = 2V \quad (7.4)$$
$$\therefore P_s = 82.2\ kN$$

where, V is the actual shear resistance of the unretrofitted member, which was shown from test 1A-U-S to be 41.1 kN. The load required to cause a flexural failure, P_m, is given as:

$$P_m = \frac{4M}{L} \quad (7.5)$$
$$\therefore P_m = 87.6\ kN$$

where, M is the actual moment capacity of the unretrofitted member, which was shown from tests 2A-U-S and 5B-U-S to be 21.9 kNm, and L is the clear span length. The ratio of the load that causes shear failure to the load that causes a flexural response, μ, is given as:

$$\mu = \frac{P_s}{P_m} \tag{7.6}$$

which for the 1 m spanning unretrofitted member (1A-U-S) is 0.94. A value less than unity indicates that shear failure will govern the response. In order to prevent the brittle shear failure in the retrofitted tests, P_s must be increased to a desired level through the addition of external CFRP reinforcement. This leads to a slight modification of equation 7.6 to take this into account:

$$\mu = \frac{P_s+2V_f}{P_m} \tag{7.7}$$

The additional CFRP reinforcement was designed to be identical for each of the specimens. It was decided to increase the shear capacity of the specimens so that μ was 1.2 which was assumed would give a suitable factor of safety and ensure that the full flexural capacity was reached without over strengthening. Using this μ value, equation 7.7 can be rearranged to give V_f, which in this case is 11.5 kN. This can then be used in equation 6.3 to find the width of the CFRP strips needed to achieve the desired increase in the members shear capacity. Using this value for V_f leads to a requirement of 28.5 mm for the strip width.

Specimen preparation

The surface of the concrete specimens was prepared in advance by wire brushing to remove laitance and create a rough surface to ensure a good bond with the resin. The corners of the members were rounded slightly to prevent stress concentrations developing in these regions which may lead to premature failure of the wraps. The CFRP strips came as a fabric sheet from which the correct width and length were cut. These strips were then bonded to the specimen with the use of Sikadur 330 epoxy resin. The strips were fully wrapped once around the member with the lap occurring on the top surface of the member. The specimens were left for a minimum of 7 days before testing to ensure full curing of the resin.

Test specimen 6B-R-S

Specimen 6B-R-S was tested under quasi-static loading. The purpose of the test was to ascertain the improvement in the behaviour of the member under quasi-static loads due to retrofitting when compared with the unretrofitted test.

The load-deflection plot for the test is shown in Figure 7.6. These results indicate that a ductile flexural behaviour was achieved. The figure also shows two parts to the loading curve. This was caused by the capacity of the first test rig being reached at 100 kN. At this load level the specimen had not failed and a it was therefore decided to stop the loading and re-commence the test in a rig with a higher capacity.

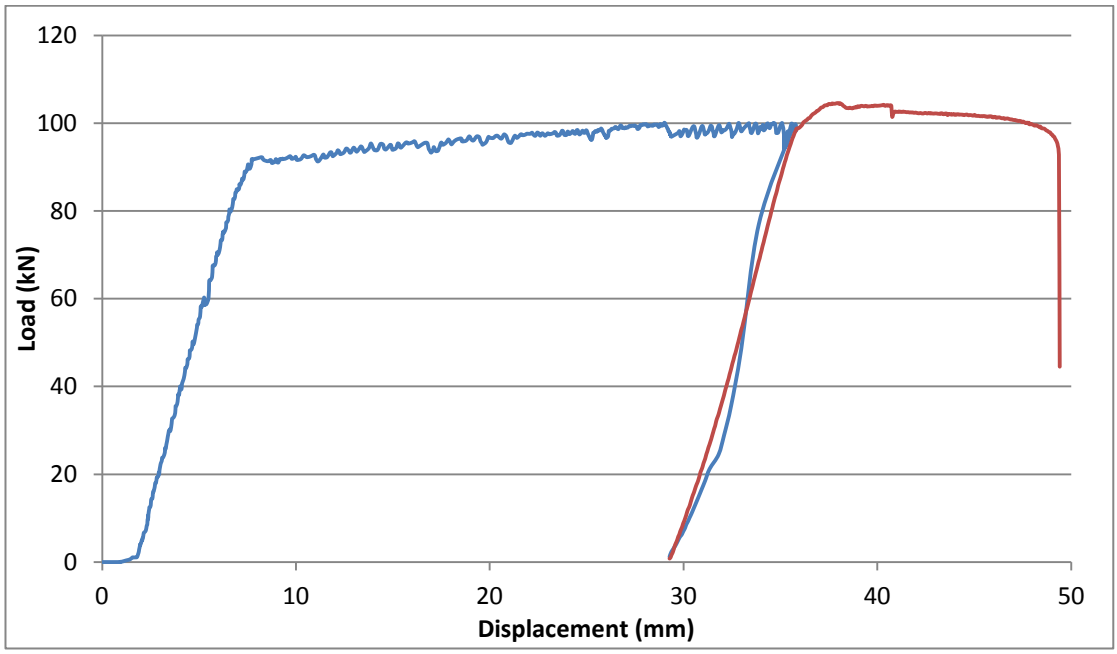

Figure 7.6: Load deflection for specimen 6B-R-S

The member deformed significantly prior to failure (Figure 7.7), reaching a peak deflection of around 50 mm before failure which occurred through snapping of one of the steel bars (Figure 7.8). The behaviour demonstrated in Figure 7.6 indicates a high level of ductility, it is also clear that a significant amount of strain hardening of the steel occurred prior to failure.

Figure 7.7: Maximum deflection post-failure

Figure 7.8: Snapping of tensile reinforcement

This type of behaviour represents a desirable failure mode and contrasts markedly with the brittle shear behaviour of specimen 1A-U-S and 5B-U-S. Measuring the area under the force-displacement graph gives a simple quantitative measure of energy dissipation. As discussed previously, the requirement for ductility from blast and impact loaded members is one of the most important characteristics of a member's response. It is estimated that the energy dissipated in this specimen (6B-R-S) was approximately 4300 joules, this contrasts greatly with specimen 1A-U-S which dissipated only 420 joules and specimen 5B-U-S which was estimated to have dissipated 1120 joules. It is clear

from this that the addition of only a small amount of CFRP can make a significant difference to the behaviour of a member.

An interesting observation from Figure 7.7 is that shear cracks can clearly be seen on the surface of the concrete, running either side of the CFRP strips. This clearly indicates that the failure of the member is being prevented by the CFRP strips. As failure of the CFRP strips has not occurred it is interesting to inspect the strips for debonding. This can be difficult to inspect visually, so a simple method, known as a tap test, can be used to check for debonding. Where debonding has occurred a coin tapped on the surface will make a different sound compared to where debonding has not occurred. The CFRP strips were marked with a simple grid and areas where debonding had occurred were shaded in red, the results from this test are shown in Figure 7.9. When compared with the positions of the cracks this clearly shows that debonding has primarily occurred locally around where shear cracks have formed in the concrete.

Figure 7.9: Results of tap test on specimen 6B-R-S (shaded areas indicate debonding)

From Figure 7.6 it can be seen that flexural yielding occurred at a load of approximately 90.5 kN, which suggests the moment capacity of the section in this test to be around 22.6 kNm. This is somewhat larger than that predicted by the design codes (18.7 kNm) but similar to the values seen in tests 2A-U-S and 5B-U-S which was, on average, 21.9 kNm. The fibre orientation of the transverse wraps suggests that there should be no effect on the moment capacity. Although the slight increase in the moment capacity of the section maybe due to the confining effects of the transverse strips. This is investigated experimentally in Section 7.4.

Test specimen 7B-R-I

The impact height and weight for both impact tests (7B-R-I and 8B-R-I) was selected based on achieving a constant kinetic energy in both tests. The target energy level selected was 4500 joules which was based on the energy dissipated in straining of the quasi-static retrofitted specimen. It was desired that, within the constraints of having constant kinetic energy, the velocity and weight of the impacting mass would be varied as much as possible. The constraints of the impact rig meant that the maximum achievable velocity was 6.5 m/s. Test specimen 7B-R-I was therefore selected as the high velocity test and impacted with a mass of 210 kg at a velocity of 6.5 m/s.

Both impact tests were filmed with a high speed camera at 3000 fps with a resolution of 1024 x 512. Load cells and strain gauges located on the FRP strips were also used and sampled at a rate of 10,000 Hz. The general test layout and labelling system is shown in Figure 7.10. As described previously the specimen was tested with a clear span of 1 m. Strain gauges FRP 1 and FRP 2 were located in the centre of the FRP strip at a distance of 45 mm and 105 mm from the surface respectively, which were expected to coincide with the primary shear crack.

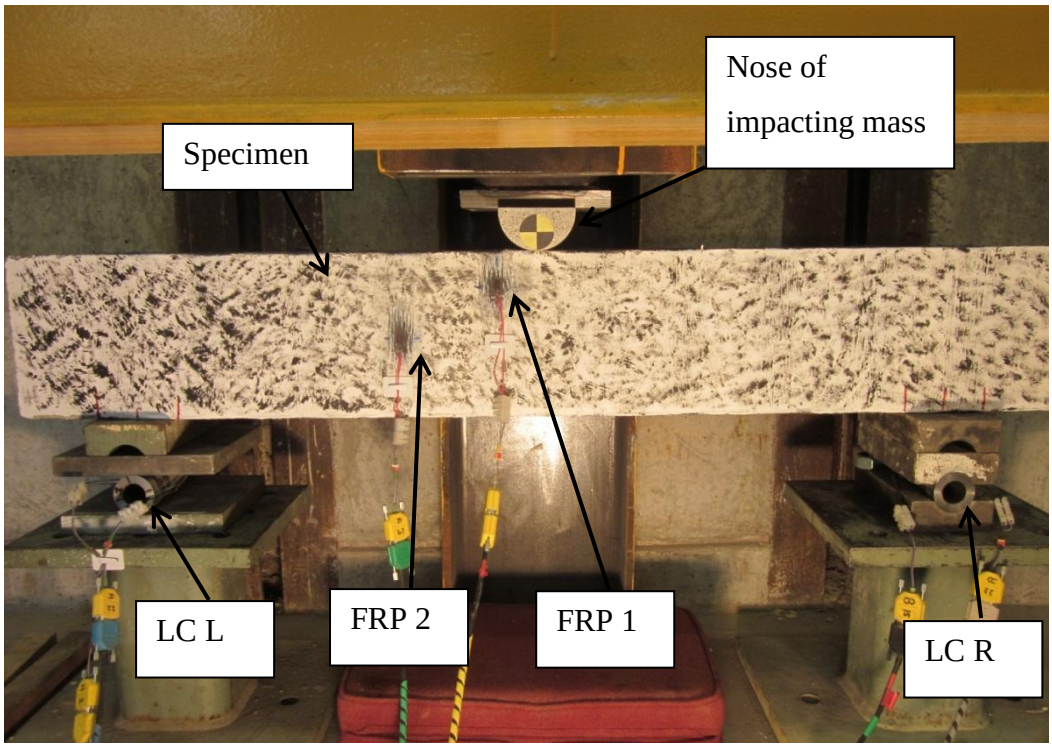

Figure 7.10: General impact test layout

Still images from the high speed camera up to the point of peak deflection (which occurred at around 14 ms after the initial impact) are shown in Figure 7.11. From these images it is clear that the FRP wraps have prevented the specimen from failing in shear. From the images it is also possible to measure the peak deflection as approximately 44 mm.

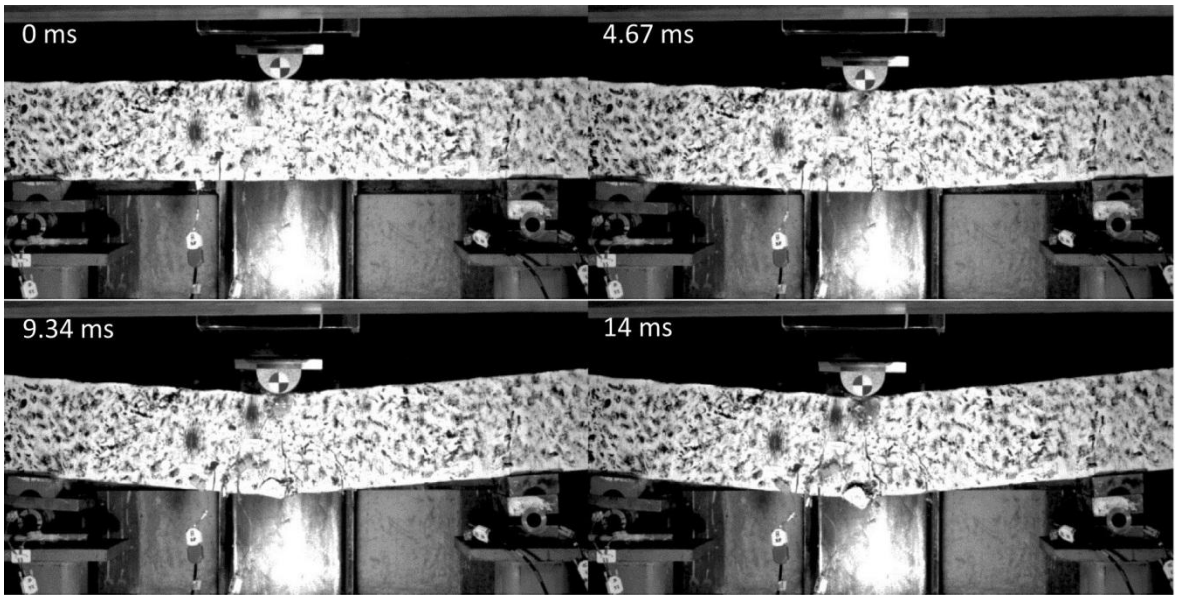

Figure 7.11: High speed camera images for specimen 7B-R-I up to peak deflection

The test event was much more violent than had been anticipated and the specimen moved laterally a significant distance which interrupted the data acquisition of the load cells. It also meant that difficulties were encountered when attempting to scale-off the residual displacement from the high speed images. The best estimate for the residual displacement showed it to be approximately 38 mm.

Results from the load cells and accelerometers are shown in Figure 7.12 plotted for the first 0.004 seconds of the member's response. During this time duration it was confirmed by the high speed camera images (Figure 7.11) that the peak deflection of around 44 mm had been reached (at 0.014 seconds). The readings shown for the impact mass accelerometer indicate that a significant amount of high frequency vibration was picked up. Also due to limited resources only a 30g accelerometer was available, therefore, data points are missing in places. However, the data is still useful for reference and has therefore been included in Figure 7.12. It is clear from Figure 7.12 that the left hand load cell (LC L) is reading significantly lower values than the right hand load cell (LC R). Images from the high speed camera indicated that this pin rolled

sideways and this is likely to have led to a lower reading. The same finding was reported on in tests presented in Chapter 5. The data from LC R, which was prevented from moving sideways, indicates that the maximum reaction force was approximately 168 kN, indicating a peak impact force of 336 kN. The time difference between the point of first impact and the load cells experiencing the force can also be estimated from Figure 7.12. The accelerometer readings appear to indicate that first impact occurred at around 0.0025 seconds and that the right sided load cell experienced this force 0.0006 seconds after the first impact and the left sided load cell 0.0009 seconds after the impact. This indicates the force propagated at a velocity of between 550 – 830 m/s.

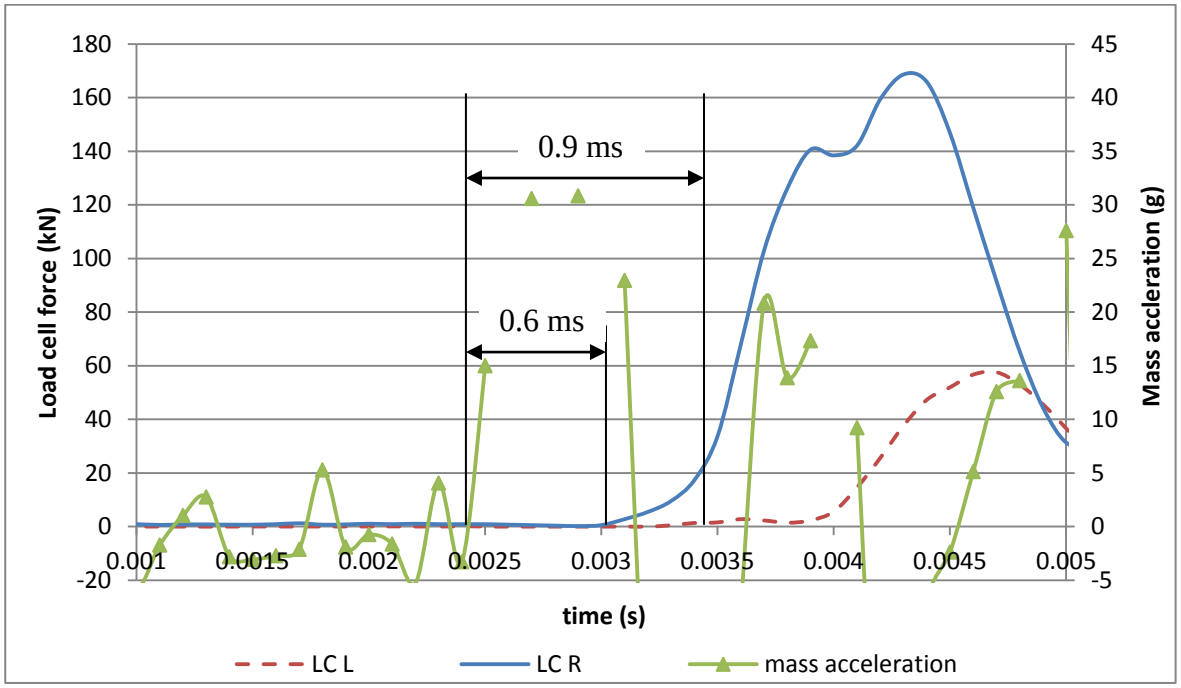

Figure 7.12: Load cell and accelerometer data from test 7B-R-I

The results of the strains measured in the CFRP strips are shown in Figure 7.13, plotted for the first 0.03 seconds of the response. These readings indicate that the strain in the FRP strip closest to the impact point reached the highest level. It is also clear that this strip also started straining earlier than the second strip (FRP 2) which would have been expected given that it is closest to the impact point and again indicates a wave dominated response as outlined in Chapter 4. It can be seen that the strains in FRP 2 become constant after reaching the peak whereas those in FRP 1 drop off from the peak before becoming constant. As the strain gauges are only capable of measuring the strain at discrete locations it is difficult to draw firm conclusions from the strain readings. The

strain readings are greater than the debonding strain of 4000 microstrain which suggests that debonding should have occurred. This is confirmed by the results of the tap test shown in Figure 7.14, where the strain gauge locations have been circled for clarity. The tap test results also show that the FRP strips closest to the impact location have debonded fully along their length, whereas the next strip out has only debonded in a small localised region around the crack indicating a steep shear crack. Also of interest is that the third strip on each side has not debonded at all.

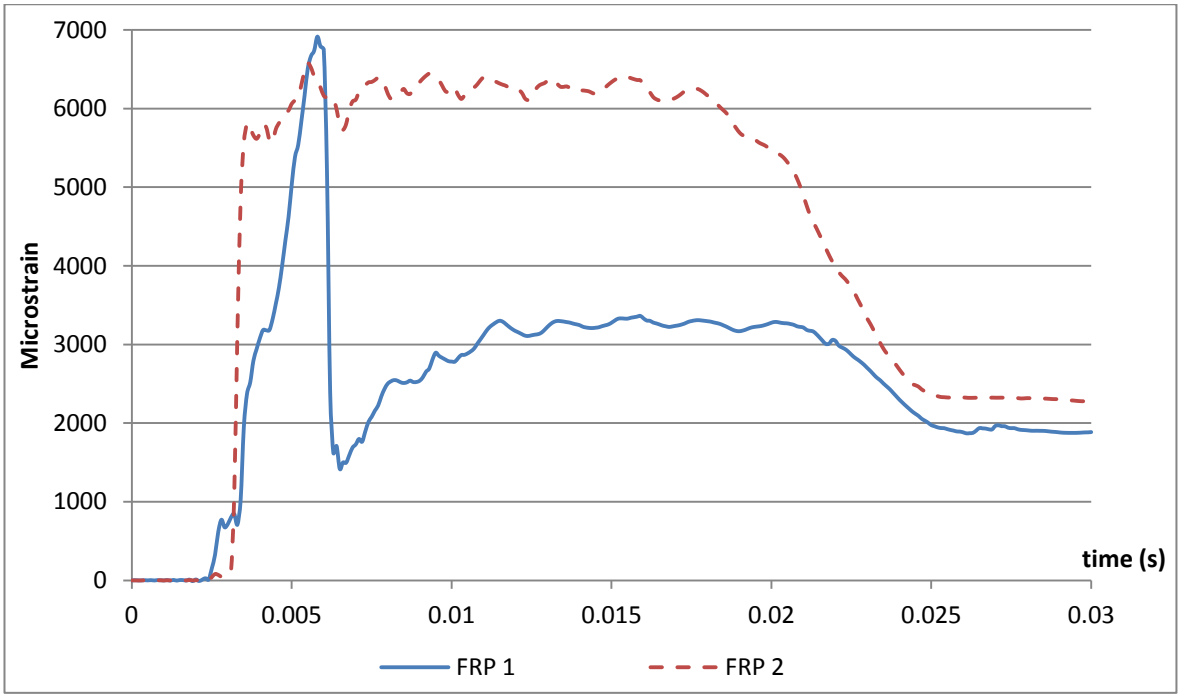

Figure 7.13: Strain readings from CFRP strips

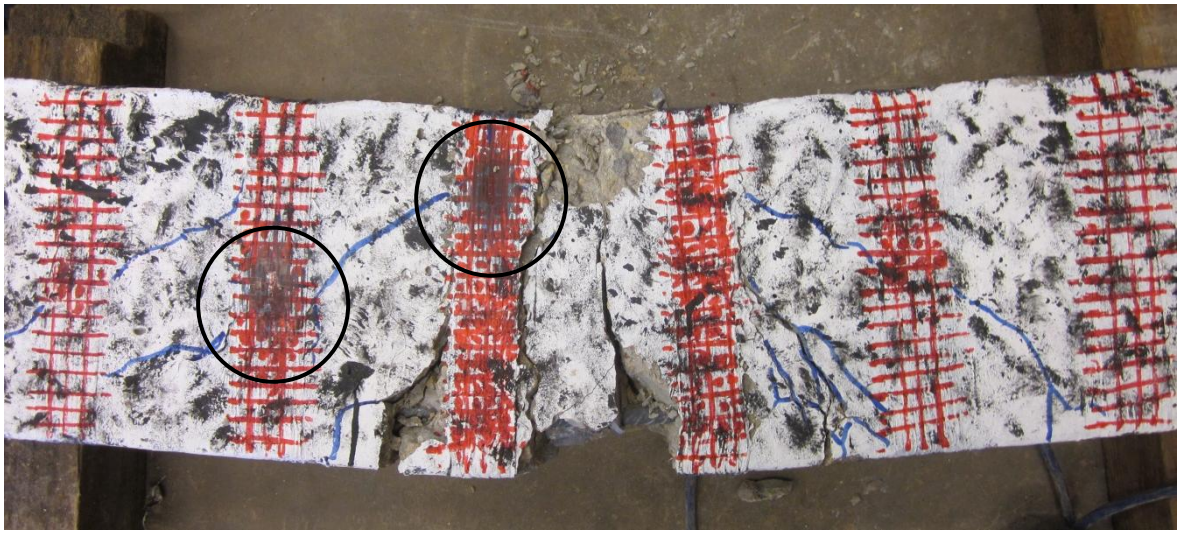

Figure 7.14: Results of tap testing on specimen 7B-R-I

Test specimen 8B-R-I

As mentioned previously, it was planned that the two impact tests on the wrapped specimens would be carried out with identical impact kinetic energies but that the impact characteristics (mass and velocity) would be varied. For this reason, as test 7B-R-I was carried out at the maximum rig velocity, whereas test 8B-R-I was carried out with the maximum rig weight of 360 kg. In order to achieve the required 4500 joules of energy the drop height was selected as 1.3 m, giving an impact velocity of 5 m/s. An identical test setup to that shown in Figure 7.10 was used.

Still images from the high speed camera and a photo taken post-test confirm that the FRP wraps prevented shear failure of the member. Unfortunately a technical problem with the high speed camera meant that not all of the images were transferred which prevents the peak deflection from being calculated. The residual deflection can be estimated by scaling off the photographs taken after the test was carried out which indicates a residual deflection of approximately 42 mm.

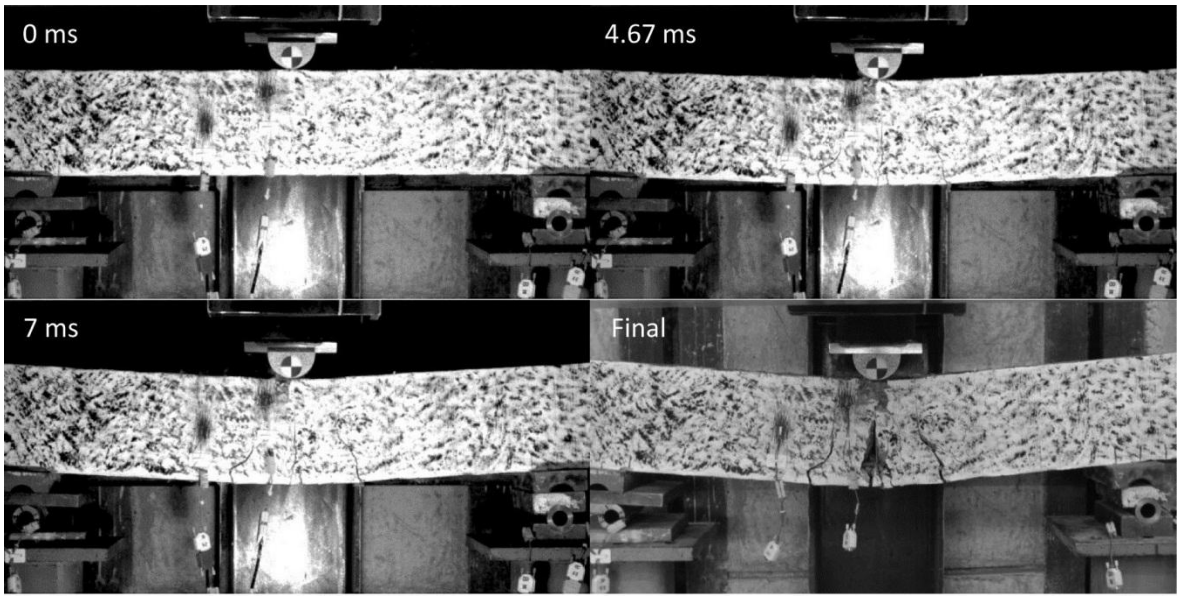

Figure 7.15: Images of test specimen 8B-R-I

Data from the load cells and the accelerometer are shown in Figure 7.16. Once again it can be seen that a large scatter exists in the data from the accelerometer which was believed to be caused by high frequency vibrations being picked up. Also only a 30g accelerometer was available for the test which meant that peak data points are missing.

The peak reading from the right sided load cell (LC R) was 183 kN which suggests that the impact force may have been in the region 370 kN although, as outlined in Chapter 5, the accuracy of the load cells was questionable. The reading taken from LC L was significantly lower than the reading taken from the right sided load cell due to the pin rolling, as discussed in test 7B-R-I.

From the accelerometer and load cell data it is possible to estimate the force propagation velocity. The data from the accelerometer shown in Figure 7.16 indicates that impact occurred at 0.0016 seconds. The right hand load cell experienced this force 0.0007 seconds later and the left hand load cell 0.0014 seconds later. This indicates a force propagation velocity of between 360 m/s and 710 m/s.

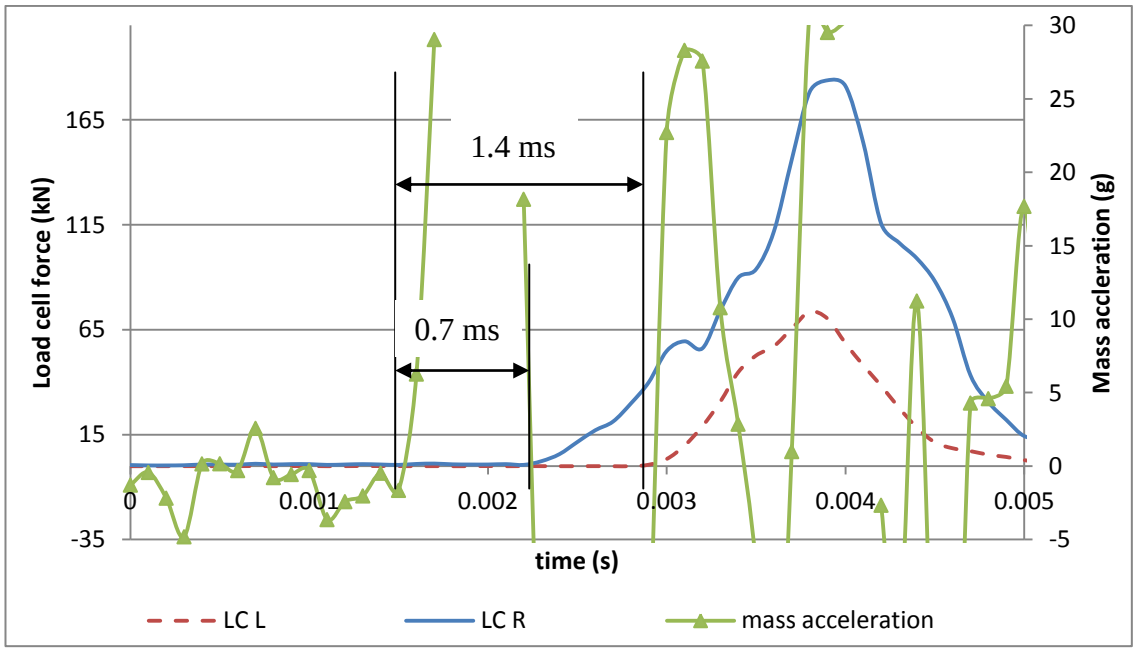

Figure 7.16: Load cell and accelerometer data from test 8B-R-I

Two of the CFRP strips were again strain gauged to ascertain their effectiveness. The results for this are shown in Figure 7.17. From this it is clear that of the two CFRP strips the one furthest from the impact point recorded the highest strain. This could be a result of the strain gauges only being capable of recording the strain at a discrete location therefore if the shear crack passed directly under the strip then it would register a greater strain. It may also have been due to the crack at this location being wider. Both arguments appear to be supported by the photo in Figure 7.18. After reaching the peak level both strips strain constantly for a period of time which indicates debonding might have occurred. It can also be seen that the reading for FRP 2 also goes off scale after a

certain period. In the absence of high speed images the reason for this cannot be accurately assessed although it may indicate a second impact on the specimen. It should however, be pointed out that neither strip ruptured but that the debonding strain was surpassed in the strip FRP 2. From Figure 7.17 it can again be seen that the strain gauge closest to the point of impact responded first.

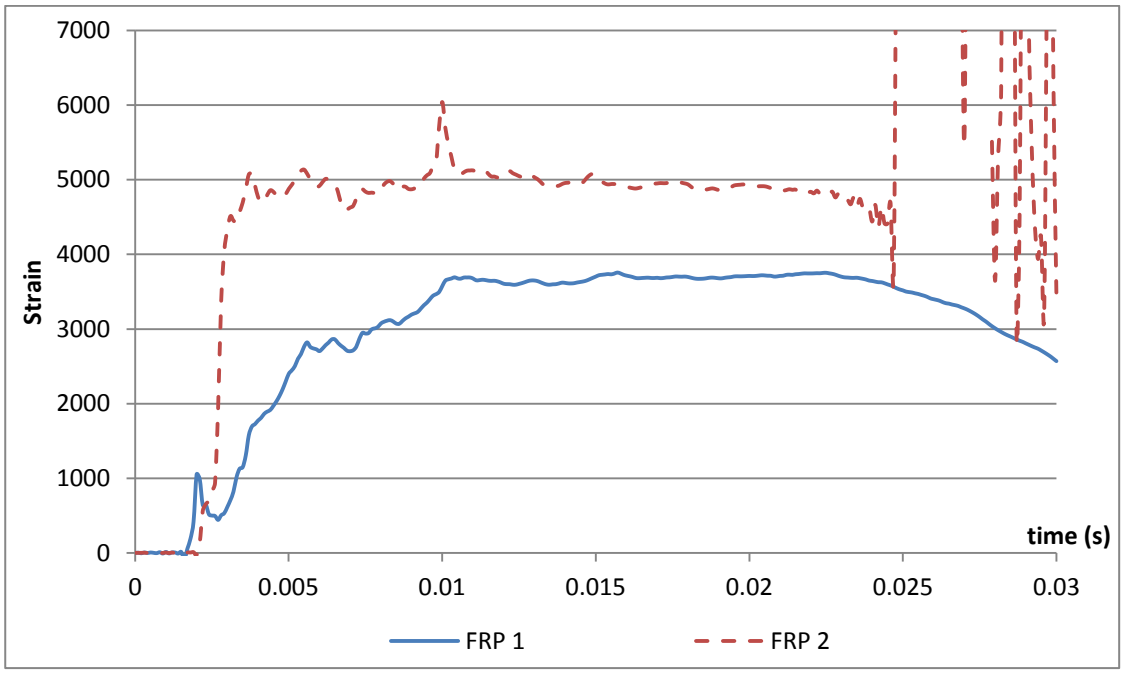

Figure 7.17: Strain readings from CFRP strips

A photo showing the results of the tap test performed to assess the level of debonding is given in Figure 7.18. The results indicate that the strips either side of the impact point debonded fully. An interesting observation from the photo is the asymmetry in the crack pattern. It appears that the second strip to the right of the impact point has not debonded and that no concrete crack passes across this strip. Both the second and third strips on the left have undergone local debonding around the cracks which pass under them. This asymmetry is likely a result of the roller support on the left hand side moving laterally.

Figure 7.18: Photo showing level of debonding of CFRP strips for specimen 8B-R-I

7.3.4. Discussion and comparison of test results

The results from the three tests carried out on retrofitted members demonstrated comprehensively the benefits of strengthening with FRP wraps. It was shown from the quasi-static tests on unretrofitted members that a load of 82.2 kN was sufficient to cause shear failure in a 1 m spanning member. The additional CFRP strips were intended to increase the shear capacity, relative to the flexural capacity. Due to errors made in cutting the CFRP strips they eventually ended up being on average 36 mm wide rather than the intended 29 mm. Therefore the actual shear capacity is calculated to be 26% greater than the flexural capacity. It may be expected that this value is a conservative estimate of the strength as it comes from design guidelines. Although this is still considerably lower than the estimated peak force from the impact tests, it is also not clear how reliable this data is.

The strains recorded on the FRP strips can also be used to assess the forces acting on the member for different impact velocities. The results of the strains on the FRP strips for specimen 7B-R-I and 8B-R-I are shown combined in Figure 7.19. These indicate that the strains in the FRP strips in test 7B-R-I both reached a higher level than the strains generated in test 8B-R-I (although only momentarily for strip 1). This appears to indicate that the impact force was greater when the impact velocity was greater, without providing concrete proof. At no stage in the initial response of the member did the strains in the FRP strips exceed the failure strain determined from coupon testing. The disparity in the results from the FRP strips and the load cells may therefore indicate that the force was initially greater in the higher velocity test (7B) but decayed more quickly

before the force reached the supports. It is also interesting to note that in test 7B the peak strain was recorded in the strip closest to the impact point, this may be further evidence of the higher impact force in this test and the steeper crack angles that are seen as the loading rate increases.

One limitation in the use of strain gauges is that they are only capable of measuring the strain at a discrete location. From a rudimentary assessment it would appear that in the case of the first strain gauge on specimen 7B-R-I the gauge is actually located directly above a shear crack (Figure 7.14). In contrast it would appear that the first strain gauge on specimen 8B-R-I was located below a shear crack (Figure 7.18). It is difficult to say precisely what effect this placement of the gauges may have had on the results, however, it would have been expected that the strain would be highest directly above a shear crack. In future DIC could possibly be used to avoid the problem of being able to only read the strains at discrete locations.

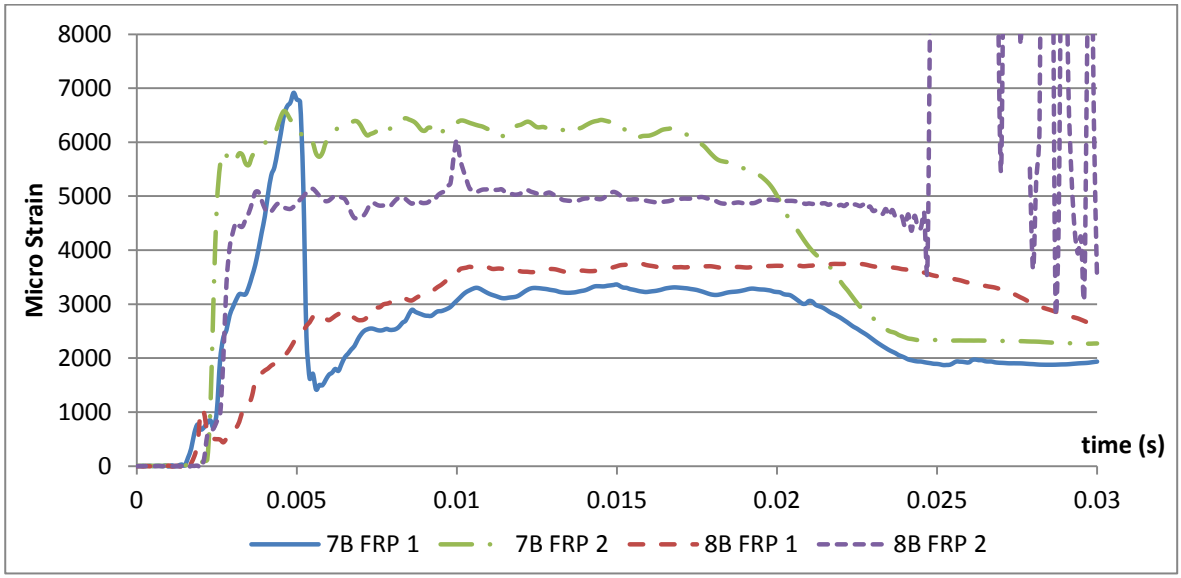

Figure 7.19: Strains in CFRP strips for test 7B-R-I and 8B-R-I

It is also useful to compare the variation in the FRP debonding seen between the quasi-static and impact tests. Figure 7.9 indicates that the shear cracks in specimen 6B-R-S have developed past the third strip of FRP on each side and that debonding has occurred only locally around the crack. This contrasts substantially with the results shown in Figure 7.14 for the high velocity impact on specimen 7B-R-I. This shows that the shear cracks have formed at a much steeper angle, that the strips closest to the impact point have debonded fully along their length and that the second strips have only debonded

locally around the crack. The third strips on each side from the point of impact have not debonded at all. This indicates that a more catastrophic event has occurred in test 7B-R-I and that a central shear wedge with steep angles has formed, which was not the case for specimen 6B-R-S. The results for specimen 8B-R-I appear to fit somewhere in between the quasi-static test and the higher velocity test, suggesting the failure was less brittle than the higher velocity test. Again it is clear from Figure 7.18 that the strips closest to the point of impact have debonded fully. In this particular test the crack pattern is seen to be asymmetric which is caused by the roller support on the left hand side moving out laterally.

It is estimated from Figure 7.14 and Figure 7.18 that the steepest cracks formed at angles of around 55 degrees to the horizontal. It is therefore clear that shear theories used for quasi-static cases, which usually assume a maximum angle of 45 degrees, may not be applicable for determining the dynamic shear capacity of a member. In contrast the steepest crack angle in the unwrapped quasi-static test (2A-U-S) was around 40 degrees. Further investigation of these issues falls outside the scope of the current work.

An important parameter outlined in the theoretical work presented in Chapter 3 was the displacement propagation velocity. Although the results from the tests presented above are not conclusive due to limitations with the data acquisition systems, they do appear to suggest a displacement propagation velocity that is dependent on the impact velocity. The results shown in Figure 7.12 suggest a displacement propagation velocity of between 550 m/s and 830 m/s for test 7B-R-I. The displacement propagation velocity in the lower velocity test (8B-R-I) was between 360 m/s and 710 m/s. This finding is consistent with the research of Velmorel *et al.* (2009) who suggested that there was a relationship between the impact velocity and the transverse wave propagation velocity in thin plates.

7.3.5. Comparison of set B specimens with theory

The impact tests carried out on the retrofitted members provide useful data which can be compared with the theoretical work outlined in Chapter 3. Predictions using this model were made by taking the upper-bound force propagation velocity measured for each specimen. In the case of test 7B-R-I this was taken as 830 m/s and in the case of specimen 8B-R-I this was taken as 710 m/s. This value was chosen as it appeared representative of each test from the available data.

Shown in Figure 7.20 is the theoretical variation in the impact force with time for the first few milliseconds of the response, predicted using the model outlined in Chapter 4. This duration represents the theoretical time that it takes the impact force to reach the supports based on the displacement propagation velocity discussed above. The theoretical results predict that the forces generated from the impact of the higher velocity, lighter mass (test 7B-R-I) are greater. The model predicts that the maximum impact force in test 7B-R-I would be approximately 940 kN and in test 8B-R-I 770 kN both of which are predicted to occur at around 0.0002 seconds. This is substantially greater than the experimentally determined value of 336 kN for test 8B-R-I which was estimated from the load cell data. Unfortunately it is not possible to verify the peak impact force due to the limitations of the 30g accelerometer used in the tests. It was also discussed previously how the results from the strain readings in the FRP strips appeared to suggest that initially the force generated by the high velocity impact was greater. Combining this with the results from the load cells may therefore suggest that the force of the high velocity impact was greater than the lower velocity impact test.

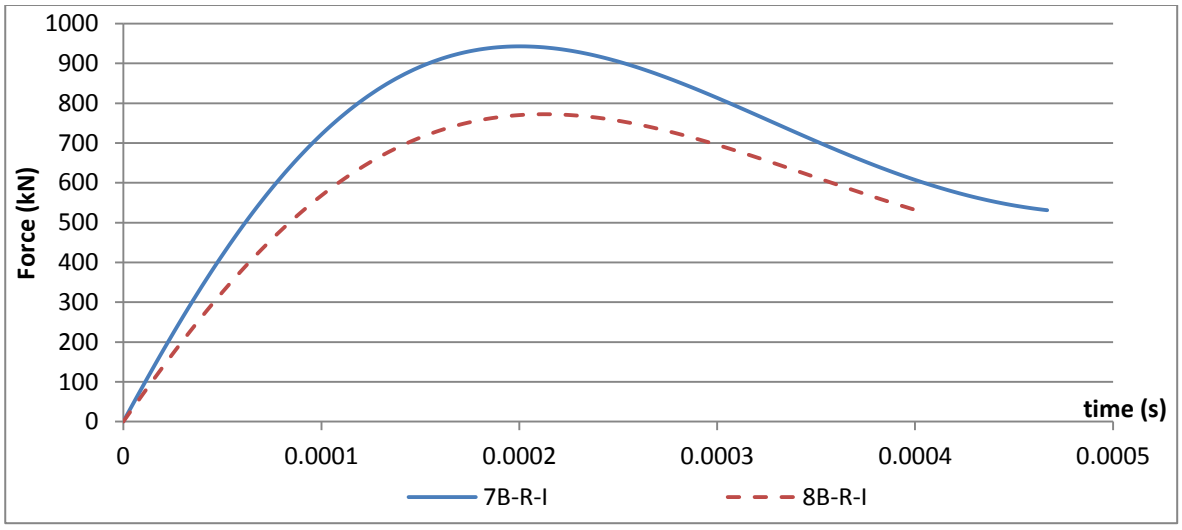

Figure 7.20: Predicted variation in impact force with time for tests 7B-R-I and 8B-R-I

As discussed in Chapter 4 Section 4.5.4, it would be expected that the impact force recorded from the tests would not be as high as that predicted from the theory due to the assumption that energy is conserved and that the contact zone stiffness is linear elastic.

The results from both impact tests demonstrate the effectiveness of the CFRP strips in preventing a catastrophic shear failure. The post-test analysis of both specimen 7B-R-I and 8B-R-I appear to suggest that a shear plug forms with steep crack angles in the

region of 55 degrees. The shear plug appears to be prevented from failing fully by the CFRP strips, despite the observed debonding (Figure 7.14 and Figure 7.18). The results from the model predicting the variation in the shear demand on each specimen for the initial stage in the members' response are shown compared with the theoretical shear capacity according to TR55 (Concrete Society, 2012) in Figure 7.21. The model predicts that the shear force acting on the member significantly exceeds the static capacity according to code designs. In the case of specimen 7B-R-I the peak demand is almost 6 times the capacity and in specimen 8B-R-I the demand is approximately 4 times the capacity. These results would therefore appear to suggest that catastrophic failure of the member should have occurred despite the presence of the FRP. This predicted behaviour can be contrasted with the strain readings from the CFRP strips (Figure 7.19) which show that in the initial stage of the response, the strain in the CFRP strips does not exceed the rupture strain of 13450 micro-strain, determined from the coupon tests. This suggests that the force does not last long enough to cause sufficient straining such that failure would occur. The high initial force is also likely attributable to the high stiffness in the contact zone which occurs early on in the response when the specimen has had insufficient time to deform. It may also be postulated that the CFRP is stiffer due to strain-rate effects, although it is not possible to substantiate.

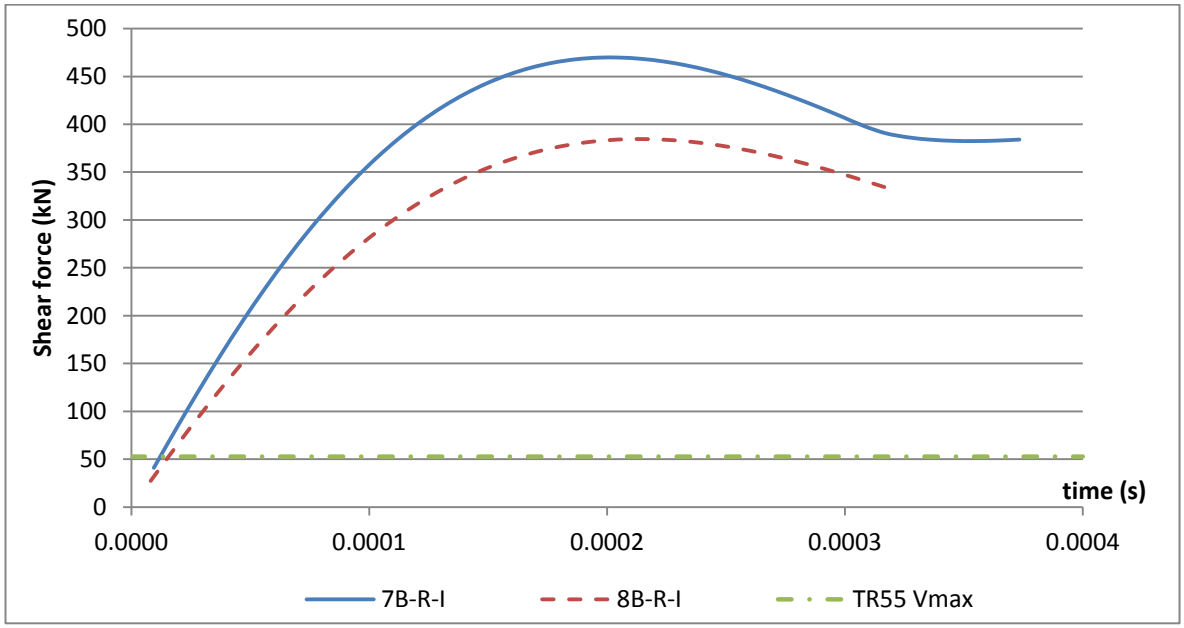

Figure 7.21: Variation in predicted shear demand for tests 7B-R-I and 8B-R-I

7.4. Increasing flexural capacity in Impact

Besides preventing shear failure, it was also shown that the retrofits applied to specimen 6B-R-S led to a minor increase in the flexural capacity of a member. During the course of this project the opportunity arose to collaborate with researchers working at George Washington University, USA, on testing the effects of transversely applied FRP on the flexural capacity of RC members. The results of these tests are summarised below.

In total 6 columns were tested, 3 of which were retrofitted. The specimens were designed as columns and the reinforcement was symmetrical. The specimens had a cross section of 140 x 140 mm and spanned 1980 mm. Specimens were reinforced longitudinally with 4 US D10 (10 mm diameter) bars (Figure 7.23b) and transversely with a D5 helix (5 mm diameter) with a pitch of 50 mm. The 28 day mean compressive cylinder strength of the concrete was 31 N/mm^2. The longitudinal reinforcement had a yield strength and ultimate strength of 432.6 N/mm^2 and 710.7 N/mm^2 respectively. The yield strength of the transverse steel reinforcement was 413.7 N/mm^2. The CFRP sheets had a yield strength of 1500 N/mm2 and a Young's modulus of 210,000 N/mm^2. A photo of the test set up is shown in Figure 7.22.

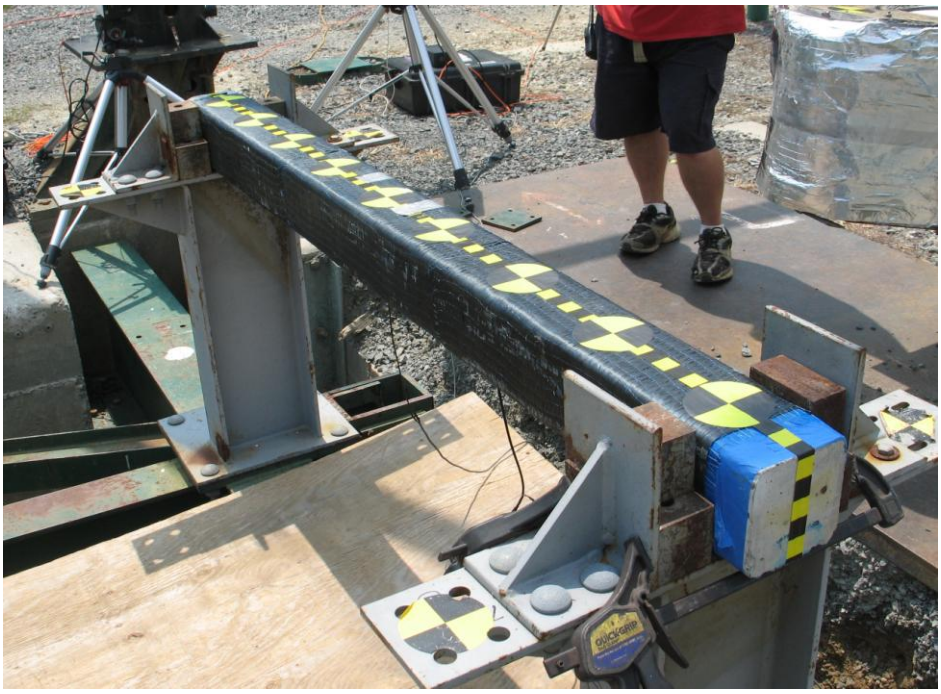

Figure 7.22: Photo of CFRP wrapped test specimen

The specimens were divided between 2 categories, with an 'F' indicating a central impact followed by either an 'A' or 'R' to signify whether they were tested as-built or

retrofitted. A full summary of the testing arrangement is given in Table 7.3 and shown diagrammatically in Figure 7.23. It was intended that all specimens would be tested with the same impact velocity. However, errors in the test setup meant that test specimens FR-1/2/3 were generally impacted at a lower velocity.

Table 7.3: Test matrix

Ref	Retrofit configuration	Impact point	Impact mass (kg)	Average impact velocity (m/s)	Impact energy (J)
FA-1/2/3	None	Mid-span	743	2.99	3320
FR-1/2/3	2 wraps	Mid-span	743	2.54	2400

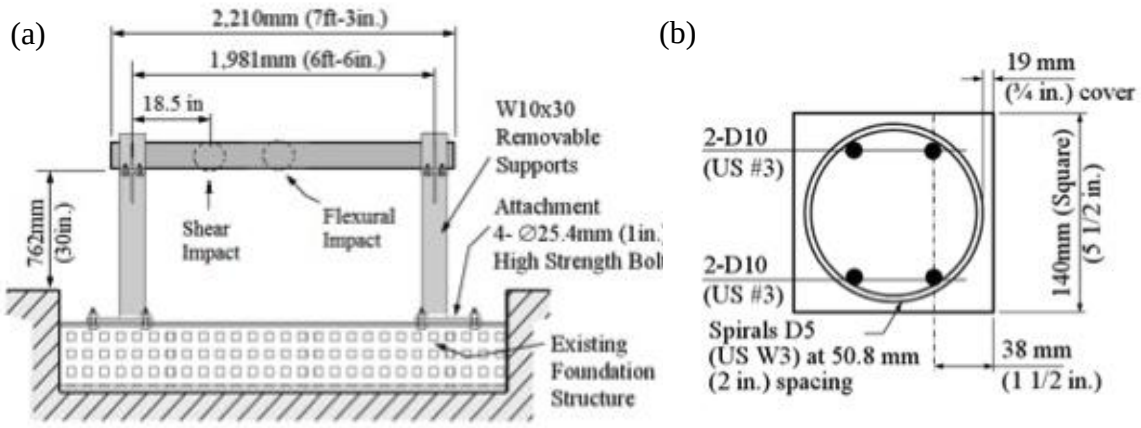

Figure 7.23: (a) Specimen support structure and (b) cross sectional dimensions and reinforcement arrangement

The test rig employed for these tests was a pendulum system located at FHWA Turner Fairbanks in McLean, Virginia, USA. The use of the pendulum system meant the load was applied laterally on a horizontally supported member rather than vertically as is the case for the drop tests described in Section 7.3. A photo of this set-up is shown in Figure 7.24.

Figure 7.24: Pendulum test rig

The results for the peak displacement and residual displacements of the specimens are given in Table 7.4, which were determined using motion tracking software. The impacting mass was 743 kg which allows the kinetic energy in Table 7.4 to be calculated. The variation in the peak displacement with kinetic energy is shown in Figure 7.25. The results indicate that on average the retrofitted specimens experienced lower peak and residual displacements than the as-built specimens. However, they also show that on average the impact kinetic energy for the retrofitted specimens was lower. This occurred due to errors made in the experimental procedure and is unfortunate. However, two specimens, FA1 and FR3, have almost identical impact characteristics and indicate a 32% reduction in the peak displacement and a 28% reduction in the residual displacement between the as-built and retrofitted specimens.

Table 7.4: Summary of results from specimens impacted at mid-span

Specimen	Impact velocity (m/s)	Kinetic Energy (J)	Peak displacement (mm)	Residual displacement (mm)
FA1	2.83	2970	132.9	86.1
FA2	3.06	3480	129.7	83.5
FA3	3.08	3520	130.3	84.1
FR1	2.5	2320	97.4	58.7
FR2	2.31	1980	100.6	61.3
FR3	2.81	2930	90.5	61.6

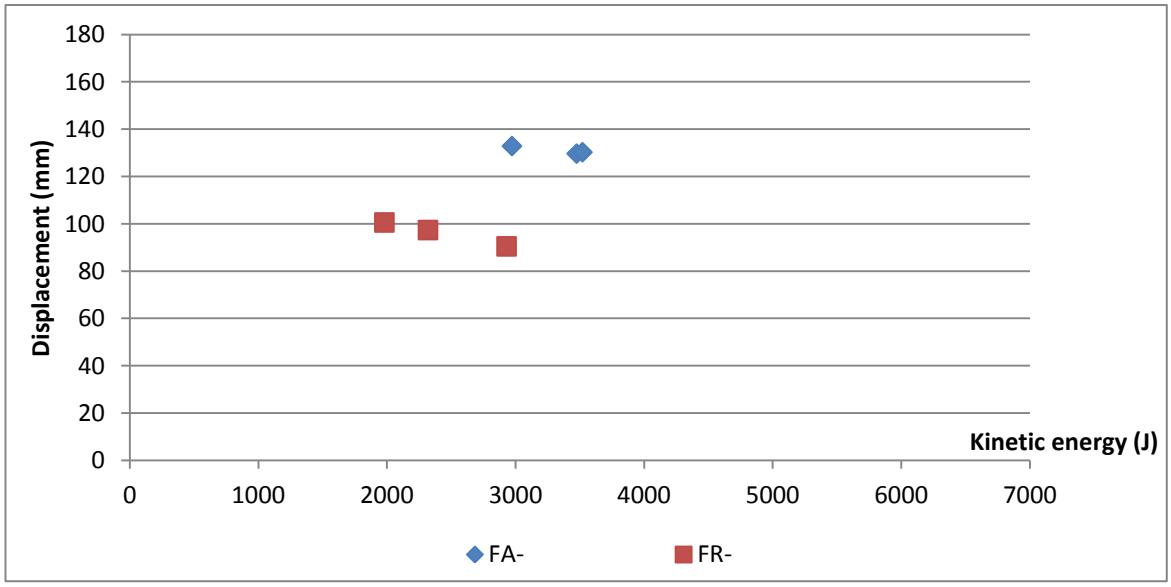

Figure 7.25: Variation in peak displacement of specimens FA and FR with kinetic energy

7.4.1. Discussion on benefits of transverse FRP on flexural capacity

The results outlined above appear to highlight the potential reduction in the peak and residual displacement that can be achieved by transversely wrapping RC members with CFRP. Retrofits applied with the fibres orientated transversely are intended to prevent shear failures. In this case no additional longitudinal reinforcement is provided so it may be expected that the effect on the flexural resistance of the member would be negligible.

This improvement in the behaviour is most likely attributable to the confining effects of the CFRP which allows higher strains to be reached in the concrete prior to failure. In

addition to this, the concrete retains its integrity meaning that a greater proportion of the section is able to resist the load and dilation is prevented. TR55 suggests that, in cases where the concrete is effectively confined, failure strains of the concrete can increase, up to around 1%, almost three times the unconfined value of 0.35%. This increase in failure strain has the effect of increasing the ductile plateau of the moment-curvature relationship for a section. By preventing failure of the concrete in crushing the section is able to reach a higher ultimate moment capacity as the effects of strain hardening become more pronounced. The effects of strain hardening were shown in specimen 6B-R-S where the ultimate load on the member was 104.6 kN which indicated a maximum moment capacity of 26.2 kNm. This was almost 20% higher than the capacity at yield. It was discussed in Chapter 6 that when the moment capacity is increased, a greater amount of energy is required to rotate a plastic hinge through a certain rotation.

7.4.2. Comparison with theoretical predictions

Theoretical work to predict the peak displacement of impact loaded RC members was presented in Chapter 6. This work proposed the use of an iterative, energy based solution whereby the peak displacement was predicted by considering the motion over a series of small time-increments. The primary benefit of the proposed model was the ability to accurately account for strain-rate effects when determining the section's moment capacity, which, as was discussed in Chapter 6, has a noticeable effect.

Results for the peak displacement of the specimens were predicted in two parts. Firstly the theoretical model outlined in Chapter 4 was used to predict the velocity at which coincidental motion occurred. This was discussed in Chapter 6 to be an approximate method for estimating the energy lost in the contact zone as the impacting mass comes into contact with the member. After obtaining the velocity at which coincidental motion occurs, the peak displacement was predicted using the method outlined in Chapter 6. The results for the predicted peak displacements compared with the experimental data are shown in Figure 7.26. For both cases the theoretical predictions are made using the average initial impact velocity (2.8 m/s for unwrapped specimens and 2.54 m/s for wrapped ones) and compared with the average peak displacements across the three specimens. As the concrete is fully confined, these results are predicted assuming that concrete can reach an ultimate strain of 1%.

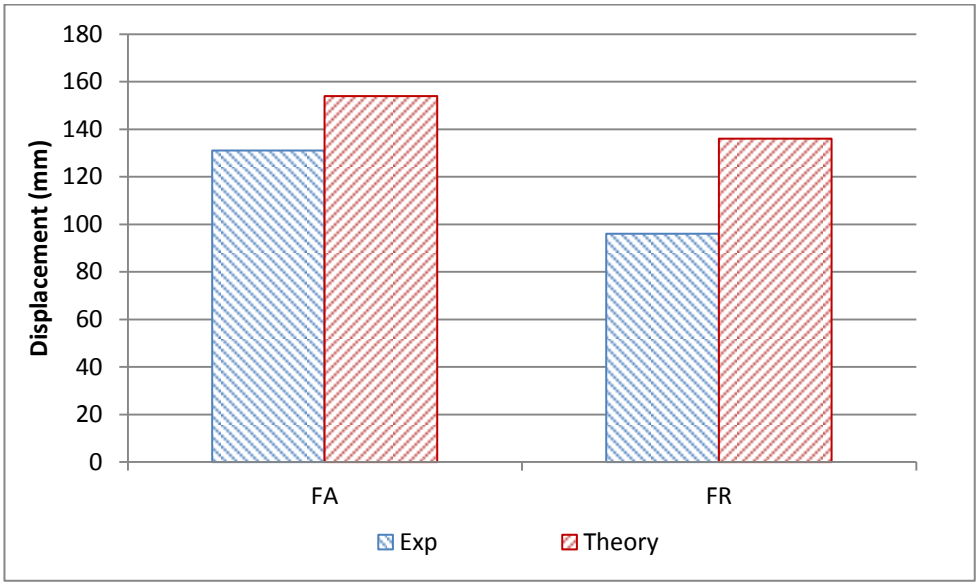

Figure 7.26: Results for the average peak displacement of 'F' specimens

The results in Figure 7.26 indicate that the theoretical model is capable of predicting the same trend of a reduction in the peak displacement of retrofitted specimens (FR) compared with unretrofitted (FA). This predicted behaviour is predominantly due to the increased moment capacity of the retrofitted specimens caused by the increased strain capacity of the confined concrete. It is clear also that the theory over-predicts the displacements. This suggests that the amount of energy dissipated in the specimen is under-predicted or that the energy supplied is over-predicted.

7.5. Applications to Blast situations

The work outlined above in the application of FRP to prevent brittle shear failures and reduce the peak deflection of members subjected to impact loads could be extended to blast situations. Discussed in Chapter 2 were the results of simulated blast tests carried out by researchers working at UCSD on improving the resistance of RC columns to blast loads through external wrapping with CFRP. These tests were able to show a dramatic improvement in the member's response with as few as two layers of CFRP. Specimens that were shown to fail in shear when tested without any retrofit were able to withstand significantly larger impulsive blast loads and deform flexurally when retrofitted with CFRP. Unfortunately carrying out blast tests was not possible within the scope of the current project. However, in the future, as more data from UCSD becomes available, it is likely that new efforts can be made to develope rational design guidelines for the use of FRPs in this area.

7.6. Conclusion

The results of impact tests performed as part of this project have demonstrated the significant improvement in a member's response that can be achieved through externally applied transverse FRP retrofit. It was shown how specimens, which fail in shear under quasi-static loads, are able to withstand much higher impact forces and still respond flexurally after being retrofitted. Also presented was a comparison of this work with the theoretical model outlined in Chapter 4, which again shows potential in predicting the general trends observed in the tests, for example more brittle failures and more damage when the impact velocity is greater.

It was also shown that the application of transverse FRP had a benefit in terms of reducing the peak deflection of a flexurally deforming member, despite the discrepancies in the results. These discrepancies were largely down to inconsistencies in the test procedure, however, in the two tests which had comparable impact characteristics, the improvement seen by wrapping the specimen was considerable. This was linked to the greater failure strain of confined concrete subject to an impact thus maintaining capacity through the whole deformation of the element when compared to unconfined concrete. The theoretical model displayed encouraging results in predicting the peak displacement, although further work is required in this area to look at additional energy dissipation modes. To this end the attempts to include an estimate by lowering the initial impact velocity provide some direction for future work.

8. Conclusions and Recommendations

8.1. Conclusions

Accurately understanding and being able to predict the behaviour of reinforced concrete (RC) columns to extreme impulsive loads such as blast and impact is essential if they are to be designed to effectively withstand these types of loads. Although cases of blast and impact occur relatively rarely, history is littered with examples of where insufficient robustness has lead to disproportionately high levels of damage occurring in reinforced concrete structures due to these events.

Predicting the response of a member to these types of loads is complicated due to the rapidly varying nature of the load and phenomenon, which would not be encountered in quasi-static situations, such as wave phenomena and dynamic material properties. Analysis of both blast and impact situations is typically carried out using either simplified methods such as the SDOF model or over finite element models. Both of these have their associated problems, with SDOF approaches failing to accurately represent the complex behaviour, and finite element models being too dependent on user inputs, which are often poorly understood. The present research has therefore looked at addressing some of the weaknesses of both these methods.

The research covered in this thesis covers a range of topics relating to the behaviour of RC columns subjected to blast and impact loads. A new theoretical model was developed to predict how a member subjected to an impact load would initially respond at the very outset of loading. In addition to this a separate model which focused on predicting the peak displacement of a member subjected to both blast and impact loads was developed. Experimental data to support the theoretical work was also collected using a purpose build impact rig.

The theoretical model outlined in Chapter 4 provides a new method for determining the forces acting on a member during the very initial phase of an impact event. It was recorded from experimental testing that a finite time existed between an impact occurring at the mid-span and the supports experiencing the force. The model developed analyses the response of a member over a series of small time-steps up until the impact force reaching the supports. During this time it is considered that the member has a

reduced effective length, which increases with each time-step. Use of this procedure allows the equations of motion for a two degree of freedom system to be solved, from which the forces acting on a member can be determined. The main result of this work was the clear demonstration why a higher velocity, lighter impact mass led to a more brittle shear failure than a lower velocity, heavier impact mass, for identical kinetic energies. The phenomenon of increasing brittleness with increasing loading rate has been observed by numerous researchers as well as in the tests presented in Chapter 5 but to date no theory which accurately predicts this behaviour is available.

The experimental work in Chapter 5 also demonstrated how a central shear wedge (at the point of impact) could occur in members despite the shear capacity being significantly in excess of the flexural capacity. Another feature observed from the impact tests presented in Chapter 5 was the formation of hogging cracks a short distance from the point of impact. Under quasi-static loading these hogging cracks would not form as the top face is always in compression. This, therefore, demonstrates that at some point during the response it was in tension. It is interesting to note here that this feature was actually predicted by the model outlined in Chapter 4 due to the assumption that initially the member behaves as a fixed beam with a reduced effective length.

Where it is demonstrated that a member has insufficient shear capacity to overcome the high initial forces and deform flexurally, additional strengthening is required. Currently the most effective method for this is considered to be through external FRP wraps. The experimental results in Chapter 7 were able to demonstrate how the application of only a limited amount of FRP could prevent a complete and catastrophic shear failure. Results from experimental testing carried out on flexurally deforming members also showed that the application of FRP to enhance the shear capacity could also increase the ultimate moment capacity and the energy absorbing capacity of a member. This result is due to the confining effects of the FRP which allows the concrete to retain its integrity and strain to a higher level than unconfined concrete.

The final aspect of work developed was a plasticity based model to predict the peak displacement of blast and impact loaded RC members deforming flexurally. This model also employed a time-step approach to predict the peak displacement, this time by assuming conservation of energy in the system. One of the key aspects of using the

time-step approach was that strain-rates in the section could be accurately calculated. These were then employed in determining the dynamic moment capacity of a section by using material dynamic increase factors available from the literature. Predictions using this model were shown to be more accurate than the more commonly used SDOF method despite both being of comparative simplicity.

The theoretical model outlined in Chapter 4 required some simplifying assumptions to be made which were discussed in detail above. Where appropriate, these were investigated parametrically to understand the influence they had on the results. It was found that assumptions made regarding the characteristics of the contact zone had a significant effect on the predicted behaviour of a member. It was also shown that assumptions regarding conservation of energy led to an over-prediction in the predicted forces making qualitative assessments difficult. The assumption of conservation of energy in the model outlined in Chapter 6 also led to over-predictions for the peak displacement. These limitations lead to significant opportunities for further work.

8.2. Recommendations for further work

The current research has largely focused on new methods for predicting the behaviour of RC columns to blast and impact loads with experimental testing providing valuable data, for example on the force propagation velocity which formed the basis of Chapter 4. From the discussions in each chapter it is apparent that there are substantial opportunities for further work in this field. Specific suggestions for this are as follows:

- The contact zone behaviour in the model presented in Chapter 4 was shown to have a considerable influence on the forces predicted in a member. A more detailed study on this behaviour is thus required so that improved predictions on the behaviour can be made. It may also be interesting to investigate other types of impact other than the ‘hard’ ones considered.
- Assuming conservation of energy in blast and impact events leads to considerable over-predictions in the forces or the displacements. Whilst it is difficult to account for all types of energy loss in a system, this area requires further investigation. It may be possible that a ‘damping’ coefficient could be applied in the model which takes into account the energy loss.
- By far the biggest limitation in this field is the lack of test data. The impact rig built specifically for this project and discussed in Chapter 3 provided a valuable

source of data, along with data from the UCSD blast simulator. However, considerably more is still required. This includes a more detailed study of the parameters affecting the force propagation velocity from an impact, more data relating to modes of energy loss in the system and additional data for the peak displacement of members subjected to both blast and impact loads.

References

Abrahamson, G.R. & Lindberg, H.E. 1976. Peak load-impulse characterization of critical pulse loads in structural dynamics. *Nuclear Engineering and Design,* 37**,** 35-46.

Abrate, S. 1991. Impact on laminated composite materials. *Applied mechanics reviews,* 44**,** 155.

ACI, A.C.I. 2002. 440.2 r-02: Guide for the design and construction of externally bonded frp systems for strengthening concrete structures. *Farmington Hills, MI: American Concrete Institute*.

Avnon, I. & Yankelevsky, D.Z. 1992. Crack interactions during dynamic loading on a hardened cement paste specimen. *Engineering Fracture Mechanics,* 42**,** 1041-1045.

Bangash, M.Y.H. 1993. *Impact and explosion analysis and design,* Oxford: Blackwell scientific publications.

Bertero, V., Rea, D., Mahin, S. & Atalay, M. Year. Rate of loading effects on uncracked and repaired reinforced concrete members. *In:* Fifth World Conference on Earthquake Engineering, 1973 Rome. 1461-1470.

Biggs, J.M. 1964. *Introduction to structural dynamics*: McGraw-Hill College.

Bischoff, P.H. & Perry, S.H. 1991. Compressive behavior of concrete at high-strain-rates. *Materials and Structures,* 24**,** 425-450.

Bischoff, P.H., Perry, S.H. & Eibl, J. 1990. Contact force calculations with a simple spring mass model for hard impact - a case-study using polystyrene aggregate concrete. *International Journal of Impact Engineering,* 9**,** 317-325.

Buchan, P.A. & Chen, J.F. 2007. Blast resistance of frp composites and polymer strengthened concrete and masonry structures - a state-of-the-art review. *Composites Part B-Engineering,* 38**,** 509-522.

Bulson, P.S. 1997. *Explosive loading of engineering structures,* London: E & FN Spon.

Byfield, M.P. & Paramasivan, S. 2014. Estimating safe scaled distances for columns subjected to blast. *Engineering and computational mechanics, 167 (1)*

Campbell, P. 2001. *Learning from construction failures: Applied forensic engineering*: John Wiley & Sons.

Collingwood, S.M. 2012. *Premature rupture of FRP wrap - the effect of biaxial stress*. MENG Dissertation, University of Bath

Comite euro-international du beton, (CEB). 1988. *Concrete structures under impact and impulsive loading, bulletin 187*.

Concrete Society 2012. Design guidance for strengthening concrete structures using fibre composite materials : report of a Concrete Society Working Party. 3rd ed. *Technical Report No. 55.* Camberley.

Cormie, D., Mays, G. & Smith, P. 2009. *Blast effects on buildings second edition,* London: Thomas Telford.

Cotsovos, D.M. 2010. A simplified approach for assessing the load-carrying capacity of reinforced concrete beams under concentrated load applied at high rates. *International Journal of Impact Engineering,* 37**,** 907-917.

Cotsovos, D.M., Stathopoulos, N.D. & Zeris, C.A. 2008. Behavior of rc beams subjected to high rates of concentrated loading. *Journal of Structural Engineering-Asce,* 134**,** 1839-1851.

Crawford, J.E. & Magallanes, J.M. 2010. The effects of modeling choices on the response of structural components to blast effects. *The First International Conference of Protective Structures.* Manchester.

Crawford, J.E., Malvar, L., Morrill, K.B. & Ferritto, J. 2001. Composite retrofits to increase the blast resistance of reinforced concrete buildings. *Tenth International Symposium on Interaction of the Effects of Munitions with Structures.* San Diego.

Doyle, J.F. 1997. *Wave propagation in structures: Spectural analysis using fast discrete fourier transform,* Berlin: Springer.

El-Dakhakhni, W.W., Rezaei, S.H.C., Mekky, W.F. & Razaqpur, A.G. 2009. Response sensitivity of blast-loaded reinforced concrete structures to the number of degrees of freedom. *Canadian Journal of Civil Engineering,* 36**,** 1305-1320.

Erofeev, V., Lisenkova, E. & Smirnov, P. 2008. Velocities of energy and wave pulse transfer by flexural waves propagating in a beam lying on a nonlinear elastic base. *Journal of Machinery Manufacture and Reliability,* 37**,** 568-571.

Fu, H.C., Erki, M.A. & Seckin, M. 1991a. Review of effects of loading rate on concrete in compression. *Journal of Structural Engineering-Asce,* 117**,** 3645-3659.

Fu, H.C., Erki, M.A. & Seckin, M. 1991b. Review of effects of loading rate on reinforced-concrete. *Journal of Structural Engineering-Asce,* 117**,** 3660-3679.

Gilardi, G. & Sharf, I. 2002. Literature survey of contact dynamics modelling. *Mechanism and Machine Theory,* 37**,** 1213-1239.

Grady, D.E. & Kipp, M.E. 1985. Geometric statistics and dynamic fragmentation. *Journal of Applied Physics,* 58**,** 1210-1222.

Graff, K.F. 1975. *Wave motion in elastic solids*: Dover Pubns.

Hao, H., Li, Z.X., Zhu, X.Q. & Wang, M. 2008. *Blast fragments prediction - current approaches and challenges*.

Haskett, M.H., Oehlers, D.J., Mohamed, S., Mohamed, A.S.; Wu, C. 2009 Rigid body moment-rotation mechanism for reinforced concrete beam hinges, *Engineering Structures*; 31(5), 1032-1041

Highways Agency 2002. Strengthening of concrete bridge supports using fibre reinforced polymers. *BD 84/02.* UK: Department for Transport.

Highways Agency 2004. The design of highway bridges for vehicle collision loads. *BD 60/04.* UK: Department for Transport.

Isaac, P., Darby, A., Ibell, T. and Evernden, M. C., 2011. Plasticity based approach for evaluating the blast response of RC columns retrofitted with FRP. *International Journal of Protective Structures (IJPS),* 2 (3), pp. 367-380.

Isaac, P., Darby, A., Ibell, T. and Evernden, M. C. 2013. Influence of loading-rate on the failure mode of RC columns. *Proceedings of the ICE-Engineering and Computational Mechanics*, 167 (4), pp 194-203

John, R. & Shah, S.P. 1990. Mixed-mode fracture of concrete subjected to impact loading. *Journal of Structural Engineering-Asce,* 116**,** 585-602.

Kinney, G.F. 1962. *Explosive shocks in air,* New York: Macmillan.

Kishi, N., Mikami, H., Matsuoka, K.G. & Ando, T. 2002. Impact behavior of shear-failure-type rc beams without shear rebar. *International Journal of Impact Engineering,* 27**,** 955-968.

Krauthammer, T., Shanaa, H.M. & Assadi, A. 1994. Response of structural concrete elements to severe impulsive loads. *Computers & Structures,* 53**,** 119-130.

Lee, Y., Hamilton, J. & Sullivan, J. 1983. The lumped parameter method for elastic impact problems. *Journal of Applied Mechanics,* 50**,** 823.

Li, Q.M. & Meng, H. 2002. Pressure-impulse diagram for blast loads based on dimensional analysis and single-degree-of-freedom model. *Journal of Engineering Mechanics-Asce,* 128**,** 87-92.

Lu, Y. & Xu, K. 2004. Modelling of dynamic behaviour of concrete materials under blast loading. *International Journal of Solids and Structures,* 41**,** 131-143.

Magnusson, J., Hallgren, M. & Ansell, A. 2010. Air-blast-loaded, high-strength concrete beams. Part i: Experimental investigation. *Magazine of Concrete Research,* 62**,** 127-136.

Malvar, L.J. 1998. Review of static and dynamic properties of steel reinforcing bars. *Aci Materials Journal,* 95**,** 609-616.

Malvar, L.J. & Crawford, J.E. 1998. Dynamic increase factors for concrete. *Twenty-Eighth DDESB Seminar.* Orlando, Fl.

Malvar, L.J., Crawford, J.E. & Morrill, K.B. 2007. Use of composites to resist blast. *Journal of Composites for Construction,* 11**,** 601-610.

Malvar, L.J. & Ross, C.A. 1998. Review of strain-rate effects for concrete in tension. *ACI Materials Journal,* 95**,** 735-739.

May, I.M., Chen, Y., Owen, D.R.J., Feng, Y.T. & Thiele, P.J. 2006. Reinforced concrete beams under drop-weight impact loads. *Computers and Concrete,* 3**,** 79-90.

Mays, G. & Smith, P.D. 1995. *Blast effects on buildings: Design of buildings to optimize resistance to blast loading,* New York: Thomas Telford.

Morison, C.M. 2006. Dynamic response of walls and slabs by single-degree-of-freedom analysis - a critical review and revision. *International Journal of Impact Engineering,* 32**,** 1214-1247.

Muszynski, L.C. & Purcell, M.R. 2003. Composite reinforcement to strengthen existing concrete structures against air blast. *Journal of Composites for Construction,* 7**,** 93-97.

Ngo, T., Mendis, P., Gupta, A. & Ramsay, J. 2007. Blast loading and blast effects on structures–an overview. *Electronic Journal of Structural Engineering,* 7**,** 76-91.

Olsson, R. 2000. Mass criterion for wave controlled impact response of composite plates. *Composites Part a-Applied Science and Manufacturing,* 31**,** 879-887.

Pierron, F., Sutton, M.A., Tiwari, V. 2011. Ultra high speed DIC and virtual fields method analysis of a three point bending test on an aluminium bar. *Experimental Mechanics*, 51, 537-563.

Qasrawi, Y. 2014. *The dynamic response of concrete filled FRP tubes subjected to blast and impact loads.* PHD, Queen's University, Ontario

Razaqpur, G., Mekky, W. & Foo, S. 2009. Fundamental concepts in blast resistance evaluation of structures. *Canadian Journal of Civil Engineering,* 36**,** 1292-1304.

Rodriguez-Nikl, T. 2006. *Experimental simulations of explosive loading on structural components: Reinforced concrete columns with advanced composite jackets.* PhD, University of California in San Diego.

Rodriguez-Nikl, T., Kobayashi, T., Oesterle, M.G., Lan, S., Morrill, K.B., Hegemier, G.A. & Seible, F. Year. Carbon fiber composite jackets to protect reinforced concrete columns against blast damage. *In,* 2009. ASCE.

Rossi, P. & Toutlemonde, E. 1996. Effect of loading rate on the tensile behaviour of concrete: Description of the physical mechanisms. *Materials and Structures,* 29**,** 116-118.

Saatci, S. & Vecchio, F.J. 2009a. Effects of shear mechanisms on impact behavior of reinforced concrete beams. *ACI Structural Journal,* 106**,** 1 78-86.

Saatci, S. & Vecchio, F.J. 2009b. Nonlinear finite element modelling of reinforced concrete structures under impact loads. *ACI Structural Journal,* 106**,** 717-725.

Silva, P.F., Mesia, W.D., Marzougui, D. & Badie, S.S. 2009. Performance evaluation of flexure impact resistance capacity of reinforced concrete members. *Aci Structural Journal,* 106**,** 726-736.

Smith, P.D. & Hetherington, J.G. 1994. *Blast and ballistic loading of structures,* Oxford: Butterworth-Heinemann.

Soroushian, P. & Obaseki, K. 1986. Strain-rate-dependent interaction diagrams for reinforced-concrete sections. *Journal of the American Concrete Institute,* 83**,** 108-116.

Suter, R. & Chang, K. Year. Reinforcement of bridge piers with frp sheets to resist vehicle impact: Tests on large concrete columns reinforced with aramid sheets. *In:* FRP Composites in Civil Engineering. Proceedings of the International Conference on FRP composites in Civil Engineering, 2001 Hong Kong.

Tachibana, S., Masuya, H. & Nakamura, S. 2010. Performance based design of reinforced concrete beams under impact. *Natural Hazards and Earth System Science,* 10**,** 1069-1078.

Takeda, J., Tachikawa, H. & Fujimoto, K. 1977. Effects of straining rate on deformation and fracture of reinforced concrete members. *Sixth World Conference on Earthquake Engineering.* New Delhi.

Tang, T. & Hamid Saadatmanesh, P. 2003. Behavior of concrete beams strengthened with fiber-reinforced polymer laminates under impact loading. *Journal of Composites for Construction,* 7**,** 209.

Teng, J., Chen, J., Smith, S. & Lam, L. 2002. *Frp-strengthened rc structures*: John Wiley & Sons Inc.

TM5-1300 1990. Structures to resist the effect of accidental explosions. Washington DC: US Department of Army, Navy and Air Force.

UFC 4-020-01. 2008. DoD Security Engineering Facilities Planning Manual. Washington DC: US Department of Defense

Vecchio, F.J. & Collins, M.P. 1986. The modified compression-field theory for reinforced concrete elements subjected to shear. *ACI Journal,* 83, 219-231

Vermorel, R., Vandenberghe, N. & Villermaux, E. 2009. Impacts on thin elastic sheets. *Proceedings of the Royal Society a-Mathematical Physical and Engineering Sciences,* 465**,** 823-842.

Wu, C.Q. & Hao, H. 2007. Numerical simulation of structural response and damage to simultaneous ground shock and airblast loads. *International Journal of Impact Engineering,* 34**,** 556-572.

Wu, C., Oehlers, D.J., Day, I.J. 2009. Layered Blast Capacity Analysis of FRP Retrofitted RC Member, *Advances in Structural Engineering*, 12(3), 435-449

Young, C.Y. & Budynas, R.G. 2002. *Roark's formulas for stress and strain, 7th Edition*: McGraw-Hill Professional

Zheng, D. & Li, Q. 2004. An explanation for rate effect of concrete strength baed on fracture toughness including free water viscosity. *Engineering Fracture Mechanics,* 71, 2319-2327